Measurement of the Pion Charge Exchange Differential Cross Section on Argon with the ProtoDUNE-SP Detector

Kang Yang

Lady Margaret Hall

University of Oxford

A thesis presented for the degree of

Doctor of Philosophy

Trinity 2023

Copyright © 2023 by Kang Yang
All Rights Reserved

Acknowledgements

I'm grateful to a special group of people who have greatly contributed to my academic journey and the completion of this thesis. Without them, I would have never reached this point, and their support and guidance have been crucial in shaping me as a researcher.

First and foremost, I want to thank my supervisor, Dr. Xianguo Lu. I feel incredibly fortunate to be working with you. You have provided me with numerous ideas and guidance, helping me grow both as a researcher and an individual. Your close supervision has made me work more efficiently, and I am proud to be your student.

A huge thank you goes out to everyone I met while working on ProtoDUNE, including Jake, Heng-Ye, Sungbin, Yinrui, Milo, and Richie. Special thanks to Sungbin; we had a great collaboration dinner in Manchester, and your advice has been crucial for my analysis. As I prepare to move to the LHCb experiment, I wish all of you the best and hope we can meet up again someday.

To Tingjun, Leigh, Wenqiang, and Tom, I extend my gratitude for your hard work leading efforts at ProtoDUNE and providing guidance on this analysis and other projects. Tom, your advice on using the Lagrangian Multiplier for kinematic fitting is immensely helpful. Tingjun, thank you for your close collaboration and unwavering support throughout this analysis. Leigh, your assistance has been invaluable. I am also thankful to Tingjun and Leigh for writing the recommendation letter for my postdoc application.

Thank you, Matthew Birch, whom I met during our first year of undergrads at Manchester. Being your lab partner for three years has been a great experience. Your introduction to the visual studio code has saved me so much time in coding and plotting, and I am delighted to continue working with you at Imperial again.

Lastly, I want to express my deepest thanks to my parents, whose unwavering support made my studies possible from the very beginning. Their constant encouragement and invaluable guidance have been instrumental in my educational journey.

Declaration

I hereby declare that this thesis is the result of my own original work, and I have not used any sources other than those duly acknowledged. Any quotes or ideas borrowed from other authors have been appropriately referenced within the thesis.

Kang Yang

17 September 2023

Abstract

The Deep Underground Neutrino Experiment (DUNE) utilizes Liquid Argon Time Projection Chamber (LArTPC) technology in its pursuit of uncovering the origins of matter. As a crucial prototype for the DUNE far detector (FD) module, ProtoDUNE-SP at CERN Neutrino Platform Facility employs a hadron test beam with a momentum range of 0.3 to 7 GeV$/c$ to study the detector response to particles that could be produced in the neutrino interactions at the DUNE FD. Furthermore, ProtoDUNE-SP is dedicated to testing event reconstruction and performing detector calibration under controlled conditions. Neutral pion reconstruction performance is an important benchmark of the calorimetric and tracking capability of LArTPC, and understanding neutral pion in LArTPC is crucial to characterize backgrounds to oscillation measurements and rare searches. To improve neutral pion reconstruction in LArTPC, a kinematic fitting algorithm is developed, achieving a 12% resolution in neutral pion energy in ProtoDUNE-SP. This enhancement enables the first measurements of the pion-argon charge exchange differential cross-section. By comparing these results with the current model, valuable constraints can be made to improve generator simulations in the future DUNE experiment.

Table of Contents

Introduction **1**

1 Neutrino Physics **3**

1.1 The Standard Model 3

1.2 A Brief History of Neutrinos 4

1.3 Neutrino Oscillation 6

1.4 CP-Violation and Mass Hierarchy 9

1.5 Neutrino Interactions and Nuclear Effects 11

1.6 Neutrino Sources 14

1.6.1 Artificial Neutrino Sources 15

1.6.2 Astrophysical Neutrino Sources 16

1.7 Neutrino Detection Methods 18

1.7.1 Liquid Scintillator Detector 18

1.7.2 Cherenkov Detector 18

1.7.3 Liquid Argon Time Projection Chamber 19

1.8 Ionisation Energy Loss of Charged Particles 20

2 The Deep Underground Neutrino Experiment **22**

2.1 Experiment Overview 22

2.1.1 Beam 23

2.1.2 Near Detector 24

2.1.3 Far Detector 26

2.2 DUNE's Research Goal 27

2.3 Significance of Secondary Pion Interactions 29

3 ProtoDUNE-SP Detector **31**

3.1 Beamline . . . 31

3.2 Detector Design and Construction . . . 35

3.2.1 Cryostat . . . 37

3.2.2 Time Projection Chamber . . . 39

3.2.3 Photon Detector System . . . 40

3.2.4 Cosmic Ray Tagger . . . 42

3.2.5 Data Acquisition, Timing and Trigger System . . . 42

3.3 Detector Calibration . . . 43

3.3.1 Space Charge Effect . . . 44

3.3.2 Recombination . . . 46

3.3.3 Drift Electron Lifetime . . . 47

3.3.4 Charge and Energy Calibration . . . 49

3.4 Simulation and Reconstruction Chain . . . 51

3.4.1 TPC Signal Processing and Hit Finding . . . 52

3.4.2 Pandora . . . 53

3.5 Event Display . . . 55

3.6 Hadronic Cross-Section Measurements in Argon . . . 58

3.6.1 Thin-Slice Method . . . 58

3.6.2 Energy-Slice Method . . . 60

4 Transverse Kinematic Imbalance **64**

4.1 Definition . . . 64

4.2 Longitudinal Momentum Imbalance . . . 68

4.3 Predictions in DUNE ND-GAr . . . 71

4.3.1 Understanding the Resonant Production . . . 75

4.4 Predictions in ProtoDUNE-SP . . . 77

5 Kinematic Fitting **81**

5.1 Method of Lagrange Multiplier . . . 82

5.1.1 Double Minimisation . . . 84

5.2 Theory of Kinematic Fitting 87
5.2.1 Monte-Carlo Example 88

6 Particle Identification and Selection 90
6.1 Beam Pion Selection 91
6.2 Daughter Particles Identification 103
6.2.1 Track Selection 105
6.2.1.1 Protons 107
6.2.1.2 Charged Pions 111
6.2.2 Shower Selection 113
6.3 Particle Selection Efficiency 116

7 Neutral Pion Reconstruction 118
7.1 Decay Kinematics 119
7.2 Single Gamma Reconstruction Performance 120
7.3 Energy Correction in Shower Reconstruction 126
7.4 Neutral Pion Reconstruction 129
7.5 Improved Measurement by Kinematic Fitting 134

8 Measurement of the Pion Charge Exchange Cross-section 139
8.1 Signal Definition 139
8.2 Pion Charge Exchange Event Selection 141
8.3 Analysis Strategy 143
8.4 Pion Beam Energy Measurement 144
8.5 Control Samples 146
8.6 Sideband Background Tuning 151
8.7 Incident and Interacting Pion Events 156
8.8 Unfolding Procedure 159
8.9 Systematic Uncertainty 163
8.10 Results with Systematic Errors 166

9 Conclusion **170**

List of Abbreviations **182**

Appendix A Beam Scraper Definition **185**

Appendix B Reconstruction Bias and Resolution **186**

Appendix C Single Gamma Stepwise Comparison **189**

Appendix D Shower Energy Correction **191**

Appendix E Neutral Pion Energy Calculation **192**

Appendix F Covariance Matrix in Kinematic Fitting **193**

Appendix G Kinematic Fitting Performance **194**

Appendix H Neutral Pion Unfolding **196**

Appendix I Neutral Pion Systematic Uncertainty **197**

List of Figures

Figure 1.1 The Standard Model 4
Figure 1.2 Neutrino Mass Hierarchy 11
Figure 1.3 Nuclear Effect in Neutrino Interactions 14
Figure 1.4 Accelerator Neutrinos 16
Figure 1.5 Ionisation Energy Loss Curves 21

Figure 2.1 DUNE Experiment Setup 23
Figure 2.2 DUNE Unoscillated Neutrino Fluxes 24
Figure 2.3 DUNE Near Detector Hall 25
Figure 2.4 Underground Caverns for DUNE Far Detector 27

Figure 3.1 H4 Very Low Energy Beamline 32
Figure 3.2 Beamline Instrumentation 33
Figure 3.3 Time of Flight Particle Identification 35
Figure 3.4 One View of ProtoDUNE-SP LArTPC 36
Figure 3.5 Membrane Cryostat Layout 38
Figure 3.6 Front View of ProtoDUNE-SP Anode Plane 40
Figure 3.7 The Operating Principle of the LArTPC 41
Figure 3.8 Space Charge Effect in ProtoDUNE-SP 44
Figure 3.9 Electron Lifetime in ProtoDUNE-SP 48
Figure 3.10 2D Cluster Producing Algorithm 54
Figure 3.11 Pandora Reconstruction Chain 55
Figure 3.12 Elastic Scattering Event Display 56
Figure 3.13 Charge Exchange Scattering Event Display 57
Figure 3.14 LArTPC Thin Slicing 60

Figure 3.15 Populating Cross-Section Histograms 61

Figure 4.1 Transverse Kinematic Imbalance Variables 65
Figure 4.2 Longitudinal Missing Momentum and Polar Angle 69
Figure 4.3 Geometric Illustration of Missing Momentum 70
Figure 4.4 QE Mode Only Fermi Motion Distribution 70
Figure 4.5 Transverse Boosting Angle in ND-GAr 72
Figure 4.6 Struck Neutron Momentum in ND-GAr 74
Figure 4.7 New Decomposition in RES Mode 76
Figure 4.8 TKI Definition in ProtoDUNE-SP 78
Figure 4.9 ProtoDUNE-SP Transverse Boosting Angle 80
Figure 4.10 ProtoDUNE-SP Struck Neutron Momentum 80

Figure 5.1 Visualization of Method of Lagrangian Multiplier 83
Figure 5.2 Double Minimisation Process 85
Figure 5.3 Lagrange Multipliers Example 86
Figure 5.4 Toy Example Kinematic Fitting Comparison 89

Figure 6.1 Beam Trigger - Distribution of Beam EndZ 92
Figure 6.2 Beam Start Position Distribution 93
Figure 6.3 Beam Quality Cut Start Z 95
Figure 6.4 Beam Quality Cut Angle 95
Figure 6.5 Beam Quality - Distribution of Beam EndZ 96
Figure 6.6 APA3 - Distribution of Beam EndZ 97
Figure 6.7 Beam End Vertex Michel Score 98
Figure 6.8 Beam Proton χ^2/NDF 98
Figure 6.9 Final - Distribution of Beam EndZ 99
Figure 6.10 Beam Scraper Definition 100
Figure 6.11 Beam Scraper Cuts Performance 101
Figure 6.12 Beam Momentum Reconstruction Bias 103
Figure 6.13 Daughter Particle Size 104

Figure 6.14 CNN Track Score Distribution . . . 106
Figure 6.15 Track Completeness VS nHits . . . 106
Figure 6.16 Track Truncated Mean $\mathrm{d}E/\mathrm{d}x$ . . . 108
Figure 6.17 Daughter Tracks Proton χ^2 Distribution . . . 108
Figure 6.18 Reconstructed Proton Momentum . . . 110
Figure 6.19 Proton Momentum Reconstruction Bias . . . 110
Figure 6.20 Reconstructed Pion Momentum . . . 112
Figure 6.21 CNN EM Shower Score Distribution . . . 112
Figure 6.22 Definitions of Shower Distance and Impact Parameter . . . 113
Figure 6.23 Reconstructed Shower Distance Distribution . . . 115
Figure 6.24 Average Completeness Versus Impact Parameter . . . 115
Figure 6.25 Daughter Particle Selection Efficiency . . . 117

Figure 7.1 Neutral Pion True Energy Spectrum . . . 120
Figure 7.2 Step-wise Comparison in Single Gamma Sample . . . 122
Figure 7.3 Mean Bias in Hits Energy . . . 123
Figure 7.4 Resolution in Hits Energy . . . 123
Figure 7.5 Pandora Shower Energy Reconstruction Bias . . . 124
Figure 7.6 Angular Dependence of Pandora Shower Reconstruction . . . 125
Figure 7.7 Summary of the Performance . . . 126
Figure 7.8 Shower Energy Resolution Versus True Photon Energy . . . 127
Figure 7.9 Shower Energy Correction Function . . . 127
Figure 7.10 Shower Energy After Correction . . . 129
Figure 7.11 Neutral Pion Invariant Mass . . . 130
Figure 7.12 Opening Angle of Shower Pair . . . 132
Figure 7.13 Neutral Pion Selection Efficiency . . . 132
Figure 7.14 Neutral Pion Total Energy . . . 133
Figure 7.15 Neutral Pion Theta Angle . . . 133
Figure 7.16 Absolute Difference in Opening Angle . . . 135
Figure 7.17 Neutral Pion Energy Post-Fitting . . . 135

Figure 7.18 1D π^0 Energy Resolution Improvement . . . 138
Figure 7.19 2D π^0 Energy Resolution Improvement . . . 138

Figure 8.1 Signal and Background Definition . . . 140
Figure 8.2 Event Selection Statistics . . . 141
Figure 8.3 Roadmap to Cross-section Measurement . . . 143
Figure 8.4 Upstream Energy Loss . . . 145
Figure 8.5 Stopping Muon Sample . . . 148
Figure 8.6 Beam Momentum Reweight . . . 148
Figure 8.7 Long Track Sample . . . 150
Figure 8.8 Muon Reweighting . . . 150
Figure 8.9 Sideband Channels Zero π^0 . . . 152
Figure 8.10 Sideband Channels Multiple π^0 . . . 152
Figure 8.11 Sideband Scaling Factors . . . 153
Figure 8.12 Interacting Energy After Tuning . . . 153
Figure 8.13 π^0 Mass Sideband . . . 155
Figure 8.14 π^0 Kineitc Energy After Tuning . . . 155
Figure 8.15 Initial Energy Distribution . . . 157
Figure 8.16 Interacting Energy Distribution . . . 157
Figure 8.17 CEX Interacting Energy . . . 158
Figure 8.18 π^0 Kinetic Energy . . . 158
Figure 8.19 Energy Histogram Unfolding . . . 161
Figure 8.20 Interacting Energy Unfolding Efficiency . . . 162
Figure 8.21 Interacting Energy Response Matrix . . . 162
Figure 8.22 Total Fractional Uncertainty . . . 164
Figure 8.23 Integrated CEX Cross-Section Measurement . . . 167
Figure 8.24 Differential π^0 KE Cross-Section Measurement . . . 168
Figure 8.25 Differential θ_{π^0} Cross-Section Measurement . . . 168

Figure A.1 Beam Scraper Definition . . . 185

Figure B.1 Beam Momentum Reconstruction Bias 186
Figure B.2 Beam Angle Reconstruction Bias 187
Figure B.3 Proton Momentum and Angle Reconstruction Bias 188

Figure C.1 Single Gamma GEANT4 Bias 189
Figure C.2 Single Gamma Pandora Bias 190

Figure D.1 Shower Energy Correction Slices 191

Figure E.1 Different π^0 Energy Calculation Methods 192

Figure F.1 Covariance Matrix 193

Figure G.1 Shower Energy Kinematic Fitting 194
Figure G.2 Kinematic Fitting Convergence Rate 195

Figure H.1 Unfolded Neutral Pion Histograms 196

Figure I.1 Multi-Universe Approach Evaluation 197
Figure I.2 Systematic Uncertainty of Differential π^0 Kinematics 198

List of Tables

Table 1.1 Forces Experienced by Twelve Fundamental Fermions 5
Table 1.2 Three ν Oscillation Parameters 12

Table 2.1 DUNE Physics Milestones in Exposure Years 29

Table 3.1 Identification of 1 GeV$/c$ Beam Particle Types 34
Table 3.2 Parameters of Energy Calibration 51

Table 6.1 Beam Cuts Purity and Efficiency 102
Table 6.2 Summary of Proton Selections 109
Table 6.3 Summary of Pion Selections 111
Table 6.4 Summary of Shower Selections 114

Table 7.1 Single Gamma Variable Definitions 121
Table 7.2 Summary of Neutral Pion Selections 131

Table 8.1 CEX Event Purity and Efficiency 142
Table 8.2 Summary of the Systematic Uncertainties 165

Table I.1 Summary of the T_{π^0} Systematic Uncertainties 199
Table I.2 Summary of θ_{π^0} Systematic Uncertainties 200

Introduction

Neutrinos, the most abundant constituents of our universe, are gaining significant attention at the forefront of particle physics. The way they act, as revealed through neutrino oscillation, challenges our conventional understanding of neutrinos and their properties. Even more intriguingly, the study of neutrino oscillation could hold the key to understanding why our universe is filled with matter rather than equal amounts of matter and antimatter. This puzzle, termed CP-violation, is a mystery physicists are eager to unravel.

The field of neutrino oscillation research is now in a phase that demands precise measurements. Achieving such precision necessitates great efforts to minimize systematic uncertainties. This pursuit of precision has led the DUNE experiment to embark on the prototyping of its far detector with ProtoDUNE-SP. With a capacity of 0.77 kt of liquid argon, ProtoDUNE-SP not only serves as a platform for testing DUNE's detector components and refining event reconstruction but also acts as the starting point for the detector calibration. Moreover, ProtoDUNE-SP collects valuable physics measurements by utilizing its charged particle beamline, providing essential inputs for simulations in DUNE.

Among the particles provided by this beamline, the π^+ holds particular significance for investigation due to its frequent occurrence in the final state of neutrino interactions. Its presence can impact the accurate reconstruction of the incoming neutrino's energy or its flavour identification. For instance, when a π^+ emerges from a neutral current interaction involving ν_μ, it might undergo charge exchange with nearby argon, transforming into a π^0. This π^0 decays into two photons, generating showers in the detector. These showers could mimic an electron shower, potentially leading to the misidentification of a ν_μ neutral current interaction as a ν_e charged current interaction. DUNE's oscillation analyses address these errors by employing Monte Carlo simulations to model events in its far detector. Nevertheless, if the rate of pion charge exchange interactions is miscalculated, it could introduce biases in DUNE's neutrino oscillation measurements. This thesis presents the first measurement of π^+-Ar charge exchange differential cross-section, aiming to reduce these systematic uncertainties within oscillation analyses in DUNE.

This thesis is structured as follows:

Chapter 1 presents a comprehensive review of neutrino oscillation, neutrino production, and detection methods. Additionally, it explores various nuclear effects that have the potential to complicate neutrino measurements.

Chapter 2 provides an overview of the DUNE detector design and its physics program, along with the motivation for the analysis conducted in this thesis.

Chapter 3 describes the ProtoDUNE-SP detector employed in this study, including its design, calibration, and the methodology used to extract cross-section information.

Chapter 4 introduces a novel kinematic variable called transverse kinematic imbalance and explores its application to DUNE and ProtoDUNE-SP using Monte Carlo simulations.

Chapter 5 delves into the kinematic fitting technique used in this analysis to enhance the accuracy of neutral pion energy measurements.

Chapter 6 focuses on the development of the pion beam and final state particle selection criteria in ProtoDUNE-SP.

Chapter 7 discusses the process of shower energy correction and neutral pion reconstruction, highlighting improvements in neutral pion energy measurement achieved through kinematic fitting.

Chapter 8 presents the results, including both integrated and differential π^+-Ar charge exchange cross-section measurements, and addresses potential systematic uncertainties.

Chapter 9 summarizes the key aspects and conclusions drawn from this thesis.

1 | Neutrino Physics

1.1 The Standard Model

The Standard Model is a theoretical framework in particle physics that provides a description of the fundamental constituents of matter and their interactions. It is based on the principles of quantum field theory and incorporates the gauge symmetry group $SU(3) \times SU(2)_L \times U(1)_Y$, which encompasses the strong and electroweak forces. The Standard Model, while successful in explaining various experimental results, remains incomplete, lacking an explanation for gravity and the presence of dark matter. Ongoing efforts, such as those at the Large Hadron Collider (LHC) at CERN [1], aim to extend the Standard Model and search for new particles and interactions.

The particles in the Standard Model are divided into two main categories, fermions and bosons, as shown in Fig. 1.1. Fermions are the building blocks of matter and include the quarks and leptons, which are divided into three generations. Bosons are the force carriers that mediate the interactions between fermions. These include the photon, which is responsible for the electromagnetic force, the W and Z bosons that govern the weak force, and the eight gluons that mediate the strong force. The Higgs boson, which was found by the ATLAS and CMS experiments at the LHC in 2012 [2], is the last piece of the Standard Model. It plays a unique role and holds significant importance within the Standard Model. Specifically, it provides the mechanism through which all other particles obtain their mass.

The twelve fundamental fermions can be classified according to the interactions they undergo, as outlined in Table 1.1. Neutrinos, along with electrons, muons, and tau leptons, are fundamental particles of the lepton family, which do not experience the strong force. Being electrically neutral, neutrinos also do not interact via the electromagnetic force. Consequently, neutrinos only participate in the weak interaction, which makes their detection and study challenging. In the Standard Model, there are three flavours of neutrinos: electron neutrinos (ν_e), muon neutrinos (ν_μ), and tau neutrinos (ν_τ). Initially, neutrinos

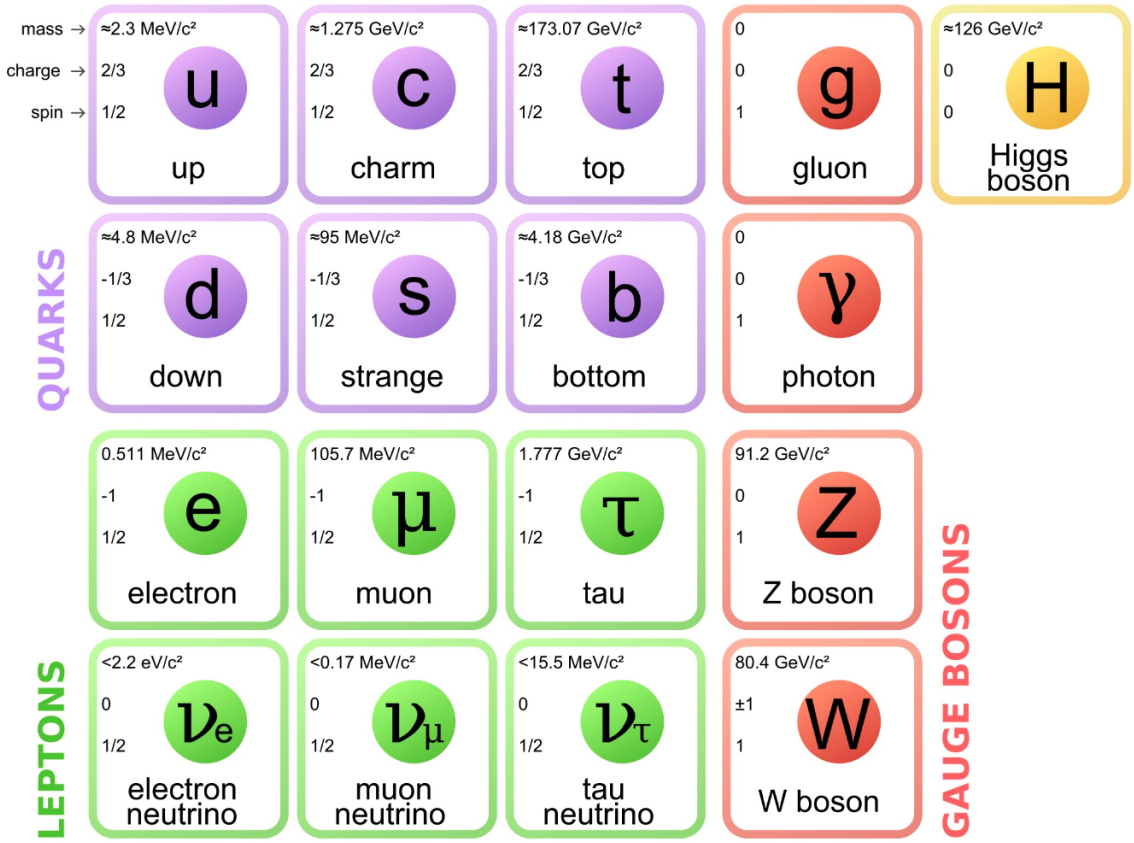

Figure 1.1: Elementary particles of the Standard Model. These particles are divided into quarks, leptons and gauge bosons. The mass, charge and spin of each particle are denoted on the left-hand side of each box. Taken from [3].

were assumed to be massless to explain the observed parity violation in weak interactions. However, this simplistic view of neutrinos was challenged by the solar neutrino problem. Observations showed that only one-third of the expected number of neutrinos from the Sun were detected [4], conflicting with predictions based on the solar model. This discrepancy indicated the existence of new physics beyond the Standard Model.

1.2 A Brief History of Neutrinos

Over the past few decades, our understanding of neutrino physics with the Standard Model has undergone a remarkable revolution. The origins of neutrino research can be traced back to 1930 when Wolfgang Pauli proposed the existence of a new particle with specific properties to explain the conservation of momentum and energy in beta decays [5]. It was

Table 1.1: A summary of forces experienced by twelve different fermions in the Standard Model, where the gravity force has been neglected.

				Strong	Electromagnetic	Weak
up-type quarks	u	c	t	✓	✓	✓
down-type quarks	d	s	b	✓	✓	✓
charged leptons	e	μ	τ		✓	✓
neutrinos	ν_e	ν_μ	ν_τ			✓

Enrico Fermi who coined the term "neutrino", derived from the Italian word meaning "little neutral one", to capture the essential physical properties of this particle. Neutrinos have an almost negligible mass and carry no electric charge. Consequently, their interactions with other particles are solely mediated by the weak force, making them exceptionally challenging to detect using conventional particle detectors.

In 1933, Fermi successfully incorporated neutrinos into his theory of beta decay [6], providing a comprehensive framework for understanding this fundamental process. However, despite theoretical advancements, the direct detection of neutrinos remained an elusive task. Pauli himself expressed concerns about postulating a particle that seemed beyond the reach of experimental detection. Fortunately, a breakthrough came with the discovery of a copious source of antineutrinos produced through nuclear fission. In 1953, Frederick Reines and Clyde Cowan [7] successfully detected neutrinos using a liquid scintillator detector, capturing neutrino interactions through the inverse beta decay process,

$$\bar{\nu}_e + \mathrm{p} \rightarrow e^+ + \mathrm{n}. \tag{1.1}$$

The interaction yields an immediate burst of light as the positron annihilates with an electron, generating two high-energy gamma (γ) rays. Subsequently, the neutron moves about a few microseconds before being captured by an atomic nucleus, resulting in the emission

of another gamma-ray due to the release of excess energy. The distinctive "delayed" coincidence of both occurrences, positron annihilation and neutron capture, provides a unique signature of an antineutrino interaction.

1.3 Neutrino Oscillation

Neutrino oscillations are phenomena that have revolutionized the field of neutrino physics. In the Standard Model, neutrinos are assumed to be massless particles, and therefore, it was initially believed that they did not undergo mixing or oscillations. However, experiments conducted in the late 20th century provided evidence that neutrinos do, in fact, have mass. Neutrino oscillation is a quantum mechanical phenomenon that arises due to the fact that neutrinos have slightly different masses and travel at slightly different energies, leading to a change in their flavour as they propagate through space.

The neutrino oscillation is described by the mixing of the three known neutrino flavours: electron neutrinos, muon neutrinos, and tau neutrinos. Neutrino mixing is described by the Pontecorvo-Maki-Nakagawa-Sakata (PMNS) matrix [8], which relates the three flavour eigenstates (ν_e, ν_μ, and ν_τ) to the three mass eigenstates (ν_1, ν_2, and ν_3) as,

$$\begin{pmatrix} \nu_{\mathrm{e}} \\ \nu_{\mu} \\ \nu_{\tau} \end{pmatrix} = \mathrm{U}_{\mathrm{PMNS}} \begin{pmatrix} \nu_1 \\ \nu_2 \\ \nu_3 \end{pmatrix} = \begin{pmatrix} \mathrm{U}_{\mathrm{e}1} & \mathrm{U}_{\mathrm{e}2} & \mathrm{U}_{\mathrm{e}3} \\ \mathrm{U}_{\mu 1} & \mathrm{U}_{\mu 2} & \mathrm{U}_{\mu 3} \\ \mathrm{U}_{\tau 1} & \mathrm{U}_{\tau 2} & \mathrm{U}_{\tau 3} \end{pmatrix} \begin{pmatrix} \nu_1 \\ \nu_2 \\ \nu_3 \end{pmatrix}. \tag{1.2}$$

This matrix contains three mixing angles, $\theta_{12}, \theta_{23}, \theta_{13}$, and one complex phase δ_{CP},

$$
\begin{aligned}
\mathrm{U_{PMNS}} &= \begin{pmatrix} 1 & 0 & 0 \\ 0 & \mathrm{c}_{23} & \mathrm{s}_{23} \\ 0 & -\mathrm{s}_{23} & \mathrm{c}_{23} \end{pmatrix} \begin{pmatrix} \mathrm{c}_{13} & 0 & \mathrm{s}_{13}e^{-i\delta_{\mathrm{CP}}} \\ 0 & 1 & 0 \\ -s_{13}e^{i\delta_{\mathrm{CP}}} & 0 & \mathrm{c}_{13} \end{pmatrix} \begin{pmatrix} \mathrm{c}_{12} & \mathrm{s}_{12} & 0 \\ -\mathrm{s}_{12} & \mathrm{c}_{12} & 0 \\ 0 & 0 & 1 \end{pmatrix} \\
&= \begin{pmatrix} \mathrm{c}_{12}\mathrm{c}_{13} & \mathrm{s}_{12}\mathrm{c}_{13} & \mathrm{s}_{13}e^{-i\delta_{\mathrm{CP}}} \\ -\mathrm{s}_{12}\mathrm{c}_{23} - \mathrm{c}_{12}\mathrm{s}_{23}\mathrm{s}_{13}e^{i\delta_{\mathrm{CP}}} & \mathrm{c}_{12}\mathrm{c}_{23} - \mathrm{s}_{12}\mathrm{s}_{23}\mathrm{s}_{13}e^{i\delta_{\mathrm{CP}}} & \mathrm{s}_{23}\mathrm{c}_{13} \\ \mathrm{s}_{12}\mathrm{s}_{23} - \mathrm{c}_{12}c_{23}\mathrm{s}_{13}e^{i\delta_{\mathrm{CP}}} & -\mathrm{c}_{12}\mathrm{s}_{23} - \mathrm{s}_{12}\mathrm{c}_{23}\mathrm{s}_{13}e^{i\delta_{\mathrm{CP}}} & \mathrm{c}_{23}\mathrm{c}_{13} \end{pmatrix},
\end{aligned} \tag{1.3}
$$

where c_{ij} and s_{ij} represents the $\cos_{ij}$ and $\sin_{ij}$, respectively. The matrix element describes the amount of mixing between the different weak eigenstates and is experimentally determined.

Several key aspects of neutrino oscillation can be derived in the approximation of only two neutrino flavour mixing [9]. In the two-flavour treatment, the mixing matrix between mass eigenstates and weak eigenstates can be expressed with a single mixing angle θ as,

$$
\begin{pmatrix} \nu_\alpha \\ \nu_\beta \end{pmatrix} = \begin{pmatrix} \cos\theta & \sin\theta \\ -\sin\theta & \cos\theta \end{pmatrix} \begin{pmatrix} \nu_1 \\ \nu_2 \end{pmatrix}. \tag{1.4}
$$

Suppose at time t = 0, a neutrino is produced with flavour α. The wavefunction of this flavour state ν_α is the coherent linear superposition of two mass state, ν_1 and ν_2,

$$
|\psi(0)\rangle = |\nu_\alpha\rangle \equiv \cos\theta\,|\nu_1\rangle + \sin\theta\,|\nu_2\rangle\,. \tag{1.5}
$$

The state subsequently evolves with the time dependence of the mass state. If the neutrino interacts at a space-time point with time T and distance L along its travel, then the neutrino state is

$$|\psi(L,T)\rangle = \cos\theta\,|\nu_1\rangle\, e^{-i(E_1T-p_1L)} + \sin\theta\,|\nu_2\rangle\, e^{-i(E_2T-p_2L)}, \tag{1.6}$$

where E_i and p_i correspond to the energy and momentum of the mass eigenstate ν_i. Eq. 1.6 can be expressed in terms of the flavour eigenstates as,

$$\begin{aligned}|\psi(L,T)\rangle = \cos\theta(\cos\theta\,|\nu_\alpha\rangle - \sin\theta\,|\nu_\beta\rangle)e^{-i(E_1T-p_1L)} \\ + \sin\theta(\sin\theta\,|\nu_\alpha\rangle + \cos\theta\,|\nu_\beta\rangle)e^{-i(E_2T-p_2L)}.\end{aligned} \tag{1.7}$$

The relative sizes of two flavour components of the wavefunction can be obtained as,

$$|\psi(L,T)\rangle = c_\alpha\,|\nu_\alpha\rangle + c_\beta\,|\nu_\beta\rangle\,, \tag{1.8}$$

$$c_\alpha = \langle\nu_\alpha|\psi\rangle = e^{-i(E_1T-p_1L)}\left[\cos^2\theta + e^{i\{(E_1-E_2)T-(p_1-p_2)L\}}\sin^2\theta\right], \tag{1.9}$$

$$c_\beta = \langle\nu_\beta|\psi\rangle = e^{-i(E_1T-p_1L)}\left[(e^{i\{(E_1-E_2)T-(p_1-p_2)L\}}-1)\cos\theta\sin\theta\right], \tag{1.10}$$

where one could assume that the momenta of the two mass eigenstates are equal, $p_1 = p_2 = p$, then the phase difference can be expressed as,

$$\begin{aligned}(E_1-E_2)T-(p_1-p_2)L &= \left[p\left(1+\frac{m_1^2}{p^2}\right)^{\frac{1}{2}} - p\left(1+\frac{m_2^2}{p^2}\right)^{\frac{1}{2}}\right]T \\ &\approx \frac{m_1^2-m_2^2}{2p}L.\end{aligned} \tag{1.11}$$

Then, writing $p = E_\nu$, the probability of a neutrino oscillating into a different flavour is,

$$P_{\alpha\to\beta,\alpha\neq\beta} = c_\beta c_\beta^* = \sin^2(2\theta)\,\sin^2\left(\frac{(m_1^2 - m_2^2)L}{4E_\nu}\right) \tag{1.12}$$

$$= \sin^2(2\theta)\,\sin^2\left(1.27\,\frac{\Delta m^2 L}{E_\nu}\,\frac{[\mathrm{eV}^2]\,[\mathrm{km}]}{[\mathrm{GeV}]}\right), \tag{1.13}$$

where α and β are two generic neutrino flavour states, Δm^2 is the mass square difference of these two states, L and E_ν are the oscillation distance and the neutrino energy, respectively. Eq. 1.13 is formulated using units that are well-adapted to the practical length and energy scales encountered, with L measured in km, Δm^2 in eV^2, and the neutrino energy in GeV. Therefore, the probability of finding the neutrino changing its flavour depends on the distance it has travelled and the neutrino energy.

Neutrino oscillations in matter refer to when neutrinos propagate through a dense medium, such as the Sun, where the electron density is high. In this case, the neutrinos can interact with the medium and undergo a phenomenon called the Mikheyev-Smirnov-Wolfenstein (MSW) effect [10], which can cause the oscillation parameters to be modified. The electrons can change the energy of the neutrinos through a process called coherent forward scattering. This process can cause the effective mass of the neutrinos to change, which modifies the neutrino mixing angles and can lead to enhanced or suppressed oscillations. The MSW effect depends on the density and profile of the medium through which the neutrinos are propagating. If the electron density is high, as in the core of the Sun, the MSW effect can lead to a resonant enhancement of the neutrino oscillations. The MSW effect has important implications for solar neutrino detection and has been experimentally verified by the Kamiokande [11] and SNO [12] experiments.

1.4 CP-Violation and Mass Hierarchy

The violation of parity was first proposed by Lee and Yang in 1956 [13], and it was followed by the famous Wu's experiment [14], which studied the nuclear β-decay of polarized cobalt-60,

$$^{60}\text{Co} \rightarrow {}^{60}\text{Ni}^{*} + e^{-} + \bar{\nu}_{e}. \tag{1.14}$$

In the experimental setup, cobalt-60 nuclei were aligned in a strong magnetic field, and the emitted electrons were detected at two different hemispheres relative to this axis. Since the magnetic field and spin are axial vectors that remain unchanged under a parity transformation (where spatial coordinates are reversed), only the momentum vector of the electrons is affected. According to the conservation of parity, the rate of electron emission should be the same before and after the parity transformation. However, experimental observations revealed that more electrons were emitted in the hemisphere opposite the direction of the magnetic field. This violation of parity indicates that the weak interaction does not conserve parity, and the V-A chiral structure of the weak charged current implies maximal parity violation. Furthermore, this violation of parity also implies a maximal violation of charge-conjugation symmetry, which involves replacing particles with their antiparticles.

Neutrino oscillations can also exhibit the charge parity (CP) violation, which refers to a violation of the combined symmetry of charge conjugation (C) and parity (P). In the case of neutrino oscillations, CP violation can arise due to a complex phase in the PMNS mixing matrix. The discovery of CP violation in the neutrino sector is of great interest to particle physicists, as it may help to explain the observed matter-antimatter asymmetry in the universe. However, the measurement of CP violation in neutrino oscillations is challenging due to the small size of the effect and the need for precise measurements of the neutrino mixing parameters.

Another important aspect of neutrino oscillations is the determination of the neutrino mass hierarchy, which refers to the ordering of the three neutrino mass eigenstates. There are two possible hierarchies as shown in Fig. 1.2, the normal hierarchy, in which the lightest mass eigenstate is ν_1, the next lightest is ν_2, and the heaviest is ν_3, or the inverted hierarchy, in which ν_3 is the lightest and ν_2 is the heaviest.

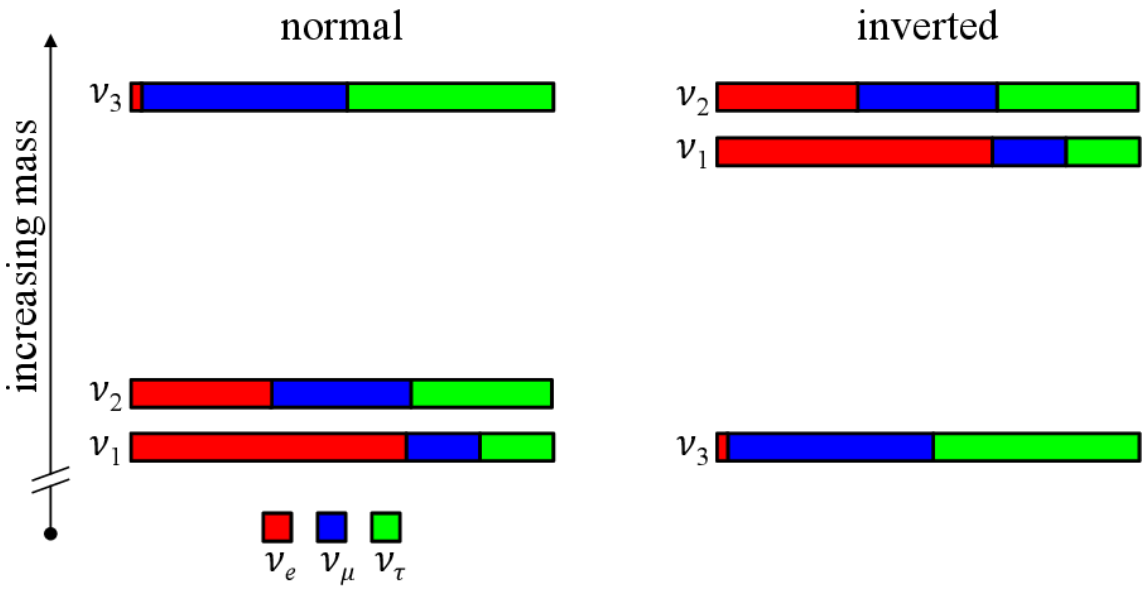

Figure 1.2: A schematic sketch of two possible neutrino mass orderings. Different colours indicate different flavour components in the mass eigenstate. Taken from [15].

The study of CP violation and mass hierarchy in neutrino oscillations is a topic of active research in particle physics and has important implications for our understanding of fundamental physics. The current world average values of the three mixing angles and the differences in the squares of the masses are summarized in Table 1.2 under the normal mass ordering assumption.

1.5 Neutrino Interactions and Nuclear Effects

The study of neutrinos poses unique challenges. In the GeV regime, the energy of neutrino beams is never monotonic. Even using the off-axis configuration where the detector is placed several degrees away from the beamline, the energy spectrum still has a significant spread. Understanding neutrino oscillations necessitates knowledge of both the interaction cross-sections and the initial neutrino energy. In principle, one could reconstruct the neutrino energy from the final state products in an exclusive measurement on an event-by-event basis. However, the lack of knowledge of nuclear physics is restricting us from reconstructing the initial neutrino energy precisely.

Table 1.2: A summary of the best-fit values for the three flavours of neutrino oscillation parameters obtained from various global analyses of neutrino data assuming the normal mass ordering [16].

Parameters	Best-Fit Value	3σ Range
$\theta_{12}[^\circ]$	$33.82^{+0.78}_{-0.76}$	$31.61 \rightarrow 36.27$
$\theta_{23}[^\circ]$	$48.3^{+1.2}_{-1.9}$	$40.8 \rightarrow 51.3$
$\theta_{13}[^\circ]$	$8.61^{+0.13}_{-0.13}$	$8.22 \rightarrow 8.99$
$\delta_{\mathrm{CP}}[^\circ]$	222^{+38}_{-28}	$141 \rightarrow 370$
$\Delta m^2_{21}[10^{-5}eV^2]$	$7.39^{+0.21}_{-0.20}$	$6.79 \rightarrow 8.01$
$\Delta m^2_{31}[10^{-3}eV^2]$	$2.449^{+0.032}_{-0.030}$	$2.358 \rightarrow 2.544$

Neutrino interactions can occur through different processes, including charged-current (CC) interactions and neutral-current (NC) interactions. In CC interactions, the neutrino interacts with a nucleon in the target nucleus, changing the identity of the nucleon and producing a charged lepton (an electron or muon). The interaction is mediated by the exchange of a W boson, and the cross section for this process is approximately proportional to the neutrino energy. Additionally, the detected lepton enables the determination of the neutrino's flavour. In NC interactions, the neutrino interacts with a nucleon in the target nucleus, transferring energy and momentum to the nucleus, while the neutrino itself remains unchanged. The interaction is mediated by the exchange of a Z boson. In experimental measurements, the observable is the recoil or break-up of the target nucleus.

In accelerator neutrino physics, where neutrinos have energies on the order of a few GeV, the primary focus lies in CC interactions, where the neutrino transforms into its charged lepton partner. Nevertheless, NC interactions, where the neutrino remains unchanged, also play a significant role. One area of interest is understanding how NC interactions generate background events in CC processes. Depending on the initial energy, neutrinos can interact with matters in several ways. At energy less than $\sim$ 1 GeV, the charged-current quasi-elastic interaction (CCQE) is the dominant process. Neutrino (anti-neutrino) scat-

ters from a neutron (proton) which will convert to a proton (neutron). This nucleon will be ejected along with the charged lepton partner in the final state. As energy increases, the neutrino is allowed to produce a Δ baryon, which will decay to a nucleon and produce extra pions. This process is referred to as resonant production (RES). Neutrinos with even higher energy could break up the nucleon and produce additional hadrons in the final state, known as deep inelastic scattering (DIS). These processes are relatively well studied on an isolated and static nucleon. However, most accelerator neutrino experiments used heavy nuclear targets (atomic number $Z \geq 6$), which complicates the situation.

In general, when considering a nuclear target, individual nucleons are not free and static except for hydrogen. Consequently, several nuclear effects introduce uncertainties in determining the initial neutrino energy spectrum and the interaction cross sections. Four main effects can modify the basic neutrino-nucleon interaction, as illustrated in Fig. 1.3. Firstly, it is well known that nucleons within the nucleus are not stationary. Nucleons suffer from the isotropic Fermi motion (FM), and their momentum is peaked at $\sim$ 0.2 GeV/c. Secondly, as nucleons are bound inside the nucleus, the energy required to release one of them needs to be considered in the calculation, which further complexes the kinematics. Thirdly, the electron-proton scattering experiment has revealed that approximately $\sim$ 20% of nucleons are correlated [17]. These correlated nucleons, primarily proton-neutron pairs, arise due to the presence of meson-exchanging currents (MEC) and short-range correlations (SRC). When a neutrino scatters from one nucleon in these pairs, the momentum transfer is shared between them. Consequently, two correlated nucleons might be knocked out, leading to a 2p2h process. Finally, the final-state interactions (FSIs) are present when final-state hadrons propagate out through the nuclear medium. FSIs can affect not only the neutrino energy spectrum but also the event topology. There is a finite probability that a pion produced in the RES process can be absorbed inside the nucleus, which mimics a CCQE event signal. Therefore, it is convenient to group the neutrino interactions according to the number of pions in the final state. The CC0π event is defined as one muon, any number of protons and zero pion in the final state and includes all types of interactions discussed above due to the pion absorption inside the nuclear medium.

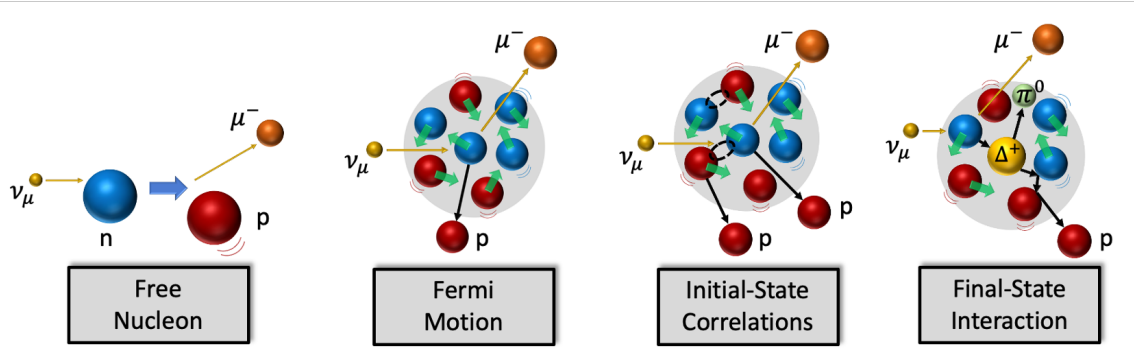

Figure 1.3: A cartoon diagram showing several nuclear effects - Fermi motion, initial state correlations, and final state interaction - that could modify the simple neutrino-nucleon interaction.

1.6 Neutrino Sources

Neutrinos are generated from various natural and artificial sources, such as nuclear reactions in stars like the sun, radioactive decay, and particle accelerators. The fundamental principles governing neutrino production sources, as outlined by Fred Reines in a 1960 review article [18], have remained largely unchanged. These principles can be summarized as follows:

- Fission reactors are an optimal source for generating low-energy $\bar{\nu}_e$.
- The production of ν_μ ($\bar{\nu}_\mu$) involves allowing π^+ (π^-) to decay in flight while stopping the other products with a dense absorber.
- The Sun is a rich source of ν_e. However, the detectability is limited to high-energy solar neutrinos produced from the fusion side chains of boron (^{8}B) and beryllium (^{7}Be).
- Significant fluxes of neutrinos from charged pion decay are expected as a result of cosmic rays colliding with the Earth's atmosphere.
- High-energy neutrinos emitted by astrophysical objects provide unique information which is not obtainable from cosmic rays or photons due to their deflection by the Galaxy's magnetic field and absorption by dense matter, respectively.

1.6.1 Artificial Neutrino Sources

Artificial neutrinos can be produced through two main principles [19]. Fission reactors produce $\bar{\nu}_e$ via the beta decay of fission fragments, while the high-energy protons colliding with a fixed target leads to the production of ν_μ ($\bar{\nu}_\mu$) through the decay of pions in flight.

Neutrinos are produced in fission reactors when heavy nuclei, like U-235, fragment and create unstable fission fragments with an excess of neutrons. These fragments undergo beta decay, resulting in the release of approximately 200 MeV of energy and about 6 electron-type antineutrinos per fission event. Understanding the neutrino energy spectrum is crucial, but it poses a challenge due to the complex nature of nuclear fission. The interaction probability of neutrinos and the phenomenon of neutrino oscillation both depend on the energy of the neutrinos. There are two methods to calculate the spectrum:

- The neutrino energy spectrum can be determined through fundamental calculations, utilizing the data collected over the past several decades on fission products and their associated beta-decay spectra.
- Electrons and neutrinos produced through beta decay have correlated energy spectra. The neutrino spectrum can be deduced from the measured electron spectrum, along with prior knowledge about the underlying beta decay process.

Therefore, modern reactor neutrino experiments often consist of a near detector (ND) located in close proximity to the reactor and a far detector (FD) placed at a carefully chosen distance. This configuration allows for the examination of the beam's properties as they evolve with distance. Analyzing the ratios between the measurements obtained from the near and far detectors provides numerous benefits, including the cancellation of uncertainties associated with the reactor neutrino flux.

The production of accelerator neutrinos is illustrated in Fig. 1.4. Initially, the high-energy proton beam is extracted from the synchrotron accelerator. These protons are then directed towards a secondary target, leading to collisions that generate charged pions and kaons as secondary particles. Magnetic horns are employed to manipulate and focus these

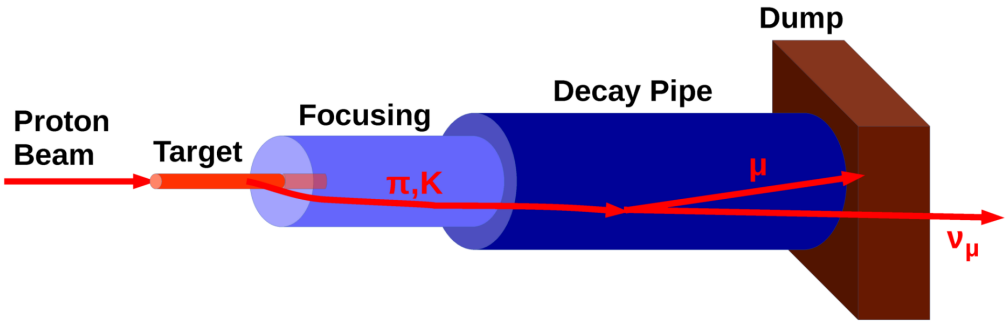

Figure 1.4: A schematic sketch of a typical neutrino beam production procedure. Both neutrino and anti-neutrino beams can be produced by switching modes of the focusing horns to select pions of the preferred charge. Taken from [15].

secondary particles into a lengthy decay pipe, where they can decay while in flight. Neutrinos are produced as decay products, following the Lorentz boost, in a direction similar to that of the focused charged meson beam. To separate the neutrinos from other particles, including remaining protons and other decay products, a dense absorber is positioned at the end of the decay pipe. This absorber stops all particles except the neutrinos. The final neutrino beam, which has a relatively wide energy spectrum, is collimated and points toward the detector. Production of beyond-the-Standard-Model neutrinos at conventional accelerator neutrino beamline is also being considered [20].

1.6.2 Astrophysical Neutrino Sources

One of the most striking phenomena in neutrino physics, neutrino oscillations, was first observed and subsequently discovered through the study of neutrinos originating from the Sun and the Earth's atmosphere.

The Sun serves as an abundant source of neutrinos. The emission of neutrinos arises from the conversion of protons to neutrons during the fusion process. Although the flux of solar neutrinos is enormous, the majority of them originate from the initial production of deuterium, known as pp neutrinos, which have very low energy and are challenging to detect. Therefore, most experiments focus on detecting the rarer ^{8}B and ^{7}Be neutrinos produced in side fusion chains, which have higher energies but are less common. The detection of solar neutrinos by Ray Davis's pioneering experiment initially observed only

about one-third of the predicted number, leading to the famous Solar Neutrino Problem [4]. It took many years and subsequent experiments to confirm that neutrino oscillation was responsible for this discrepancy.

The Earth experiences a constant influx of cosmic-ray particles from outer space, primarily composed of protons. When these high-energy protons collide with the Earth's atmosphere, they interact with air molecules, resulting in the production of secondary pions. These pions subsequently decay, giving rise to muons and muon neutrinos. While some of these muons reach the Earth's surface and are detected as cosmic rays, others decay during their flight, generating additional muon-neutrinos and electron-neutrinos. This process closely resembles the mechanism used to generate neutrino beams in particle accelerators, as discussed in Sec. 1.6.1. Early observations of atmospheric neutrinos yielded contradictory results, with some experiments detecting significantly fewer muon neutrinos than anticipated. This inconsistency was known as the Atmospheric Neutrino Anomaly. After a long period of debate, the data collected from the Super-Kamiokande experiment ultimately convinced the community that the observed deficit was indeed real and a consequence of neutrino oscillations [11].

Neutrinos are also produced during the core collapse of supernovae. According to simulations, these neutrinos play a critical role in the explosion process, as the star would not explode without their presence. In fact, approximately 99% of the released energy during a supernova is carried away by neutrinos within a time frame of 10 seconds. Since neutrinos rarely interact with matter, which allows them to quickly escape from the dense core of the supernova, providing initial information about the supernova explosion. Supernova neutrinos serve as valuable sources for studying neutrino properties, including their behaviour over long distances and the determination of their maximum possible mass. Additionally, the detection and analysis of supernova neutrinos offer opportunities to explore the life cycles of stars and shed light on the formation processes of neutron stars and black holes [21].

1.7 Neutrino Detection Methods

Neutrinos can interact with matter through two different types of interactions as described in Sec. 1.5. The first is the CC interaction, in which the neutrino transforms into its corresponding charged lepton. In experimental detectors, it is actually the charged lepton that is detected. The second is the NC interaction, where the neutrino remains as a neutrino but transfers energy and momentum to the particle it interacts with. This energy transfer can be detected either through the recoil or breakup of the target particle. In general, the CC interaction is easier to detect as the presence of the charged lepton leaves clear signatures in the detector. Over the years, a variety of detector technologies have been employed in neutrino experiments, chosen based on the specific requirements of each study [19].

1.7.1 Liquid Scintillator Detector

The liquid scintillator detector has played an important role in understanding neutrinos since neutrinos were discovered using this type of detector [7]. The scintillator detector focuses on the detection of $\bar{\nu}_e$ CC interaction (Eq. 1.1). The signature of this kind of event is a prompt signal (positron-electron annihilation produces two photons) followed by a delayed signal (neutron capture releases a photon with an energy of a few MeV) detected by the photomultiplier tubes (PMTs).

1.7.2 Cherenkov Detector

The Cherenkov detector operates based on the principle of the Cherenkov effect, which occurs when charged particles move through a medium at a speed greater than the speed of light in that medium. In such a scenario, Cherenkov radiation is emitted, which can be detected by PMTs in the form of a Cherenkov ring.

This type of detector is capable of detecting both CC and NC interactions as long as the final-state particles possess sufficient energy to generate Cherenkov radiation. The NC current interaction refers to the neutrino scattering off an atomic electron, transferring energy to it and causing it to emit Cherenkov light. In the case of CC interactions, neu-

trinos manifest themselves as leptons, producing distinctive types of Cherenkov rings, a fuzzy ring for electrons and a sharp ring for muons, allowing for easy identification of the incoming neutrino type. Moreover, by reconstructing the Cherenkov ring, directional information about the neutrino event can be obtained. However, it is worth noting that the discrimination between electron signals and background signals originating from photons is challenging, as both produce a similar signature in the detector. This limitation affects the ability of the detector to accurately distinguish between electron signals and photon backgrounds [22].

1.7.3 Liquid Argon Time Projection Chamber

The concept of using liquid argon (LAr) as a target for neutrino experiments was proposed in 1977 by Carlo Rubbia [23], driven by several key advantages. Firstly, LAr possesses a high density, enabling the design of compact detector configurations. Secondly, LAr exhibits low electron attachment, which permits the utilization of long drift volumes, thereby enhancing the efficiency of charge collection. Thirdly, LAr demonstrates high electron mobility, facilitating efficient charge transport within the medium. Additionally, LAr is relatively inexpensive, making it a cost-effective option for experimental setups. Moreover, its easy purification ensures high purity conditions. Lastly, LAr is chemically inert and readily liquefied. One potential challenge is the requirement for a cryostat to maintain the liquid argon at a low temperature $\sim$ 83K.

The liquid argon time projection chamber (LArTPC) serves as a neutrino detector due to its numerous advantages, particularly its unprecedented spatial resolution. As charged particles traverse the detector, they ionize atomic electrons along their trajectory and generate prompt vacuum ultraviolet (VUV) scintillation photons. These electrons are then drifted by a constant electric field and ultimately collected by wire planes on the anode. By placing wire planes with different orientations, a two-dimensional image of the interaction can be reconstructed. Additionally, the VUV photons can serve as the starting time of the event, as the scintillation light is collected within a few nanoseconds, while the drift time for electrons is on the scale of microseconds. Consequently, by knowing the

drift velocity of electrons, it becomes feasible to acquire three-dimensional information, allowing for the reconstruction of charged particle tracks on an event-by-event basis.

One significant advantage of this type of detector is its ability to discriminate against photon backgrounds. Utilizing the track information is a more powerful method than analyzing the Cherenkov ring, as mentioned in 1.7.2. The energy loss per unit distance ($\mathrm{d}E/\mathrm{d}x$) in the initial part of the track can be used to distinguish between photons and electrons. This background discrimination is crucial for experiments focused on detecting electrons as signals, such as the ν_e appearance signal in neutrino oscillation experiments.

1.8 Ionisation Energy Loss of Charged Particles

As a relativistic charged particle traverses a material, such as LAr, it undergoes electromagnetic interactions with the atomic electrons. This leads to the particle losing energy through the process of ionizing the atoms in the medium. Specifically, for a particle carrying a single charge with velocity $\mathrm{v} = \beta c$, passing through a medium with atomic number Z and material density ρ, the ionization energy loss per unit length is described by the Bethe-Bloch equation [9],

$$\frac{\mathrm{d}E}{\mathrm{d}x} \approx \frac{-4\pi\hbar^2 c^2 \alpha^2 \rho}{m_u m_e \mathrm{v}^2} \frac{Z}{A} \left[\ln\left(\frac{2m_e c^2 \beta^2 \gamma^2}{I_e} \right) - \beta^2 \right], \tag{1.15}$$

where A is the atomic mass number, $m_u = 1.66 \times 10^{-27}$ kg is the unified atomic mass unit. m_e is the electron mass, α is the fine-structure constant, and γ is the Lorentz factor. $I_e = (10\ \mathrm{eV})Z$ is the mean excitation energy of atoms averaged over all atomic electrons.

All charged particles lose energy by ionization when propagating through a medium. In the case of non-relativistic particles, the terms within the brackets of Eq. 1.15 do not change much. For a given medium, the rate at which a charged particle loses ionization energy depends on its velocity. Due to the presence of the $1/\mathrm{v}^2$ term in the Behte-Block equation, the energy loss per unit distance is highest for particles with lower velocities.

The rate of energy loss due to ionization is not significantly dependent on the material,

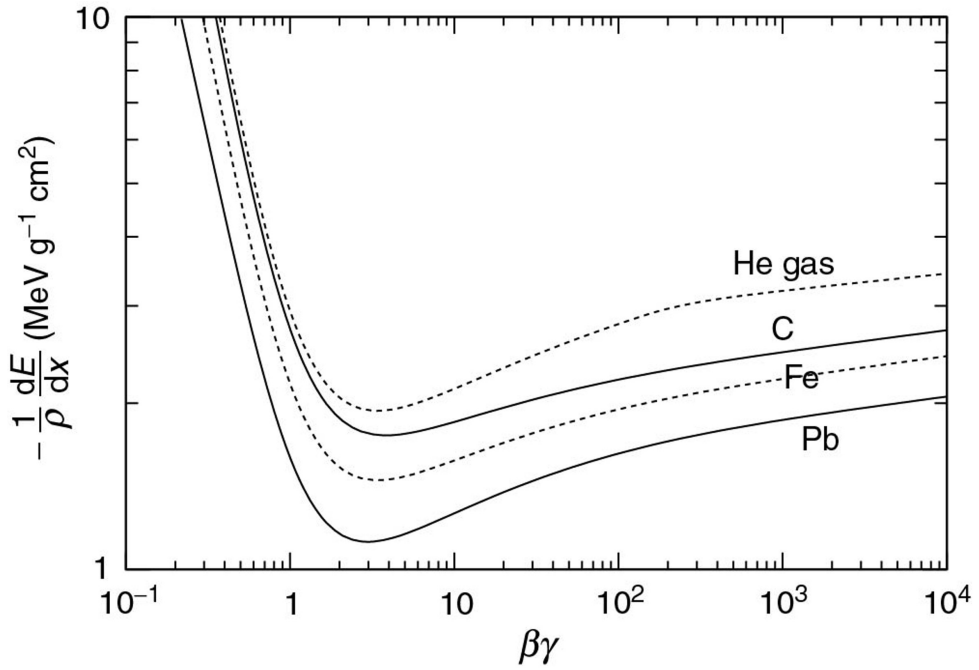

Figure 1.5: The energy loss curves due to ionization for a singly charged particle passing through various materials, including lead, iron, carbon, and gaseous helium. Taken from [9].

only proportional to the material density. Figure 1.5 shows the ionisation energy loss (in units of MeV g^{-1}cm^2) as a function of $\beta\gamma$ for single charged particles in various materials, such as carbon, iron and lead. The minimum point on the ionization curve is found at $\beta\gamma \approx 3$, and particles with this specific $\beta\gamma$ value are referred to as minimum ionizing particles (MIPs). The $\mathrm{d}E/\mathrm{d}x$ for a MIP in LAr is ~ 2.1 MeV/cm.

2 | The Deep Underground Neutrino Experiment

The Deep Underground Neutrino Experiment (DUNE) is an upcoming long-baseline neutrino oscillation experiment hosted by the Fermi National Accelerator Laboratory (Fermilab) [24]. The experiment is located at the Sanford Underground Research Facility in Lead, South Dakota, USA and will utilize the world's most intense neutrino beam from Fermilab in Chicago. The construction of the neutrino source and its associated facilities will be carried out as part of the Long-Baseline Neutrino Facility (LBNF) project.

2.1 Experiment Overview

A schematic illustration of the DUNE experiment setup is shown in Fig. 2.1. The experiment will consist of a far detector located about 1.5 km underground at the Sanford Underground Research Facility (SURF), situated 1,300 kilometres downstream from the neutrino source. The far detector comprises four FD modules based on the LArTPC technology. Each module holds 17 kt of liquid argon (at least 10 kt fiducial mass), and the total mass of liquid argon will be almost 70 kt in the FD complex. The near detector will be positioned roughly 574 meters away from the neutrino source. The ND will comprise a range of components, including a highly flexible LArTPC, a magnetized TPC using gaseous argon, and a large, magnetized beam monitor.

The primary goals are to:

- Measure the neutrino oscillation by looking for the appearance of $\nu_e(\bar{\nu}_e)$ from a pure $\nu_\mu(\bar{\nu}_\mu)$ beam from Fermilab, including measurements of charge-parity phase and the determination of neutrino mass hierarchy.
- Search for proton decay.
- Observe the core-collapse supernova ν_e neutrinos.

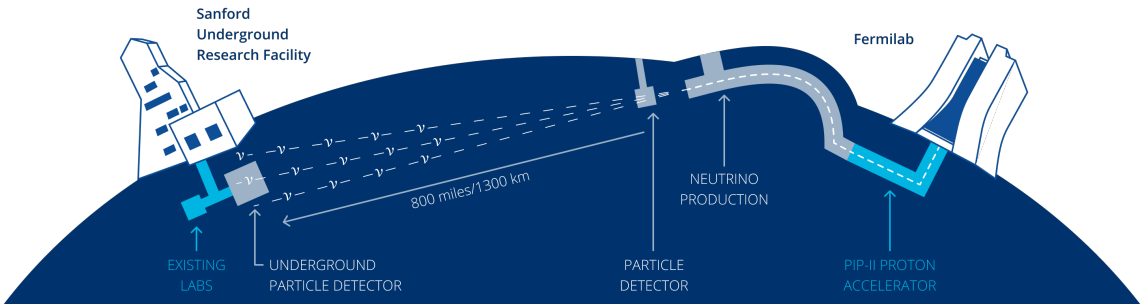

Figure 2.1: A visual representation of the DUNE experiment configuration. Neutrinos generated at Fermilab will pass through a near detector and travel a distance of 1300 km to reach the far detector located at Sanford Underground Research Facility. Taken from [25].

2.1.1 Beam

Neutrinos cannot be accelerated or guided by themselves due to their lack of electric charge. Therefore, they are generated as secondary particles from a manipulated particle beam. The Fermilab Accelerator Complex [26] accelerates proton beams to high energies, which are extracted for experiments with various objectives. In the high-energy neutrino experiment, the energy of the proton beam can be selected within the range of 60 to 120 GeV, corresponding to a beam power ranging from 1.0 to 1.2 MW [27]. The proton beam is directed towards a graphite target, resulting in collisions that produce charged pions and kaons. These secondary particles are then focused with the help of magnetic horns and allowed to travel through a long decay pipe filled with helium. During their journey through the decay pipe, the pions and kaons decay into neutrinos and charged by-products. Other secondary particles and remaining protons are captured while the neutrinos pass through a beam absorber at the end of the decay pipe. The entire apparatus is angled into the earth at 101 milliradians ($5.8°$), pointing toward the far detector to account for the earth's curvature.

The produced neutrino beam will have a well-defined direction and intensity, which will be measured by a near detector located at Fermilab. This information will be used to improve the understanding of the neutrino beam and to reduce the systematic uncertainties in the measurement of the neutrino oscillation parameters. The predicted unoscillated ν_μ

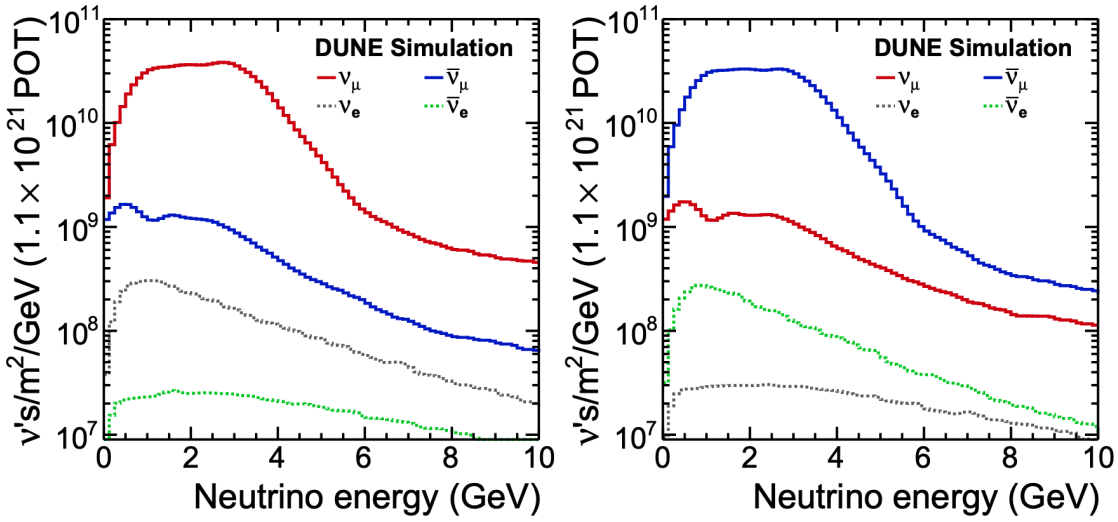

Figure 2.2: The predicted unoscillated neutrino fluxes at the DUNE far detector module for neutrino mode (left) and anti-neutrino mode (right). The 1.1×10^{21} POT corresponds to the integrated protons-on-target per year at a proton energy of 120 GeV. Taken from [28].

and $\bar{\nu_\mu}$ fluxes at the far detector are shown in Fig. 2.2. The beam will have a wide energy spectrum, spanning from 1 to 3 GeV [28], with the aim of maximizing the probability of neutrino oscillation, which depends on the L/E ratio (Eq. 1.13).

2.1.2 Near Detector

The near detector serves as an initial measurement of the beam, enabling a reliable assessment of the initial state of the neutrinos. The primary goal of the near detector is to provide a comprehensive understanding of the neutrino beam's composition and spread.

The DUNE ND comprises three main detector components, two of which can move off the beam axis. Each of these components performs essential functions that are unique yet complementary to the overall goals of the ND. Since each component has distinct features, the DUNE ND is commonly regarded as a detector suite or complex with varying capabilities. Figure 2.3 shows the DUNE ND components in the ND hall, with both on-axis and off-axis settings. It consists of three detector components: ND-LAr (Liquid Argon), ND-GAr (Gaseous Argon), and SAND (System for on-Axis Neutrino Detection). ND-LAr is a LArTPC constructed using ArgonCube technology, which has the same target nucleus

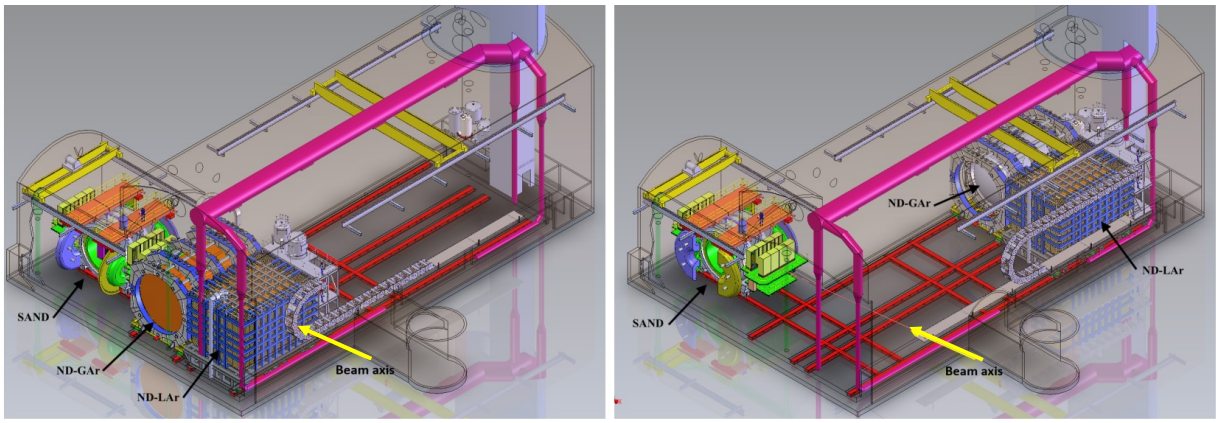

Figure 2.3: One view of the DUNE near detector complex in the ND hall, featuring both on-axis and off-axis configurations. The neutrino beam is depicted by the yellow arrow. Taken from [29].

and detection principles as the FD. However, it loses acceptance for muons above 0.7 GeV/c due to the lack of containment, which is accomplished by the ND-GAr detector. The ND-GAr detector consists of a high-pressure gaseous argon TPC surrounded by an ECAL and a muon system in a 0.5 T magnetic field. It provides a lower-density medium with excellent tracking resolution to momentum analyze the muons from ND-LAr. It also offers an independent sample of ν-Ar interactions that can be studied with a low momentum threshold and excellent tracking resolution. Finally, SAND is a magnetized beam monitor that stays on-axis to monitor the flux of neutrinos going to the FD. It is much more sensitive to variations in the neutrino beam and provides an excellent on-axis neutrino flux determination. ND-LAr and ND-GAr can move off-axis, while SAND remains on-axis to serve as a dedicated neutrino spectrum monitor. By varying the position of the detectors sideways, the neutrino beam can be measured at different off-axis configurations, resulting in various neutrino energy spectra. This off-axis effect concentrates the neutrino energy spectrum into a narrower range due to the relativistic kinematics of two-body decay, leading to a more monoenergetic neutrino source but with reduced intensity. By linearly combining these spectra, it becomes possible to replicate oscillated far detector measurements, enabling the determination of neutrino oscillation parameters in a model-independent approach.

2.1.3 Far Detector

The DUNE FD will consist of four LArTPC modules, as shown in Fig. 2.4, each with a LAr mass in the active region of the cryostat (fiducial mass) of at least 10 kt, installed approximately 1.5 km underground. This technology offers excellent tracking and calorimetry performance, making it an ideal choice.

DUNE is planning for and currently developing two LArTPC technologies:

- Single-Phase (SP) technology: In this technology, all the detector elements inside the cryostat are immersed in liquid. Ionization charges drift horizontally in the LAr under the influence of an electric field towards a vertical anode, where they are read out. This design requires very low-noise electronics to achieve readout with a good signal-to-noise ratio because no signal amplification occurs inside the cryostat. This technology was pioneered in the ICARUS project and is now mature. It is the technology used for Fermilab's currently operating MicroBooNE detector, as well as the SBND (Short-Baseline Near Detector) detector, which is under construction.
- Dual-Phase (DP) technology: In this technology, some components operate in a layer of gaseous argon above the liquid. Ionization charges drift vertically upward in LAr and are transferred into a layer of argon gas above the liquid. Devices called Large Electron Multipliers (LEMs) amplify the signal charges in the gas phase before they reach a horizontal anode. The gain achieved in the gas reduces the stringent requirements on the electronics noise, and the overall design increases the possible drift length, which, in turn, requires a correspondingly higher voltage. This technology was pioneered by the WA105 DP demonstrator collaboration [30] at CERN and is less mature than SP technology, but it offers several advantages.

Each LArTPC fits inside a cryostat of internal dimensions 15.1 m (width) x 14.0 m (height) x 62.0 m (length), containing a total LAr mass of about 17.5 kt. However, The ProtoDUNE-SP at the CERN neutrino platform (Chapter 3) achieved a remarkable signal-to-noise ratio thanks to the high liquid argon purity, enabling the realization of a substantial 6.5 m drift distance [32]. This superior performance rendered the gaseous phase of

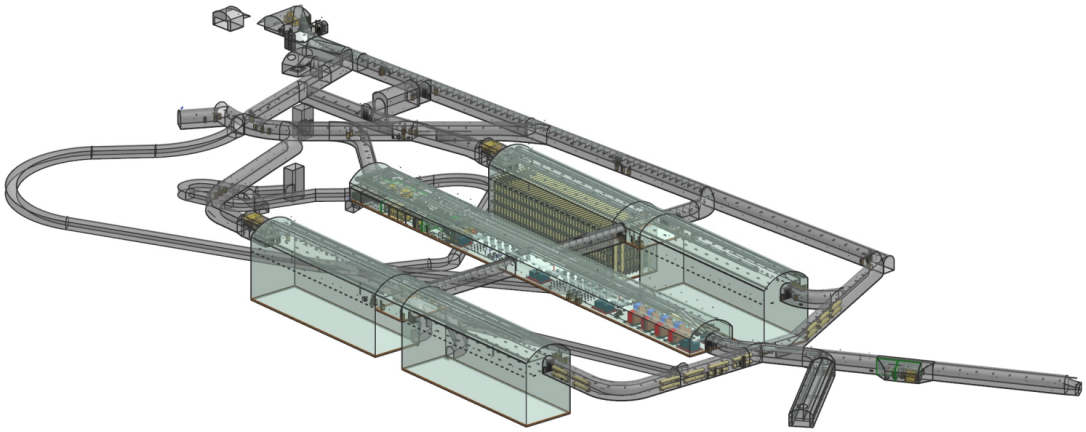

Figure 2.4: The layout of the DUNE far detector underground caverns comprises four detector module caverns and a central service cavern in the middle. Taken from [31].

the dual-phase technology unnecessary, leading to a shift away from Dual-Phase as the baseline technology. Based on the experience gained from the ProtoDUNE, a novel vertical drift technology was developed for the second DUNE FD. This technology leverages the advantages of the ProtoDUNE dual-phase design while simplifying the system by eliminating the challenges associated with the liquid-gas interface.

2.2 DUNE's Research Goal

The primary objective of the DUNE experiment is to study neutrino oscillation by detecting the appearance of electron neutrinos from a beam of pure muon neutrinos from Fermilab. DUNE's significant advantage lies in its 1300 km baseline and the high-intensity neutrino beam from LBNF, which provides sensitivity to the matter effect. This effect introduces a distinct asymmetry in the probabilities of $\nu_\mu \rightarrow \nu_e$ versus $\bar{\nu}_\mu \rightarrow \bar{\nu}_e$ oscillations, with the sign determined by the currently unknown mass hierarchy. The observed neutrino asymmetry serves as a valuable metric, representing the normalized difference between the appearance of neutrinos and antineutrinos as,

$$\mathcal{A}_{\mu e} = \frac{P(\nu_\mu \to \nu_e) - P(\bar{\nu}_\mu \to \bar{\nu}_e)}{P(\nu_\mu \to \nu_e) + P(\bar{\nu}_\mu \to \bar{\nu}_e)}, \tag{2.1}$$

This will enable the measurement of various parameters such as the charge-parity phase and the determination of neutrino mass hierarchy [33]. In practice, the energy spectra of neutrinos and antineutrinos measured by the far detector are fitted simultaneously, allowing for the determination of all neutrino oscillation parameters simultaneously.

The sensitivity studies conducted in DUNE's physics program demonstrate great potential. After 10 years of its nominal run plan, DUNE can identify the presence of CP violation at a 5σ significance level for half of the range of the possible true δ_{CP} values. If δ_{CP} = -π/2, indicating maximum CP-violating effect, CP violation can be discovered in just seven years of operating. The determination of the mass hierarchy can be achieved within two years for any value of δ_{CP}, or less than one year if the CP violation is maximum [33].

The resolution on δ_{CP} measurement improves to approximately 10 degrees for CP-conserving values and 20 degrees for maximum CP-violating values after 8 and 12 years of nominal running, respectively. Furthermore, increased exposure leads to a measurement precision of $\sin^2(2\theta_{13})$ that approaches that of reactor experiments, which are currently the main constraints on this angle. However, the sensitivity varies significantly with the value of other oscillation parameters, such as $\sin^2(2\theta_{23})$ [33]. Table 2.1 provides a concise overview of significant sensitivity milestones related to neutrino mass ordering and CP-violation discovery, along with precision measurements for δ_{CP} and $\sin^2(2\theta_{13})$. The assumptions made in the table are based on the normal mass ordering and equal running time in both neutrino and antineutrino modes.

DUNE has broader scientific objectives beyond studying neutrino oscillation. It seeks to investigate proton decay in various significant decay modes, which, if observed, would revolutionize our understanding of physics and offer insights into the Grand Unification of forces. Additionally, DUNE aims to capture the ν_e flux emitted during core-collapse supernovae throughout its lifespan. This observation has the potential to provide valuable

Table 2.1: An overview of major milestones in sensitivity regarding neutrino mass ordering and CP-violation discovery, as well as precision measurements for δ_{CP} and $\sin^2(2\theta_{13})$. The quoted values are highly dependent on the input $\sin^2(2\theta_{23}) = 0.580$. Taken from [33].

Physics Milestones	**Exposure Years**
5σ Mass Ordering ($\delta_{\text{CP}} = -\pi/2$)	1
5σ Mass Ordering (100% of δ_{CP} values)	2
3σ CP Violation ($\delta_{\text{CP}} = -\pi/2$)	3
3σ CP Violation (50% of δ_{CP} values)	5
5σ CP Violation ($\delta_{\text{CP}} = -\pi/2$)	7
5σ CP Violation (50% of δ_{CP} values)	10
3σ CP Violation (75% of δ_{CP} values)	13
δ_{CP} Resolution of 10 degrees ($\delta_{\text{CP}} = 0$)	8
δ_{CP} Resolution of 20 degrees ($\delta_{\text{CP}} = -\pi/2$)	12
$\sin^2(2\theta_{13})$ Resolution of 0.004 (nominal analysis)	15

knowledge about the processes involved in stellar explosions. Through these scientific goals, DUNE aims to expand our understanding of the fundamental properties of neutrinos and the universe.

2.3 Significance of Secondary Pion Interactions

DUNE's objective is to accurately determine the oscillation parameters by distinguishing the flavour and energy of interacting neutrinos within the detector. The significance

of this determination is highlighted in Eq. 1.13 for oscillation measurements. Incorrect identification of the flavour will alter the overall interaction rates of different neutrino flavours, impacting the extracted oscillation probability. Similarly, inaccurately estimating the energy will distort the energy spectrum of events and further affect the appearance oscillation probability. Both the flavour and energy of neutrinos are deduced from the particles produced in the final state of interactions. As previously discussed in Sec. 1.5, the final state resulting from neutrino interactions can be highly intricate and complex.

To identify the flavour of neutrinos, the focus is on detecting the outgoing leptons in CC interactions. In the case of ν_e CC events, the presence of an e^- that forms an electromagnetic shower in the detector indicates the neutrino flavour. However, there is a background to this interaction caused by ν_μ NC interactions, where the neutrino transfers additional energy that can produce a final state π^+. If this π^+ interacts with a nearby Ar nucleus, a charge exchange scattering can produce a π^0, which promptly decays into two photons. These photons exhibit a shower pattern similar to the e^-, potentially leading to the incorrect identification of the event as a ν_e CC event. Corrections for such background are obtained from simulations, and uncertainties in the rate of π^+-Ar charge exchange interactions introduce uncertainties in determining the true number of ν_e events, thereby affecting the precision of oscillation measurements.

This example highlights one aspect where uncertainty in secondary pion interaction rates contributes to DUNE's systematic uncertainty budget. Additional examples can be found in Ref. [34]. Although not an exhaustive list, it illustrates the objective of the analysis presented in this thesis. By measuring these pion charge exchange interaction cross-sections with argon, constraints can be placed within DUNE's oscillation analyses, reducing systematic uncertainty. The T2K (Tokai-to-Kamiokande) experiment has illustrated the practicality of using pion scattering data in neutrino experiments [35], where they employ global π^+ scattering data to constrain the nuclear model used in their simulations of neutrino interactions. This task is crucial, as DUNE aims to limit its systematic uncertainty to 2% [33] in order to achieve the physics goals outlined in Table 2.1.

3 | ProtoDUNE-SP Detector

Thorough testing and evaluation of the production and installation of detector components are essential prerequisites before the final construction of the DUNE far detector of this scale. The ProtoDUNE-SP detector is the prototype of the DUNE far detector modules located in the CERN North Area. ProtoDUNE-SP contains a total liquid argon mass of 0.77 kt. The installation of the ProtoDUNE-SP was completed in July 2018. The full data-taking started on October 10, 2018, and the beam data-taking ended on November 11, 2018, due to upgrades in the LHC accelerator complex. Subsequently, the detector remained operational until July 19, 2020, serving the purpose of testing and validating technologies for the DUNE FD modules [24]. In addition to verifying the production and installation processes, ProtoDUNE-SP aimed to test event reconstruction and conduct detector calibration under controlled conditions.

A charged particle test beam is produced by the Super Proton Synchrotron (SPS) at CERN and delivered to the ProtoDUNE-SP. This test beam simulates the charged particles resulting from neutrino interactions at DUNE FD in the closest way possible, with a momentum range from 0.3 to 7 GeV/c. The test beam consists of protons, pions, muons, kaons and positrons. The primary physics objective of ProtoDUNE-SP is to measure the interaction cross-sections for these different charged particle species with an argon nucleus. These measurements hold significant value in the accurate modelling of neutrino interactions at DUNE.

3.1 Beamline

The H4 Very Low Energy (VLE) beamline at CERN is an additional branch of the H4 beamline specifically designed to produce lower energy beam particles for ProtoDUNE-SP. A conceptual layout of the H4-VLE beamline is shown in Fig. 3.1. It functions as an extension of the primary H4 beamline, which utilizes 400 GeV/c primary protons extracted from the CERN SPS. These protons are directed towards a beryllium target, re-

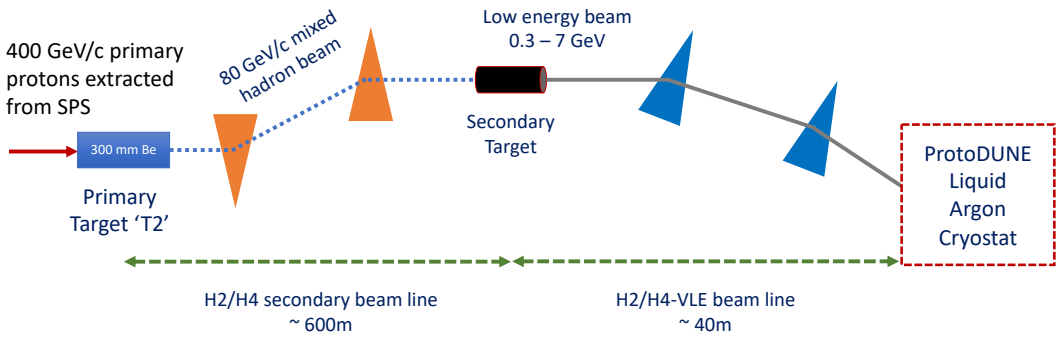

Figure 3.1: A conceptual layout of the H4-VLE beamline, which leads to the ProtoDUNE-SP detector. High-energy protons strike the primary target, generating a mixed secondary hadron beam. This secondary beam subsequently interacts with a secondary target, resulting in a tertiary very low-energy beam. Reproduced from [37]

sulting in a mixed hadron beam with a reduced momentum of 80 GeV/c. The secondary beam is then directed onto a secondary target, generating the tertiary VLE beam consisting of positrons, pions, muons, kaons, and protons with momenta ranging from 0.3 to 7 GeV/c with a resolution of $\Delta p/p \leq 3\%$ [36]. The polarity of the beam-focusing magnets can be adjusted to generate a beam consisting of either positively or negatively charged particles. However, all test-beam data collected in 2018 was obtained in the positive polarity configuration, resulting in all beam particles having a positive charge.

The choice of secondary target material depends on the desired VLE beam particle compositions. Tungsten is used for beam momenta below 4 GeV/c, as it increases the hadron content of the beam. Copper, on the other hand, is employed for momenta ranging from 4 GeV/c to 7 GeV/c. As a result, the composition of the beam varies depending on its momentum. At the lower end of the momentum range, the beam is primarily composed of positrons. As the momentum increases, pions become the dominant particles in the higher momentum beams. The detailed design of the beamline is documented in [37].

Dedicated beamline instrumentation is positioned between the beam production point and the front face of the cryostat to facilitate the guidance of the VLE beam towards the ProtoDUNE-SP detector. This instrumentation includes various components and devices that aid in monitoring and controlling the beam, ensuring its proper injection through the beam plug (described in the next section). The beam instrumentation (BI) also plays a

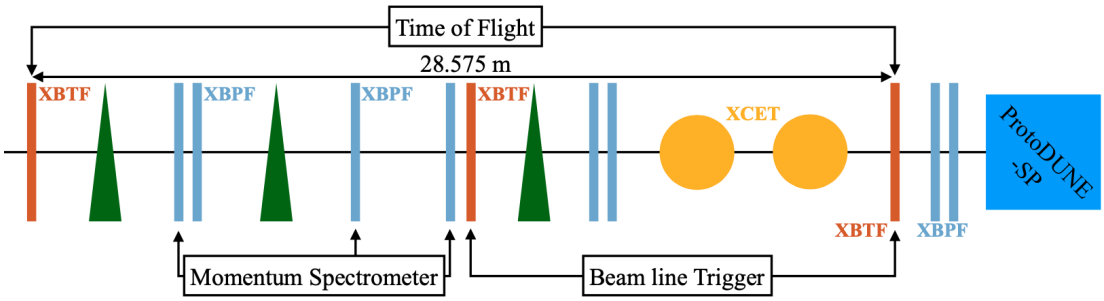

Figure 3.2: A schematic illustration displaying the spatial arrangement of various components in the H4-VLE beamline: trigger counters (XBTFs), bending magnets (triangles), profile monitors (XBPFs), and Cherenkov detectors (XCETs). Integrating data from these instruments enables triggering, momentum reconstruction, and TOF measurement. Taken from [24]

crucial role in the measurement and identification of particles within the beamline. It consists of several components strategically positioned to provide trigger capabilities, particle identification (PID), and momentum measurement on an individual particle basis.

The BI setup includes eight profile monitors called "XBPF" used for profiling, tracking, and momentum reconstruction, three trigger counters referred to as "XBTF" for triggering and time-of-flight (TOF) measurements and two threshold Cherenkov counters known as "XCET" used in the PID process. The arrangement of these different instrumentation components can be visualized in Fig. 3.2. There are also three bending magnets (indicated by the green triangle in the figure) that direct the beam towards the ProtoDUNE-SP detector. The second magnet serves a dual purpose, acting as part of both the beam guiding system and the momentum spectrometer. The in-depth information regarding these components can be found in [38].

The XBPFs are scintillating fibre detectors consisting of 192 square fibres arranged in a planar configuration. They cover an area of approximately 20×20 cm^2 and measure one spatial coordinate per device. Multiple pairs of these detectors, rotated by 90 degrees, are placed along the beamline to track the beam position on a particle-by-particle basis. The XBPF data is used for reconstructing the momentum of particles and measuring their trajectories, particularly for the last two sets of XBPF devices, which are extrapolated to the face of the ProtoDUNE-SP TPC to give the reconstructed beam position.

Table 3.1: A summary of beamline instrumentation logic used in the identification of particle types for 1 GeV/c. The TOF value is given for the value of the lower and upper cuts. Only the low-pressure XCET is used to distinguish particles in 1 GeV/c beam momentum, where zero and one represent the absence and presence of the Cherenkov counter's signal, respectively. Taken from [24].

1 GeV/c	e	π/μ	K	p
TOF(ns)	0, 105	0, 110	-	110, 160
XCET-LowP	1	0	-	0
XCET-highP	-	-	-	-

The XBTFs operate similarly to the XBPFs but with a different readout approach. Instead of individual fibre readout, the fibres are grouped into two bundles, resulting in no position resolution. The signals from upstream and downstream planes are connected to a time-to-digital converter for TOF measurements. The resolution of the TOF measurement is approximately 900 ps [38]. Coincident signals from the middle and downstream XBTFs serve as a general trigger, which is used as a condition for high-level triggers (HLTs). The measured efficiencies of the XBPFs with respect to these triggers are consistently above 95% for all chambers during data acquisition across the desired momentum range.

The two Cherenkov counters (XCETs) in the H4-VLE have a similar design, with one able to handle higher radiator gas (CO_2) pressure. These counters are adjusted with different internal pressures to identify particle species at various momenta. Combining the TOF information with signals from both the high and low-pressure Cherenkov counters enables PID across the entire momentum range.

At momenta below 3 GeV/c, the Cherenkov counter distinguishes electrons (e) from other particles, while TOF distinguishes muons (μ) and pions (π) from protons (p). However, it cannot further differentiate between muons and pions. A summary of beamline instrumentation logic used in the identification of particle types is shown in Table 3.1 and Fig. 3.3 for 1 GeV/c beam momentum. The signals from these counters are used to generate HLTs for different beam particle species during the beam run.

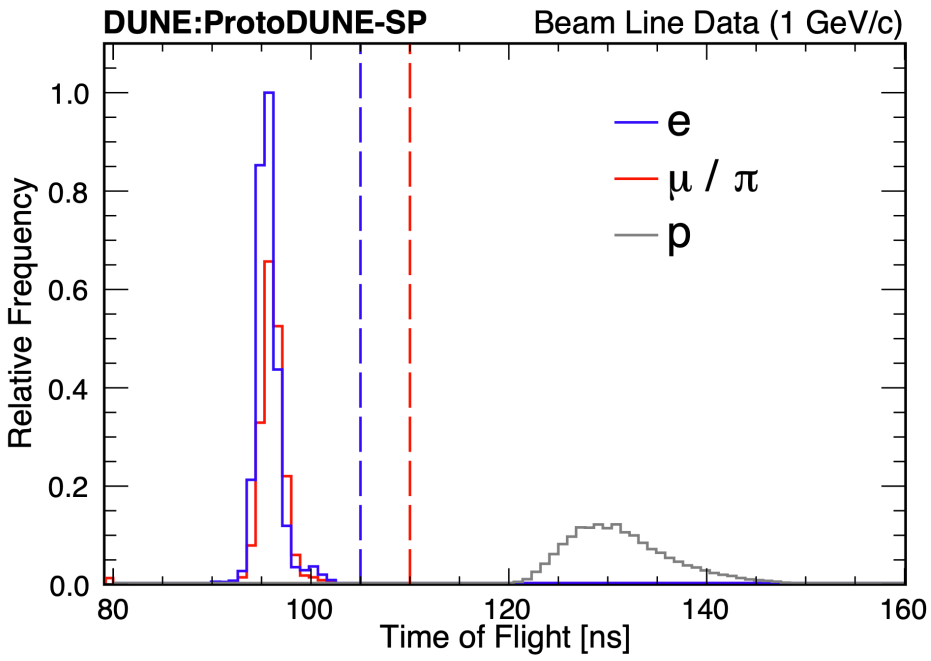

Figure 3.3: Nominal beam momentum = 1 GeV/c. Vertical dashed lines represent the upper value of the TOF cuts used for electrons (blue), and muons/pions (red). Taken from [24]

3.2 Detector Design and Construction

The ProtoDUNE-SP detector is one of the two largest LArTPC that serves as a prototype for the DUNE far detector. The design and construction of ProtoDUNE-SP will be discussed in the following sections.

The liquid argon based technology was first developed for and used in the ICARUS experiment [39]. Figure 3.4 shows a view of the ProtoDUNE-SP's TPC [24]. The active volume is 6 m (height) $\times$ 6.9 m (length) $\times$ 7.2 m (width), which is at 1:20 of the size of one DUNE FD module. The ProtoDUNE-SP uses a right-handed Cartesian coordinate, as illustrated at the bottom of Fig. 3.4. The TPC is divided in half by the Cathode Plane Assembly (CPA) at x = 0 in the y-z plane and comprises two drift volumes with a maximum drift distance of 3.6 m. There are six Anode Plane Assemblies (APAs) in total and three on each side. A homogeneous electric field is created within the liquid argon of 500 V/cm. The beam enters the TPC through the beam plug, as shown in Fig. 3.4. To

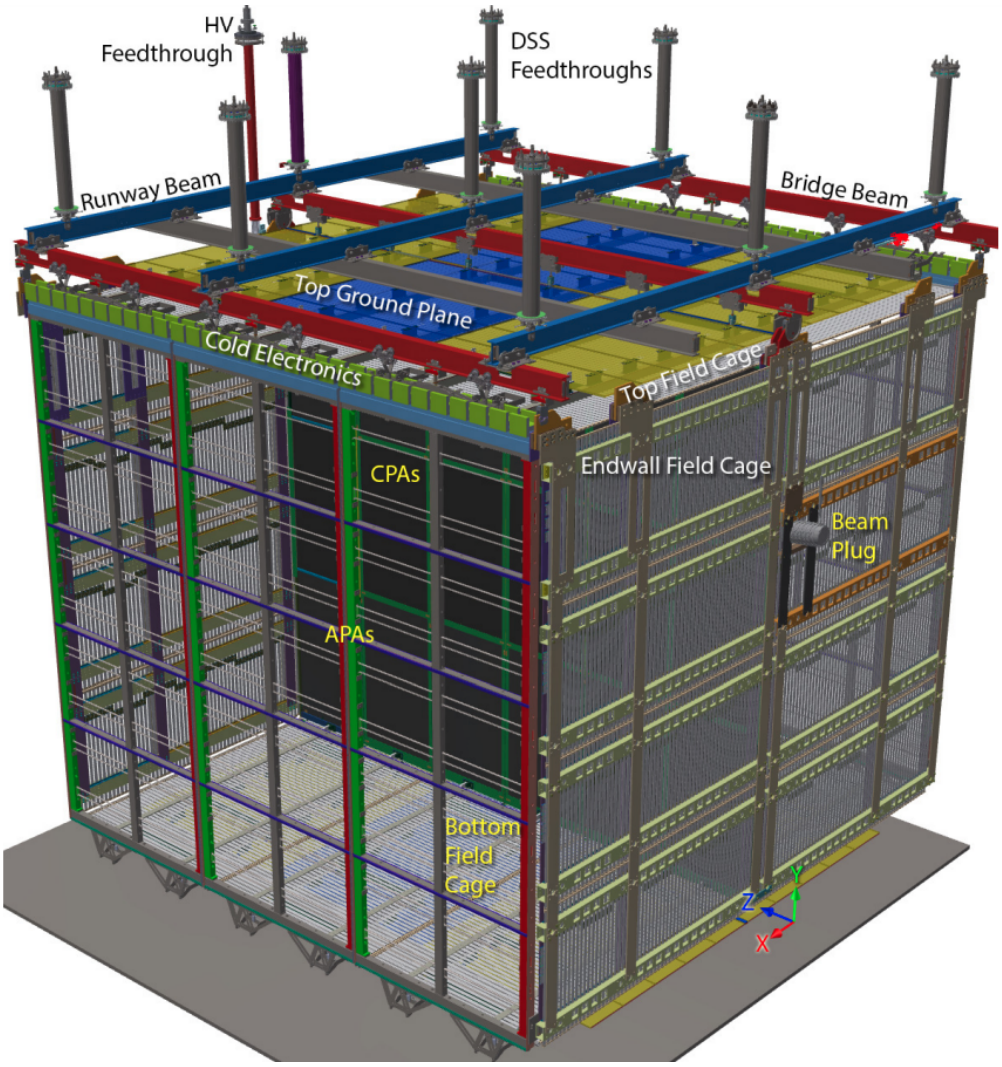

Figure 3.4: One view of the ProtoDUNE-SP LArTPC with coordinates and major components labelled. The right-handed Cartesian coordinate is labelled at the bottom of the figure. Taken from [24].

minimize the upstream energy loss of beam particles before they enter the TPC, a portion of the beam path, initially filled with LAr, is replaced with dry nitrogen gas, which has a lower density. This nitrogen gas is contained within the beam plug, which is constructed from alternating fibreglass and stainless steel rings, forming a cylindrical structure installed in front of the TPC. The beam direction is closely aligned with the z-axis, which is approximately 10° downward and 11° towards the anode plane.

The drift volume of a LArTPC is constrained by electron lifetime, which will be discussed in Sec. 3.3.3. In ProtoDUNE-SP, with a drift length of 3.6m, the maximum drift time is

around 2.25 ms, with a transverse diffusion of 2 mm perpendicular to their travel direction. In comparison, in a high-pressure gaseous argon TPC, which is a proposed upgrade for one of the DUNE ND, electrons experience significantly faster drift and less diffusion. In this type of chamber, the electron drift velocity is about ten times higher, and the transverse diffusion is reduced to approximately 0.6 mm [40].

While using a LArTPC for particle detection in a large volume provides excellent track resolution, determining the precise position of a detected particle can be challenging. This is because the arrival time of external particles and electron travel time to the anode is unknown in a significant number of events, leading to ambiguity in the starting timing (t_0) of the interactions. As a result, the structure of any connected track can be identified, but its exact position in the drift direction cannot be determined. However, liquid argon can solve this problem by using its scintillation properties. When energy is deposited, argon produces a flash of 128 nm photons [41]. These scintillation photons travel nearly instantaneously compared to the drift electrons, enabling the precise time of track creation to be determined.

3.2.1 Cryostat

The cryostat is a standalone structure that is electrically insulated and has outer dimensions of 11.4 m $\times$ 11.4 m $\times$ 10.8 m (width $\times$ length $\times$ height). Its inner dimensions measure 8.5 m $\times$ 8.5 m $\times$ 7.9 m [42]. The design of the inner vessel is based on the technology developed by GTT (Gaztransport & Technigaz) for the transportation and storage of liquefied natural gas (LNG). A cross-sectional view of the insulation and membrane layers can be seen in Fig. 3.5. The inner membrane, which is made of 1.2 mm thick 304L stainless steel, can expand or contract in two dimensions as a function of the temperature due to its corrugated configuration, acting as a two-dimensional spring and preserving the integrity of the detector structure during filling and operation.

The insulation layer, located just inside the inner membrane, consists of two 390 mm thick layers of expanded polyurethane foam with a density of 90 kg/m^3. It is supported by plywood plates of varying thicknesses. The outer insulation layer is attached to the

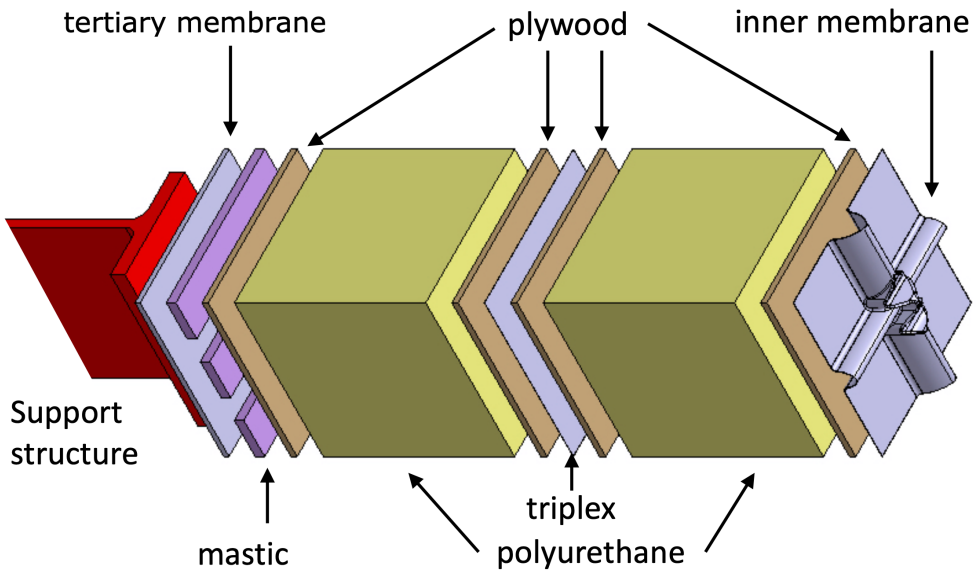

Figure 3.5: The cross-sectional view of the membrane cryostat inner vessel layout, designed to keep the liquid argon contained and stable with low temperature. Taken from [43].

tertiary membrane by rods and mastic. Between the two insulation layers is a secondary LAr containment layer made of GTT-proprietary Triplex, a composite material consisting of a thin sheet of aluminium laminated with glass cloth and resin [43]. The purpose of using multiple layers of thermally insulating material is to ensure that the argon inside the cryostat is maintained at a stable and low temperature.

ProtoDUNE-SP's operation requires the drift of electrons through liquid argon for a distance of 3.6 m. The argon received from the supplier contains water, oxygen, and nitrogen at parts per million level, with water and oxygen capable of capturing drifting electrons. Therefore, the concentration of these contaminants needs to be reduced by at least a factor of 10^4 and maintained at this level to enable proper operation of the TPC. The current system for purifying the liquid argon in ProtoDUNE-SP is an extension of purification systems previously developed for ICARUS and Fermilab. The system utilizes the same filter materials and is designed to achieve a low concentration of contaminants. Due to the high rate of recirculation and the prevention of leaks, the level of oxygen contamination in the liquid argon is reduced to a few parts per trillion, which results in near-optimal signal strength from all areas of the TPC, including the furthest regions.

3.2.2 Time Projection Chamber

ProtoDUNE-SP is equipped with a TPC that detects the ionisation signal of particles as they move through the detector volume. The electric field is generated by a set of anode and cathode plane assemblies. The CPA is held at a voltage of -180 kV, which creates an electric field of 500 V/cm throughout the detector volume. It divides the TPC volume into two drift volumes, with each located on either side of the CPA. The electric field is confined to the drift volumes by ground planes at the top and bottom of the TPC, ensuring its uniformity. The APAs at either side of the detector complete the drift volumes.

Figure 3.6 shows the front view of an APA, turned on its side, in ProtoDUNE-SP. The APA consists of a rectangular stainless steel frame that is 6.1 m high, 2.3 m wide, and 76 mm thick. On each side of the frame, there are four planes of wires that are bonded to the surface. The wire planes are arranged in the following order (from the outermost plane inwards): the Grid (G) plane, which is vertical; the U plane, which is inclined at +35.7° from the vertical direction; the V plane, which is inclined at -35.7° from the vertical direction; and the X plane, which is again vertical.

Each wire plane within the APA is positioned 4.75 mm above the previous layer, accounting for the wire mesh. Wire termination is carried out on wire boards at the short ends of the APA. The G and X layers have an identical wire pitch of 4.79 mm, but their positions are staggered by half a wire pitch. On the other hand, the U and V wires have a wire pitch of 4.67 mm and are helically wrapped around the frame to save the cost of electronics. The wire planes are biased at different potentials to allow primary ionization electrons to pass through the G, U, and V planes without being captured and finally collected on the X wires. As a result, the X plane wires are also known as the collection wires, and the U and V plane wires as the first and second induction plane wires. The G plane wires function as an electrostatic discharge (ESD) protective shield and are not read out. To ensure the collection of electrons only on the collection-plane wires, the nominal wire-plane bias voltages are V_G = -665 V, V_U = -370V, V_V = 0V, and V_X = +820V.

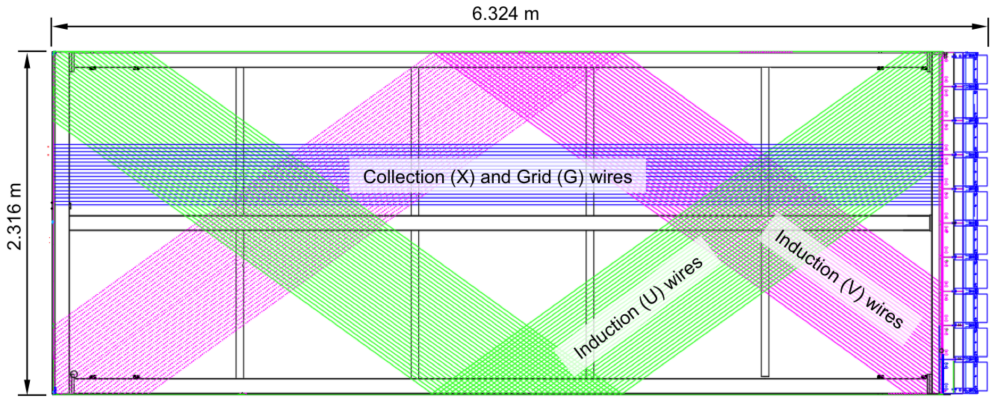

Figure 3.6: Sketch of the ProtoDUNE-SP anode plane assembly turned on its side, highlighting the U, V, and X wires and their angular relationships to the frame. The blue boxes on the right indicate the location of the cold electronics. Taken from [43].

A typical LArTPC is shown in Fig. 3.7 with its operating principle [44]. As charge particles traverse through the LArTPC, electrons will be ionised along their trajectories, and the VUV scintillation photons will be produced as well. The constant electric field will drift these electrons towards the anode plane. These signals will be collected by three wire planes with different orientations on the anode. As electrons pass through the first two induction planes, a bipolar waveform will be produced since electrons will alter the measured electric field. The collection plane will finally collect these electrons and produce a unipolar waveform. From the coincidence of signals collected by these three wire planes, the y-z position of the charged particle can be identified. Whereas the VUV photons are collected by the photo-multiplier tubes (PMTs) embedded in the detector's APAs, providing the so-called t_0 information to measure the time of interaction. The x position can be determined from the drift electron's arrival time if the electron drift speed is precisely known.

3.2.3 Photon Detector System

The photon system is a crucial component of ProtoDUNE-SP for accurately measuring interaction times and obtaining independent measurements of deposited energy. It plays an integral role in addressing the issue of t_0 ambiguity, which arises due to the unknown arrival time of charged particles and electron travel time to the anode. To overcome this

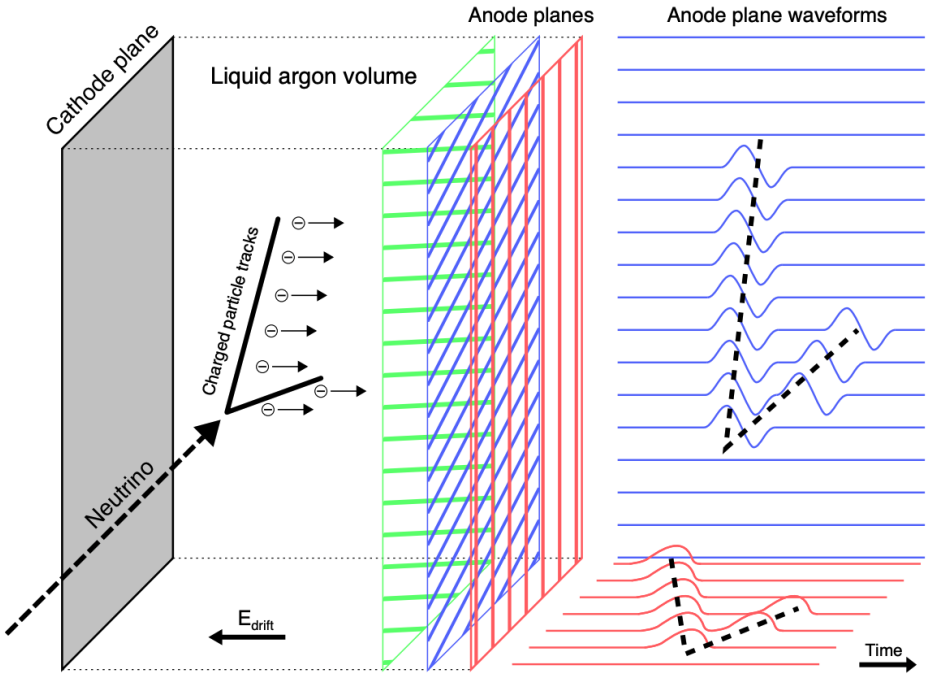

Figure 3.7: The operating principle of the LArTPC and an example signal that is obtained on the anode wire planes. Charged particles resulting from a neutrino interaction generate a track of ionized electrons, which are then drifted towards the anode planes by a constant electric field. Taken from [45].

challenge, the scintillation properties of liquid argon are utilized, and the photon detectors are embedded within the APAs, as the field cage blocks the scintillation light. The ten bar-shaped photon detectors have dimensions of 8.6 cm (height) $\times$ 2.2 m (length) $\times$ 0.6 cm (thickness) and contain horizontally oriented bars made of waveguide and wavelength-shifting material. To enable detection by the silicon photomultipliers (SiPMs), the scintillation light created in liquid argon, with a wavelength of 128 nm, is converted to visible light using a wavelength shifter. Within the size constraint of the detector, various designs of photon-detector technologies are employed in ProtoDUNE-SP, utilizing SiPMs to convert scintillation light into electrical signals, which are then transmitted out of the cryostat on copper cables. While most of the photon detectors are designed to sense the light that reaches the ends of the bars, the ARAPUCA design, adopted by the DUNE FD module, collects light at multiple positions along the bar. The ARAPUCA design uses reflective internal walls to trap photons and then detects them with SiPMs in the compartment walls. This ARAPUCA photon detection system (PDS) has been successfully

installed and tested in ProtoDUNE-SP. The integration of the PDS into the APAs results in a compact and efficient design that maximizes the detection of scintillation light within the detector volume.

3.2.4 Cosmic Ray Tagger

The ProtoDUNE-SP detector is situated on the surface, leading to a high rate of incident cosmic muons. To address this issue, the Cosmic Ray Tagger (CRT) is incorporated into the detector. The CRT system is comprised of scintillation counters that cover nearly the entire upstream and downstream faces of the TPC. To construct the CRT, scintillation counters from the outer veto of the Double Chooz experiment [46] are repurposed. The CRT is constructed using four large assemblies, with two mounted upstream and two downstream of the cryostat. Its primary function is to trigger a set of cosmic-ray muons that move in a direction parallel to the TPC readout planes with known timing and direction. Due to most muons entering the TPC being untagged, the CRT tags both untagged and tagged (if muons cross the cathode plane) cosmic muons to provide crucial calibration data and performance indicators.

3.2.5 Data Acquisition, Timing and Trigger System

The data acquisition (DAQ) system in ProtoDUNE-SP is responsible for collecting and processing the raw data produced by the detector. The DAQ system is composed of custom-built electronics, software, and computing infrastructure that operate together to store data from the detector. The transfer of physics data from the detector front-end to storage servers is regulated by two DAQ systems in ProtoDUNE-SP: Front-End LInk eXchange (FELIX) and Reconfigurable Cluster Element (RCE). The former manages data from only one APA, while the latter handles data from five of the six APAs of the TPC. The TPC contains 2560 wires per APA that are read at 2 MHz, resulting in a total data flow of approximately 90 GB/s for the entire TPC of ProtoDUNE-SP. The main objective of the data acquisition system is to record data created by test beam particles or cosmic rays within a time window of 3 ms.

The timing system in ProtoDUNE-SP distributes a 50 MHz clock on an 8b/10b encoded data stream to all endpoints. It is responsible for switching between data-taking modes with and without the beam, and the system can be partitioned, allowing different parts of the experiment to operate independently. Additionally, the timing system provides trigger distribution, and the clock is synchronized with the global positioning system, which provides 64-bit timestamps used to mark the trigger and data times, independent of the file name, run, or trigger record numbers.

The hardware triggering system in ProtoDUNE-SP is used for event selection, with the Central Trigger Board (CTB) being the main element of the system. The CTB is a custom printed circuit board (PCB) that processes the status of the auxiliary detectors (PDS, BI, and CRT) to facilitate prompt readout decisions. The CTB houses a commercial PCB called MicroZed, which serves as an interface between the auxiliary detectors and the DAQ through the timing system. The CTB has 32 individual CRT pixel inputs, 24 optical inputs for the PDS, and seven inputs for BI signals, which are translated into digital pulses and forwarded to the Programmable Logic (PL) for further processing. The CTB triggering firmware is organized into a two-level hierarchy of low-level and high-level triggers (LLTs and HLTs), which are configurable in real time by the DAQ system. A typical physics run usually spans several hours.

3.3 Detector Calibration

The calibration of the ProtoDUNE-SP detector is accomplished through data-driven techniques. The data-driven calibration involves analyzing the signals produced by cosmic ray muons that pass through the detector. By measuring the track and energy deposition of these muons, one can determine the response of the detector to known particles and energies. In addition to these techniques, ProtoDUNE-II plans to use dedicated calibration devices, such as a laser-based system that produces known patterns of light in the detector. These devices are used to provide additional data for calibration and validation in the next run.

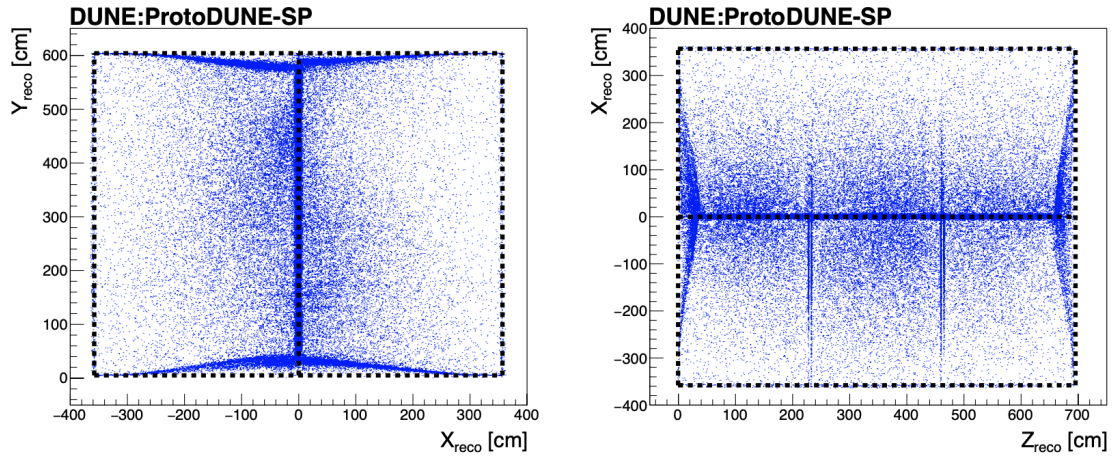

Figure 3.8: The left and right panels show projections of reconstructed and t_0-tagged cosmic-ray track endpoints in the xy plane and zx plane, respectively, using ProtoDUNE-SP data. The selected tracks are t_0-tagged by requiring that they cross the cathode plane (x = 0). The dashed lines indicate the boundary of the TPC active volume where track endpoints should be reconstructed in the absence of space charge effects. The vertical streaks in the middle of the zx plane projection correspond to gaps between the APAs. Taken from [43].

3.3.1 Space Charge Effect

Space charge is a phenomenon that arises from the accumulation of charged ions in a detector. This accumulation occurs due to the presence of cosmic muons and can result in distortions in reconstructed signals and ultimately impact detector performance. In the case of ProtoDUNE-SP, the space charge effect (SCE) is primarily caused by the ionization of argon atoms by cosmic muons and charged beam particles, as the detector is situated at the surface. The cloud of ions produced by the SCE causes a non-continuous distortion of the electric field, which varies over time and depends on the duration of the run and the nominal field strength of the detector. The effects of significant space charge in ProtoDUNE-SP can be observed in Fig. 3.8, which shows the t_0-tagged cosmic-ray tracks from early ProtoDUNE-SP data. However, it is important to note that DUNE, being located underground, will not be affected by this phenomenon.

To mitigate the impact of the SCE, the ProtoDUNE-SP collaboration developed a set of calibration and correction techniques. To address the inadequacy of simulation in repro-

ducing the observed SCE in data, a data-driven simulation of space charge is introduced. This approach involves developing a set of spatial and electric field distortion maps to alter the nominal simulations. The maps created in this way can be used to correct the SCE in both data and simulation by recovering the original positions and accounting for the modified electric field. The process of creating these maps involves the following steps:

1. A 2D map of scale factors at each of the relevant faces of the detector is produced by taking the ratio of the data to the simulated map on a pixel-by-pixel basis.

2. In order to adjust the simulated three-dimensional spatial distortion map, the scale factor maps are applied by conducting linear interpolations between the top and bottom faces of the detector for spatial distortions in the y-direction, between the upstream and downstream faces for spatial distortions in the z-direction, and by taking the average of the linear interpolations in these two directions for spatial distortions in the x-direction. This generates a voxel-by-voxel scale factor that can be used to rescale the spatial distortion magnitude in the corresponding three-dimensional voxel, where a voxel denotes a volumetric pixel.

3. The resulting distortions in each 3D map are reversed to create maps that can be utilized to correct the spatial distortions in both data and simulation. This correction involves repositioning the reconstructed ionization charge depositions to their original locations.

4. Using the reversed maps and the known drift velocity, 3D electric field distortion maps are formed based on the gradient of the spatial distortion along the local drift direction.

The data-driven maps have been utilized to modify the reconstructed position of ionization charge in simulation, as well as to enhance the prediction of prompt recombination effects. Through the implementation of these maps, the data-driven simulation of space charge in ProtoDUNE-SP has been able to effectively correct for the notable distortions caused by space charge, thereby improving the accuracy of the reconstructed events.

3.3.2 Recombination

Charged particles passing through the TPC generate a cloud of ions and ionized electrons. However, before these electrons are drifted to the anode plane by an electric field, there is a possibility for them to recombine with positive Ar ions created by the charged particle or other impurities. This recombination effect alters the charge observed by the wires, requiring precise calibration to accurately measure the energy deposited by charged particles. The recombination factor, denoted as $\mathcal{R}$, represents the fraction of electrons that do not recombine and is used to relate the observed charge to the integrated charge created. Several theoretical models exist to describe electron recombination, such as the Jaffe-Birks model [47] and the Box model [48]. In the Box model, the recombination factor is expressed as,

$$\mathcal{R} = \frac{1}{\xi}\ln(\alpha + \xi), \text{ and } \xi = \frac{\beta(\mathrm{d}E/\mathrm{d}x)}{\rho\mathcal{E}}, \tag{3.1}$$

where α and β are fitted parameters, ρ is the material density, and $\mathcal{E}$ is the electric field strength. The energy deposition can be related to the charge deposition as,

$$\frac{\mathrm{d}E}{\mathrm{d}x} = \frac{(\mathrm{d}Q/\mathrm{d}x)W_{\text{ion}}}{\mathcal{R}}, \tag{3.2}$$

where W_{ion} is the energy required for the ionisation per electron. Substituting Eq. 3.1 into Eq. 3.2 gives,

$$\frac{\mathrm{d}E}{\mathrm{d}x} = \left[\exp\left(\frac{\mathrm{d}Q}{\mathrm{d}x}\frac{\beta W_{\text{ion}}}{\rho\mathcal{E}}\right) - \alpha\right]\left(\frac{\rho\mathcal{E}}{\beta}\right). \tag{3.3}$$

The canonical version of the model assumes $\alpha = 1$, but this performs poorly at low $\mathrm{d}E/\mathrm{d}x$. To address this issue, a modified Box model allows $\alpha < 1$, resulting in better agreement with experimental data, as demonstrated by previous experiments like ArgoNeuT [48]. ProtoDUNE-SP also adopted this modified Box model to account for recombination effects.

3.3.3 Drift Electron Lifetime

Electron lifetime is a crucial parameter for the performance of LArTPCs. The electron lifetime is defined as the average distance that an ionization electron travels before being captured by an impurity in the LAr. The electron lifetime is directly related to the attenuation of the ionization signal, and a lower electron lifetime leads to a degraded energy resolution and tracking performance. This effect is modelled as an exponential decay with respect to time:

$$Q(t) = Q_0(t)\text{exp}\left[\frac{-\left(t_{\text{hit}} - t_0\right)}{\tau}\right], \tag{3.4}$$

where Q is the measured charge at the APA wire plane and Q_0 is the initial charge created by the charged particle, while t_0 indicates the time when the ionization took place and t_{hit} is the arrival time of the drifting charge measured by the APA wire planes and τ is the so-called electron lifetime. A higher electron lifetime implies a higher argon purity in the TPC, leading to fewer electrons getting captured by impurities.

Accurately determining the ionization electrons that survive their journey across the drift volume is important for particle detection and reconstruction. In the ProtoDUNE-SP, the electron lifetime (τ) is measured using long cosmic ray muons tracks. To measure the electron lifetime, the charge deposition of long muon tracks that cross both the cathode and anode planes is compared between the cathode and anode. The ratio of the charge collected near the anode (Q_{A}) to that near the cathode (Q_{C}) is calculated to determine the fraction of ionization electrons that reach the anode, which is directly related to the electron lifetime as,

$$\frac{Q_{\text{C}}}{Q_{\text{A}}} = \text{exp}\left(\frac{-t_{\text{max}}}{\tau}\right), \tag{3.5}$$

where t_{max} is the fixed full drift time of electrons from the cathode to the anode plane. in Fig. 3.9, the ratio of $Q_{\text{C}}/Q_{\text{A}}$ is presented for the data-taking period in November 2018.

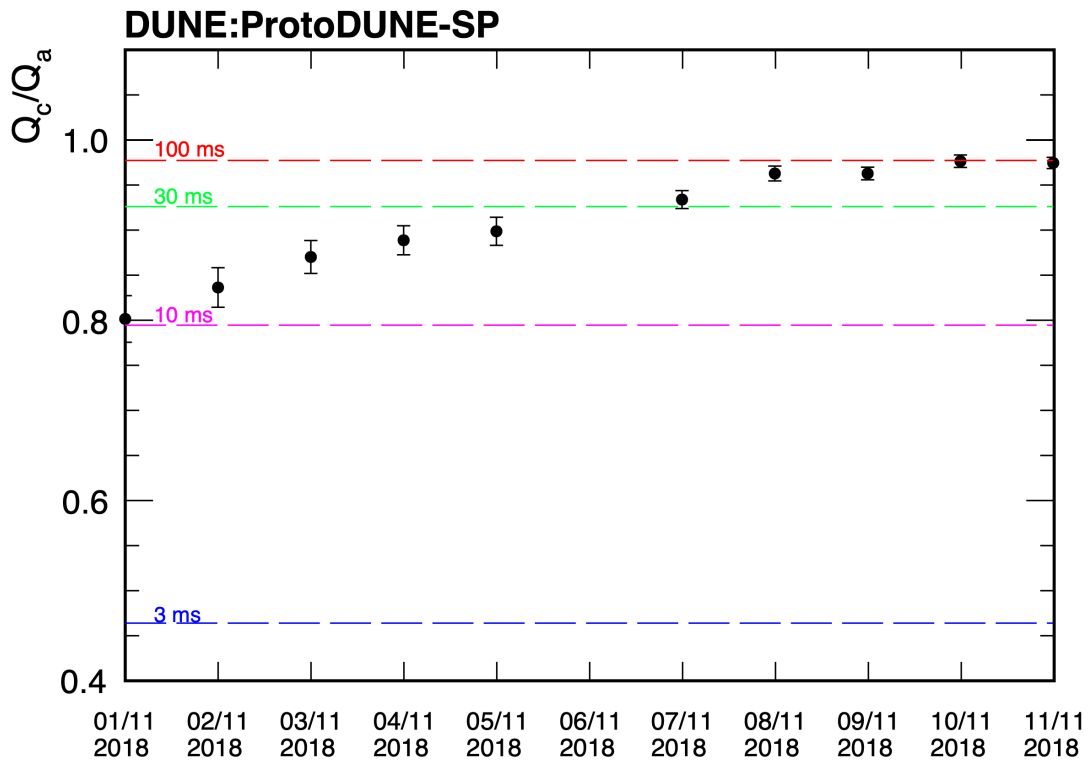

Figure 3.9: The ratio of charge measured at the cathode (Q_{C}) to the charge measured at the anode (Q_{A}) in ProtoDUNE-SP during November 2018. Toward the end of data-taking, higher argon purity was achieved, resulting in an increased electron lifetime. Taken from [43].

With an electron drift velocity of approximately 1.6 m/ms in ProtoDUNE-SP and a drift distance of 3.6 m, the maximum drift time is calculated to be 2.25 ms. Consequently, the lower bound of the electron lifetime is set at 3 ms, as indicated by the dashed blue line.

The electron lifetime can be influenced by various factors, including impurities in the liquid argon, the presence of electronegative contaminants, and temperature variations. Throughout the data-taking period, efforts are made to maintain a stable and high electron lifetime. Figure 3.9 illustrates that at the beginning of data-taking, the argon purity is relatively low, resulting in an electron lifetime of 10 ms. However, towards the end of the data-taking, high argon purity is achieved, significantly increasing the electron lifetime value to nearly 100 ms, far surpassing the baseline value.

3.3.4 Charge and Energy Calibration

Energy calibration is a crucial process in the ProtoDUNE-SP experiment, which establishes the relationship between the recorded signal in the detector and the corresponding deposited energy by a particle. The LArTPC can measure the deposited energy per unit length, but it is important to correct and calibrate the extracted information to ensure that the measured quantity is free from any detector effects. The goal of the calibration is to convert the measured analogue-to-digital converter (ADC) signals to energy in MeV, enabling particle identification and precise energy measurements for the reconstructed particle. The accuracy of energy calibration is essential for achieving the desired physics goals of the ProtoDUNE-SP experiment.

To obtain reliable calorimetric information, a two-stage calibration process is utilized, based on the approach developed by the MicroBooNE collaboration [49]. The first stage involves equalizing the detector response by making use of throughgoing cosmic-ray muons, while the second stage entails determining the absolute energy scale by stopping cosmic-ray muons. Cosmic muons that cross the cathode are employed in both stages since their t_0 can be reconstructed.

During the equalization step, variations in the charge deposition due to different factors that depend on the position of the hit in the x and y-z planes are taken into consideration. In order to correct these non-uniformities, two correction factors are employed: YZ correction factors and X correction factors.

- YZ correction factors take into account the factors affecting the $\mathrm{d}Q/\mathrm{d}x$ values in the yz plane, such as non-uniform wire response, electron diverters, and transverse diffusion. The correction is done by dividing the yz plane into a number of 5×5 cm^2 bins and calculating the median $(\mathrm{d}Q/\mathrm{d}x)^{\text{local}}_{YZ}$ value in each bin. The global median $(\mathrm{d}Q/\mathrm{d}x)^{\text{global}}_{YZ}$ value is then calculated considering the hits throughout the whole drift volume. The YZ correction factor is defined as,

$$C(y,z) = \frac{(\mathrm{d}Q/\mathrm{d}x)^{\text{local}}_{YZ}}{(\mathrm{d}Q/\mathrm{d}x)^{\text{global}}_{YZ}}. \tag{3.6}$$

- X correction factors correct for the non-uniformities affecting the $\mathrm{d}Q/\mathrm{d}x$ values along the drift direction caused by factors such as attenuation due to impurities and longitudinal diffusion. The correction is done by dividing the total drift volume into 5 cm bins in the x coordinate and applying YZ correction factors to correct for the effects depending on y and z coordinates. Then, the median $(\mathrm{d}Q/\mathrm{d}x)^{\text{local}}_{X}$ value is then calculated for each bin, and the global median $(\mathrm{d}Q/\mathrm{d}x)^{\text{global}}_{X}$ value is calculated for the whole TPC. The X correction factor is defined as,

$$C(x) = \frac{(\mathrm{d}Q/\mathrm{d}x)^{\text{local}}_{X}}{(\mathrm{d}Q/\mathrm{d}x)^{\text{global}}_{X}}. \tag{3.7}$$

Finally, the corrected $\mathrm{d}Q/\mathrm{d}x$ after the equalization is defined as,

$$\mathrm{d}Q/\mathrm{d}x = \mathrm{N}_Q C(y,z) C(x) (\mathrm{d}Q/\mathrm{d}x)_{\text{reco.}}, \tag{3.8}$$

where N_Q is a normalization factor that normalizes the $\mathrm{d}Q/\mathrm{d}x$ to the average value at the two anodes to equalize the two halves of the detector.

The calibration process for the absolute energy scale involves selecting cathode-crossing stopping muons, where the calibrated $\mathrm{d}Q/\mathrm{d}x$ (in ADC/cm) needs to be converted into the particle's energy loss per unit length $\mathrm{d}E/\mathrm{d}x$ (in MeV/cm). To calculate $\mathrm{d}E/\mathrm{d}x$, the calibrated $\mathrm{d}Q/\mathrm{d}x$ values along the muon track within its minimum ionizing region (120 to 200 cm from the track endpoint) are used in Eq. 3.9 from the modified Box model [48]. This equation corrects for the recombination effect as described in Sec. 3.3.2, and the resulting $\mathrm{d}E/\mathrm{d}x$ values are fitted to the predictions of the Landau-Vavilov theory [50] as a function of the residual range for stopping muon tracks. The residual range refers to the distance measured to the particle's end-point. During this fitting process, the charge calibration constant C_{cal} is a free parameter in the χ^2 minimization. C_{cal} serves

Table 3.2: The parameter used in Eq. 3.9 from the Modified Box Model for the calibrated $\mathrm{d}E/\mathrm{d}x$ calculation.

W_{ion}	23.6×10^{-6} MeV/electron (work function of argon)
$\mathcal{E}$	Local electric field based on the measured SCE map
ρ	1.38 g/cm^3 (liquid argon density at a pressure of 124.106 kPa)
α	0.93
β'	0.212 (kV/cm)(g/cm^2)/MeV.

as a scaling factor, taking into consideration electronics gain, ADC conversion, and other residual effects that have not been directly calibrated.

$$\left(\frac{\mathrm{d}E}{\mathrm{d}x}\right)_{\text{calibrated}} = \left\{\exp\left[\frac{\left(\frac{\mathrm{d}Q}{\mathrm{d}x}\right)_{\text{calibrated}}}{C_{\text{cal}}}\frac{\beta' W_{\text{ion}}}{\rho\mathcal{E}}\right] - \alpha\right\}\left(\frac{\rho\mathcal{E}}{\beta'}\right) \tag{3.9}$$

The calibrated $\mathrm{d}E/\mathrm{d}x$ calculation uses the parameter W_{ion}, which represents the energy required to ionize one atomic electron in argon. The $\mathcal{E}$ corresponds to the measured electric field from the SCE map, while ρ represents the density of liquid argon at the operating temperature. The parameters α and β' are the Modified Box Model parameters measured by the ArgoNeuT experiment [48]. The specific values of each parameter used in the Eq. 3.9 are provided in Table 3.2.

3.4 Simulation and Reconstruction Chain

The simulation of test beam events in the ProtoDUNE-SP TPC begins with a dedicated Geant4 [51] simulation of the beamline that transports particles from their production point toward the TPC. The rest of the simulation chain is based on the Liquid Argon Software (LArSoft) analysis framework. An event generator module creates particles to be simulated by Geant4 when a primary particle travels through two triggering planes and reaches the outside of the ProtoDUNE-SP cryostat structure. Each event created by the event generator is assigned a primary particle, and other particles in time with the beam

are passed on to the next stage of the simulation. Cosmic-ray particles, as simulated by CORSIKA [52], are overlaid on the event as well. All particles are then given to Geant4 to simulate their transport through the detector, including interactions of hadrons with the detector material. The ionization created by charged particles as they travel through the LAr portion of the detector is passed to the drift simulation step of the simulation, which transports the ionization electrons produced during the Geant4 simulation stage along field lines toward the wire planes. The full electronics response to the ionization drift and collection onto the wires is simulated, creating waveforms that are then passed to the reconstruction chain, as discussed in the following sections.

3.4.1 TPC Signal Processing and Hit Finding

The signal processing and hit reconstruction in ProtoDUNE-SP involve several steps that transform the raw detector data into meaningful physical quantities for analysis. Initially, the signals from the TPC wires are amplified, shaped, and then converted into digital form using an ADC. The induction plane produces a bipolar waveform, while the collection plane generates a unipolar waveform. To signal deconvolution technique, first introduced by ArgoNeuT [53] and further developed by the MicroBooNE collaboration [54, 55], is applied to filter out the noise and eliminate detector effects. During the deconvolution process, the bipolar signals from the induction plane are transformed into unipolar waveforms. Ideally, after the deconvolution, the waveforms in both the induction and collection plane will contain potentially overlapping peaks.

The subsequent step is hit finding, where the detector regions containing particle charge deposits are identified. This involves searching for peaks in the wire waveforms that exceed a specified threshold and fitting them with Gaussian shapes to create hits. A hit represents the charge deposition on a wire at a specific time, and its peak time, maximum amplitude, and area under the fitted Gaussian are recorded. Given that two induction planes consist of wires wrapped around the APA, disambiguation procedures are necessary to determine which segment of the wrapped wire actually recorded the signal. For a collection plane hit, a narrow time window of 1.25 μs is considered. If only a single pair

of induction wires is matched within this window, there are no ambiguities in the hits. However, if more than one candidate induction wire is matched, a χ^2 test is performed on the difference of charge collected between the collection wire and the potential induction wires to identify the correct match. Based on simulation studies, less than 1% of hits are incorrectly assigned to their wire segments [24]. Ultimately, each wire plane provides a 2D view of particle interactions, and these views are fed into the pattern recognition algorithms discussed in the following section.

3.4.2 Pandora

The Pandora Software Development Kit (SDK) [56] is an integral part of the LArSoft framework, which is a widely utilized tool in various LArTPC experiments. Pandora was originally designed for event reconstruction in future linear e^+e^- colliders [57, 58]. It has since demonstrated its effectiveness in various LArTPC experiments, including MicroBooNE [59], and is currently being used in ProtoDUNE-SP. Pandora adopts a multi-algorithm approach for pattern recognition and incorporates experiment-specific content libraries to enrich its capabilities.

Pandora takes hits as input to perform pattern recognition and particle reconstruction. The input hits are categorized into three groups, each corresponding to the three wire planes. Within each group, a 2D cluster is formed when a continuous and unambiguous line of hits is present. However, if any bifurcation or ambiguity arises, the cluster creation stops, and a new cluster is initiated to continue the clustering process. This results in several small clusters with high purity but limited completeness, as depicted in Fig. 3.10 (a). Subsequently, clusters that are close or pointing towards each other are merged into one cluster, as illustrated in Fig. 3.10 (b). The following step involves reconstructing 3D tracks using the merged 2D clusters from the three wire planes. Clusters from any two planes are used to predict the view of the same cluster on the third plane. If the prediction matches, a 3D track is generated using the three 2D clusters. In addition, there are a variety of algorithms in Pandora to deal with cases where some ambiguities are found.

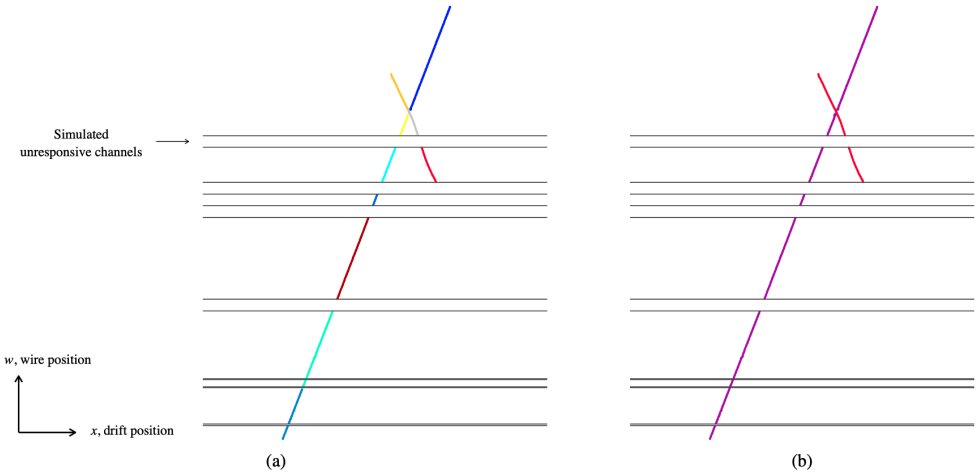

Figure 3.10: Example outputs from two algorithms utilized in Pandora for cluster reconstruction. (a) Clusters produced by the Cluster-Creation algorithm. (b) Completed clusters produced by the Cluster-merge algorithm. Taken from [59].

There are two main reconstruction paths to analyse ProtoDUNE-SP data as shown in Fig. 3.11: PandoraCosmic, focused on identifying cosmic muons and delta rays (track-oriented), and PandoraTestBeam, designed to reconstruct charged beam particles (interaction vertex-oriented). The PandoraCosmic algorithm initially processes the input hits to find any obvious cosmic rays. Once cosmic-tagged hits are identified, they are removed from the initial hit collections. The remaining hits are then subjected to a 3D slicing algorithm that divides the 3D space into distinct regions. Each slice is subsequently passed through both PandoraCosmic and PandoraTestBeam to determine whether it corresponds to a cosmic ray or a beam particle. Finally, a hierarchical relationship is established among particles, involving mother-daughter associations. For instance, a primary track may give rise to two daughter showers and one daughter track, and the daughter track might, in turn, generate a granddaughter track. Following the completion of the particle reconstruction chain, particle identification and selection can be carried out during the physics analysis stage. A detailed description of Pandora reconstruction in ProtoDUNE-SP can be found in Ref. [60].

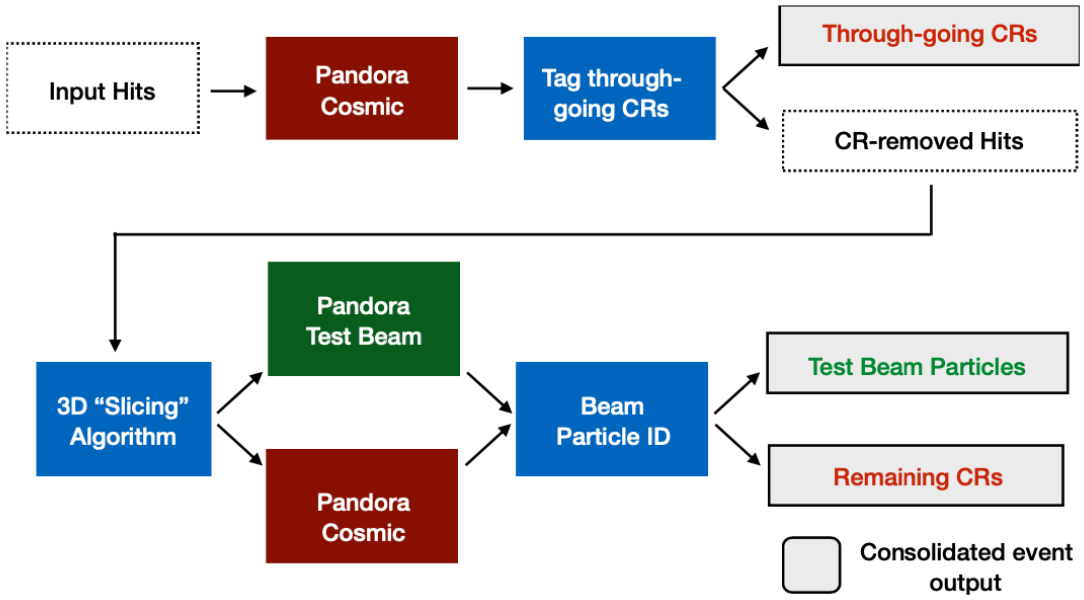

Figure 3.11: A simplified Pandora reconstruction chain in ProtoDUNE-SP. Taken from [61].

3.5 Event Display

This section provides some examples of the event display of charged pion beam interactions. The displayed events are based on data collected in October 2018. Figure 3.12 showcases two candidates for pion quasi-elastic scattering. The y-axis represents the electron drift time in microseconds, while the x-axis corresponds to the wire number, with a wire pitch of 4.7 mm. The vertical track crossing the selected TPC region corresponds to cosmic muons that are not successfully removed by Pandora.

The pion beam travels from left to right. The absence of the beam track at the edge of the TPC is because the beam enters the detector through a beam plug that penetrates inside the TPC. Additionally, the ProtoDUNE-SP is subject to a large SCE, which is particularly significant at the detector's edge. The colour scale in these plots represents the amount of charge deposited along the trajectory of the particles. In LArTPC, pions behave like MIPs, while protons tend to lose more energy, especially towards the end of their tracks.

The final state pion can be identified by observing a Michel electron in the decay chain of

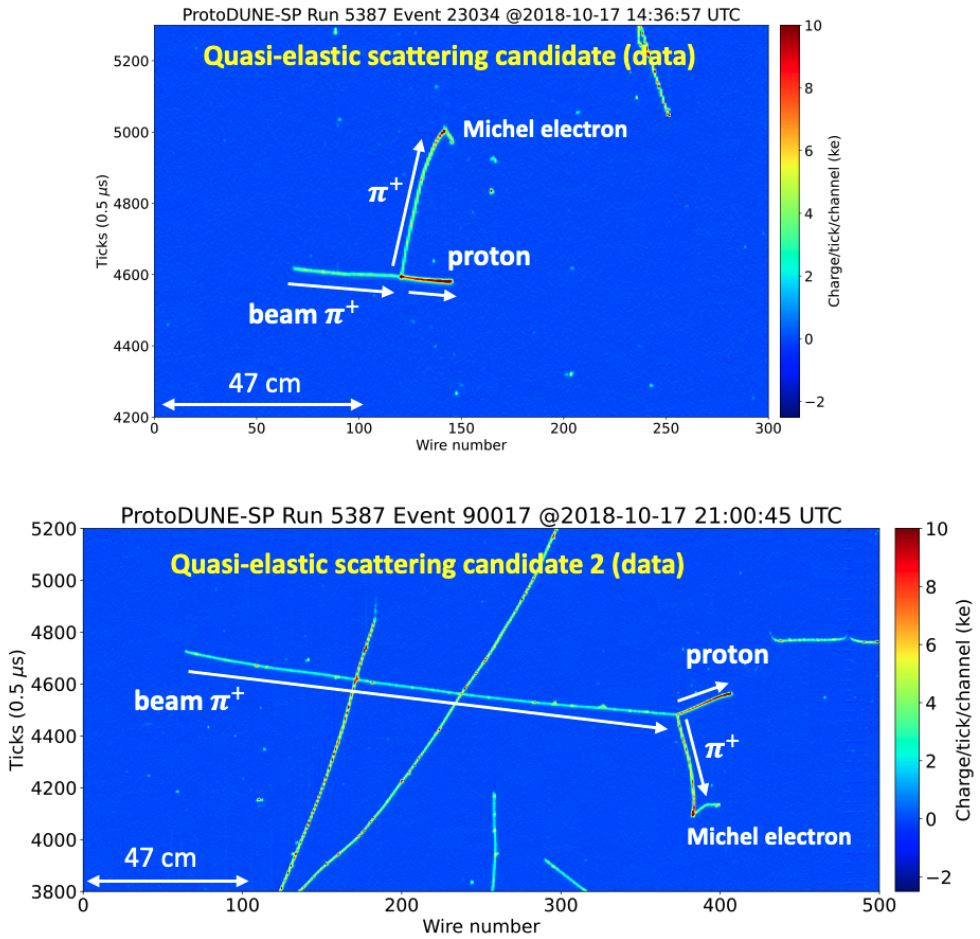

Figure 3.12: Two event displays of 1 GeV/c pion quasi-elastic scattering in ProtoDUNE-SP using data collected in 2018. The beam comes from the left, and the colour represents the charge deposit inside the detector.

the pion. The decay process involves the pion decaying into a muon, which subsequently decays into a Michel electron. In the energy range of the pions in ProtoDUNE-SP, the intermediate muon is not detected inside the detector. Thus, only the Michel electron is observed from the muon's decay at rest. As a result, a kink or change in direction can be seen at the end of the pion track, as demonstrated in the event display.

Figure 3.13 illustrates two candidate pion charge exchange scattering events. In this case, the pion interacts with argon and undergoes a charge exchange, converting itself into a neutral pion. The neutral pion then quickly decays into two photons, resulting in the formation of two electromagnetic showers in the detector. The distance between the starting

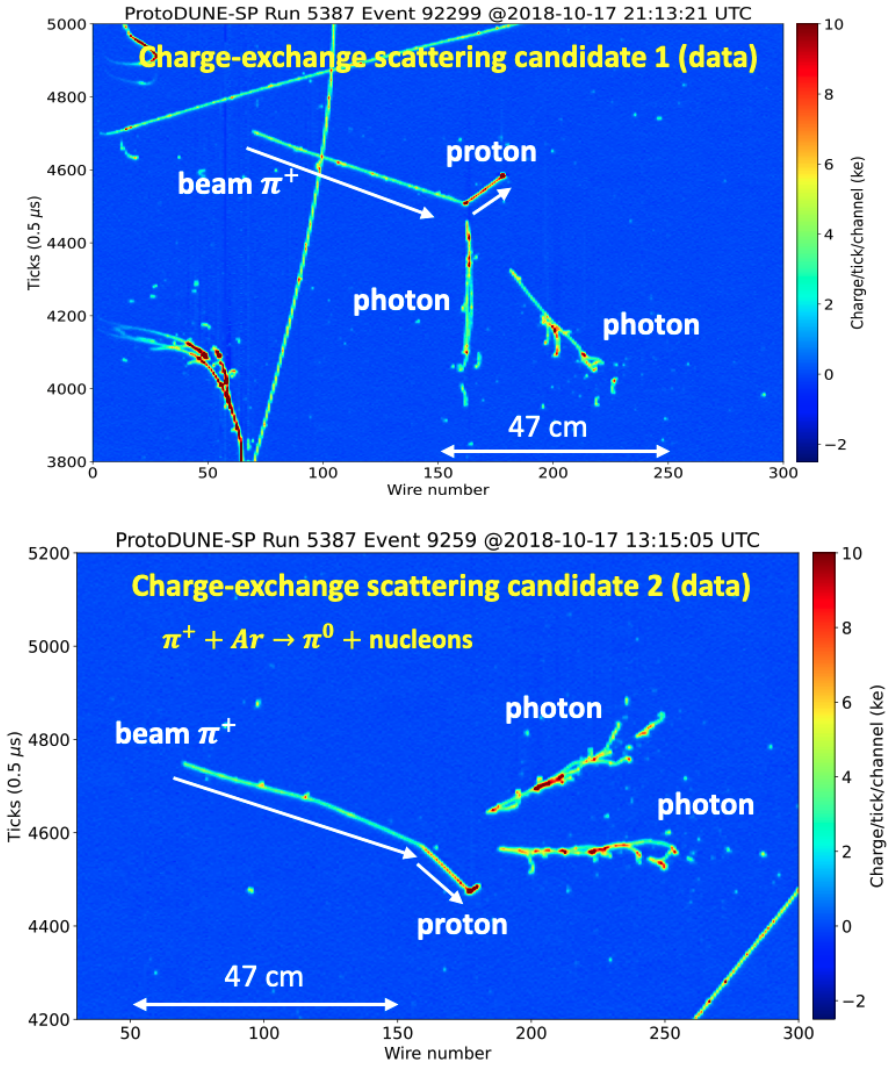

Figure 3.13: Two event displays of 1 GeV/c pion charge exchange scattering in ProtoDUNE-SP using data collected in 2018. The beam comes from the left, and the colour represents the charge deposit inside the detector.

positions of these showers and the interaction vertex is known as the conversion length. By combining the information from the two photon showers, it is possible to calculate the momentum and energy of the neutral pion. However, the reconstruction of two distinct showers can be challenging if the two photons are produced in close proximity to each other or if one of the photons has very low energy. In such cases, it becomes more difficult to accurately separate and identify the individual showers, which can impact the precision of determining the properties of the neutral pion.

3.6 Hadronic Cross-Section Measurements in Argon

The growing use of LArTPC neutrino detectors, such as the DUNE and SBN programs, has renewed interest in hadronic cross sections, particularly those involving argon. These detectors can track particles with high accuracy, measure their energy, and identify them based on their interactions. Pions, in particular, are commonly produced in neutrino interactions and can help determine the type of interaction. However, the lack of research on hadronic interactions of particles produced in neutrino interactions on argon for energies below 1 GeV creates a data gap that contributes to the uncertainty of pion interactions on argon. This uncertainty affects the accuracy of neutrino event generators and detector simulations.

Previous experiments have used pion beams to study pion-nucleus interactions on various nuclei, including He, Li, C, S, Fe, and Pb [62, 63, 64, 65]. These studies used thin targets with thicknesses much smaller than the typical interaction length in the material. In these experiments, a beam of pions with known flux is directed at a thin slab of material, and the outgoing flux is recorded. From this, the interacting flux can be retrieved, and the cross-section can be calculated at a given beam energy.

The objective of this thesis is to expand on these previous studies by addressing the data gap in pion-argon cross-section measurements. The analysis will focus on measuring the hadronic interactions of charged pions on argon for energies between 450 to 950 MeV, using data from the ProtoDUNE-SP. By filling this gap, this measurement can reduce the uncertainty related to pion interactions on argon, which is essential for improving the accuracy of neutrino oscillation measurements in DUNE.

3.6.1 Thin-Slice Method

Traditionally, the determination of pion hadronic cross sections involved the use of thin targets, which are targets with a thickness much smaller than the average interaction length in the material. The typical LArTPC does not satisfy this requirement as a whole, but its unprecedented tracking capabilities enable the creation of a methodology that uti-

lizes the conditions of thin target experiments.

The probability of pion interaction, denoted as P_{Int}, in an argon target with a thickness of δx is connected to the interaction cross section σ by the following relationship,

$$P_{Int} = 1 - e^{-\sigma n \delta x}, \tag{3.10}$$

where $n = \rho N_A / m_{Ar}$ is the number density of the target, where ρ is the mass density of the argon in g/cm^3, N_A is the Avogadro constant in 1/mol and m_{Ar} is the argon atomic mass in g/mol. The probability of a pion interacting with the target can be estimated statistically by calculating the ratio of the number of pions that interact with the thin target (known as the interacting flux, N_{Int}) to the number of incident pions (known as the incident flux, N_{Inc}). This assumption holds true when the interaction length is much greater than the thickness of the target. This is the so-called thin target approximation. By using this approximation, it becomes feasible to derive a straightforward proportional correlation between the cross-section and the interaction probability. This is achieved through the application of the first term of a Taylor expansion of the exponential function as,

$$\sigma = \frac{1}{n \delta x} \frac{N_{Int}}{N_{Inc}}, \tag{3.11}$$

by assuming the $N_{Int} \ll N_{Inc}$.

As the interaction length of pions in liquid argon is around 50 cm, the ProtoDUNE-SP detector, with $\sim$ 7 m long, cannot be considered a thin target. Nonetheless, the high granularity of the LArTPC enables the measurement of the kinetic energy of each pion at intervals of approximately 4.7 mm (wire pitch described in Sec. 3.2.2) along its trajectory in the detector's active volume. Therefore, one can view the argon volume as a sequence of many adjacent thin targets, as shown in Fig. 3.14, and restore the thin target approximation in each slice of argon [66]. As a result, the cross-section measurement at each thin slice can be treated as a separate thin target experiment. When the energy of beam pion is measured as it enters each slice, the energy dependence is incorporated into Eq. 3.11 as follows,

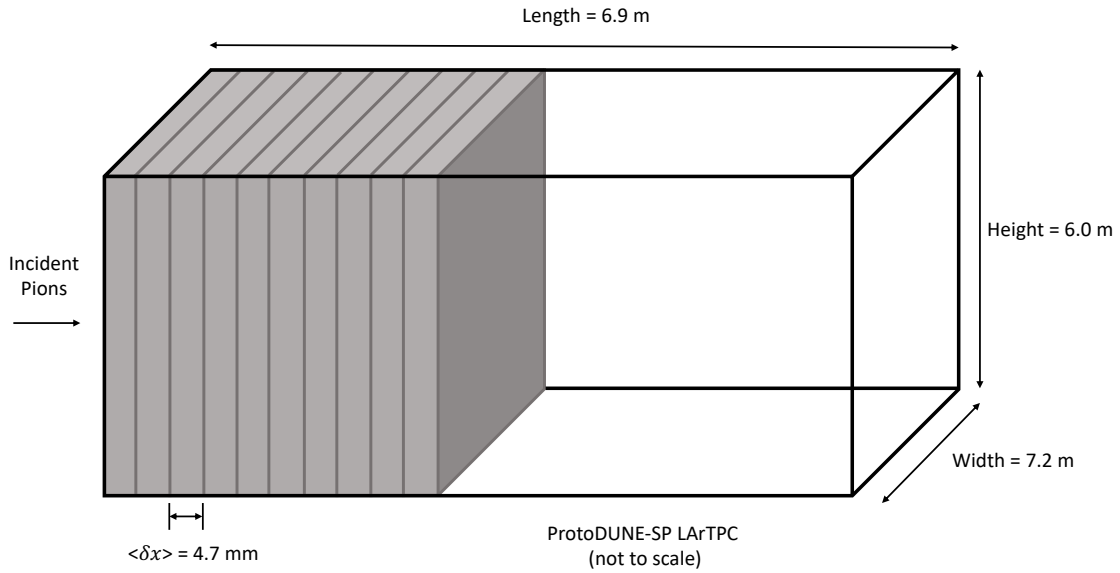

Figure 3.14: Cartoon demonstration of the thin-slice method where the slicing width is 4.7mm and the detector is not to scale. Reproduced from [66].

$$\sigma_i(E) = \frac{1}{n\delta x}\frac{\mathrm{N_{Int}}(E)}{\mathrm{N_{Inc}}(E)}\Big|_{\mathrm{slice}_i}. \tag{3.12}$$

From this point onward, the energy dependence notation will be omitted and will simply be represented by the index i. Generally, if the assumption of $\mathrm{N_{Int}} \ll \mathrm{N_{Inc}}$ not holds, the more accurate formula gives,

$$\sigma_i(E) = \frac{m_{\mathrm{Ar}}}{\rho \mathrm{N}_A \delta x} \ln\left(\frac{\mathrm{N_{Inc}}}{\mathrm{N_{Inc}} - \mathrm{N_{Int}}}\right)\Big|_{\mathrm{slice}_i}, \tag{3.13}$$

where δx represents the thin slice width which is the wire pitch $\sim$ 4.7 mm. The index i represents the slice number.

3.6.2 Energy-Slice Method

The ProtoDUNE-SP detector is affected by spatial distortions caused by strong SCE, which distort the track pitch more at the boundaries. These effects are difficult to replicate precisely in simulations, so it is better to avoid using spatial slicing in measurements.

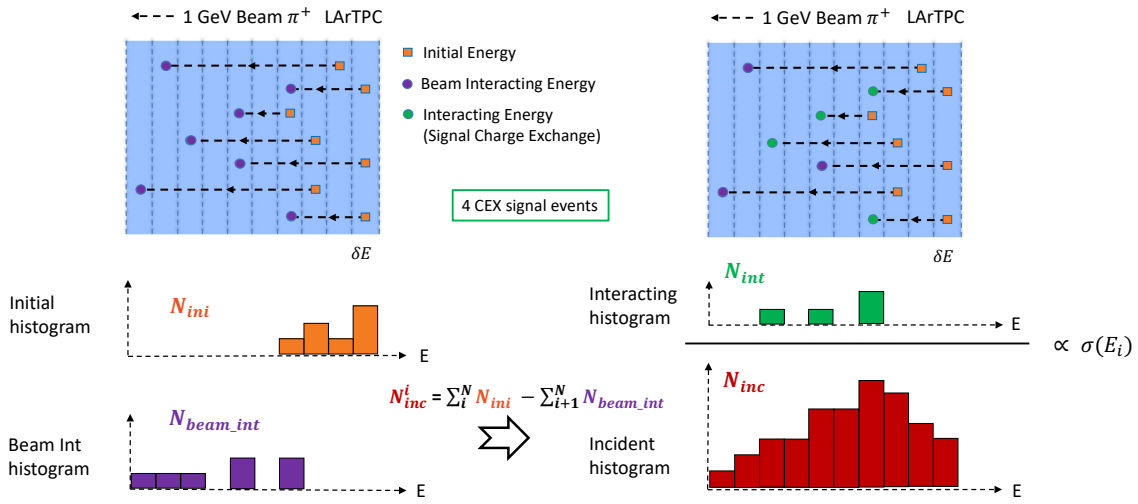

Figure 3.15: An illustration demonstrating the process of populating the Incident and Interacting Histograms for cross-section measurements. Pions enter the TPC with different initial energy and subsequently lose energy due to ionization until they interact inside the detector.

Instead, the proposed E-Slice method involves directly slicing the measurement in the energy phase space, which simplifies the process and eliminates the need for an additional variable associated with uncertainty in the final cross-section equation.

Figure 3.15 provides an illustrative example of the procedure for calculating the incident and interacting fluxes in the cross-section formula. To begin, the energy of each pion beam at the front face of the TPC is measured and recorded in an Initial Histogram. If a pion interacts or comes to a stop inside the TPC, the energy at that interaction point is also recorded in a separate histogram called the Beam Interacting Histogram. The incident flux at each bin can then be determined by computing the difference between the number of pions in the Initial Histogram and the number of pions that interact in the Beam Interacting Histogram as,

$$\mathrm{N}^i_{\mathrm{Inc}} = \sum_i^n \mathrm{N}^i_{\mathrm{Ini}} - \sum_{i+1}^n \mathrm{N}^i_{\mathrm{BeamInt}}. \tag{3.14}$$

In this analysis, the signal events are defined as the pion charge exchange events, which are described in detail in Chap. 8. If a pion beam interacts with the signal event topol-

ogy, the Interacting Histogram is filled accordingly. The Incident Histogram provides the number of pions that have traversed without interacting for each energy bin, whereas the Interacting Histogram records the number of pions that have undergone the pion charge exchange process for each corresponding energy bin. To compute the cross-section at each beam energy bin i, the following formula is used,

$$\sigma_i = \frac{m_{\text{Ar}}}{\rho \text{N}_A \delta E} \frac{\text{d}E}{\text{d}x}\Big|_{E_i} \ln\left(\frac{\text{N}_{\text{Inc}}}{\text{N}_{\text{Inc}} - \text{N}_{\text{Int}}}\right)\Big|_{\text{slice}_i}, \tag{3.15}$$

where the pre-factors related to argon are defined in Eq. 3.13 and δE represents the energy slicing width and dE/dx is the pion energy loss per unit distance at a specific energy of E_i. The bin content of the Incident and Interacting Histogram at each beam energy bin i is denoted by N_{Inc} and N_{Int}, respectively.

Following Eq. 3.15, the integrated pion charge exchange cross-section as a function of beam energy can be calculated. In addition, the differential cross-section for a particular beam interacting energy bin i, with π^0 kinematics can be calculated as,

$$\left(\frac{\text{d}\sigma}{\text{d}T_{\pi^0}}\right)_{ij} = \frac{m_{\text{Ar}}}{\rho \text{N}_A \delta E} \frac{\text{d}E}{\text{d}x}\Big|_{E_i} \frac{1}{\Delta T_{\pi^0}} \frac{\text{N}^{ij}_{\text{Int}}}{\text{N}^{i}_{\text{Inc}}}, \tag{3.16}$$

where the index j represents the π^0 energy bin and the $\text{N}^{ij}_{\text{Int}}$ is the number of entries at π^0 energy bin j with the beam interacts within the beam energy bin i. The ΔT_{π^0} is the bin width of the π^0 kinetic energy distribution. In the approximation of $\text{N}_{\text{Int}} \ll \text{N}_{\text{Inc}}$, Eq. 3.15 can be simplified to,

$$\sigma_i = \frac{m_{\text{Ar}}}{\rho \text{N}_A \delta E} \frac{\text{d}E}{\text{d}x}\Big|_{E_i} \frac{\text{N}^{i}_{\text{Int}}}{\text{N}^{i}_{\text{Inc}}}. \tag{3.17}$$

By substituting Eq. 3.17 into Eq. 3.16, the differential cross-section formula is,

$$\left(\frac{\text{d}\sigma}{\text{d}T_{\pi^0}}\right)_{ij} = \frac{1}{\Delta T_{\pi^0}} \frac{\text{N}^{ij}_{\text{Int}}}{\text{N}^{i}_{\text{Int}}} \sigma_i, \tag{3.18}$$

where σ_i is the measured pion CEX integrated cross-section defined in Eq. 3.15.

The main goal when measuring a cross-section is to compare the results to theoretical models. In this study, the distributions for the Incident and Interacting Histograms are measured in pion kinetic energy. However, both detector effects, which introduce energy smearing and reconstruction inefficiency, are corrected through the use of iterative Bayesian unfolding. The major systematic uncertainties, including uncertainties on beam momentum measurements, reconstruction resolution, and model-dependent uncertainties, are evaluated and included in the final result of both the pion integrated and differential CEX cross-section measurement.

4 | Transverse Kinematic Imbalance

Inclusive and semi-inclusive measurements, such as the integrated cross sections and the lepton kinematics, have been studied in great detail over the past decades. However, these observables strongly depend on neutrino energy and are difficult to access the nuclear effects. In experimental measurements, the various nuclear effects are convoluted together, making it challenging to study them individually. However, there is a promising approach to investigate specific nuclear effects using a novel set of kinematic variables known as transverse kinematic imbalance (TKI). This concept closely resembles the methodology employed in collider physics to determine neutrino energy through the analysis of missing energy.

The concept of using TKI to probe nuclear effects in neutrino interactions has been explored in previous studies [67, 68, 69, 70, 71] and effectively applied in experiments such as MINERνA (Main INjector ExpeRiment ν-A) [72, 73, 74], T2K [75, 76], and MicroBooNE [77]. Benefiting from advanced tracking capabilities, DUNE ND-GAr will leverage the TKI to investigate neutrino-argon interactions with remarkable precision [40, 29]. A noteworthy application of this approach is the analysis of TKI between the final state nucleon and charged lepton in CC0π events, with minimal dependence on neutrino energy.

4.1 Definition

This subsection presents a review of TKI definitions [68] and derivations [69]. Suppose that a muon neutrino scatters from a bound neutron inside the nucleus via the CCQE interaction, leaving a muon and only one proton in the final state as

$$\nu_\mu + \mathrm{n} \rightarrow \mu^- + \mathrm{p}. \tag{4.1}$$

Once the proton is produced, it starts to propagate through the nuclear medium and undergoes FSIs. The momentum of the final-state proton weakly depends on the neutrino

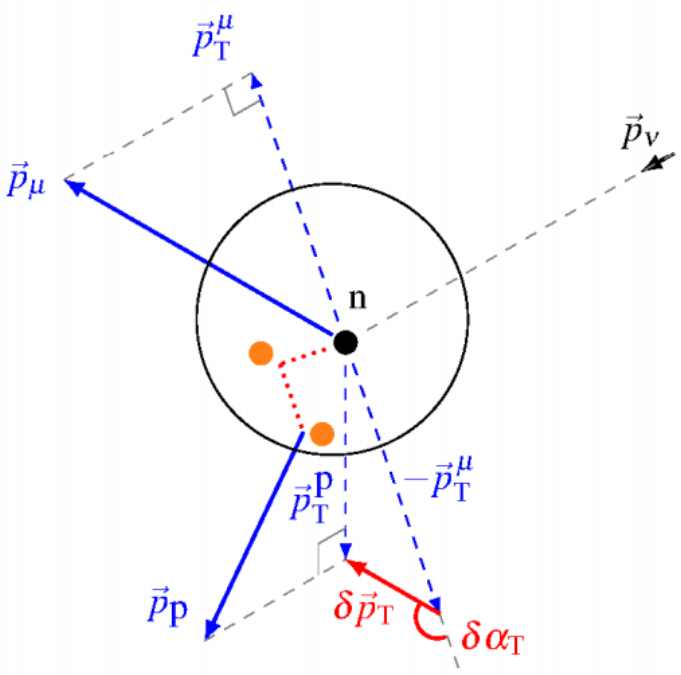

Figure 4.1: Schematic illustration of transverse kinematic imbalance variables. The TKI variables are shown in red and defined in a plane perpendicular to the neutrino direction. Taken from [68].

energy as discussed in Ref. [68]. Suppose the energy-momentum transfer from the proton to the nuclear medium is $(\Delta E, \Delta\vec{p})$, then the intranuclear momentum transfer (IMT), $\Delta\vec{p}$, would be an ideal observable to measure the nuclear effects independent of neutrino energy. However, this is not experimentally accessible since the initial momenta of both neutron and neutrino are not known in the first place. Instead, as shown in Fig. 4.1, one could define the following single-transverse kinematic imbalance, the transverse momentum imbalance $\delta\vec{p}_{\mathrm{T}}$ and the boosting angle $\delta\alpha_{\mathrm{T}}$ which are related to $\Delta\vec{p}$,

$$\delta\vec{p}_{\mathrm{T}} \equiv \vec{p}_{\mathrm{T}}^{\,\mu} + \vec{p}_{\mathrm{T}}^{\,p}, \tag{4.2}$$

$$\delta\alpha_{\mathrm{T}} \equiv \arccos\frac{-\vec{p}_{\mathrm{T}}^{\,\mu}\cdot\delta\vec{p}_{\mathrm{T}}}{p_{\mathrm{T}}^{\mu}\delta p_{\mathrm{T}}}, \tag{4.3}$$

where $\vec{p}_{\mathrm{T}}^{\,\mu}$ and $\vec{p}_{\mathrm{T}}^{\,p}$ are the transverse momenta projection of the outgoing muon and proton, respectively. Since the initial neutrino has zero momentum in the transverse direction, resulting in $\vec{q}_{\mathrm{T}} = -\vec{p}_{\mathrm{T}}^{\,\mu}$, where $\vec{q}_{\mathrm{T}}$ is the transverse component of the momentum transfer $\vec{q}$.

Ideally, the sum of the transverse component of muon and proton momenta, $\delta\vec{p}_{\mathrm{T}}$, would vanish if the target nucleon is static and free since there is no initial momentum in the transverse direction. For a nucleon in a nucleus, if there are no FSIs present, then $\delta\vec{p}_{\mathrm{T}}$ and $\delta\alpha_{\mathrm{T}}$ would be the transverse momentum of the struck neutron and the transverse projection of the angle between the neutron momentum $\vec{p}_{\,n}$ and momentum transfer $\vec{q}$ respectively as shown in Fig. 4.1. In the first approximation, the distribution of $\delta\vec{p}_{\mathrm{T}}$ is independent of the neutrino energy [68]. Since the isotropic property of the Fermi motion, the value of $\delta\alpha_{\mathrm{T}}$ would be uniformly distributed. With FSIs switched on, the outgoing proton could be boosted or dragged as it propagates through the nuclear medium, making $\delta\alpha_{\mathrm{T}} \to 0^{\circ}$ or 180°.

The transverse momentum imbalance, $\delta\vec{p}_{\mathrm{T}}$, can also be interpreted as the sum of the transverse component of the Fermi motion (associated with initial neutron) and IMT, $\Delta\vec{p}$ (associated with final state proton) as defined above. Thus, the momentum imbalance, $\delta\vec{p}$ which includes the longitudinal component, in a neutrino-nucleus interaction is

$$\delta\vec{p} = \vec{p}_{\mathrm{FM}} - \vec{p}_{\mathrm{IMT}}, \tag{4.4}$$

For a pure QE interaction (zero IMT contribution), the neutron momentum is

$$p_{\mathrm{n}} = \delta p. \tag{4.5}$$

Therefore, in the basic interaction (Eq. 4.1), the energy and momentum conservation laws give,

$$E_{\nu} + M_A = E_{\mu} + E_p + E_{A-1}, \tag{4.6}$$

$$E_\nu = p_{\mathrm{L}}^{\mu} + p_{\mathrm{L}}^{p} - \delta p_{\mathrm{L}}, \tag{4.7}$$

$$0 = \vec{p}_{\mathrm{T}}^{\,\mu} + \vec{p}_{\mathrm{T}}^{\,p} - \delta\vec{p}_{\mathrm{T}}, \tag{4.8}$$

where $\vec{p}^{\,\mu(p)}$ and $\delta\vec{p}$ are the muon (proton) momentum and the momentum imbalance, respectively. M_A is the mass of the target nucleus, E_ν, $E_{\mu(p)}$ and E_{A-1} are the energy of the initial neutrino, the final state muon (proton) and the remnant nucleus [69]. If the initial nucleus is at rest, one could assume,

$$\delta\vec{p} = \vec{p}_{A-1}, \tag{4.9}$$

Then substitute Eq. 4.7 into Eq. 4.6 to eliminate the E_ν,

$$\begin{cases} \delta p_{\mathrm{L}} = \dfrac{1}{2}R - \dfrac{M_{A-1}^2 + \delta\vec{p}_{\mathrm{T}}^{\,2}}{2R}, \\ \\ R \equiv M_A + p_{\mathrm{L}}^{\mu} + p_{\mathrm{L}}^{p} - E^{\mu} - E^{p}. \end{cases} \tag{4.10}$$

If the final state proton and muon momenta are measured, then the initial neutron momentum is calculated as

$$p_{\mathrm{n}} = \delta p = \sqrt{\delta\vec{p}_{\mathrm{T}}^{\,2} + \delta p_{\mathrm{L}}^2}, \tag{4.11}$$

providing the binding energy is taken into account when calculating the mass of nucleus $M_{A(A-1)}$. The p_{n} is referred to as the emulated neutron momentum.

4.2 Longitudinal Momentum Imbalance

It is intriguing to investigate which part of the momentum imbalance dominates the calculation of p_{n}. The Giessen Boltzmann-Uehling-Uhlenback (GiBUU) Project [78] is employed as the event generator in this study. The GiBUU 2019 version is used to produce Monte Carlo (MC) simulations of ν_μAr CC0π events with the DUNE neutrino flux.

The ratio of the longitudinal momentum imbalance δp_{L} and the transverse momentum imbalance $\delta\vec{p}_{\mathrm{T}}$ is studied as shown in Fig. 4.2 (a). It can be seen that δp_{L} is only a small correction in $\delta\vec{p}_{\mathrm{T}}$ as the ratio is peaked around the origin. Consider a Cartesian coordinate system with the x-axis to be $\delta\vec{p}_{\mathrm{T}}$ and the y-axis to be δp_{L} as shown in Fig. 4.3. Then in the polar coordinate, neutron momentum p_{n} as defined in Eq. 4.11 is the polar radius. One could also calculate the polar angle θ_{L} as shown in Fig. 4.2 (b). The depleted region around $\theta_{\mathrm{L}} = 90^\circ$ also confirms that δp_{L} is small compared with $\delta\vec{p}_{\mathrm{T}}$. Therefore, p_{n} can be considered as $\delta\vec{p}_{\mathrm{T}}$ in the first order with an $\mathcal{O}(20\%)$ correction.

To demonstrate the relation between the transverse momentum imbalance $\delta\vec{p}_{\mathrm{T}}$ and the neutron momentum p_{n}, also the true Fermi motion of the initial neutron, the distributions of these three variables in the QE mode are plotted in Fig. 4.4. There is a cut-off momentum $p_{\mathrm{FM}}^{\mathrm{max}} = 0.3$ GeV$/c$ in the true Fermi motion distribution. This is a simplified case since the momentum distribution in heavy nuclei is commonly simulated using a Fermi Gas model. There are nucleons with momentum much larger than $p_{\mathrm{FM}}^{\mathrm{max}}$ due to the short-range correlations [79] which is not included in the model. If there are no FSIs, then the neutron momentum would correspond to the true Fermi motion. However, a small tail is found in the distribution of p_{n}, which indicates the presence of FSIs in a QE mode. The p_{n} distribution is shifted towards a larger momentum relative to the δp_{T} distribution due to the correction made by δp_{L}.

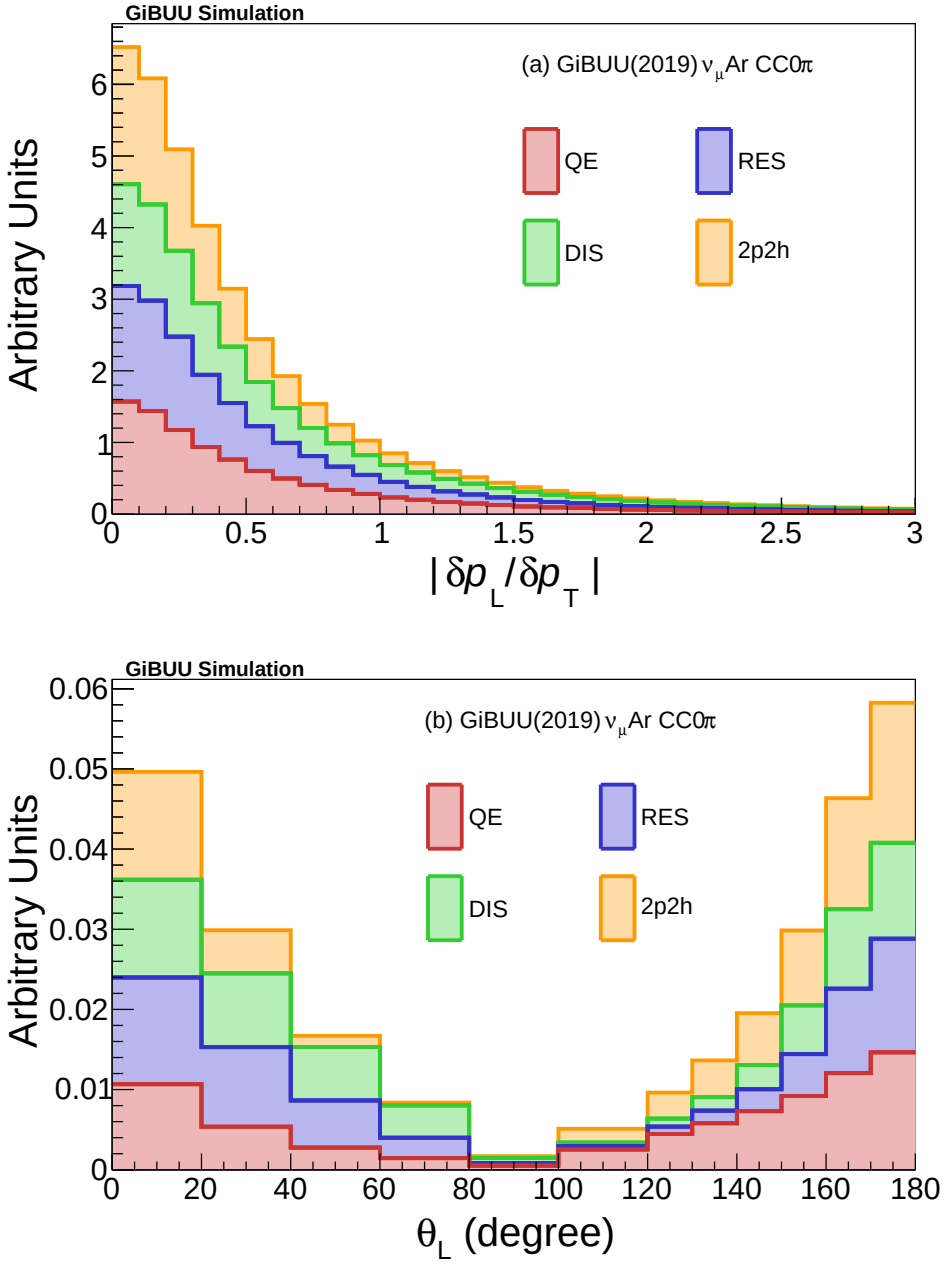

Figure 4.2: **(a)** The ratio of the longitudinal momentum imbalance δp_{L} and the transverse momentum imbalance $\delta\vec{p}_{\mathrm{T}}$ in a stack histogram. In the region where the majority of events occur (with a ratio < 0.6), the mean value of $\delta p_{\mathrm{L}}/\delta p_{\mathrm{T}}$ is 0.24, with a RMS of 0.16. **(b)** The distribution of the polar angle $\theta_{\mathrm{L}} = \arctan(\delta p_{\mathrm{L}}/\delta p_{\mathrm{T}})$ as defined in Fig. 4.3. Each component in the stack histogram is area normalised.

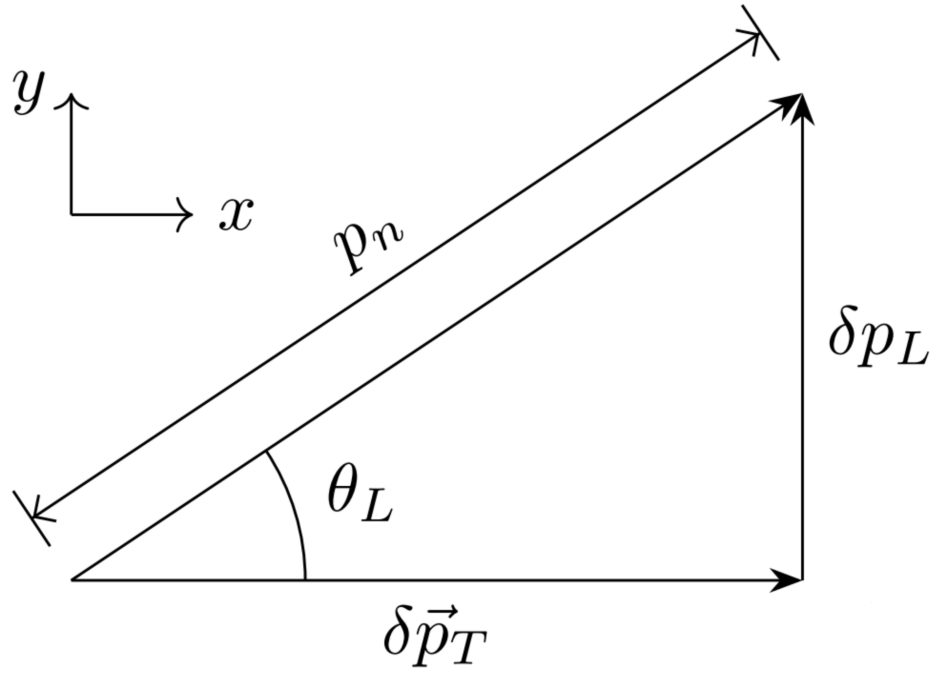

Figure 4.3: Geometric illustration of the relation between $\delta\vec{p}_{\mathrm{T}}$, δp_{L} and p_{n} in Cartesian and polar coordinates.

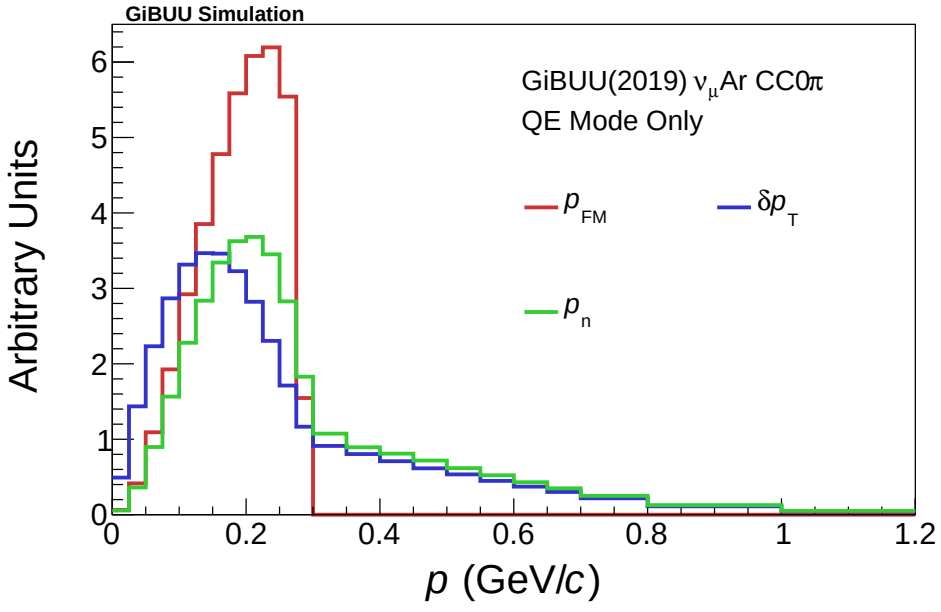

Figure 4.4: The distributions of the true Fermi motion p_{FM}, transverse momentum imbalance δp_{T} and neutron momentum p_{n}.

4.3 Predictions in DUNE ND-GAr

This section aims to demonstrate nuclear effects via the TKI variables p_{n} and $\delta\alpha_{\mathrm{T}}$ in DUNE ND-GAr. The signal channel used in this study is the ν_μ-Ar CC0π interaction, where there are no momentum thresholds imposed on pions. The MINERνA results [72] serve as a reference in this context and are compared to those of ND-GAr, with different neutrino beam flux, detector response, and nuclear target. This comparison illustrates the advantage of the ND-GAr detector in probing nuclear effects using the TKI technique.

MINERνA is the pioneering experiment that investigates neutrino interactions with various nuclei within the 1-10 GeV neutrino energy range. The detector employs the scintillator-based active target tracker to measure the products of neutrino interactions. In this study, the carbon nucleus target is used for the TKI analysis. The signal phase space of MINERνA experiment is defined as [72],

$$\begin{cases} 1.5\ \mathrm{GeV}/c < p_\mu < 10\ \mathrm{GeV}/c\ , \theta_\mu < 20^\circ, \\ \\ 0.45\ \mathrm{GeV}/c < p_{\mathrm{p}} < 1.2\ \mathrm{GeV}/c\ , \theta_{\mathrm{p}} < 70^\circ, \end{cases} \tag{4.12}$$

where $p_{\mu(\mathrm{p})}$ and $\theta_{\mu(\mathrm{p})}$ are the muon (proton) momentum in the lab frame and polar angle relative to the direction of the neutrino beam, respectively.

ND-GAr is proposed to be employed as one of the near detectors in the DUNE experiment. The detector is filled with an Argon-CH_4 (90%- 10%) gas mixture at 10 bar [40]. It can provide an unprecedented resolution on neutrino-argon scattering and detect both muons and protons with kinetic energy larger than 3 MeV in the full angle acceptance. This leads to the signal phase space of DUNE ND-GAr to be

$$\begin{cases} p_\mu > 0.0254\ \mathrm{GeV}/c, 4\pi \text{ full angle}, \\ \\ p_{\mathrm{p}} > 0.0751\ \mathrm{GeV}/c, , 4\pi \text{ full angle}. \end{cases} \tag{4.13}$$

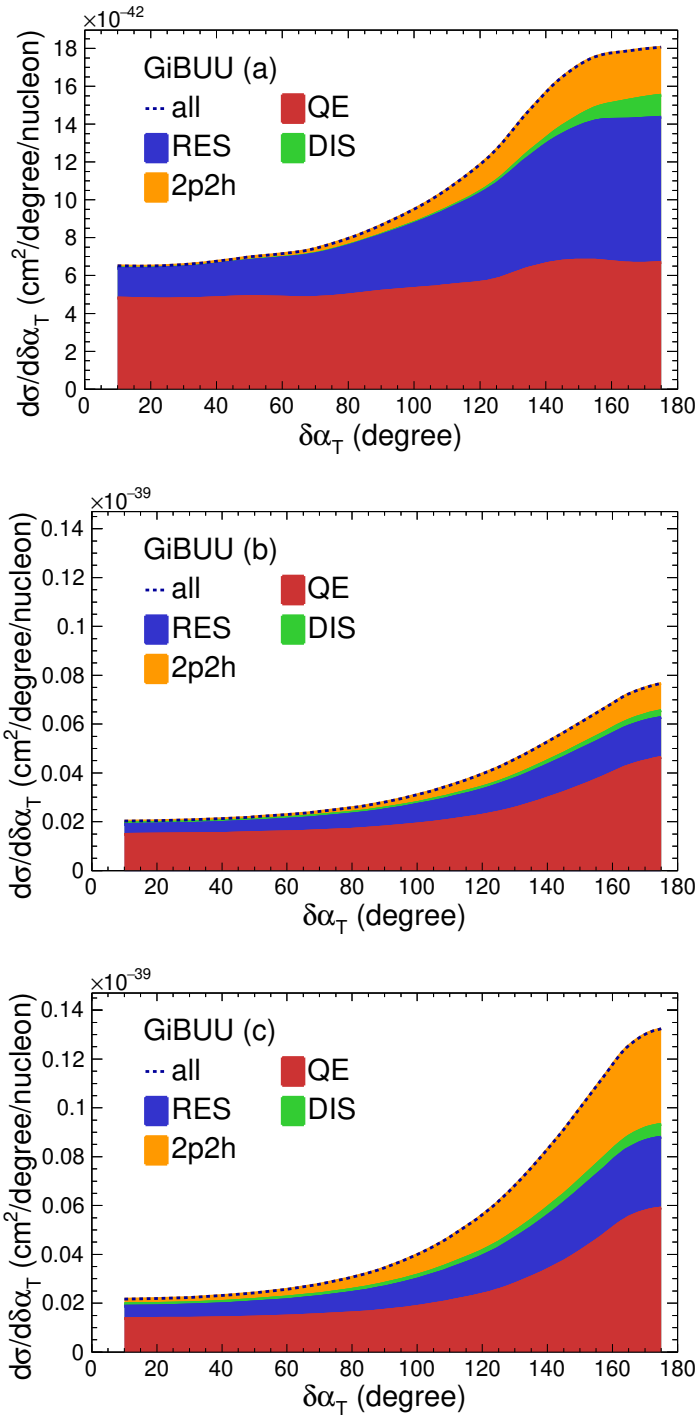

Figure 4.5: Differential cross sections per nucleon as a function of the boosting angle $\delta\alpha_{\mathrm{T}}$, for **(a)** carbon target, MINERνA ν_μ flux and detector acceptance, **(b)** carbon target, DUNE ν_μ flux and ND-GAr detector acceptance and **(c)** argon target, DUNE ν_μ flux and ND-GAr detector acceptance. The GiBUU (version 2019) model is used to generate these neutrino events.

Figure 4.5 shows the differential cross sections as the transverse boosting angle, $\delta\alpha_{\mathrm{T}}$ for

(a) carbon target, MINERνA ν_μ flux and detector acceptance (Eq. 4.12),

(b) carbon target, DUNE ν_μ flux and ND-GAr detector acceptance (Eq. 4.13),

(c) argon target, DUNE ν_μ flux and ND-GAr detector acceptance (Eq. 4.13).

It should be noted that the scale of the y-axis in plots (b) and (c) is one order of magnitude larger than plot (a) due to a higher event rate thanks to the lower threshold in ND-GAr. Using carbon as the nuclear target in DUNE ND-GAr serves as a hypothetical experimental configuration to showcase the enhanced detection capability for low-energy particles in ND-GAr.

The QE mode in MINERνA (Fig. 4.5 (a)) is rather flat. By comparing plots (a) and (b), the increased acceptance in ND-GAr allows more low energy protons to be detected, which are not available in MINERνA. These protons are decelerated as they propagate out through the nuclear medium. Hence, there is an increase in the QE mode at the higher value of $\delta\alpha_{\mathrm{T}}$ in plot (b).

When the target nucleus is switched to argon (Fig. 4.5 (c)), as it should be in ND-GAr, by comparing with the plot (b), an additional enhancement is found in all modes except for the region where $\delta\alpha_{\mathrm{T}}$ is close to zero. Since the argon nucleus has a larger radius than carbon, the final state hadrons will propagate for a longer distance inside the nuclear medium that are more likely to be decelerated, making $\delta\alpha_{\mathrm{T}}$ tend to 180°. Many pions produced in the non-QE processes are more easily absorbed inside the nucleus, which increases the contribution from the RES and DIS modes to the CC0π events category. In addition, the carbon nucleus has the same number of protons and neutrons, which leads carbon to be an isospin-0 nucleus. However, as for the argon nucleus, there are 4 more neutrons than protons, making the argon nucleus have an isospin-2. As suggested in [80], the GiBUU production of the 2p2h process is proportional to the isospin (T) of the nucleus by $\sim (T+1)$. Therefore, the predicted cross sections of argon are about three times larger than carbon in the 2p2h mode.

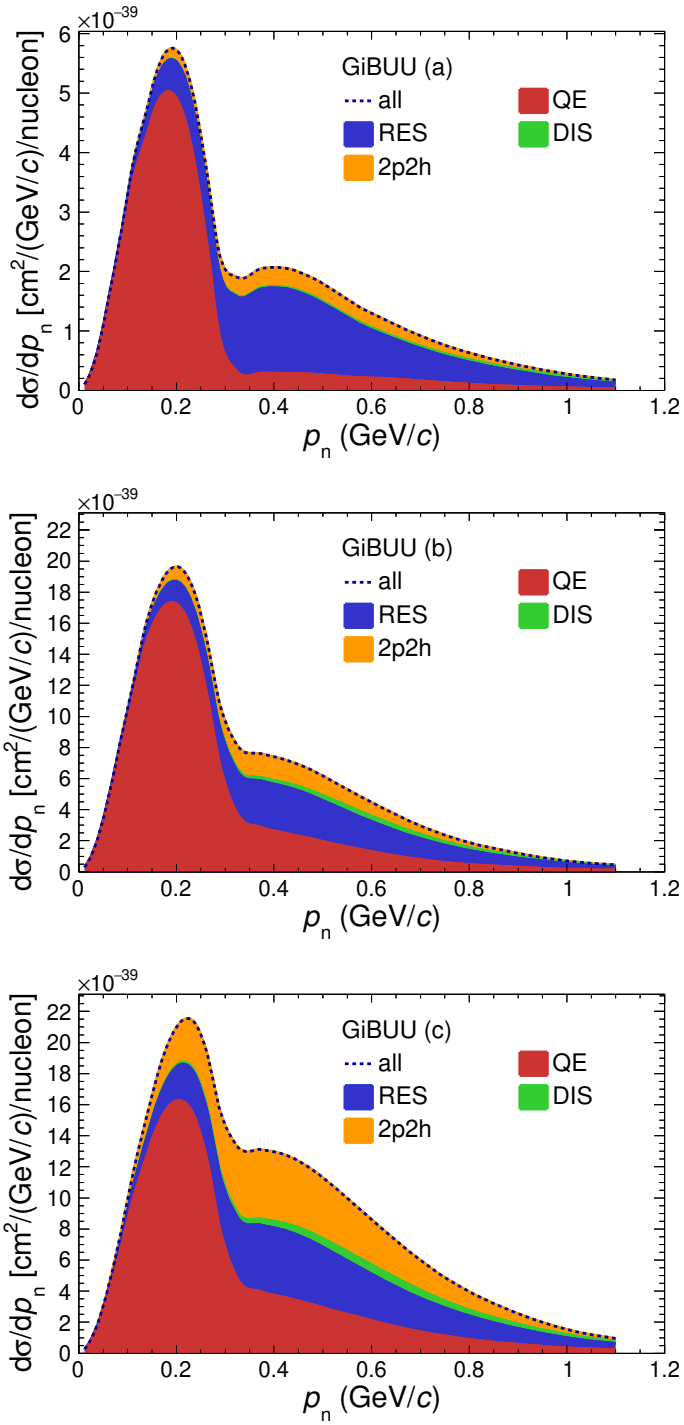

Figure 4.6: Differential cross sections per nucleon as a function of the emulated neutron momentum p_{n}, for **(a)** carbon target, MINERνA ν_μ flux and detector acceptance, **(b)** carbon target, DUNE ν_μ flux and ND-GAr detector acceptance and **(c)** argon target, DUNE ν_μ flux and ND-GAr detector acceptance.

The differential cross sections as a function of the emulated neutron momentum (Eq. 4.11) are shown in Fig. 4.6. Clearly, the first peak shows the Fermi motion of the struck neutron $\sim$ 0.2 GeV. The DUNE carbon has a higher p_{n} tail than that in MINERνA in the QE mode. This tail is filled with the low-momentum protons in the transition region, which is below the detection threshold for MINERνA. The stronger FSIs move more QE events from the peak to the tail by comparing the carbon (Fig. 4.6 (b)) and argon (Fig. 4.6 (c)). Again, the 2p2h enhancement can be seen for argon due to the isospin-2 nucleus.

In conclusion, DUNE ND-GAr offers a larger phase space with full 4π angular acceptance. This capability enables the assessment of the strength of FSI by observing deviations from a uniform distribution of $\delta\alpha_{\mathrm{T}}$ in the QE mode. Additionally, it is more sensitive to the transition region ($p_{\mathrm{n}} \sim 0.35$ GeV$/c$) within the emulated neutron momentum distribution, an area where MINERνA data has already indicated discrepancies in generator predictions [72]. Furthermore, the direct measurement of Fermi motion in argon can be obtained, and DUNE ND-GAr provides an opportunity to observe the 2p2h $\sim (T+1)$ enhancement in argon ($T = 2$).

4.3.1 Understanding the Resonant Production

In a CC0π event, there are contributions not only from the QE mode but also from RES and DIS modes at the generator-level prediction. This arises due to the effects of FSI, where additional pions may be absorbed and not propagate out of the nuclear medium. The momentum carried by these pions is not accounted for in the TKI calculations, resulting in a large transverse boosting angle $\delta\alpha_{\mathrm{T}}$. Interestingly, there are some RES events with smaller $\delta\alpha_{\mathrm{T}}$ values (Fig. 4.5 (a)), indicating that the proton momentum in the transverse plane (see Fig. 4.1) increases, leading to smaller $\delta\alpha_{\mathrm{T}}$ values. In such cases, it appears that the protons are accelerated rather than decelerated by FSI.

This can be understood by considering the decay kinematics of the Δ^+ baryon in an RES interaction. Here in the lab frame, a new TKI variable is introduced, defined as the angle between the proton and neutral pion in the transverse plane resulting from the Δ^+ baryon decay. This angle is denoted as $\delta\phi_{\mathrm{T}}^{\Delta}$. Fig. 4.7 presents the same plot as in Fig. 4.5 (a), but

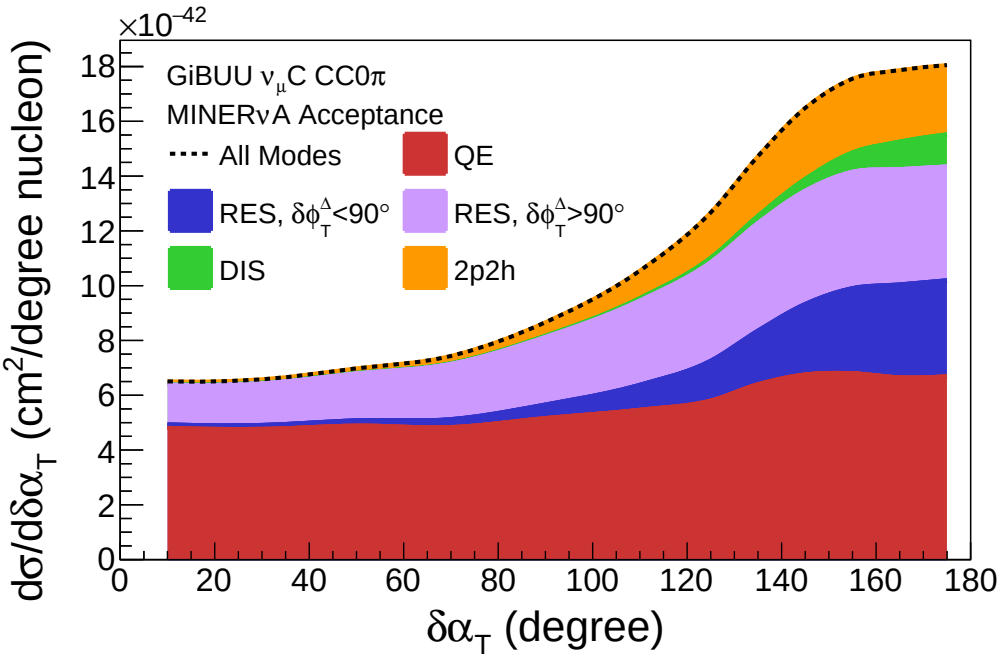

Figure 4.7: Differential cross sections per nucleon as a function of the boosting angle $\delta\alpha_{\mathrm{T}}$ for the carbon target with MINERνA ν_μ flux. The RES mode is now decomposed into two sub-modes. One with the $\delta\phi_{\mathrm{T}}^{\Delta} < 90°$ (blue) and populate at a large $\delta\alpha_{\mathrm{T}}$ value. The other with the $\delta\phi_{\mathrm{T}}^{\Delta} > 90°$ (purple), where the protons appear to be "accelerated" since it pushes an unobserved π^0 to the opposite direction.

with the RES mode further subdivided based on $\delta\phi_{\mathrm{T}}^{\Delta}$, with $\delta\phi_{\mathrm{T}}^{\Delta} < 90°$ and $\delta\phi_{\mathrm{T}}^{\Delta} > 90°$.

It becomes clear that only the component with $\delta\phi_{\mathrm{T}}^{\Delta} > 90°$ contributes to the small $\delta\alpha_{\mathrm{T}}$ values. In this scenario, the momentum vectors of the proton and π^0 point in opposite hemispheres, while the original Δ^+ baryon is situated in the same hemisphere as the proton. Consequently, the proton appears to be "accelerated" as it recoils from the unobserved π^0. Conversely, when the Δ^+ baryon is in the same hemisphere as the π^0, the momentum of the proton would be smaller, resulting in the larger $\delta\alpha_{\mathrm{T}}$ values as seen in Fig. 4.7. When $\delta\phi_{\mathrm{T}}^{\Delta} < 90°$, no such effect of the "accelerated" proton is observed, and the expected large $\delta\alpha_{\mathrm{T}}$ contribution is observed.

4.4 Predictions in ProtoDUNE-SP

The TKI introduced in Sec. 4.1, provides a direct measure of nuclear effects as demonstrated in Sec. 4.2. Recently, the MicroBooNE collaboration measured the double differential cross-section as a function of TKI variables off an argon target using a neutrino beam [77]. They demonstrated that the measured cross-section is sensitive to specific nuclear effects in different phase-space regions. While ProtoDUNE-SP presents an opportunity to measure the same nuclear effect in argon through hadronic interactions, as nuclear effects are independent of the beam, it remains crucial to corroborate this measurement with different fundamental interactions to ensure their agreement.

Within ProtoDUNE-SP, two interaction channels allow for the study of nuclear effects in argon using a pion beam. The first channel is the pion quasi-elastic scattering as,

$$\pi^+ + \mathrm{p} \rightarrow \pi^+ + \mathrm{p}, \tag{4.14}$$

while the second channel focuses on pion charge exchange scattering as,

$$\pi^+ + \mathrm{n} \rightarrow \pi^0 + \mathrm{p}, \tag{4.15}$$

and the initial nucleon is in an argon nucleus. Since TKI variables are calculated based on all measured final state particles, it necessitates an exclusive measurement where every final state particle is reconstructed. The simplest signal for such an interaction is when only one nucleon is produced in the final state, along with a π^+/π^0 for each channel. In these specific interactions, the momentum of the struck neutron can be reconstructed, enabling direct measurement of the magnitude of the Fermi motion. The strength of the FSI in argon can also be measured via the transverse boosting angle, $\delta\alpha_{\mathrm{T}}$. However, the statistics for these interactions are relatively limited, considering the available data sets in ProtoDUNE-SP. Consequently, in this context, only predictions based on MC true information within the ProtoDUNE-SP acceptance are presented, awaiting future data for comparison.

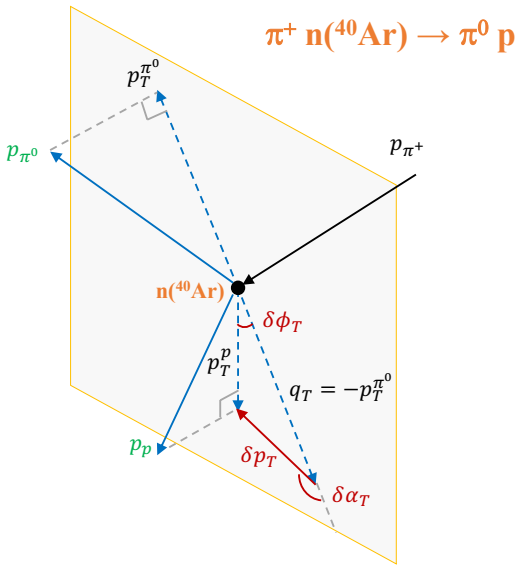

Figure 4.8: Schematic illustration of the TKI variable definition in the pion charge exchange channel. The incoming pion beam is depicted by the black arrow, and the TKI variables are defined between the final state π^0 and proton vectors, shown in red.

The TKI definition in ProtoDUNE-SP closely resembles the one previously defined for the neutrino beam case. The only modification required is to replace the final state lepton momentum vector with that of one of the mesons (π^0/π^+). Figure 4.8 illustrates the definition of the TKI variables in the context of the pion charge exchange channel.

The first TKI variable of interest is the transverse boosting angle, $\delta\alpha_{\mathrm{T}}$, as defined in Fig. 4.8. In the presence of only Fermi motion, the Fermi motion being isotropic, the distribution of $\delta\alpha_{\mathrm{T}}$ should be flat. Therefore, any deviation from a constant distribution of $\delta\alpha_{\mathrm{T}}$ can indicate the presence and strength of FSIs and other nuclear effects.

Figure 4.9 illustrates the distribution of $\delta\alpha_{\mathrm{T}}$ in the pion charge exchange interaction, where the MC is decomposed by the number of nucleons. In ProtoDUNE-SP, the momentum reconstruction threshold for protons is set to be between 0.45 GeV/c and 1 GeV/c. The lower bound is determined conservatively by the Pandora reconstruction threshold, while the upper bound is limited by the reliability of the momentum-by-range method. The considered events involve a leading proton with momentum lying within this momentum range, and a subleading proton with momentum below the detection threshold.

Therefore, only one proton is visible in the detector, but there might be many invisible low-momentum protons, as indicated by the legend in Fig. 4.9. Most events involve more than one nucleon in the final state, and the cleanest events, shown in green, represent a scenario where only one proton is produced. The significant upward tilt observed in the high $\delta\alpha_{\mathrm{T}}$ region indicates the presence of substantial missing momentum due to the unaccounted final state nucleons, especially neutrons. The distribution of signal events appears relatively flat, suggesting a small presence of FSIs. However, it is important to note that this pattern is influenced by the high proton momentum reconstruction threshold. As the outgoing protons undergo FSIs, they tend to lose energy and fall below the reconstruction threshold.

The second variable of interest is the emulated neutron momentum p_{n}, as defined in Sec. 4.1. Figure 4.10 displays the distribution of p_{n}, representing the momentum of the struck neutron in the absence of FSI. The green histogram depicts events with a single proton in the final state, revealing a distinct peak observed around 150 MeV$/c$. This peak corresponds to the magnitude of the Fermi motion of the struck neutron in argon. However, there is a large amount of missing momentum originating from other undetectable final state nucleons, causing the p_{n} distribution to peak at higher values, around 400 MeV$/c$. The influence of these undetected particles contributes significantly to the overall missing momentum in the event, leading to the observed higher peak in the p_{n} distribution.

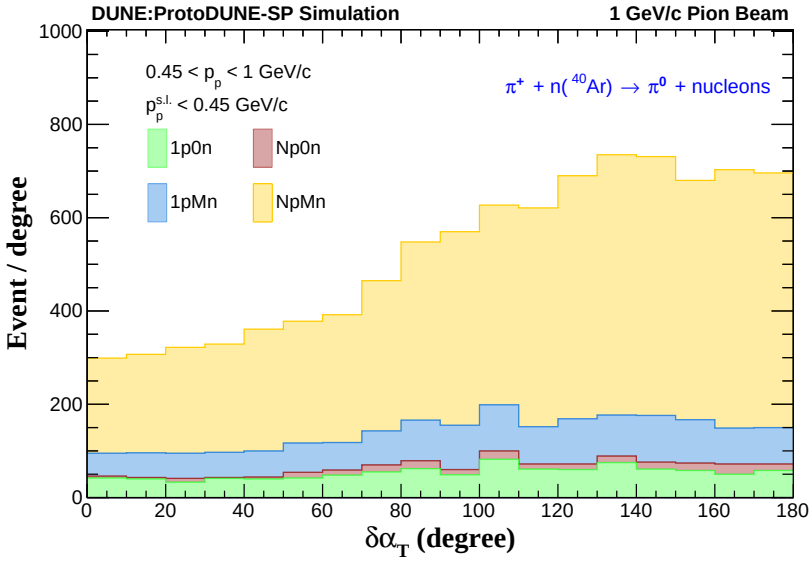

Figure 4.9: The distribution of the transverse boosting angle $\delta\alpha_{\mathrm{T}}$ of true pion charge exchange events, categorized based on different numbers of protons (p) and neutrons (n) in the final state, where N and M are ≥ 1. The phase space selections for the leading and subleading (s.l.) protons are shown. Only one proton is visible, but there can be many invisible low-momentum protons. The broad peak observed at high $\delta\alpha_{\mathrm{T}}$ is attributed to the missing momentum resulting from unmeasured neutrons.

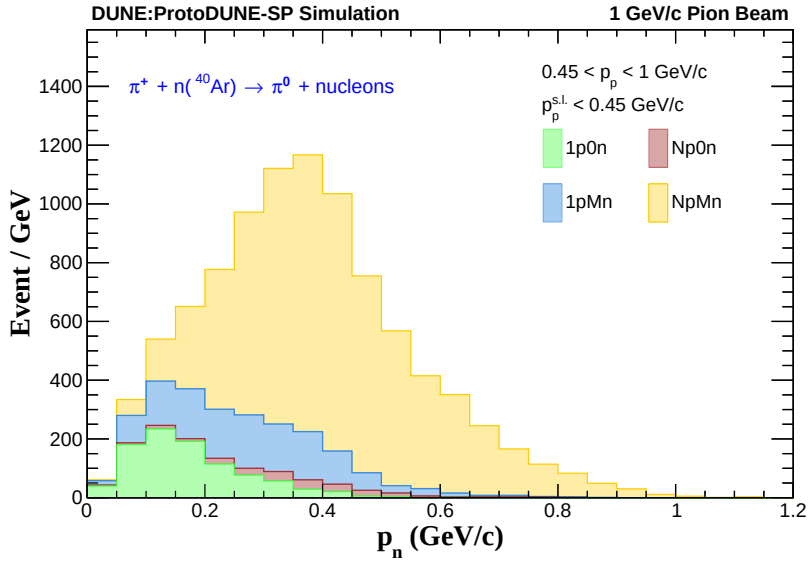

Figure 4.10: The emulated neutron momentum p_{n}, as defined in Eq. 4.11, categorized based on different numbers of nucleons in the final state, where N and M are ≥ 1. Only one proton is visible, but there can be many invisible low-momentum protons. The Fermi motion peak can be observed as the peak in the 1p0n category around 150 MeV$/c$.

5 | Kinematic Fitting

In the field of particle physics experiments, measurements inherently involve numerous uncertainties, encompassing both statistical and systematic uncertainties. However, the energy resolution of reconstructed particles has the potential to surpass the limitations imposed by detector resolution through the application of a mathematical technique known as kinematic fitting. At its core, kinematic fitting revolves around identifying and integrating the physical kinematic constraints intrinsic to the experimental system. By iteratively adjusting the measured energies and directions of particles, the fitting process aims to precisely satisfy these constraints, thereby rectifying the experimentally measured quantities and bringing them closer to their true values. It is noteworthy that the extent to which each parameter can deviate from its initial value during the kinematic fitting procedure is modulated by its corresponding measurement uncertainty, which serves as a crucial input. Consequently, parameters with larger uncertainties are more susceptible to substantial changes, whereas those with smaller uncertainties exhibit minimal deviations from their initial values. The routine incorporation of kinematic fitting in high-energy physics has been prevalent for several decades, with these fitting routines integrated into data analysis programs [81, 82].

This chapter explores the fundamental concept of kinematic fitting and its potential applications in enhancing the energy resolution of neutral pions in LArTPC detectors. Kinematic fitting finds practical utility in experiments involving the production and decay of unstable particles, such as the top quark and W bosons. Neutral pions, being unstable particles that decay into two photons, represent a significant physics signal in both the ProtoDUNE-SP and DUNE experiments. However, since the neutral pion itself cannot be directly observed, its energy and momentum must be inferred from the observed properties of its decay products, specifically the photons. One effective approach is to employ kinematic fitting with an invariant mass constraint for the π^0 particle. This fitting procedure entails adjusting the measured photon energies and opening angles between the two photons resulting from the neutral pion decay. By minimizing a constrained χ^2 function

that compares the invariant mass of the two photons to the expected mass of the neutral pion, the kinematic fit enables a more accurate determination of the neutral pion's energy and momentum. This technique has been effectively employed to enhance π^0 reconstruction in MINERνA experiment [83, 74], which serves as an inspiration for this study.

5.1 Method of Lagrange Multiplier

The Method of Lagrange Multipliers is a calculus technique used to find the maximum or minimum values of a function under a constraint or set of constraints. It involves introducing a new function known as the Lagrangian, which is the sum of the original function and a scalar multiple of the constraint function(s). This scalar multiple is referred to as the Lagrange multiplier [84].

In kinematic fitting, the Method of Lagrange Multipliers is employed to perform the fitting process. It is a commonly used approach for solving constrained optimization problems. For instance, consider an optimization problem where the objective is to optimize the function $f(x, y)$ while satisfying the constraint equation $g(x, y) = 0$. It is assumed that both functions have continuous first partial derivatives. To tackle this problem, the Lagrangian is constructed as follows,

$$\mathcal{L}(x, y, \lambda) = f(x, y) - \lambda g(x, y), \tag{5.1}$$

The optimized value is obtained at the point where the gradients of the functions $f(x, y)$ and $g(x, y)$ are tangent. This can be mathematically represented as follows,

$$\nabla_{x,y} f(x, y) = \lambda \nabla_{x,y} g(x, y), \tag{5.2}$$

where λ represents the proportionality constant as the magnitude of gradient vectors is not necessarily equal. In addition, the constraint equation must also be satisfied, $g(x, y) = 0$. To incorporate all these conditions, one needs to solve

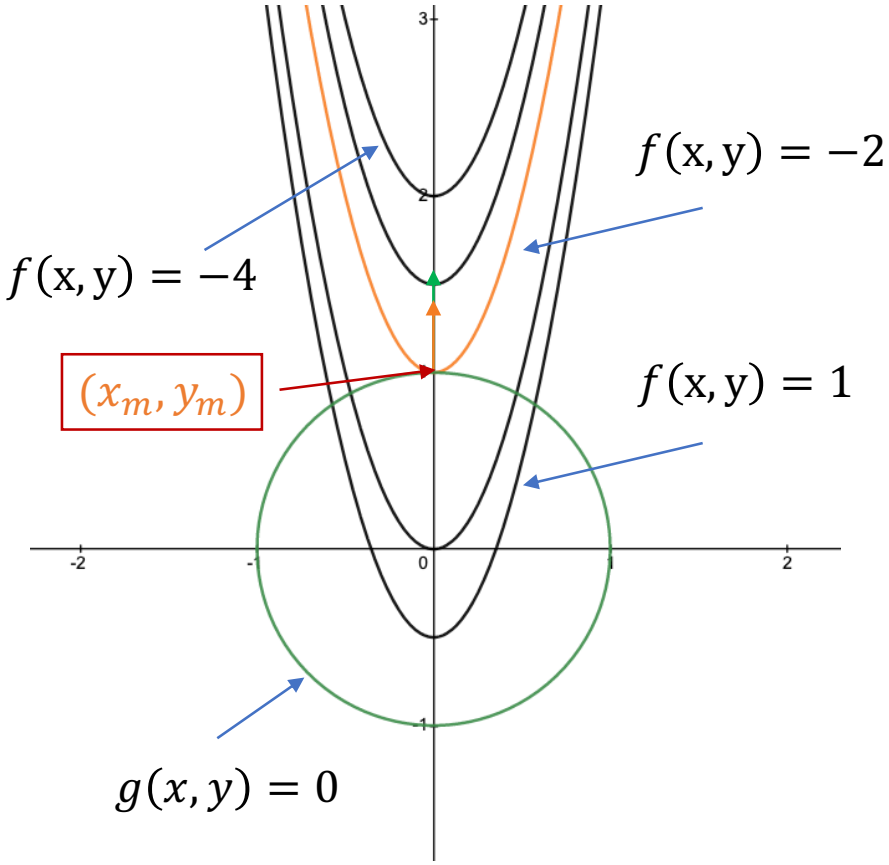

Figure 5.1: The visualization of the one text-book problem of minimising function $f(x, y) = 8x^2 - 2y$, subjected to the unit circle constraint, $g(x, y) = x^2 + y^2 - 1$. The black lines are the contour line of the function $f(x, y)$ and the unit circle constraint is shown as the green circle.

$$\nabla_{x,y,\lambda}\mathcal{L}(x, y, \lambda) = 0. \tag{5.3}$$

Note that $\nabla_\lambda\mathcal{L}(x, y, \lambda) = 0$ leads to $g(x, y) = 0$ and $\nabla_{x,y}\mathcal{L}(x, y, \lambda) = 0$ implies Eq. 5.2. Therefore, by solving a set of linear equations, one can optimise a function $f(x, y)$ subjected to a constraint $g(x, y) = 0$.

Figure 5.1 depicts an example illustrating the minimization of the function $f(x, y) = 8x^2 - 2y$ subject to the constraint of the unit circle, $g(x, y) = x^2 + y^2 - 1$. The contour lines of the function $f(x, y)$ at various values are represented by black curves, while the unit circle constraint is illustrated as a green circle centred at the origin with a radius of

one. The red arrow denotes the minimization point of the function $f(x, y)$ under the unit circle constraint, as indicated in Eq. 5.2. This point corresponds to the scenario where the gradients of the two functions are parallel, with the Lagrange Multiplier λ acting as the proportionality constant. The construction of the Lagrangian for this problem follows Eq. 5.1, yielding the following expression,

$$\mathcal{L}(x, y, \lambda) = 8x^2 - 2y - \lambda(x^2 + y^2 - 1), \tag{5.4}$$

By setting all the partial derivatives with respect to x, y, and λ equal to zero, one can obtain the following equations,

$$\begin{aligned} \frac{\mathrm{d}\mathcal{L}}{\mathrm{d}x} &= 16x - 2\lambda x = 0, \\ \frac{\mathrm{d}\mathcal{L}}{\mathrm{d}y} &= -2 - 2\lambda y = 0, \\ \frac{\mathrm{d}\mathcal{L}}{\mathrm{d}\lambda} &= x^2 + y^2 - 1 = 0, \end{aligned} \tag{5.5}$$

By solving these three equations with three unknowns, one can determine the optimized point that satisfies the constraint equation.

5.1.1 Double Minimisation

The Lagrangian function serves as a tool to find the optimized point using both the approaches discussed in the previous section and numerical methods. Numerically, an iterative optimization algorithm is employed to determine the values of variables and Lagrange multipliers that satisfy the conditions posed by the problem. The process iteratively adjusts these values in pursuit of a solution that not only optimizes the objective function but also respects the imposed constraints.

The Lagrangian (Eq. 5.1) depends on three variables: x, y and λ. As stated in Eq. 5.2, the optimised values of x and y should minimize the Lagrangian for all values of λ. The optimised value of λ should be the one that minimises the Lagrangian, and the corresponding

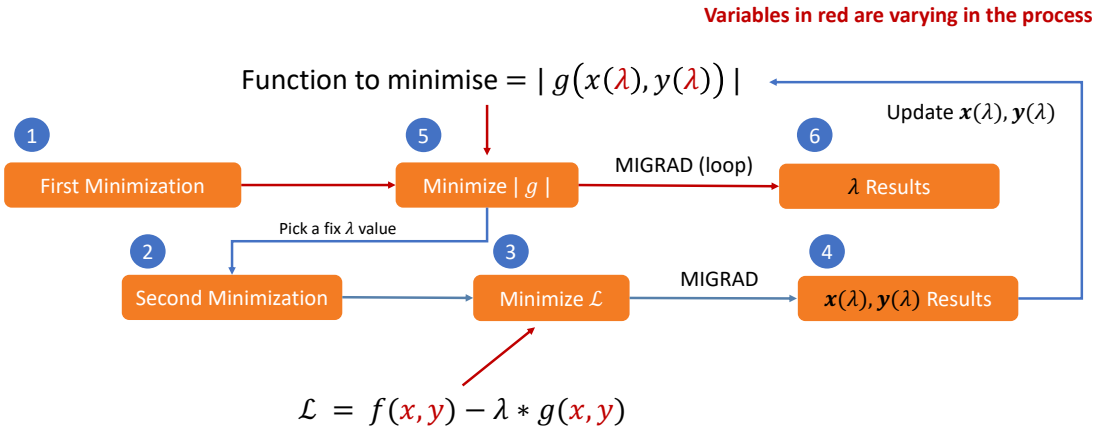

Figure 5.2: The logic of the double minimization process derived from a general Lagrange Multipliers example. The first minimization is performed with respect to the entire Lagrangian for a specific λ value, while the second minimization is conducted with respect to the magnitude of the constraint function.

x and y values of this λ also satisfy the constraint equation. Consequently, a double minimization approach, as illustrated in Fig. 5.2, is implemented. For a given λ, the optimized values of x and y are obtained by minimizing the Lagrangian. Subsequently, another λ value is selected based on user-defined boundaries and step size, and the iterative process continues. This results in a list of λ values, each corresponding to an optimized pair of x and y values. The optimized λ value is determined by minimizing the absolute value of $g(x, y)$, ensuring the associated x and y values satisfy the constraint equation. The absolute value is used to guarantee that the minimized value of $g(x, y)$ approaches zero.

The optimization in this study is performed using the TMinuit class [85] in ROOT [86], and the "MIGRAD" algorithm is employed. The code for this analysis is developed based on solving basic examples of Lagrange multipliers. In this double minimization approach, an initial value of λ is assigned to the first TMinuit object. Before invoking the "MIGRAD" algorithm for minimization, another TMinuit object is introduced to find the optimized values of x and y for the given λ value (minimized with respect to the entire Lagrangian). Subsequently, the values of x and y are updated for the first minimization, and the minimization process continues (minimized with respect to the constraint equation). This double minimization ensures the Lagrangian is minimized for a set of x, y, and λ values while simultaneously satisfying the constraint equation $g(x, y) = 0$.

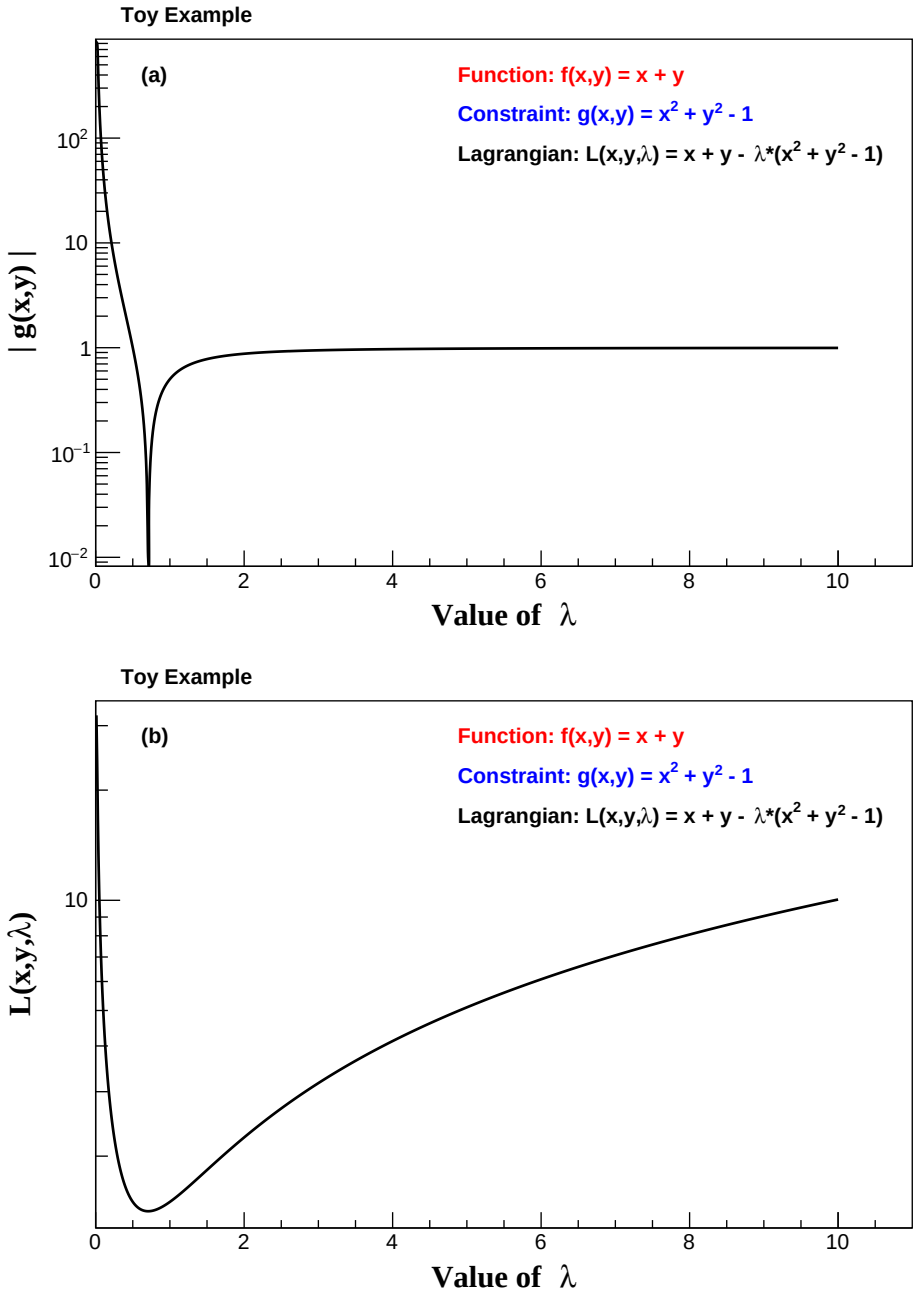

Figure 5.3: The fitting process for optimizing $f(x, y) = x + y$ subjected to the unit circle constraint $g(x, y) = x^2 + y^2 - 1 = 0$. (a) The absolute value of the constraint as a function of lambda. The absolute value is used to guarantee that the minimized value of $g(x, y)$ approaches zero. (b) The computed value of the Lagrangian as a function of lambda. In both plots, the minimum is reached when lambda hits the desired value ($\lambda = 0.707$).

To illustrate, one can consider an example where the function $f(x, y) = x+y$ is minimized under the unit circle constraint $g(x, y) = x^2 + y^2 - 1 = 0$. Figure 5.3 (a) demonstrates the absolute value of the constraint equation $g(x, y)$ as a function of λ. Notably, a significant drop in this value occurs when λ reaches the desired value during the first minimization process. Additionally, Figure 5.3 (b) presents the value of the entire Lagrangian as a function of λ, which is minimized at $\lambda = 0.707$ during the second minimization process. The code has been tested on several constrained minimization problems and successfully provides the desired solutions for x, y, and λ.

5.2 Theory of Kinematic Fitting

Consider a column vector $\boldsymbol{\alpha}$ that represents a set of true parameters, such as the true energy and angles of the measured particles. Let $\boldsymbol{\alpha_0}$ be another column vector representing the corresponding measured quantities. By calculating the χ^2 as follows, it is possible to quantify the extent to which the measured kinematics align with their true values, taking into account the experimental resolution [87]:

$$\chi^2(\alpha) = (\alpha - \alpha_0)^T V^{-1} (\alpha - \alpha_0), \tag{5.6}$$

where V^{-1} is the inverse of the covariance matrix of the true kinematics with respect to the measured ones, as defined in the latter part of this section.

In kinematic fitting, the objective is to minimize the χ^2 by adjusting quantities in $\boldsymbol{\alpha}$ while satisfying the constraint equation. The measured quantities in $\boldsymbol{\alpha_0}$ serve as the input for the fit and remain unchanged, whereas the quantities in $\boldsymbol{\alpha}$ are varied and represent the best-fit reconstructed values after the kinematic fitting.

For instance, according to the law of energy conservation, the sum of all particles in the final state must remain constant. This constraint equation can be defined as follows,

$$H(\alpha) = \Sigma\alpha_i - \mathrm{c} = 0, \tag{5.7}$$

where α_i is the fitting quantities in the vector $\boldsymbol{\alpha}$ and c is a constant. Therefore, in this case, the Lagrangian will be the constrained χ^2,

$$\chi^2(\alpha) = (\alpha - \alpha_0)^T V^{-1}(\alpha - \alpha_0) - \lambda H(\alpha). \tag{5.8}$$

The measurement uncertainty plays a vital role in kinematic fitting and is considered an important input. The covariance matrix V is calculated for different kinematic phase spaces, taking into account the varying experimental resolutions for particles with different energies. The calculation of the covariance matrix element between any two measurements is given by,

$$V_{ij} = \frac{\Sigma_{k=1}^{N}(\alpha_{\mathrm{MC}}^{k} - \alpha_{0\mathrm{MC}}^{k})_i(\alpha_{\mathrm{MC}}^{k} - \alpha_{0\mathrm{MC}}^{k})_j}{N}, \tag{5.9}$$

where $\alpha_{0\mathrm{MC}}^{k}$ and α_{MC}^{k} are the measured (reconstructed) kinematics and their corresponding true values for the k-th element. The values of $\alpha_{0\mathrm{MC}}^{k}$ and α_{MC}^{k} are both obtained from a Monte Carlo (MC) test sample. The quantity N is the total number of events in this sample.

5.2.1 Monte-Carlo Example

Consider a toy model where the energies of three particles are being measured in an experiment. It is assumed that the true energies of the particles are (4, 9, 16) MeV, and the experimental resolutions are (0.5, 1.0, 1.0) MeV, respectively. For the measurement of 10,000 events, the distribution of measured energy is simulated using a Gaussian function. The mean value of the Gaussian function corresponds to the true energy, and the standard deviation, σ, represents the experimental resolution. The resulting distribution of measured energy is shown in Fig. 5.4 using the grey histograms.

To improve the resolution of the energy measurements, kinematic fitting can be employed by utilizing a constraint equation. In this hypothetical scenario, a constraint equation reflecting the energy conservation law is chosen as given by,

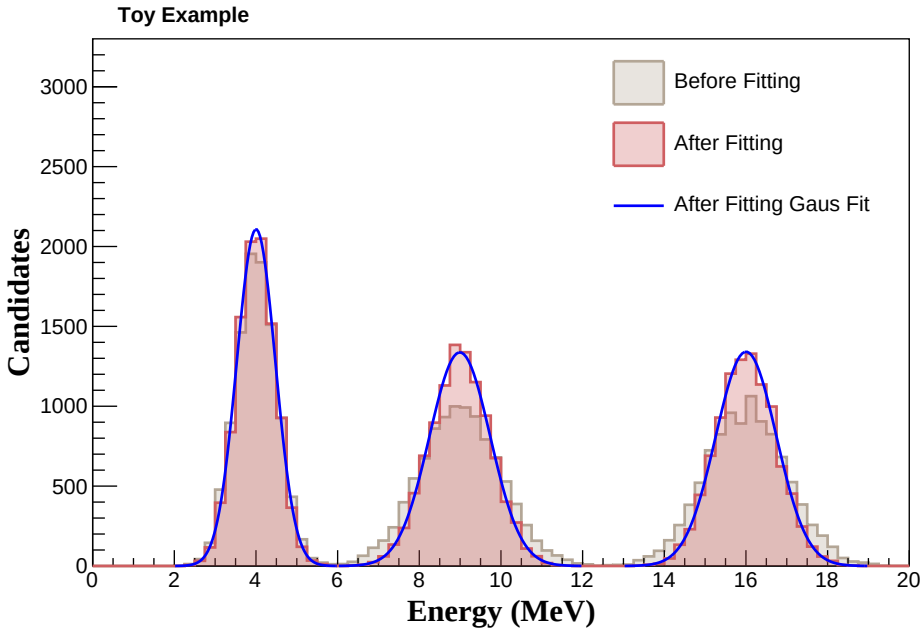

Figure 5.4: Comparison of the measured energy distribution in a toy model before and after kinematic fitting. The initial energy distribution is simulated using Gaussian functions with mean values of (4, 9, 16) MeV and σ values of (0.5, 1.0, 1.0) MeV. After the kinematic fitting, the distribution is fit to the sum of three Gaussian functions, depicted by the blue curve. The fitted σ values are (0.49, 0.72, 0.72) MeV.

$$H = E_1 + E_2 + E_3 - 29 = 0, \tag{5.10}$$

where E_i is the energy of each reconstructed particle, and the number 29 is the sum of the true momenta of the three particles. The red histograms in Fig. 5.4 illustrate the energy distributions after applying kinematic fitting. The improved energy distributions are represented by the blue curves, which are fitted Gaussian distributions with σ values of (0.49, 0.72, 0.72) MeV. These values indicate a significant enhancement in the experimental resolution. In the case of ProtoDUNE-SP, the energy resolution of the reconstructed neutral pion can be improved by a kinematic fitting using the constraint of the π^0 invariant mass. A detailed discussion is presented in Chap. 7.

6 | Particle Identification and Selection

Particle identification is a critical component in accelerator neutrino physics experiments as it involves the vital task of distinguishing and characterizing individual particles generated during neutrino interactions. In charge-current interactions of neutrinos, the flavour of the incoming neutrino is identified by the type of lepton that is produced, while the species of final state particles define the event topology.

In experiments employing LArTPC technology, such as DUNE and ProtoDUNE-SP (discussed in Chaps. 2 and 3), the reconstruction process begins with the electrical signals produced by the anode plane wires. Each wire generates a waveform, which represents the current signal over time. Subsequently, the waveform is disengaged into individual Gaussian hits after noise removal. Clustering algorithms are then employed to group together hits that are spatially close, revealing higher-level structures within the detector. These clusters can be further categorized into two types: tracks, which exhibit long, linear patterns, and showers, which are more diffuse and cloud-like. In ProtoDUNE-SP, to achieve track/shower separation, a Convolutional Neural Network (CNN) has been developed in addition to Pandora's classification of reconstructed particles, utilizing Machine Learning techniques [88]. The network uses the pixel images created from the wire readout data to perform pattern recognition. Each hit in the image is assigned three classification outputs: a track score, a shower score, and a Michel electron score. These scores range from 0 to 1. The image of the full reconstructed particle is obtained by averaging the scores of all hits associated with that particle. A high shower score close to one indicates an electromagnetic (EM) shower-like topology, suggesting a particle with shower characteristics. Additionally, the Michel score is employed to identify Michel electrons [89] originating from muon decays, which are a result of charged pion decays. This information provides the muon or pion tagging techniques, aiding in the identification of muon or charged pions (if muon is invisible in the detector) in the event. In this analysis, the categorization of reconstructed particles relies on the outputs of the CNN rather than the Pandora classification.

This chapter covers the 1 GeV/c pion beam selection in Sec. 6.1 and the final state particle selection in Sec. 6.2 within ProtoDUNE-SP. Additionally, the performance of different particle reconstructions is examined in Sec.6.3. This chapter lays the foundation for the analysis presented in this thesis by covering general PID and selections in ProtoDUNE-SP. It includes the pion beam selection, as well as the selection of charged pions and Michel electrons. This chapter also discusses shower selections, which are essential for reconstructing neutral pion candidates in Chap. 7. Importantly, the selection of the pion beam, daughter charged pions, Michel electrons, and neutral pions collectively contributes to the identification of the pion CEX sample in the cross-section analysis. Additionally, the selection of daughter protons is also included for completeness, although it is not used in the pion CEX event selection.

6.1 Beam Pion Selection

Test beam particles, with a momentum range from 0.3 to 7 GeV/c, are delivered to ProtoDUNE-SP from the CERN's H4-VEL beamline as described in Chap. 3. The beamline instrumentation consists of various devices that provide the beam particle's momentum and TOF measurements. The beam PID can be achieved by using the measured TOF and the absence or presence of a Cherenkov signal, as discussed in detail in Sec. 3.1. The analysis presented in this report uses 1 GeV/c π^+ (and μ^+) data since the beamline PID can separate π^+ from p and e^+ at 1 GeV/c, but not from μ^+.

To extract the primary pion beam candidates, seven sequential cuts are implemented as follows, and each cut will be described individually.

Beam Cut 1: Require that the beam particle passes the beamline instrumentation π^+ and μ^+ trigger logic.

Beam Cut 2: Require that the beam particle is identified as a track-like particle.

Beam Cut 3: Select primary π^+ candidates with the reconstructed initial position and direction consistent with the primary beam.

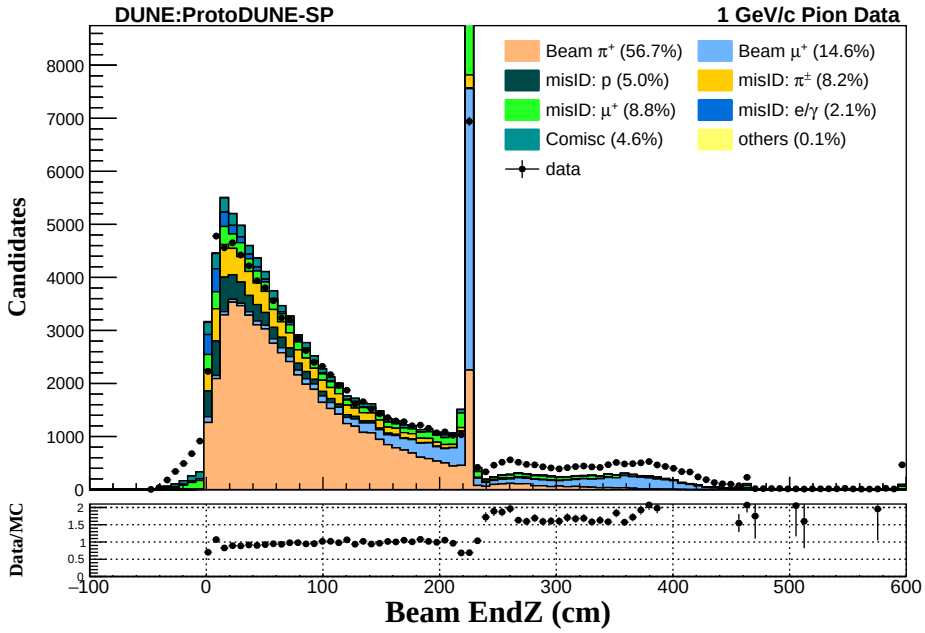

Figure 6.1: The end z distribution of selected beam candidates after Beam Cuts 1-2. Secondary daughter particles can be misidentified as primary beam particles, and these candidates are denoted as misID:p/π^+/μ^+/e/γ in the legend.

Beam Cut 4: Require the beam particle candidates to interact within the first APA of the TPC.

Beam Cut 5: Reduce μ^+ background by identifying the Michel electron from muon decays using CNN Michel score output.

Beam Cut 6: Reduce misidentified secondary proton background by checking the particle's dE/dx information.

Beam Cut 7: Require the beam particles to be aligned well with the beam plug region.

Beam Cuts 3, 5, and 6 are particularly focused on reducing the number of secondary daughter particles that are mistakenly identified as primary beam particles during the reconstruction process.

The reconstructed end z position (in the detector Cartesian coordinates) of the beam particle candidates is chosen to demonstrate the effect of each cut, as it serves as a key factor in the cross-section extraction method. In MC, each beam particle candidate is categorized

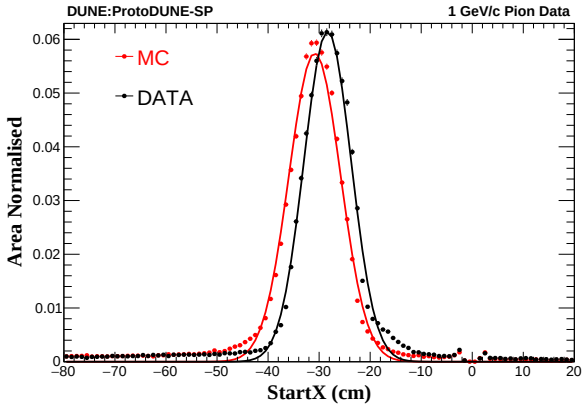

(a)

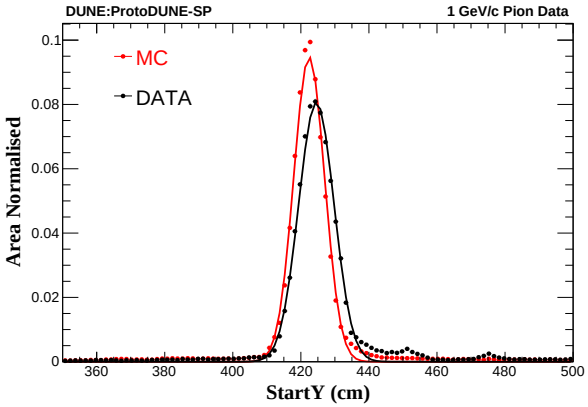

(b)

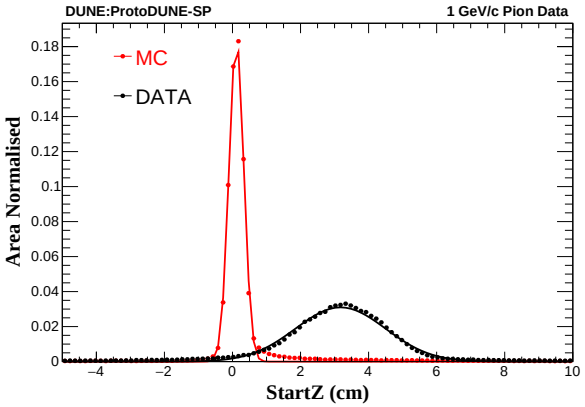

(c)

Figure 6.2: Reconstructed start position (SCE corrected) distribution of selected beam particle candidates for both data and MC. In the x and y start position, the agreement of data and simulations is reasonable. The small shift in the mean is due to the beam modelling in the simulation. A large discrepancy is found in the start z position due to the SEC is not well simulated at the beam entry region. This issue will be addressed in future ProtoDUNE simulations.

based on its truth-matched information. The data distribution is overlaid with the simulation to verify the data-MC agreement after each cut. Figure 6.1 shows the end z position distribution of the selected beam particle candidates after Beam Cuts 1-2. The primary source of background stems from misidentified secondary daughter particles, which can originate from various sources, such as cosmic muons or beam particles that interact before entering the active TPC volume. However, an effective strategy for reducing this background involves examining the reconstructed initial position and direction informa-

tion of the beam particle. By studying these characteristics, it becomes feasible to distinguish between primary beam particles and misidentified secondary daughter particles.

The reconstructed Cartesian coordinates of the start positions (start xyz-position) of the beam particles are shown in Fig. 6.2. However, it should be noted that the absolute agreement between the data and MC simulations regarding the start position is not representative due to factors such as beam mismodelling and the SCE simulation. Consequently, the cuts implemented do not directly act on the absolute reconstructed start xyz position values. To address this, each distribution is fitted with a Cauchy-Lorentz function defined as,

$$f(x;\mu,\sigma) = \frac{1}{\pi}\left[\frac{\sigma}{(x-\mu)^2+\sigma^2}\right] \tag{6.1}$$

from which the fitted peak location (μ) and half-width at half-maximum (σ) are derived. These values are then employed to determine the beam quality cuts as follows: any reconstructed beam track that deviates by at least 3σ from the mean value is identified as the misidentified secondary daughter background. Additionally, the cosine of the angle ($\cos(\alpha)$) between the track direction and the fitted mean angle of all selected tracks are calculated, and any track with $\cos(\alpha) < 0.95$ is categorized as inconsistent with the primary beam.

In Figs. 6.3 and 6.4, two of these cut observables are displayed, revealing that most cosmic muons and misidentified secondary particles tend to have angles and z coordinates that are outliers in the distributions. The impact of the beam quality cuts (Beam Cut 3) on the beam sample is demonstrated in Fig. 6.5. After implementing Beam Cuts 1-3, cosmic muon backgrounds are effectively eliminated, and upstream interaction backgrounds (misidentified secondary daughter) are significantly reduced.

Another major source of background is the beam muons, which come from π^+ decays in the beamline or before entering the active TPC volume. The beam quality cuts are insufficient to remove these muons since beam π^+ decays in flight will produce a daughter muon in a similar direction. However, since muons do not experience hadronic interactions, they

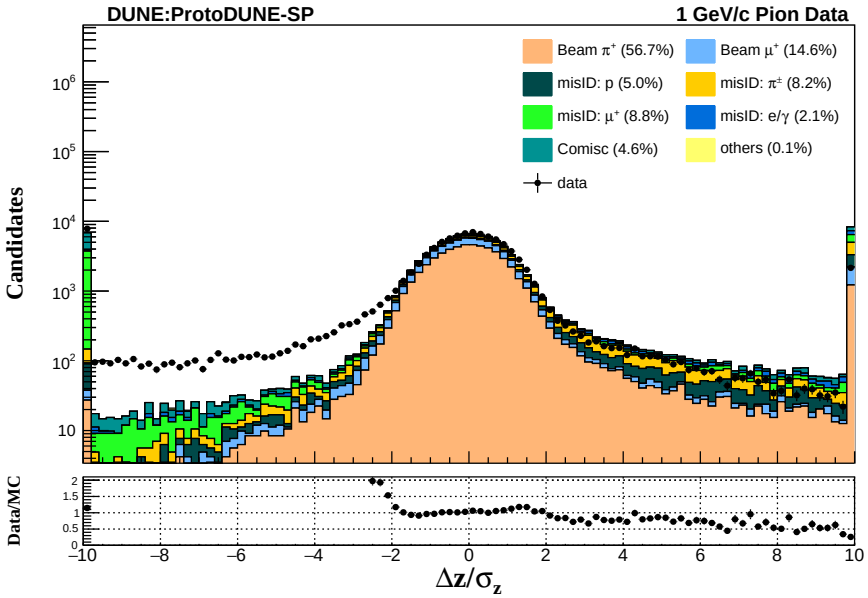

Figure 6.3: Start z position cut $|\frac{\Delta z}{\sigma_z}| < 3$ where $\Delta z = z - \mu_z$. The disagreement between data and MC is due to the misestimation of the SCE. The distributions are in the log scale.

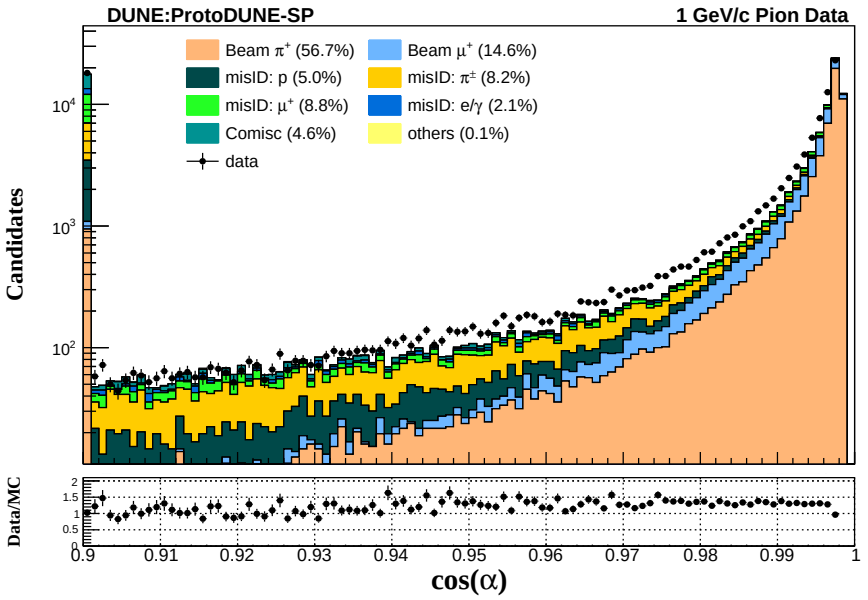

Figure 6.4: Beam direction cut $\cos(\alpha) > 0.95$ where $\cos\alpha = \cos\theta_x \cdot \cos\mu_{\theta_x} + \cos\theta_y \cdot \cos\mu_{\theta_y} + \cos\theta_z \cdot \cos\mu_{\theta_z}$ and $\theta_{x,y,z}$ are the angles between each track and the xyz axes and $\mu_{\theta_{xyz}}$ are mean values of the fitted track xyz angle distributions. The distributions are in the log scale.

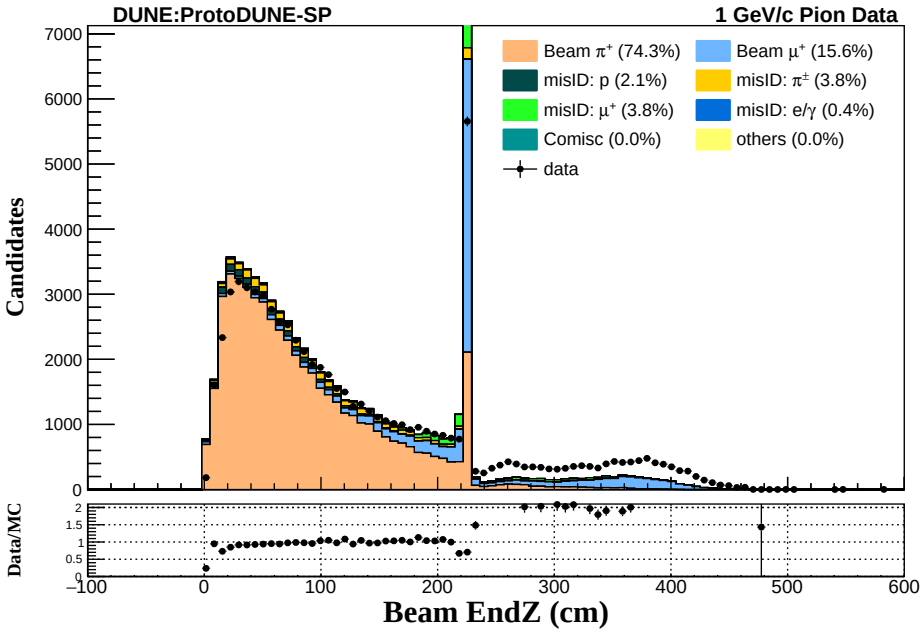

Figure 6.5: The end z distribution of selected beam candidates after Beam Cuts 1-3. The upstream interactions that produced secondary daughter particle backgrounds have been reduced, and cosmic muon backgrounds are eliminated.

will propagate further inside the detector and pass the first APA boundary. Unfortunately, the grounded electron diverter has distorted the electric field at the APA boundary during the beam run. This issue causes the reconstructed tracks to prematurely "break" when they cross one APA boundary to the next (see Fig. 6.5 at ∼220 cm). A data-driven simulation is employed to model the electric field distortions, aiming to replicate this effect in the MC. However, this effect is not well simulated. The simulations overestimate the number of broken tracks with respect to data at the APA boundary. Therefore, the MC distributions are systematically lower than the data points for end z $>$ 228 cm (Fig. 6.5).

A cut is placed at end z = 220 cm (Beam Cut 4) to remove these broken tracks and reduce the muon background content. Figure 6.6 shows the distribution of the selected beam particle end z position after Beam Cuts 1-4. Both the beam muons and misidentified daughter muons components are diminished. For those muons that decay at rest via $\mu^+ \rightarrow e^+\nu_e\bar{\nu_\mu}$, a Michel electron (positron) can be identified to tag the original muons. With the assistance of Michel electron tagging, one can further reduce the muon background in the selected beam candidates. Figure 6.7 shows the Michel score of beam candidates. Beam

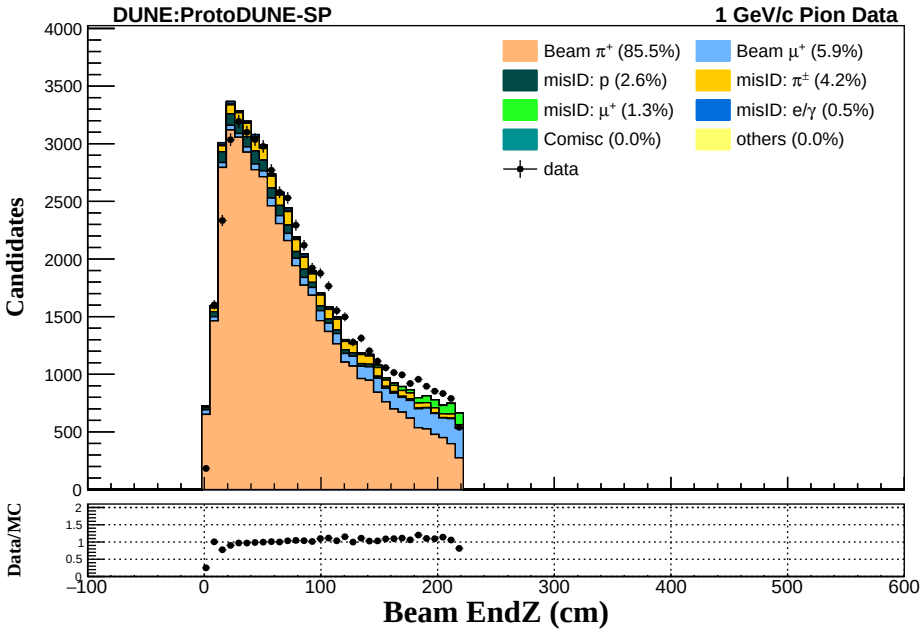

Figure 6.6: The end z distribution of selected beam candidates after Beam Cuts 1-4. Both the beam muon and misID:μ^+ background contents are reduced since muons tend to propagate further and cross the APA boundary.

muons exhibit a high Michel score at the beam end vertex. Any beam candidates with a Michel score greater than 0.55 (Beam Cut 5) are rejected to reduce muon background.

For a given momentum, protons, being much heavier than pions, have lower velocity and lose energy much quicker than pions (Sec. 1.8). Whereas pions behave as MIPs in the LArTPC. This distinction allows for the implementation of cut observables related to $\mathrm{d}E/\mathrm{d}x$ to effectively separate protons from pions and reduce misidentified secondary proton backgrounds. For each selected beam track candidate, the distribution of $\mathrm{d}E/\mathrm{d}x$ is plotted against its residual range. By assuming a proton hypothesis, a χ^2 test is performed. The resulting value of χ^2/NDF provides an indication of whether the candidate is more proton-like or pion-like. This observable enables the identification and discrimination of proton candidates from pion candidates, enhancing the ability to reduce the misidentified secondary protons in the selected beam sample. Figure 6.8 shows the calculated proton χ^2/NDF for beam candidates. Notably, secondary protons tend to have small values compared to beam pions. Consequently, a cut is applied at 80 (Beam Cut 6) to reduce the secondary proton background.

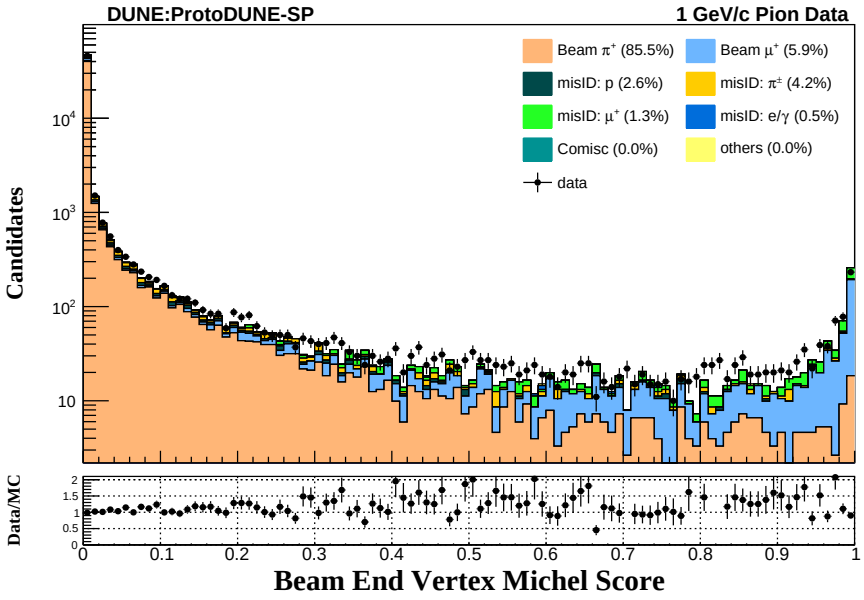

Figure 6.7: The Michel score distribution of selected beam candidates after applying Beam Cuts 1-4 in log scale. The majority of beam muons exhibit a high Michel Score. Candidates with a Michel score greater than 0.55 are rejected to reduce the muon background.

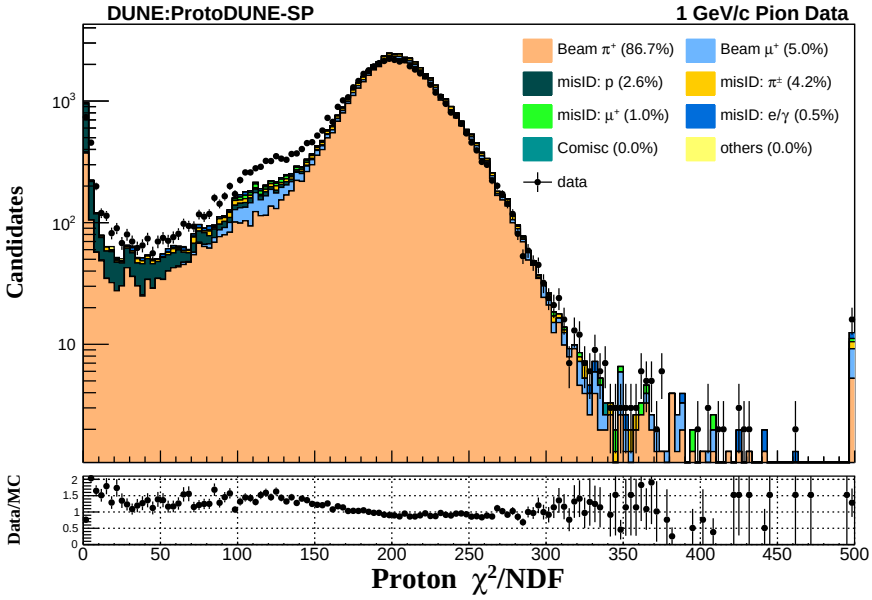

Figure 6.8: The proton χ^2/NDF distribution of selected beam candidates after applying Beam Cuts 1-5 in log scale. Secondary protons demonstrate a lower χ^2/NDF value compared to pions. Candidates with a χ^2/NDF less than 80 are rejected to reduce the proton background.

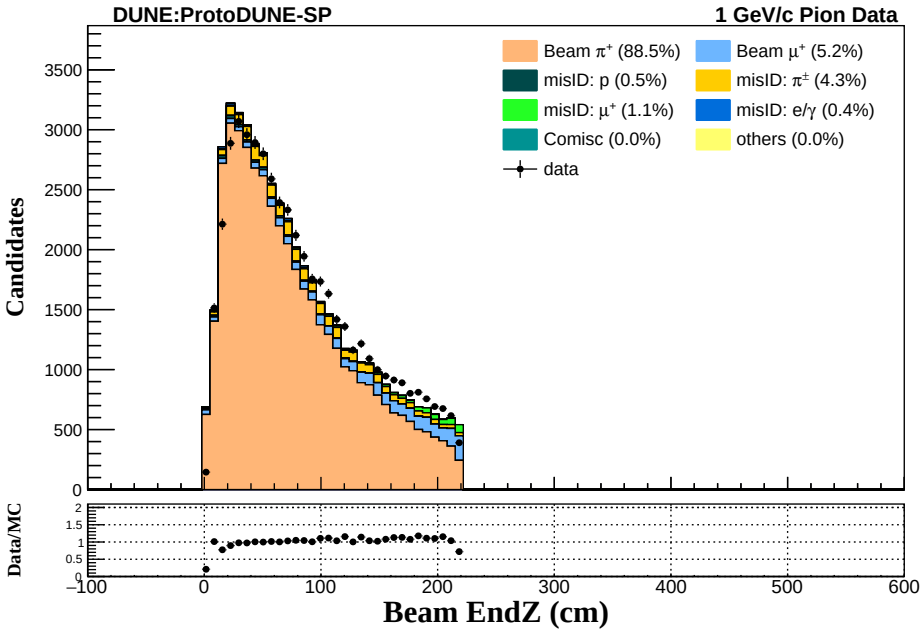

Figure 6.9: The end z distribution of selected beam candidates after Beam Cuts 1-6. Beam muon and misidentified daughter muon components are further reduced by removing candidates with an identified Michel electron at the track end. The misidentified daughter proton content is less than 1% after Beam Cut 6.

The impact of Michel electron (Beam Cut 5) and proton $\mathrm{d}E/\mathrm{d}x$ (Beam Cut 6) cuts on the beam sample can be observed in the beam end z position distribution shown in Fig. 6.9. By applying the Michel electron cut, beam candidates that exhibit an identified Michel electron at the track end are removed, resulting in a significant decrease in the beam muon and misidentified daughter muon components. Furthermore, the misidentified secondary proton background is effectively reduced to less than 1% following the application of the proton $\mathrm{d}E/\mathrm{d}x$ cut (see Fig. 6.9 legend).

One irreducible background source arises from pions undergoing elastic scattering with a small deflection angle within the detector. The reconstruction algorithm is unable to distinguish this small deflection angle and will reconstruct the daughter pion as part of the primary pion beam, leading to a misidentification. Another irreducible background is attributed to beam muons that decay, but their associated Michel electrons are not successfully identified. As can be seen in Fig. 6.9, they contribute approximately 4.3% and 5.2%, respectively, to the overall selected beam sample. Despite efforts to reduce these

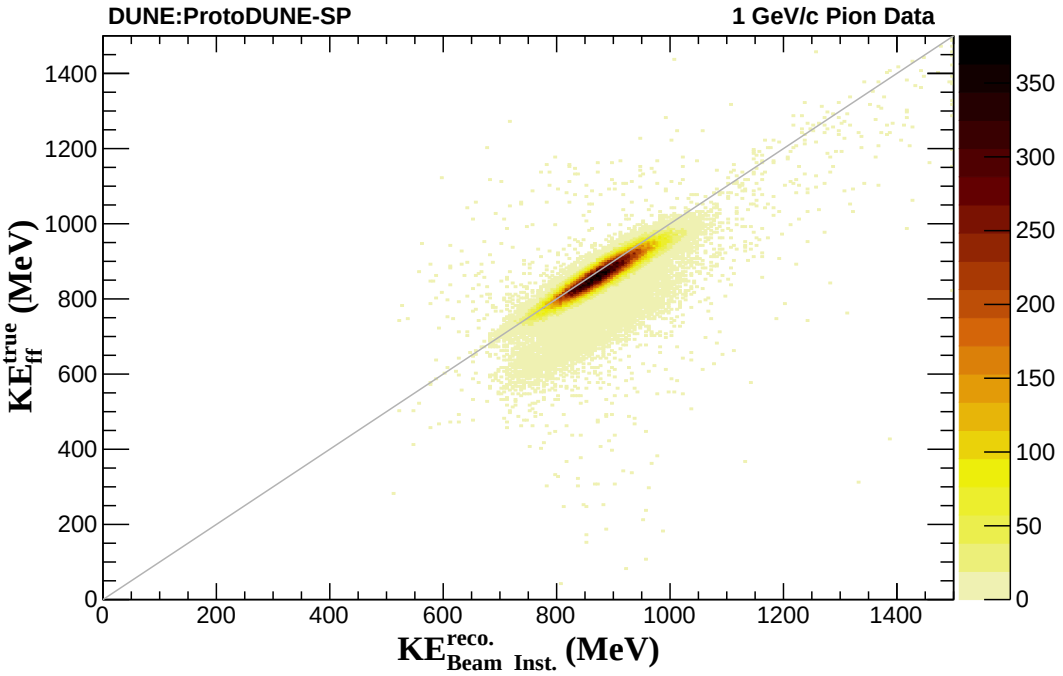

Figure 6.10: The front-face energy obtained in truth versus the reconstructed beam kinetic energy. Ordinary beam events should align along the diagonal line, exhibiting only a few MeV energy loss. On the other hand, beam scraper events create a second band below the diagonal line.

backgrounds, they remain as irreducible sources that cannot be completely eliminated due to inherent limitations in the reconstruction and identification algorithms.

The final cut (Beam Cut 7) is specifically targeted at reducing beam scraper candidates. These beam candidates are characterized by the deviation of beam particles from the expected upstream energy loss behaviour, as illustrated in Fig. 6.10. The upstream energy loss is defined as the energy loss of the beam particle between the beamline spectrometer and the entrance of the front face of the TPC. In an ideal scenario, the majority of beam particles would align along a diagonal line, with only minor (a few MeV) energy losses. However, particles that deviate from the proper alignment with the beam plug tend to experience greater energy losses as they traverse additional materials before entering the TPC. This results in the observation of a secondary band, indicating the presence of scraper events.

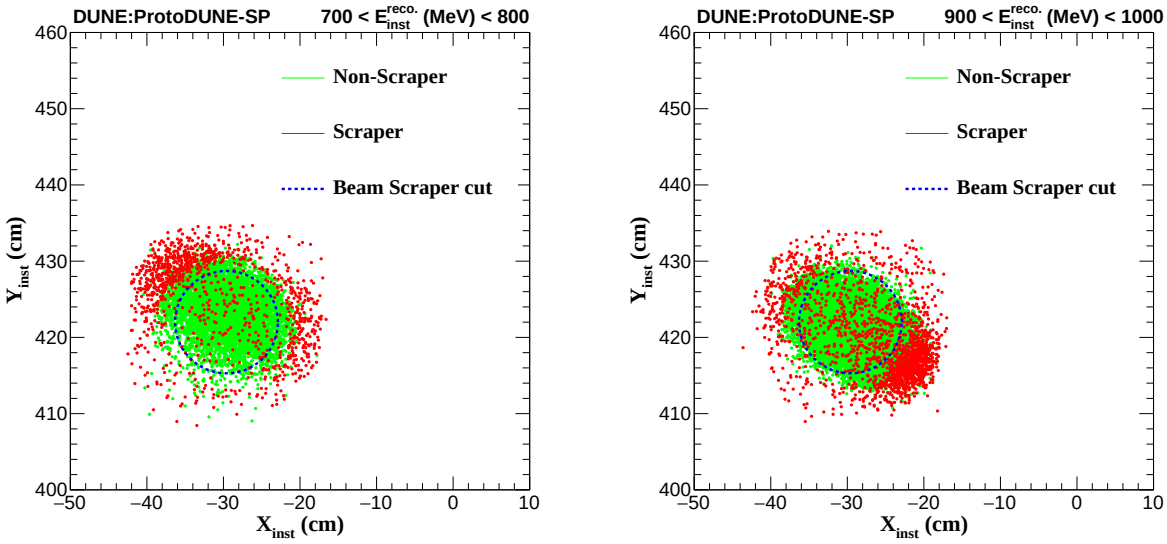

Figure 6.11: Inst. X versus inst. Y position at different beam energy. **Left**: $700 < E(\text{MeV}) < 800$. **Right**: $900 < E(\text{MeV}) < 1000$. Normal beam events are depicted in green, while scraper events are indicated in red. The beam scraper cut is defined by the dashed blue circle.

The distribution of upstream energy loss is plotted within each 100 MeV beam energy bin and fitted with a Gaussian function. Scraper events are identified as those with an upstream energy loss exceeding the 3σ region around the fitted mean value (Appendix A). To heavily reduce these scraper beam candidates, a circular shape cut [90] is developed and displayed in Fig. 6.11 for two different beam energy ranges. In the figures, scraper events are shown in red, while normal beam events are indicated in green. The circular shape of the beam plug is discernible, and it is observed that the majority of these scraper events do not penetrate the TPC within the beam plug region. This characteristic enables the effective implementation of a circular cut on the X-Y position of the reconstructed beam particle, which successfully reduces these scraper events across all beam energies. By implementing this circular cut, the number of scraper beam candidates is significantly reduced, resulting in a more accurate estimation of the upstream energy loss for the selected beam sample. It plays a crucial role in determining the initial energy of the beam when it first enters the TPC. The precise measurement of the beam's initial energy is essential for conducting the cross-section measurements in this analysis in Sec. 3.6.2.

Table 6.1: A summary of cumulative purity and efficiency for each Beam Cut.

Beam Cut	Purity	Efficiency
1. Beamline trigger cut (Beam Cut 1)	48.2%	100%
2. Pandora track-like cut (Beam Cut 2)	56.7%	98.4%
3. Beam quality cut (Beam Cut 3)	74.3%	91.3%
4. APA cut (Beam Cut 4)	85.5%	85.7%
5. Michel electron cut (Beam Cut 5)	86.7%	85.2%
6. Proton $\mathrm{d}E/\mathrm{d}x$ cut (Beam Cut 6)	88.5%	82.7%
7. Beam Scraper cut (Beam Cut 7)	90.2%	66.2%

The evaluation of the selected sample involves assessing both its purity and efficiency. Purity refers to the proportion of the true selected pion beam within the overall selected sample, while efficiency represents the fraction of the true selected pion beam in the available true pion beam sample. Notably, the efficiency is defined to be unity following the selection of the π^+ (and μ^+) beamline trigger.

Table 6.1 provides a comprehensive summary of the cumulative purity and efficiency achieved throughout the selection process. After implementing all the necessary beam cuts, the final selected pion sample demonstrates a commendable purity of 90%, rendering it suitable for subsequent pion cross-section analysis. Furthermore, the resolution of the measured beam momentum is estimated to be 3%, as shown in Fig. 6.12, indicating a reliable measurement of the beam momentum. Also, the angular resolution for the θ angle with respect to the beam direction and ϕ angle in the detector coordinates is found to be approximately 1.6 and 5.5 degrees (Appendix B), respectively. These results attest to the excellent reconstruction performance exhibited by the selected beam sample.

At this point, a sample of pion beam events has been selected. The next section will provide a discussion on the selection and reconstruction of the daughter particles associated with each beam event. This step is crucial for the event topology selection in the cross-section measurements.

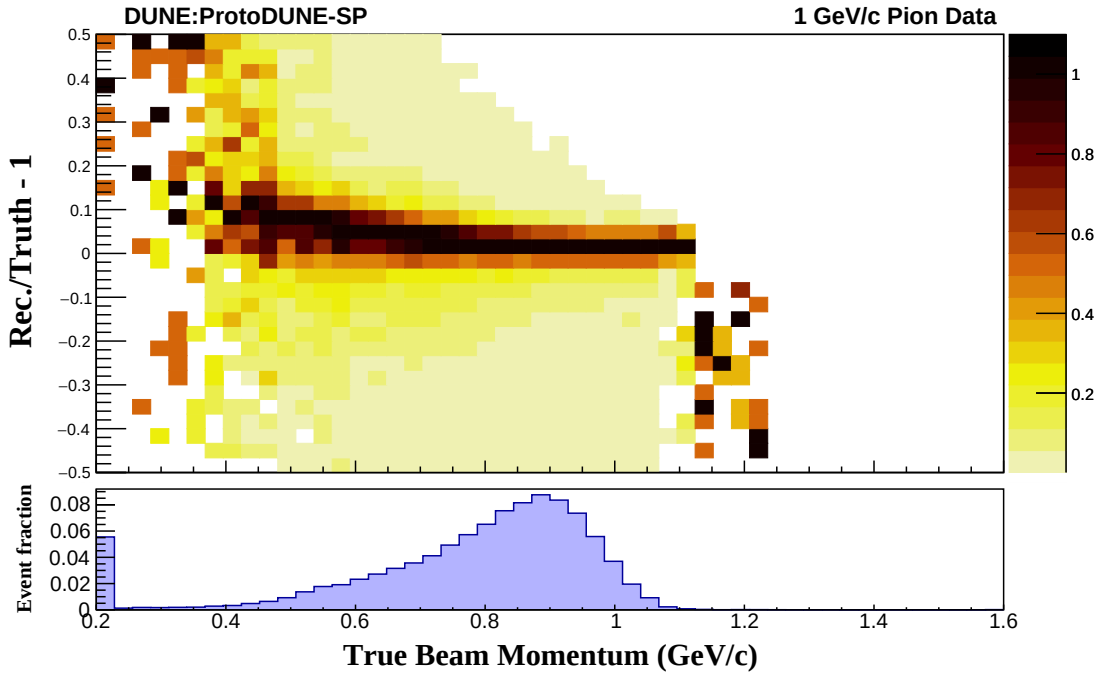

Figure 6.12: The reconstruction fractional bias of the beam momentum after Beam Cuts 1-7 as a function of the true beam momentum. The 2D histogram is column-normalized, with the highest value within each x bin set to one and all other values within the same column adjusted relative to this maximum value. The bottom panel shows the 1D distribution of true beam momentum. The spread of the y-axis distribution represents the resolution of the reconstructed beam momentum.

6.2 Daughter Particles Identification

The number of hits associated with an object serves as an indication of its physical size within the detector. In general, objects with a greater number of hits tend to possess higher energy and are relatively easier for the reconstruction process by Pandora. The quality of reconstruction performance can be assessed using two parameters: completeness and purity. Completeness refers to the fraction of hits associated with the true particle that are correctly assigned to the reconstructed object. On the other hand, purity is defined as the fraction of hits belonging to the reconstructed object that actually corresponds to its true particle. These measures help evaluate the accuracy and quality of the reconstructed particles.

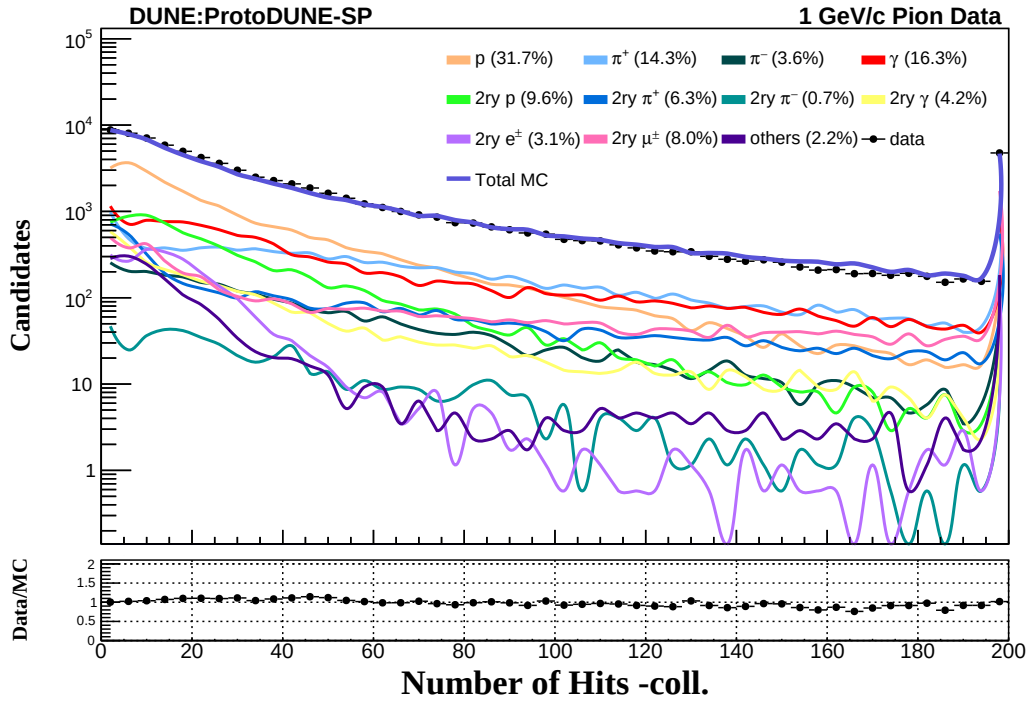

Figure 6.13: The number of collection plane hits distribution of all pion beam daughters. The simulation is decomposed into different particle types based on their truth-matched information. The γ component is originated from π^0 decays and denoted as primary daughters. The term 2ry in the legend represents the secondary particles originating from the primary daughter interactions. For example, a primary neutron daughter can interact with the nucleus to produce a secondary π^-.

Figure 6.13 provides the number of collection plane hits associated with reconstructed objects, categorized by their true particle type, highlighting the contributions by different particles [45]. Among the daughter particles, approximately 32% are identified as protons, and a significant proportion of them have a low number of hits in the TPC. Conversely, both π^+ and photons are prominently represented in the high number of hits region, suggesting that they tend to have a larger spatial extent within the detector. It is worth noting that in the 1 GeV/c pion beam event samples, electrons (only secondary $e^{\pm}$ are shown) are considerably less abundant compared to photons. The majority of these photons are primarily produced as decay products of π^0 particles.

To select proton and pion candidates from the beam daughter particles, three sequential cuts are applied, with each cut individually described in Sec. 6.2.1.

Track Cut 1: Require that the daughter particle has a track-like characteristic.

Track Cut 2: Require the daughter particle to have enough number of hits.

Proton/Pion Cut 3: Require proton/pion energy loss behaviour in the track candidates.

For the selection of shower candidates, four sequential cuts are implemented, with details of each to be discussed in Sec. 6.2.2.

Shower Cut 1: Require that the daughter particle has a shower-like characteristic.

Shower Cut 2: Require the daughter particle to have high shower completeness.

Shower Cut 3: Require the distance from the primary vertex to the initial position of the daughter particle to be consistent with the photon conversion length.

Shower Cut 4: Require a small impact parameter (defined in Sec. 6.2.2) for the daughter particle.

Finally, the selection of Michel electron candidates is straightforward (Sec. 6.2.1.2), involving only one implemented cut:

Michel Cut 1: Require the daughter particle to have a Michel-like characteristic.

6.2.1 Track Selection

The reconstructed daughter particles of the primary beam candidate are initially divided into two groups based on the output CNN scores of each particle. The first group consists of particles with track-like characteristics, which can be further analyzed to identify charged pions and protons. The second group includes particles with shower-like characteristics, allowing for the reconstruction of π^0 from two showers. The distribution of the CNN track score for all beam daughters is shown in Fig. 6.14. Protons, pions, and muons, which typically have a track-like trajectory in the detector, tend to have higher track scores. To select track-like daughter particles, a cut is applied to the track score, with a threshold value set at 0.5 (Track Cut 1). This cut helps to minimize the inclusion of shower-like particles in the track sample.

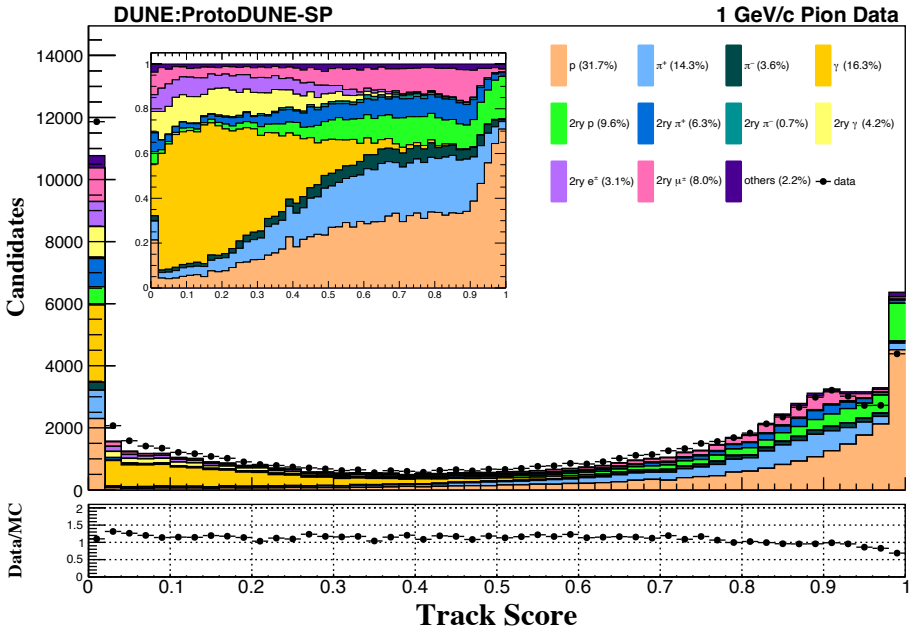

Figure 6.14: The CNN track score distribution of all daughters from the selected pion beam sample (following Beam Cuts 1-7). The inserted figure displays the bin-normalized histogram, making it easy to identify the dominant component in each bin. The separation works well if one places a cut on track score > 0.5 to select proton and pion candidates.

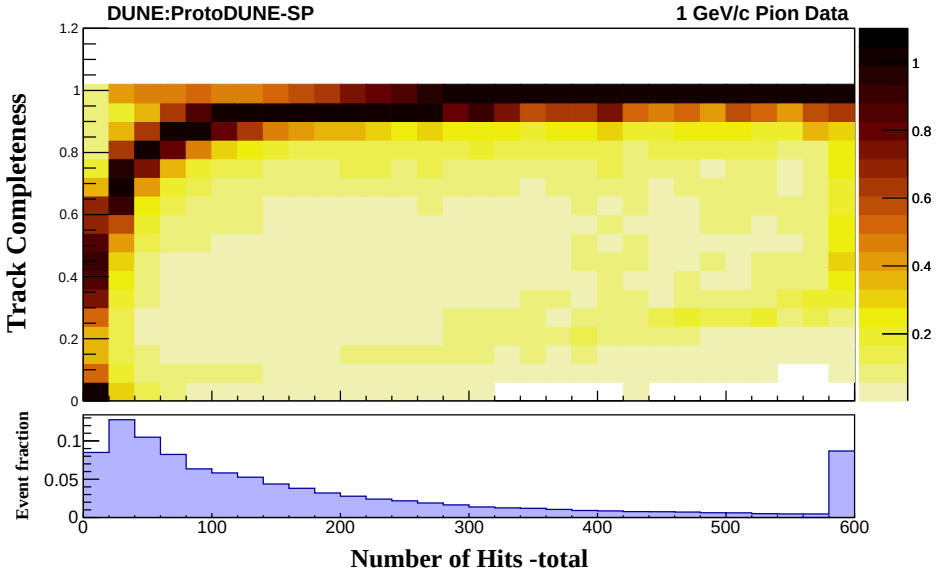

Figure 6.15: The completeness of the reconstructed tracks plotted against the number of hits after Track Cut 1. The 2D histogram is column-normalized, with the highest value within each x bin set to one and all other values within the same column adjusted relative to this maximum value. The cut on the number of hits is set to 20 to reduce the incomplete tracks with too few hits.

The reconstruction process may suffer from inefficiencies, leading to the inability to fully utilize all collected hits for forming track candidates. To address this issue, additional selection criteria are implemented to account for incomplete tracks by considering the number of hits. The completeness (defined in Sec. 6.2) of track candidates as a function of the number of hits is shown in Fig. 6.15. It is observed that tracks with a very low number of hits exhibit significantly lower completeness, indicating a substantial bias in their reconstructed energy. To enhance the quality of the selected track sample, a cut-off threshold is set, requiring a minimum of 20 hits for each track (Track Cut 2).

6.2.1.1 Protons

Due to the difference in mass between protons and pions, their energy deposition within the detector exhibits distinct characteristics. At a given momentum, protons, owing to their heavier mass, have a lower velocity, resulting in a smaller β term in the Bethe-Bloch formula (Sec. 1.8). Consequently, they deposit more energy within the detector. As a result, protons reach the Bragg peak much earlier than pions with the same energy, whereas pions behave similarly to that of MIPs in LArTPC. Therefore, observable quantities related to $\mathrm{d}E/\mathrm{d}x$ can be used to differentiate between protons and pions among the selected daughter track candidates.

Two metrics are utilized to separate daughter protons from pions. The first observable is the truncated mean [91] $\mathrm{d}E/\mathrm{d}x$ (TME), calculated by excluding the first eight hits near the vertex and the last two hits in track end regions, then computing the mean value of 5% to 60% of the remaining sorted $\mathrm{d}E/\mathrm{d}x$. This sorting is done from the smallest to the largest values, ensuring the exclusion of the Bragg peak in the TME calculation. Figure 6.16 shows the TME distribution of all track candidates. The first peak at zero corresponds to tracks with only a few hits, for which a properly calculated TME is not available. The presence of a second peak ($\sim$ 1.8 MeV/cm) indicates the MIP behaviour of daughter pions. Essentially, TME values larger than 2.8 correspond only to proton candidates. The second observable is the χ^2 per number of degrees of freedom (NDF), which follows the same definition as previously discussed for the beam selection in Sec. 6.1. Comparatively,

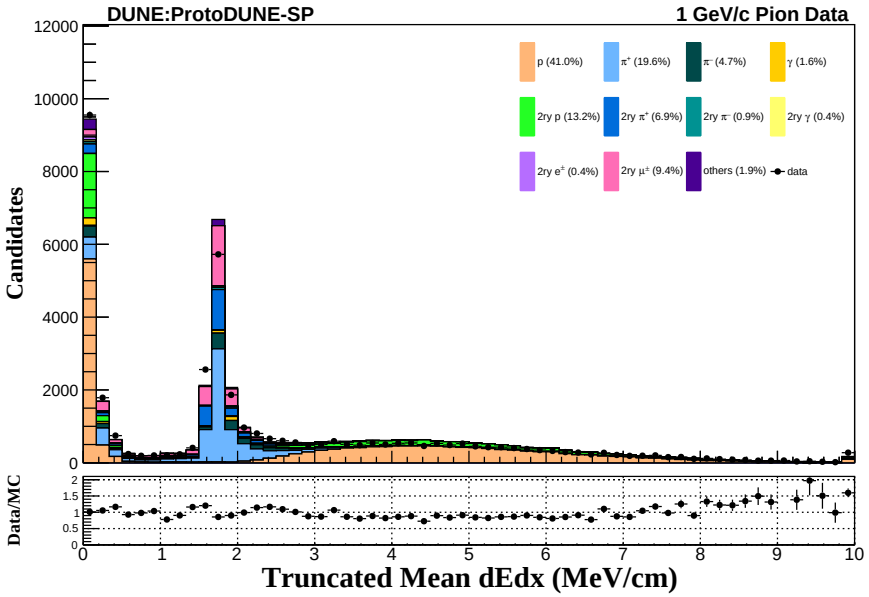

Figure 6.16: The distribution of the truncated mean $\mathrm{d}E/\mathrm{d}x$ of all daughter tracks after Track Cuts 1-2. This quantity is obtained by excluding hits near the vertex and track end regions and then computing the mean value of $\mathrm{d}E/\mathrm{d}x$ for the remaining hits. Notably, no pions are observed for $\mathrm{d}E/\mathrm{d}x$ values larger than 2.8 MeV/cm.

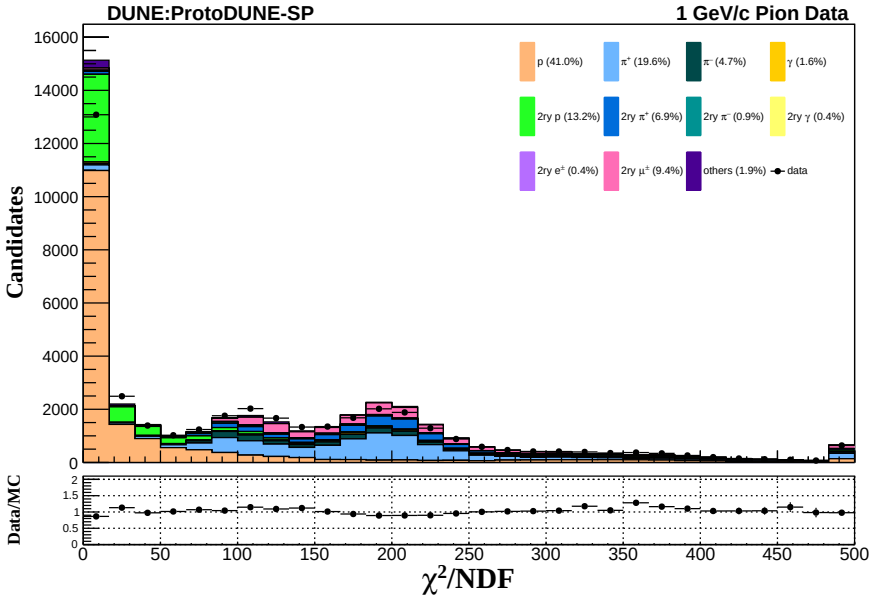

Figure 6.17: The distribution of the fitted proton χ^2/NDF of all daughter tracks after Track Cuts 1-2, calculated by assuming a proton hypothesis and performing a χ^2 test on the distribution of $\mathrm{d}E/\mathrm{d}x$ against its residual range. Proton candidates generally exhibit smaller χ^2 values.

Table 6.2: A summary of cumulative purity and efficiency for each Proton Cut. The efficiency is set to one after the Beam Cuts listed in Table 6.1.

Proton Cut	Purity	Efficiency
1. No cut (Beam Cut 1-7)	31.7%	100%
2. Track Score > 0.5 (Track Cut 1)	42.9%	82.4%
3. nHits > 20 (Track Cut 2)	41.0%	71.5%
4. $\chi^2 < 70$ or TME > 2.8 (Proton Cut 3)	68.1%	60.6%

pion candidates tend to have higher values of χ^2/NDF when compared to proton candidates, as illustrated in Fig. 6.17. A track candidate is classified as a proton if the χ^2/NDF is less than 70 or the TME is greater than 2.8 (Proton Cut 3). These specific thresholds are selected to optimize the trade-off between selection efficiency and purity.

The selection cuts for daughter protons are summarized in Table 6.2. These cuts serve two main purposes: distinguishing protons from other particles and improving the quality of the selected sample by removing incomplete tracks. The table also includes the cumulative purity and efficiency of each cut, with efficiency defined as one when no cuts are applied. The final selected proton sample has a purity of 68%, with substantial contamination originating from secondary protons.

Figure 6.18 illustrates the reconstructed momentum distribution of the selected protons. It is worth mentioning that there are secondary protons originating from the interactions of the daughter particles in the detector. Despite this, the overall purity of the selected sample remains at a commendable level of approximately 90% (including the secondary protons). The peak of the reconstructed momentum is observed at around 600 MeV$/c$. Notably, proton momentum reconstruction exhibits remarkable resolution, with 2% accuracy achieved for protons with momenta greater than 0.55 GeV$/c$, as shown in Fig. 6.19. This highlights the excellent performance of proton momentum reconstruction within the LArTPC detector. Additionally, the angular resolution for the θ angle with respect to the beam direction is approximately 4 degrees (Appendix B).

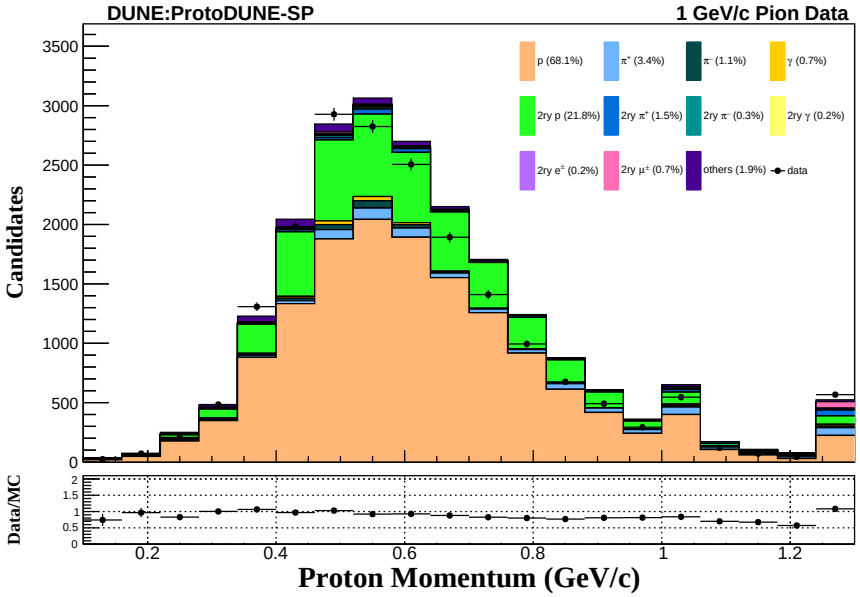

Figure 6.18: The reconstructed momentum of selected daughter protons after Track Cuts 1-2 and Proton Cut 3. The component "secondary proton" refers to protons generated from the secondary interaction of daughter particles within the detector.

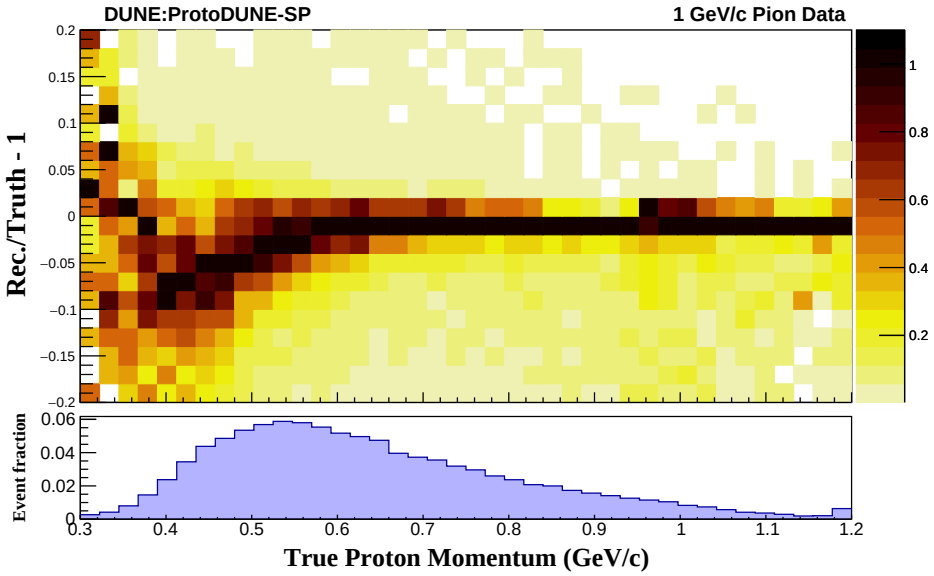

Figure 6.19: The reconstruction fractional bias of the proton momentum after Track Cuts 1-2 and Proton Cut 3 as a function of the true proton momentum (column-normalized). For the high momentum protons ($p_{\mathrm{p}} > 0.55$ GeV$/c$), the fractional bias is close to zero with a 2% resolution.

Table 6.3: A summary of cumulative purity and efficiency for each Pion Cut. The efficiency is set to one after the Beam Cuts listed in Table 6.1.

Charged Pion Cut	Purity	Efficiency
1. No cut (Beam Cut 1-7)	14.3%	100%
2. Track Score > 0.5 (Track Cut 1)	18.3%	78.4%
3. nHits > 20 (Track Cut 2)	19.6%	76.0%
4. 0.5 < TME < 2.8 (Pion Cut 3)	35.8%	73.5%

6.2.1.2 Charged Pions

The selection process for charged pion candidates relies on the same energy loss variables in the previous section. As pions exhibit behaviour akin to MIPs within the detector, their energy loss per unit length significantly differs from that of protons. These distinct energy deposition characteristics allow for the effective identification of daughter pions. A track candidate is classified as a pion if the TME is between 0.5 and 2.8 (Pion Cut 3). The selection cut for daughter pions is presented in Table 6.3.

The momentum distribution of the selected pions is shown in Fig. 6.20. The purity of the selected pion sample is relatively lower than that of the protons, as both protons and secondary muons can contribute to the background. The track momentum is determined based on the range inside the detector. However, this method encounters limitations when dealing with pion momenta above 300 MeV$/c$, as the onset of inelastic scattering causes a premature end to the range. Consequently, only a portion of the pion track is reconstructed, leading to an underestimation of its momentum. Notably, for momenta exceeding 700 MeV$/c$, the selected sample consists exclusively of muons.

Furthermore, pions decay at rest to muons, which in turn decay into electrons, which are referred to as Michel electrons. The selection process for Michel electrons is straightforward, relying on the CNN Michel score output. By setting a threshold value, typically greater than 0.5 (Michel Cut 1), the Michel score is used to identify potential Michel electrons originating from pion decay chains, allowing for the tagging of final state pions.

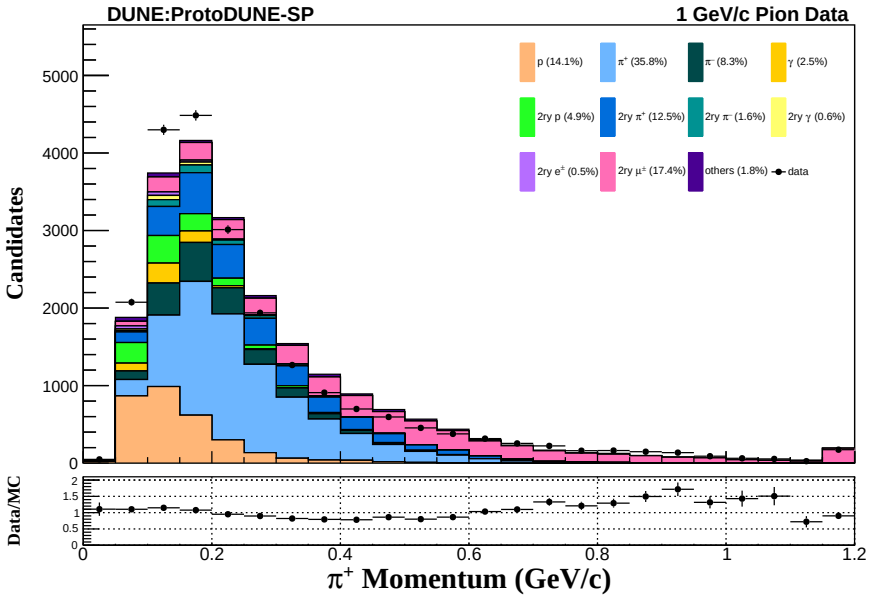

Figure 6.20: The reconstructed momentum of selected daughter pions after Track Cuts 1-2 and Pion Cut 3. The term "secondary muons" refers to muons produced from the daughter pion decays within the detector. Owing to the onset of the inelastic interaction, high-momentum pions cannot be measured precisely using the range-based method.

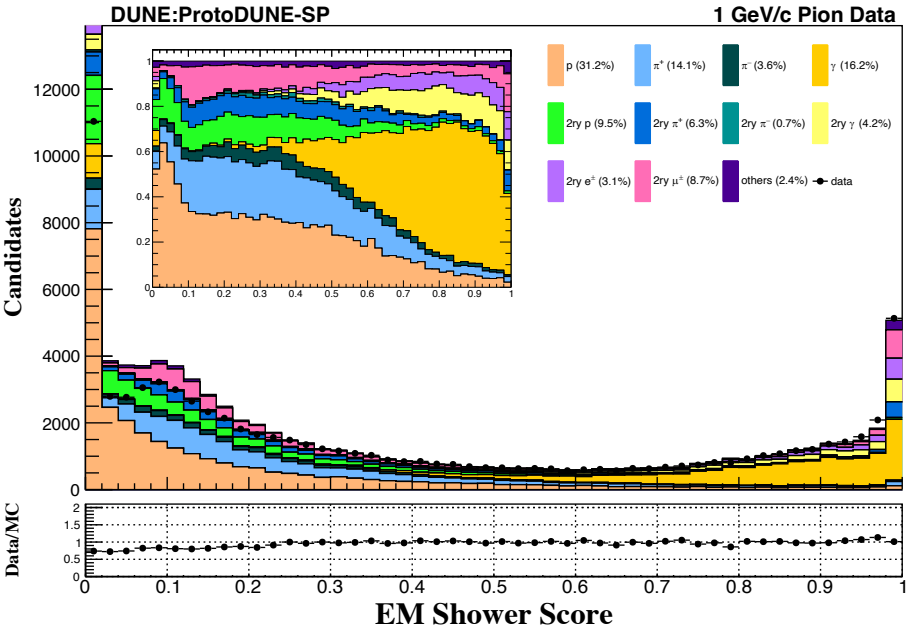

Figure 6.21: The CNN EM shower score distribution of all daughters from the selected pion beam sample (following Beam Cuts 1-7). The inserted figure shows the bin-normalized histogram, making it easy to identify the dominant component in each bin. The separation is effective if one places a cut on EM shower scores > 0.5 to select photon candidates while retaining a relatively large sample.

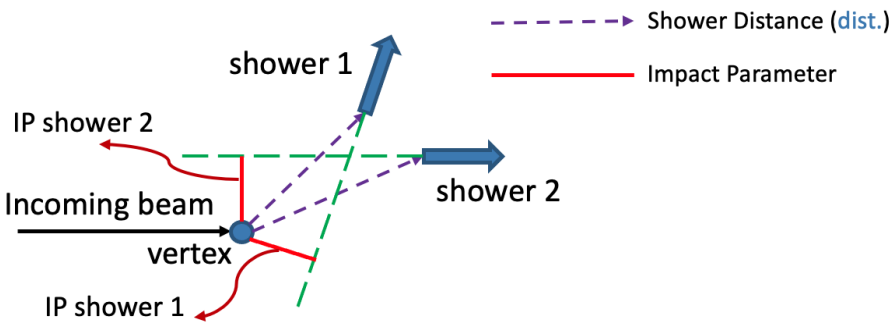

Figure 6.22: Schematic diagram of shower distance and impact parameter of reconstructed shower objects. The shower distance is shown in the purple dashed line, and the impact parameter is shown in the solid red line.

6.2.2 Shower Selection

Photon showers primarily originate from π^0 particles. Therefore, accurate reconstruction of the showers is crucial for subsequent π^0 particle reconstruction. Figure 6.21 depicts the distribution of the CNN EM shower score for all pion beam daughters. The classification of photons demonstrates good accuracy. Daughter particles with an EM score greater than 0.5 (Shower Cut 1) are selected as initial photon shower candidates. Additionally, a minimum requirement of 80 hits (Shower Cut 2) is imposed to remove low-completeness showers caused by the shower reconstruction inefficiency, which will be discussed in detail in Sec. 7.2.

Two cut observables, shower distance and impact parameter (IP), are used to increase the purity and completeness of the selected photon shower candidates. The schematic definitions of shower distance and the shower IP are shown in Fig. 6.22. The shower distance is the distance between the interaction vertex and the shower start position. In the sub-GeV energy range, photons propagate a few centimetres before undergoing interactions that initiate showers, whereas charged pions and muons begin ionizing electrons as soon as they are produced. Therefore, the shower distance can be used to reduce the pion and muon contamination in the photon shower sample, as shown in Fig. 6.23. The predominant background arises from charged pions that are reconstructed as shower objects, as they tend to have a small distance between the vertex and the start position. Conversely,

Table 6.4: A summary of cumulative purity and efficiency for each Shower Cut. The efficiency is set to one after the Beam Cuts listed in Table 6.1.

Shower Cut	Purity	Efficiency
1. No cut (Beam Cut 1-7)	16.2%	100%
2. Shower Score > 0.5 (Shower Cut 1)	45.6%	86.2%
3. nHits > 80 (Shower Cut 2)	67.3%	56.3%
4. 3cm < dist. < 90cm (Shower Cut 3)	75.2%	51.7%
5. IP < 20cm (Shower Cut 4)	79.3%	45.9%

the muon component originates from pion decays in flight can also satisfy the shower selection criteria, but it exhibits a significantly larger shower distance. Therefore, only reconstructed shower objects with a shower distance ranging from 3 cm to 90 cm (Shower Cut 3) are selected.

A shower object's IP is defined as the closest distance from the interaction vertex to a given shower position vector in the lab frame. Due to the Lorentz boost, the energetic π^0 particles tend to decay into two photons with a small IP. Therefore, a large shower IP indicates a photon shower with lower energy. The shower developed by low-energy photons is more stochastic and segmented, which is difficult to reconstruct. The shower purity and completeness as a function of the IP is shown in Fig. 6.24, and above 20 cm, the average completeness of the shower-like object drops below 0.5 due to the stochastic nature of low-energy showers. Showers with low completeness lead to a large bias in their energy reconstruction. Consequently, the kinematics of the neutral pion that produced them cannot be reconstructed correctly. Therefore, only showers with an IP less than 20 cm (Shower Cut 4) are selected.

Table 6.4 provides a summary of the shower selection criteria. If the daughter particle meets the shower selection criteria described above, it is classified as a π^0 photon shower. The selected shower sample is then used to reconstruct the π^0 particle by combining the first two leading showers, as explained in the next chapter.

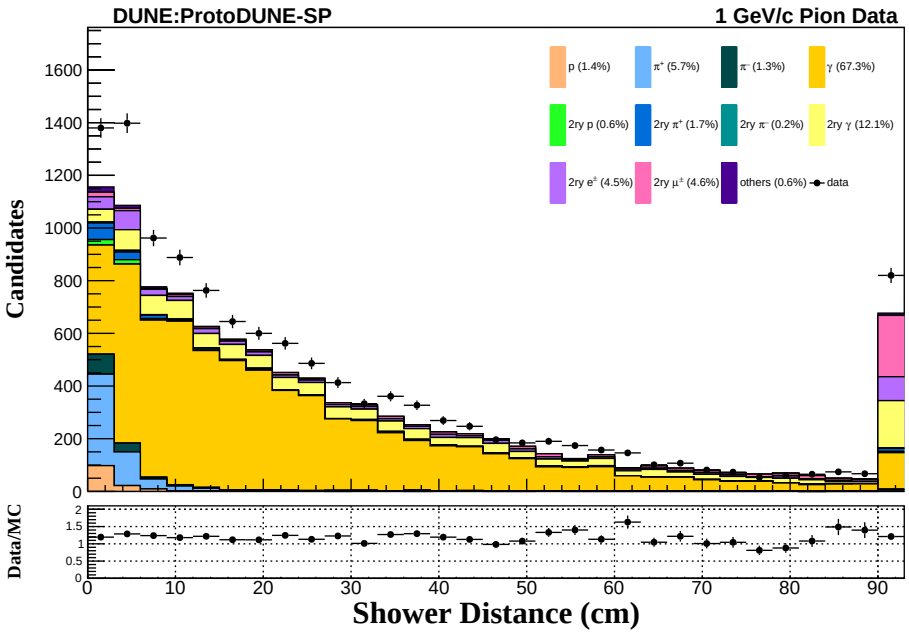

Figure 6.23: The distribution of reconstructed shower distance by true particle type after Shower Cuts 1-2. The primary contamination is from charged pions (small distance value) and secondary muons (large distance value).

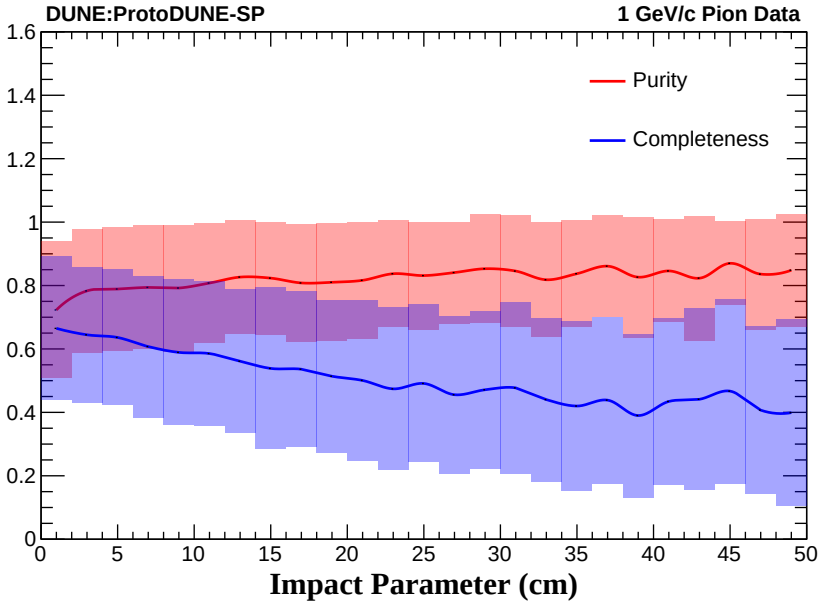

Figure 6.24: The distribution of average purity and completeness as a function of impact parameter after Shower Cuts 1-3. The completeness decreases as the IP increases. The colour bands signify a 1σ spread of the values in each bin.

6.3 Particle Selection Efficiency

The efficiency of particle reconstruction plays a critical role in determining the final selection of event topologies. As shown in Fig. 6.25(a), the leading proton selection efficiency is presented as a function of the true proton momentum. Protons with momenta below 0.3 GeV/c are not efficiently reconstructed by Pandora due to the requirement of at least 20 hits for any tracks, as discussed in Sec. 6.2.1. Notably, the efficiency peaks at approximately 80% for momenta exceeding 0.6 GeV/c, and then decreases after 0.9 GeV/c due to the limitations of the momentum-by-range reconstruction methods [72] and rescattering. When a high-momentum proton undergoes inelastic scattering, its momentum estimate becomes less accurate, making it challenging to match the true proton particle and leading to a decrease in selection efficiency. The selection efficiency goes above 40% for protons with momentum larger than 0.45 GeV$/c$.

The selection efficiency for charged pions is shown in Fig. 6.25(b), showing a peak efficiency of 60% within the momentum range of 0.2 to 0.7 GeV$/c$, followed by a gradual decrease attributed to the limitations of the momentum reconstruction methods as discussed in the proton case. The onset of the efficiency is due to the spatial granularity (wire spacing in Sec. 3.2.2) in ProtoDUNE-SP. Pions with momenta below 0.1 GeV$/c$ have low selection efficiency, with a value of less than 5%. The selection efficiency exceeds 40% for pions with momenta greater than 0.2 GeV$/c$.

The efficiency of the leading shower reconstruction is shown in Fig. 6.25(c) as a function of the true energy of the leading photon. A relatively consistent efficiency is achieved across a broad range of energies, from 0.1 to 1 GeV. Showers with energy below 0.1 GeV are not included due to the requirement of at least 80 hits for any showers, as discussed in Sec. 6.2.2. The average efficiency remains around 70%, demonstrating satisfactory performance in reconstructing single showers. Importantly, the efficiency increases with the shower energy. This is because of the larger size of the ProtoDUNE-SP LArTPC, which enables it to fully contain high-energy showers, in contrast to the ArgoNeuT experiment [92].

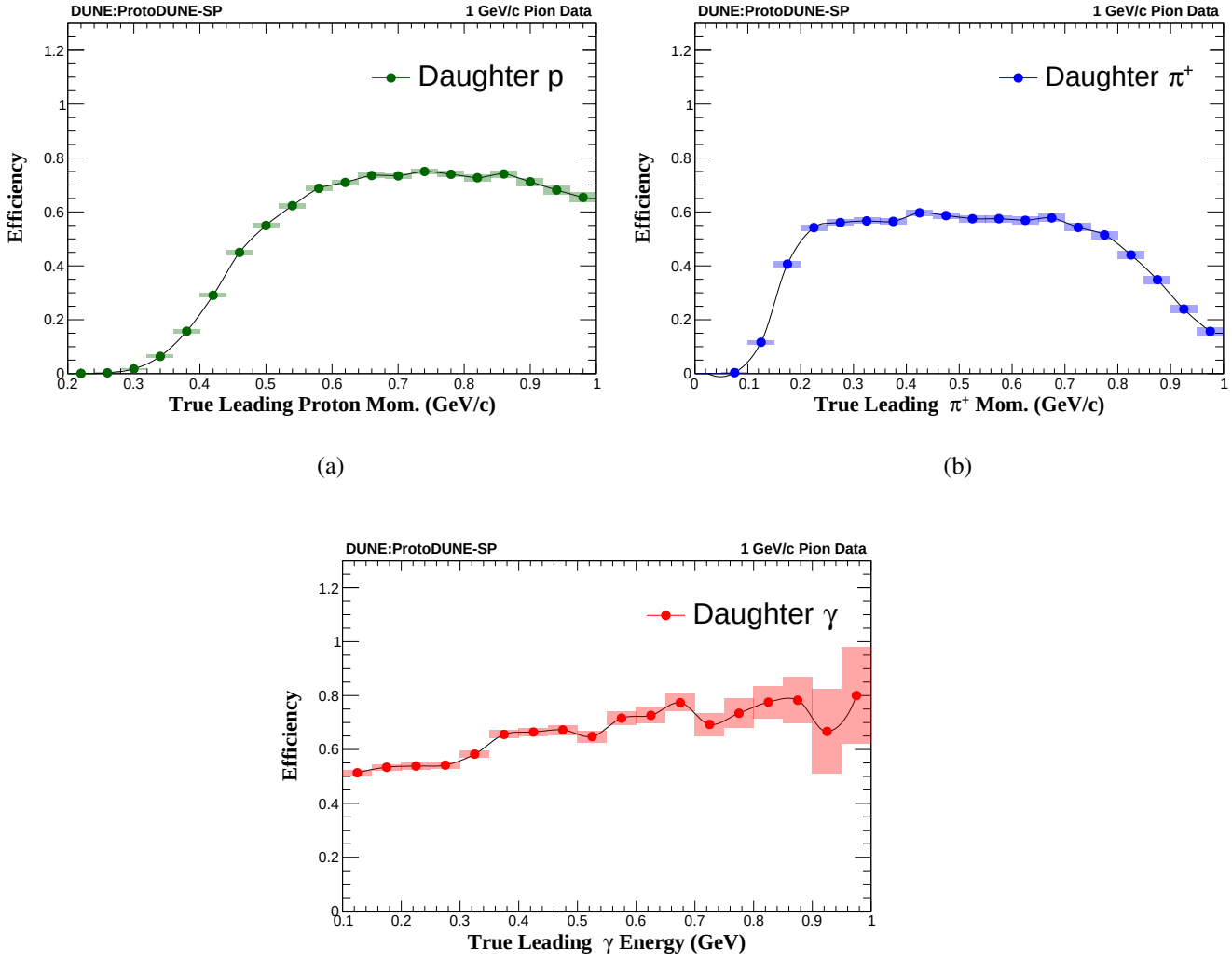

(a) (b)

(c)

Figure 6.25: (a) The selection efficiency of the leading proton as a function of the true proton momentum. The maximum efficiency is approximately 80% for momenta larger than 0.6 GeV/c. (b) The selection efficiency of the leading charged pion as a function of true pion momentum. The efficiency plateaus at a value of 60% for pion momenta between 0.2 to 0.7 GeV$/c$. (c) The selection efficiency of the leading shower as a function of true photon energy. The plot begins with a minimum true photon energy of 100 MeV with an efficiency of 50%. As the energy increases, the efficiency also rises up to 75%. The colour bands represent the statistical error in each energy bin.

7 | Neutral Pion Reconstruction

Neutral pion identification and reconstruction will be crucial in DUNE as its estimated NC background is the second-largest background in oscillation measurements [33]. Neutral pion can be produced via the neutrino NC interaction and decays into two photons, forming two showers in the detector. If two photon showers from π^0 decay overlap and are reconstructed as a single shower, it can be identified as a ν_e appearance signal event. In addition, if one of the photon showers is too small or too far away from the decay vertex, only one shower will be reconstructed in this event. Neutral pion can also be produced by the secondary interaction of neutrino products. The neutrino energy spectrum in DUNE has a broad peak of around 2 - 3 GeV, as discussed in Sec. 2.1.1. This energy range is dominated by neutrino resonance interactions that lead to pion production, and these charged pions can undergo charge exchange interactions with the surrounding argon, resulting in the production of π^0 particles. Accurately measuring the rate of these secondary interactions is of utmost importance as it provides valuable constraints on the event generator and enhances our understanding of the neutrino oscillation measurement background arising from secondary π^0 particles.

This chapter presents the reconstruction of neutral pions in the ProtoDUNE-SP. In Sec. 7.1, the physics properties of neutral pions are introduced, including an exploration of their energy spectrum using the ProtoDUNE-SP MC events. In Sec. 7.2, the examination of the shower energy reconstruction algorithm is carried out using a variety of single gamma MC samples. Sec. 7.3 presents the process of acquiring the energy-dependent correction function and its subsequent application to enhance the accuracy of the reconstructed shower energy. The performance of reconstructing of neutral pion in ProtoDUNE-SP is presented in Sec. 7.4. Finally, the improved π^0 energy achieved through kinematic fitting is presented in Sec. 7.5.

7.1 Decay Kinematics

The π^0 particle has a mass of 134.9770 $\pm$ 0.0005 MeV and a lifetime of (8.30 $\pm$ 0.19) $\times 10^{-17} s$. It mainly decays into two photons with a branching fraction of (98.823 $\pm$ 0.034) % [16]. Other rare decays, such as the Dalitz decay [16], $\pi^0 \rightarrow \gamma + e^+ + e^-$, with a branching fraction of (1.174 $\pm$ 0.035) % will not be discussed in this analysis. In ProtoDUNE-SP data, the π^0 particle can be produced via the strong interaction as follows,

$$\pi^+ + \mathrm{n} \rightarrow \pi^0 + \mathrm{p}. \tag{7.1}$$

This is also known as the pion charge exchange interaction. From the energy and direction of photons produced from π^0 decays, one can calculate the invariant mass of the π^0 as,

$$m^2_{\pi^0} = 2E_1E_2(1 - \cos\theta_{\mathrm{OA}}), \tag{7.2}$$

where E_1 and E_2 are the energy of leading and sub-leading photon shower energy, respectively, and θ_{OA} is the opening angle between two photon showers.

The energy spectrum of neutral pions and their decay photons provides insights into the characteristics and challenges associated with their reconstruction. Figure 7.1 shows the energy spectrum of all neutral pions originating from a 1 GeV/c pion beam, as well as the energy spectrum of their decay photons. The majority of π^0 particles have energies ranging from 200 to 500 MeV. Additionally, the energy distribution of the leading and sub-leading photons is shown in the same figure, and it can be seen that the majority of electromagnetic showers relevant to this analysis are concentrated within the energy range of 50 to 300 MeV.

However, a notable reconstruction challenge arises when considering the subleading photons (Fig. 7.1), as these photons typically have energies below 100 MeV. Specific shower selection criteria have been developed, as discussed in Sec. 6.2.2, to reject low-energy showers that exhibit low completeness.

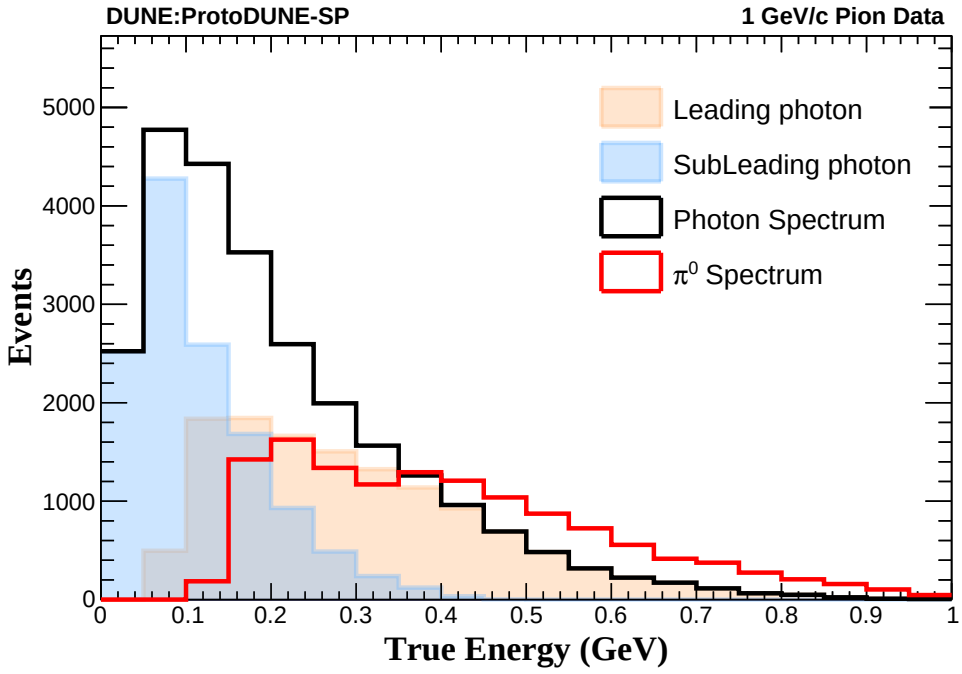

Figure 7.1: The true energy spectrum of neutral pions from a 1 GeV/c pion beam. The energy spectra for leading and sub-leading photons are also displayed. The black spectrum represents the energy distribution of both photons.

7.2 Single Gamma Reconstruction Performance

This section presents several MC studies to examine the shower energy reconstruction algorithm used in ProtoDUNE-SP. It will be shown that this algorithm encounters certain issues, prompting a detailed investigation using single shower reconstruction into the origin of the observed bias. The observations motivate an MC-driven shower energy correction technique in the next section.

In total, four single gamma samples are generated within the ProtoDUNE-SP detector setup: two isotropic and two along the beam direction; two samples aimed to assess the reconstruction performance of low-energy showers, with an average energy of 300 MeV and a 10% Gaussian energy dispersion while the other two had an energy of 1 GeV, also with a 10% Gaussian energy dispersion.

Table 7.1: A summary of all variables used to examine the single gamma reconstruction performance.

Variable	Definition
True Photon Energy	Photon energy used in the single particle generation
True Energy Deposit	Total energy deposit simulated in all detector channels
Rec. All-Hit Energy	Sum of reconstructed energy of all hits after calibration
Rec. Leading Shower Energy	Sum of reconstructed energy of hits that belong to leading shower object from Pandora reconstruction

The performance of the shower energy reconstruction is evaluated against four variables defined in Table 7.1. The first variable is the true photon energy, which represents the energy used to generate the gamma particle. The second variable is the true energy deposit inside the detector, determined by summing the simulated energy deposit over each time slice in each detector channel. The third variable focuses on the reconstructed all-hit energy. The area under each reconstructed Gaussian-shaped hit corresponds to the deposited charge. This charge is then converted into energy after applying electron recombination and lifetime corrections specific to ProtoDUNE-SP, as described in Sec. 3.3. Lastly, the reconstructed leading shower energy, i.e. the sum of reconstructed energy of hits that belong to the leading shower, is obtained directly from Pandora (Fig. 7.2). It is important to note that Pandora may reconstruct multiple showers even for a single gamma particle, and therefore, the leading shower energy is selected in this study. The evaluation of each step's performance involves calculating the fractional bias, represented as $(v_2 - v_1)/v_1$, where v_i is the general representation of variables defined in Table 7.1. The distribution of the calculated fractional bias can be fitted with a Gaussian function, where the mean value μ_E/E and spread σ_E/E correspond to the average bias and resolution in shower energy reconstruction, respectively.

To begin with, two isotropic single gamma samples with different E_γ are employed to evaluate the reconstruction performance of photon showers in each step. Firstly, the true energy deposit generated by GEANT4 closely aligns with the true photon energy, having

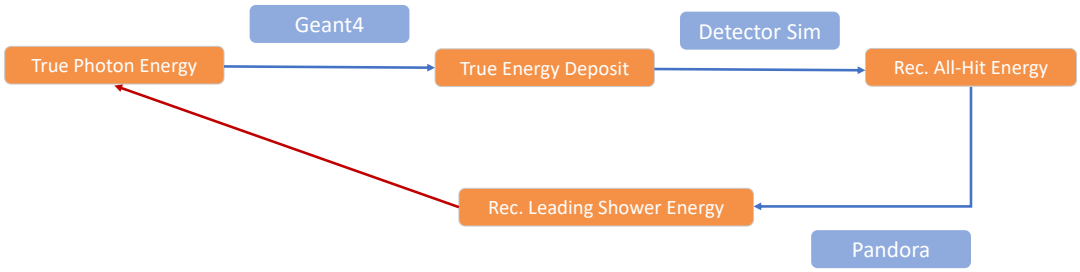

Figure 7.2: Data flow (blue arrows) in the shower energy reconstruction in ProtoDUNE-SP MC. The biases introduced at each step by GEANT4, detector simulation and Pandora can be deduced by comparing the energies at both ends of each blue arrow. The red arrow indicates the overall comparison.

a sharp peak centred around zero (see Appendix C). This indicates that the contribution of the GEANT4 simulation to the shower energy reconstruction bias is negligible. Secondly, when comparing the reconstructed all-hit energy to the true energy deposit inside the detector, the sample is divided into bins of the number of hits, and in each bin, the distribution of the energy fractional bias is fitted to a Gaussian function to the bias μ_E/E and resolution σ_E/E. It is observed that the reconstructed hits energy has a mean bias of -3.6%, which remains consistent across two isotropic gamma samples irrespective of the gamma energy (Fig. 7.3). Since high-energy gammas tend to produce large showers with a high number of hits, it is possible to study the energy dependence of hits energy reconstruction. Figure 7.3 illustrates the fitted mean bias μ_E/E as a function of the number of hits, which remains independent of energy. Moreover, the resolution of the hit energy decreases as the number of hits increases, as depicted in Fig. 7.4. To understand the energy-dependent resolution, a power function is fitted to this distribution. The energy resolution can be parameterised as [50],

$$\frac{\sigma_E}{E} = \frac{a}{\sqrt{E}} \oplus b \oplus \frac{c}{E}, \tag{7.3}$$

where the first term accounts for statistical fluctuations, while the second term represents a systematic contribution. The third term is attributed to electronic noise, as it averages to a constant. The power function fitted in Fig. 7.4 displays a clear -1 power dependence, indicating that the energy resolution is dominated by electronic noise [50].

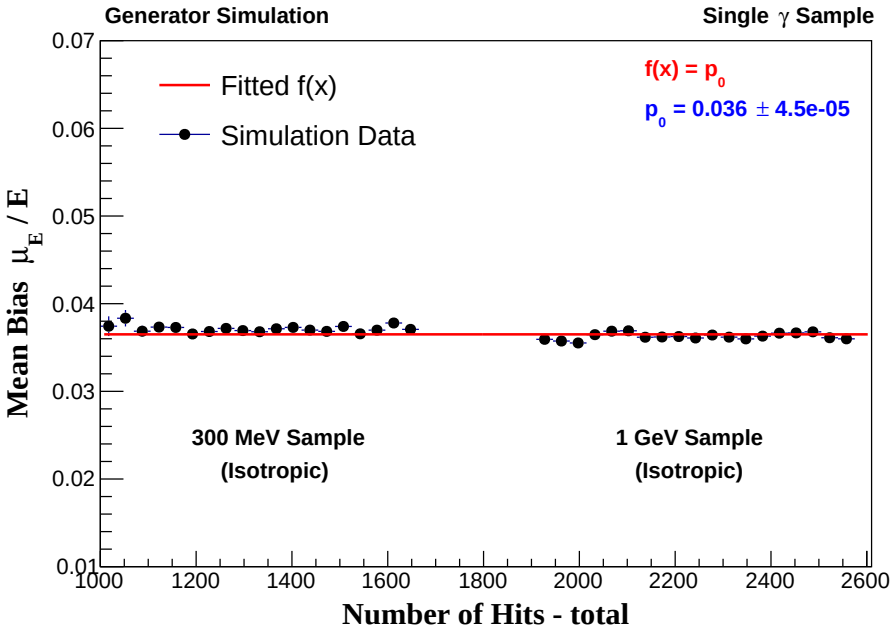

Figure 7.3: The mean bias, introduced by detector simulation (see Fig. 7.2), as a function of the number of hits from all detection planes for two isotropic gamma samples. A constant function is fitted against the distribution and yields 3.6% for two samples.

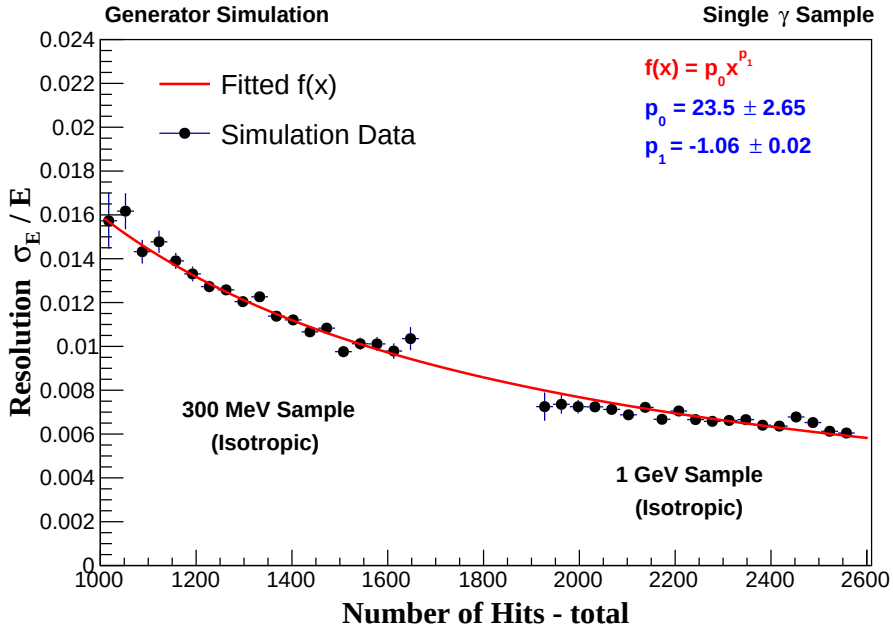

Figure 7.4: The energy resolution, introduced by detector simulation (see Fig. 7.2), as a function of the number of hits from all detection planes for two isotropic gamma samples. As the shower energy (represented by the number of hits) increases, the resolution decreases from 1.6% to 0.6%.

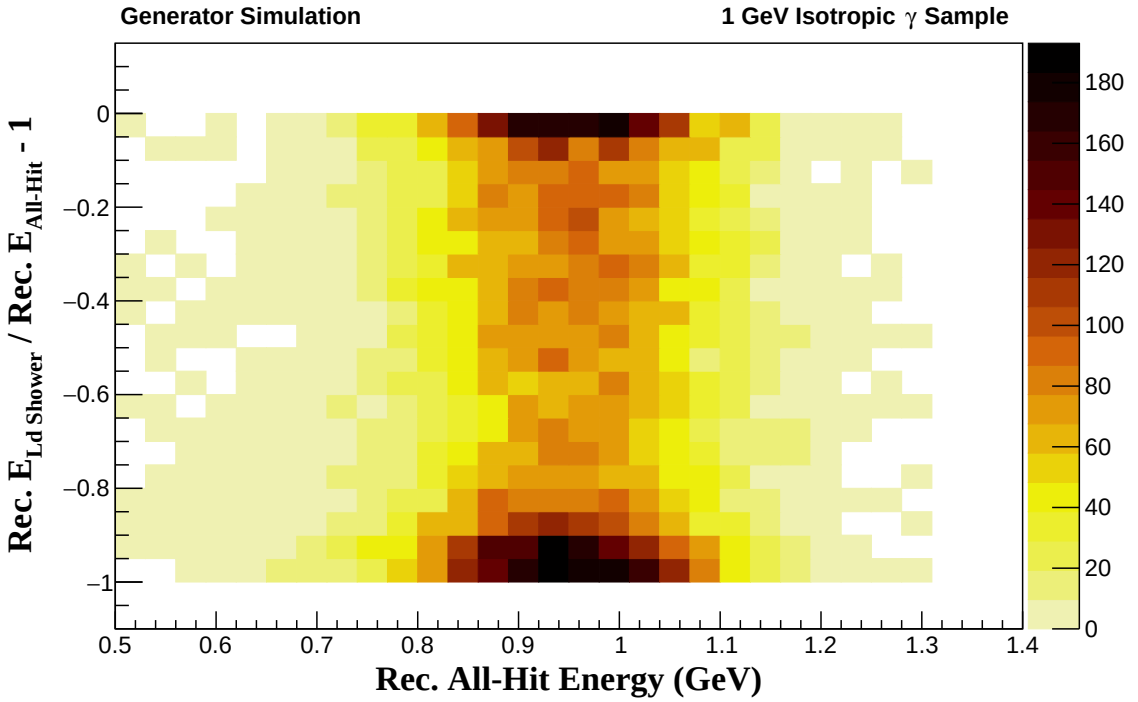

Figure 7.5: The fractional bias of rec. leading shower energy with respect to rec. all-hit energy as a function of the rec. all-hit energy. Two opposite reconstruction performances are observed for the same energy, suggesting an angular dependence in the shower reconstruction within Pandora.

Finally, the reconstructed leading shower energy is compared with the reconstructed all-hits energy to study the Pandora shower reconstruction. The fractional bias is shown as a function of the reconstructed all-hit energy in Fig. 7.5. It can be seen that there are two opposite reconstruction performances, even though the reconstructed all-hit energy is approximately the same, around 1 GeV. This suggests that the reconstruction performance of these showers in Pandora could be problematic. As shown below, it actually highly depends on the direction of the shower.

Figure 7.6 illustrates the fractional bias of reconstructed leading shower energy with respect to true photon energy as a function of the true photon angle θ_γ relative to the z-axis in the detector coordinates. Two distinct bands representing different reconstruction performances are clearly visible. Backwards-moving photons pose a challenge for the algorithm, resulting in a fractional bias close to a negative one. On the other hand, forward-moving photons are reconstructed well, albeit with a negative bias.

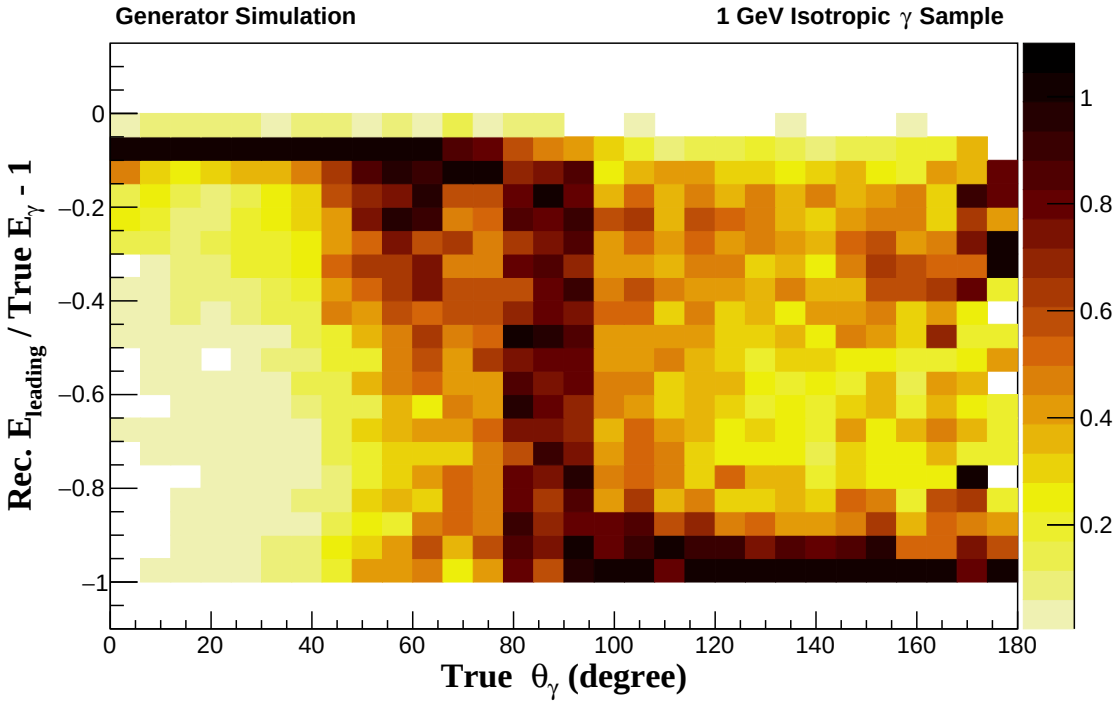

Figure 7.6: The fractional bias of reconstructed leading shower energy with respect to true photon energy (column-normalized) as a function of of the true gamma polar angle θ_γ, defined with respect to the z-axis in detector coordinate. A strong angular dependency on the reconstruction performance is observed. Only a small fraction of energy is recovered for the backward-going photons.

Starting at this point, the MC samples are switched to the two samples aligned along the beam direction to derive the reconstruction bias and resolution for forward-moving photon showers. The true energy deposit and reconstructed all-hit energy exhibit similar performance as the isotropic samples, differing mainly in the Pandora stage. A replot of Fig. 7.5 using both the 300 MeV and 1 GeV beam direction samples is shown in Appendix Fig. C.2. This results in biases of -10% and -8% for the 300 MeV and 1 GeV samples, respectively. It suggests that the significant energy loss may be attributed to additional missing hits that are not part of the reconstructed main shower object in Pandora. In future algorithmic developments, it is necessary to incorporate small segmented shower energies into the leading shower to address this issue.

An overview of the bias and resolution for the beam direction 300 MeV sample, as compared in each step, is provided in Fig. 7.7. The bias from the GEANT4 simulation is found

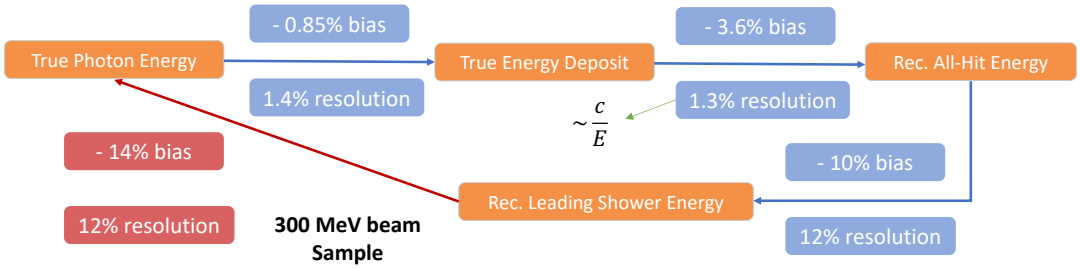

Figure 7.7: The summary of bias and resolution in each stepwise comparison, indicating a total energy reconstruction bias of -14% for the 300 MeV shower sample. The c/E dependence is the third term in Eq. 7.3. The Pandora reconstruction process contributes the largest bias.

to be less than 1%. The detector simulation stage demonstrates reliable hit-level information with a small bias of 3%. The c/E dependence on energy reflects the energy resolution is primarily dominated by electronic noise. However, the Pandora reconstruction exhibits the largest bias. For showers with a mean energy of 300 MeV, a bias of -10% with 12% energy resolution is observed in the Pandora reconstruction stage. Consequently, a significant -14% bias is found in the shower reconstruction. Two main factors contribute to this bias: the deposited charges falling below the hit forming threshold and inefficiencies in the shower clustering process, with the latter effect being predominant. As a result, the reconstruction process underestimates the shower energy. Further investigations into the shower-level information are warranted to identify potential areas for improvement in future developments. Currently, an MC-driven correction factor is used to mitigate this bias, which will be discussed in the upcoming section.

7.3 Energy Correction in Shower Reconstruction

The performance of the shower energy reconstruction is evaluated using simulation. Figure 7.8 illustrates the fractional bias of the reconstructed shower energy as a function of the true photon energy. A significant bias beyond -15% is observed across the full range, where the dominant contribution can be attributed to the Pandora reconstruction, as discussed in the previous section. Restoring the correct shower energy scale by rectifying this bias is crucial for accurately reconstructing the kinematics of neutral pions.

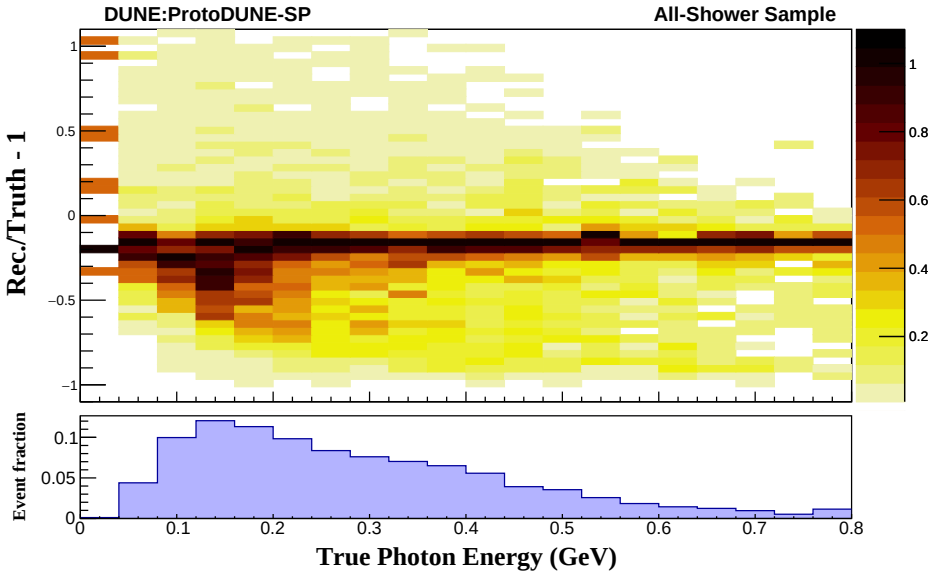

Figure 7.8: The reconstructed shower energy fractional bias (rec./truth - 1) as a function of true shower energy. The 2D histogram is column normalised, and the bottom panel shows the 1D distribution of true photon energy. The term "All Shower Sample" refers to all the reconstructed showers resulting from a 1 GeV/c pion beam.

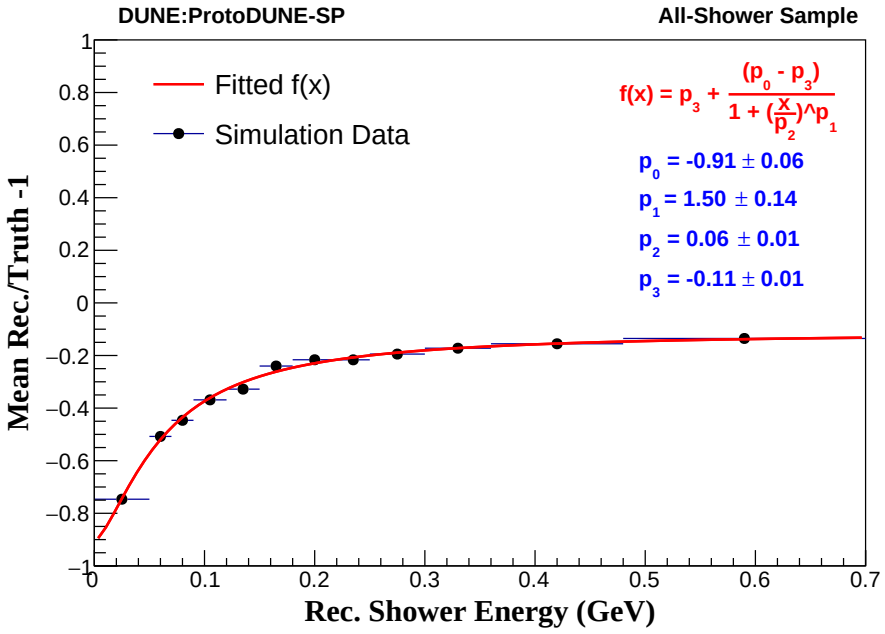

Figure 7.9: The energy-dependent shower energy correction function. This function takes raw shower energy as an input and returns a correction factor on a shower-by-shower basis. The functional form of the red curve is given in the inset with the fitted parameters.

The energy correction procedure involves the following steps:

- Bias quantification: The sample is binned in the reconstructed shower energy. Within each bin, a Cauchy-Lorentz (Eq. 6.1) function is fitted to the distribution of fractional bias. The fitted μ and its error serve as an estimate of the bias in that particular reconstructed shower energy bin (Appendix D).

- Extraction of energy-dependent correction: An energy-dependent correction function is fit to the estimated bias across the bins. This function takes the form of,

$$f(x) = p_3 + \frac{p_0 - p_3}{1 + (\frac{x}{p_2})^{p_1}}, \tag{7.4}$$

  where p_i are the fitted parameters. The function $f(x) = p_0$ when $x = 0$ and $f(x) = p_3$ when $x \to \infty$. For $p_0 - p_3 < 0$ and $p_1 > 0$, it represents a distribution that gradually increases before reaching a steady plateau.

- Application of correction: During event processing, the correction function is applied shower-by-shower in each event. With the reconstructed shower energy x as input, the function $f(x)$ is used to obtain the corrected shower energy, $x_{\text{corr}} = x/(1 + f)$.

The energy-dependent correction function is illustrated in Fig. 7.9. A near-constant bias is observed for shower energies exceeding approximately 150 MeV. The fitted correction function approximates -11%, i.e. $f \to p_3 = -0.11$, from below in the large x limit, indicating a systematic limitation of the current reconstruction algorithm. However, it can be seen that there are some overcorrections for the low-energy showers. This arises because the first few data points in Fig. 7.9 are not derived from a perfectly shaped Cauchy-Lorentz distribution, and further information can be found in Appendix D. After applying the correction factor, a bias of approximately 2% is achieved, as shown in Fig. 7.10, which is considered satisfactory for subsequent neutral pion reconstruction.

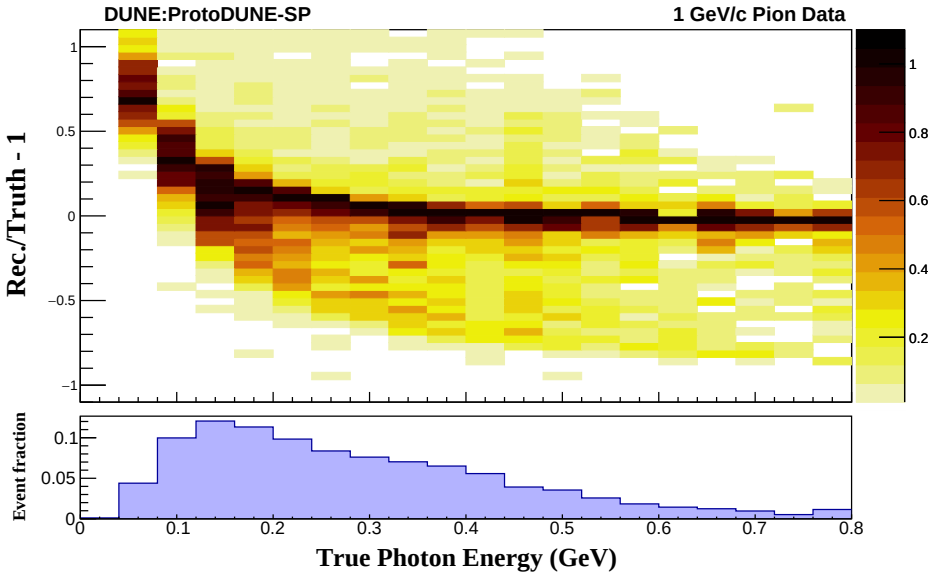

Figure 7.10: The reconstructed shower energy fractional bias as a function of true shower energy (column-normalized) after applying the energy correction (Eq. 7.4). There are some overcorrections for the low-energy showers due to the first few data points in Fig. 7.9 are not derived from a perfectly shaped Cauchy-Lorentz distribution (Appendix D).

7.4 Neutral Pion Reconstruction

The reconstruction of neutral pions relies on the combination of the first two most energetic selected shower vectors in each event. Two key metrics are employed to identify well-reconstructed neutral pions. The first metric is the reconstructed invariant mass of the diphoton system, while the second metric is the opening angle between the two reconstructed showers.

To select sufficiently reconstructed neutral pion candidates by combining two reconstructed showers, two sequential cuts are applied, with each cut individually described in the following.

Neutral Pion Cut 1: Require that the invariant mass of two showers falls within the neutral pion mass window.

Neutral Pion Cut 2: Require the opening angle between two showers to be consistent with a π^0 decay.

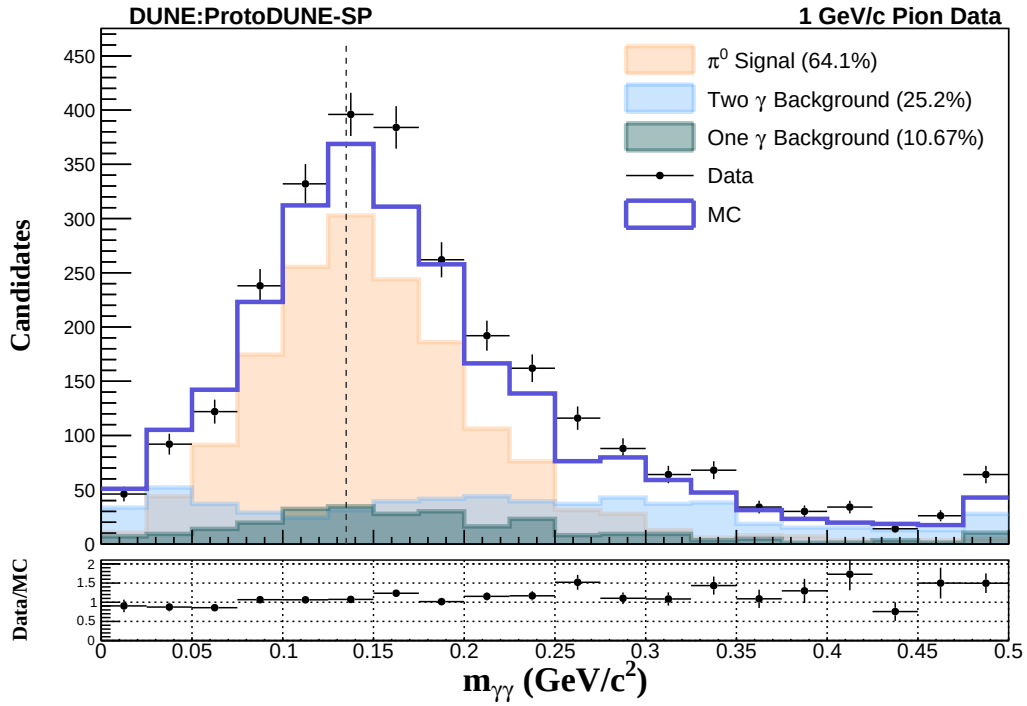

Figure 7.11: The invariant mass (Eq. 7.2) computed from the reconstructed photon showers after applying the Shower Cuts 1-4 and the energy corrections as described in Sec. 7.3. The true value of the π^0 particle's mass is shown in the dashed grey line at 0.135 GeV/c^2.

By examining the reconstructed invariant mass, it becomes possible to discern misidentified neutral pions, as they tend to deviate significantly from the expected value of the mass. The reconstructed invariant mass of the two leading photon showers in the selected sample following Sec. 6.2.2 (Table 6.4) is depicted in Fig. 7.11. The simulated truth-matched MC samples are categorized into three distinct groups. The first category (64%) represents correctly matched photon shower pairs, while the second category (25%) corresponds to shower pairs originating from different π^0 particles. The last category (11%) consists of reconstructed shower pairs with only one truth-matched photon. The contributions from the two gammas that are not from any π^0 are negligible.

The measured invariant mass of the diphoton system features uncertainties. This results in an expected peak centred on the true π^0 mass, with a width that reflects detector resolution and reconstruction effects. It can be seen that the correctly matched shower pairs show a good agreement with the expected π^0 mass, while continuous backgrounds arise from

Table 7.2: A summary of cumulative purity and efficiency for each Neutral Pion Cut. The efficiency is set to one by combining two showers selected with the Shower Cuts listed in Table 6.4.

Neutral Pion Cut	Purity	Efficiency
1. No cut (Shower Cuts 1-4)	64.1%	100%
2. $50 < m_{\gamma\gamma} < 250$ MeV/c^2 (Neutral Pion Cut 1)	74.8%	89.9%
3. $10^\circ < \theta_{\text{OA}} < 80^\circ$ (Neutral Pion Cut 2)	77.6%	85.5%

random combinations of two showers. Therefore, a cut can be applied to the reconstructed $m_{\gamma\gamma}$ to confine it within the range of $50 \leq m_{\gamma\gamma}(\text{MeV}/c^2) \leq 250$ (Neutral Pion Cut 1) for background suppression.

Additionally, the opening angle between the two showers is a valuable parameter that helps further clean up the π^0 sample. Because the decay photons from π^0 are distributed anisotropically due to Lorentz boost, while the combination of two random photons is isotropic, a distinctive peak emerges for well-matched photon pairs, while a uniform distribution characterizes randomly combined background photons. Therefore, it is possible to make a cut on the off-peak tails of the opening angle distribution. Figure 7.12 shows the distribution of the opening angle for the selected shower pair following Sec. 6.2.2 (Table 6.4). Among the correctly matched shower pairs, the opening angle peaks around 30°. However, the background is flat, reaching extreme values below 10° and beyond 80° (Neutral Pion Cut 2). A summary of the cuts for π^0 reconstruction can be found in Table 7.2. The selection reaches a purity of 78%.

Figure 7.13 depicts the selection efficiency of the π^0 particle and its daughter photons as a function of their true energy. Only photon shower pairs are considered here. Applying the cuts listed in Tables 6.4 and 7.2 removes a substantial portion of low-energy showers, resulting in a low efficiency of low-energy π^0. The π^0 selection efficiency is shown to increase with energies reaching approximately 25% at 1 GeV. The efficiencies of the two leading and subleading showers are considered only when a neutral pion is well-reconstructed from two showers. Consequently, if the subleading shower energy is

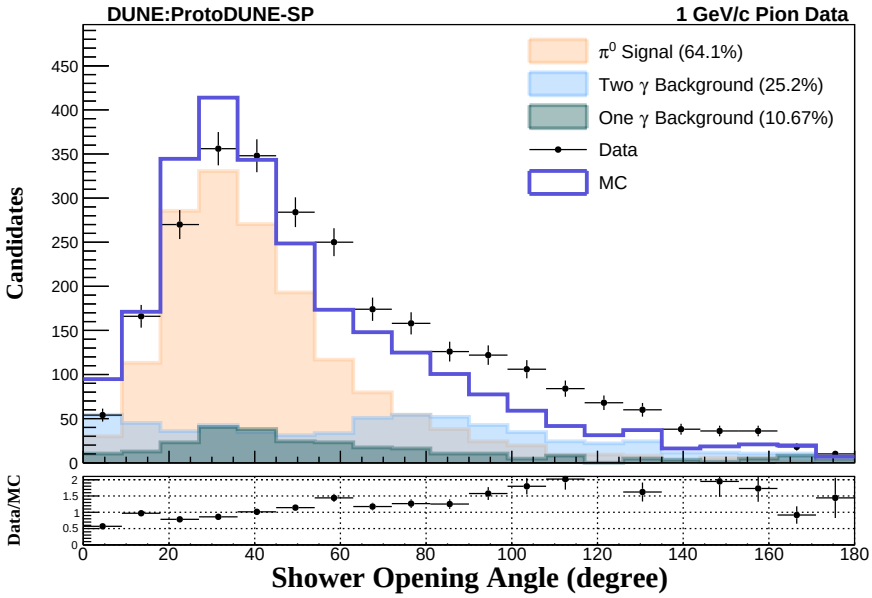

Figure 7.12: Distribution of the opening angle of the shower pair after applying the Shower Cuts 1-4. The majority of pairs have an opening angle of approximately 30°, while background events can have extreme opening angles.

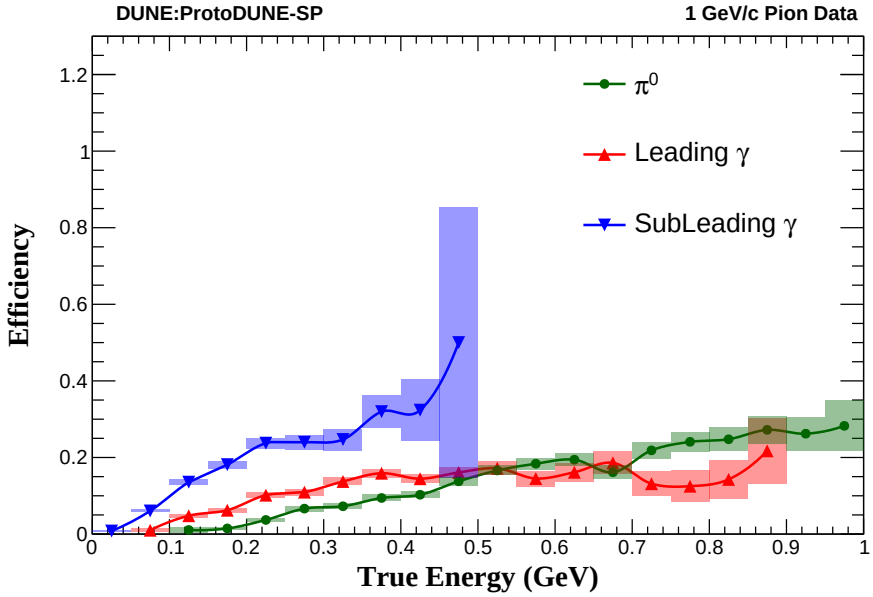

Figure 7.13: The selection efficiency of π^0 particles and their daughter photons after applying the Neutral Pion Cuts 1-2. The black, red, and blue curves represent the selection efficiency of π^0, leading shower, and subleading shower as a function of their corresponding true energy, respectively. Note that the maximum energy of the sub-leading shower is approximately 0.5 GeV. The colour band denotes the statistical errors.

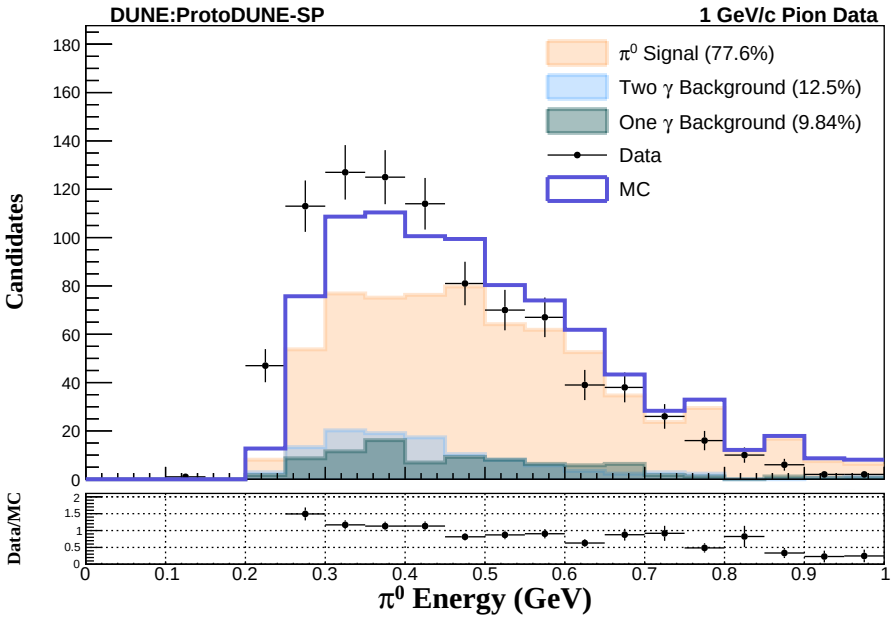

Figure 7.14: The reconstructed π^0 total energy after the Neutral Pion Cuts 1-2. The majority of π^0 particles have an energy of about 400 MeV. However, the Monte Carlo simulation only describes the data within 1+/-20% in most regions. These discrepancies will be addressed in Sec. 8.6.

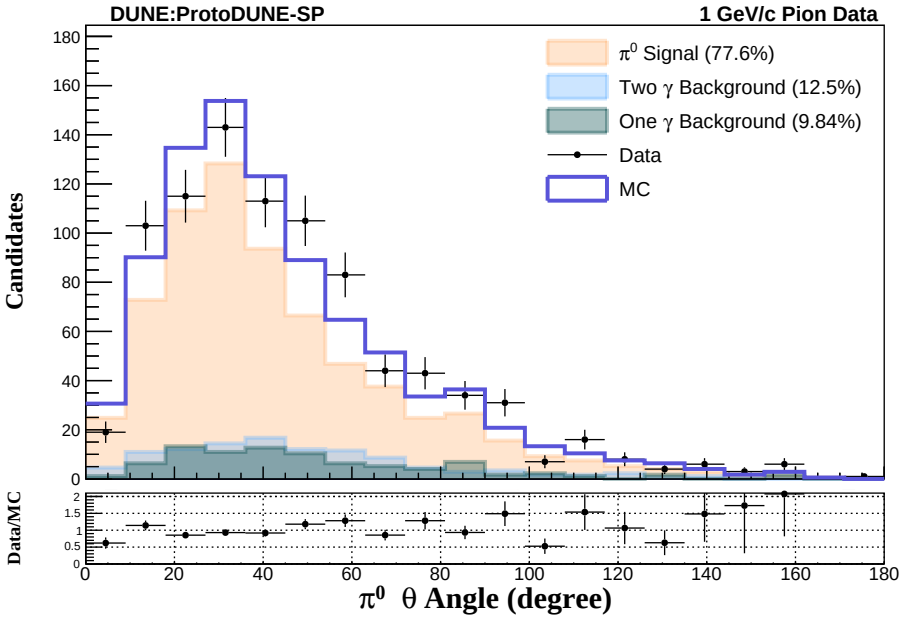

Figure 7.15: The reconstructed π^0 theta angle after the Neutral Pion Cuts 1-2, denoted as θ_{π^0} with respect to the beam direction. It has a peak near $30°$, accompanied by a long tail that extends up to $180°$.

sufficiently high (easier to reconstruct), the likelihood of having two reconstructed showers increases. Hence, the efficiency of the subleading shower reaches 50%, consistent with the result obtained in Fig. 6.25 (c). This also explains the lower efficiency of the leading shower - many events only have one reconstructed shower, resulting in no reconstructed neutral pion. These events are not included in the numerator for efficiency calculation.

The reconstructed neutral pion energy is shown in Fig. 7.14. The majority of π^0 particles have energies between 300 and 600 MeV. However, as discussed above, ProtoDUNE-SP is less efficient in reconstructing π^0 below 200 MeV. Additionally, π^0 are primarily produced at an angle of approximately 30° w.r.t the beam direction as shown in Fig. 7.15. The observed discrepancies between data and MC will be addressed in Sec. 8.6.

7.5 Improved Measurement by Kinematic Fitting

The kinematic fitting can improve the reconstructed particle's kinematics, as described in Chap. 5. Kinematic fitting is employed to enhance the π^0 energy reconstruction. Meanwhile, the measured π^0 angle (θ_{π^0}) remains unchanged after the fitting, as it cannot be determined from the fitted photon energies E_1 and E_2, along with the opening angle θ_{OA}.

Through iterative adjustments of particle energies and directions, the kinematic fitting aims to satisfy the physics constraints of the system, aligning measured quantities with their true values. Importantly, the covariance matrix plays a key role in governing parameter adjustments by accounting for measurement uncertainties. In the case of a π^0 decay, only the correctly matched shower pairs are used to calculate the covariance matrix defined in Eq. 5.9. Due to limited statistics, obtaining a differential dependence is not practical. Therefore, the E-independent matrix is employed, which captures the first-order accuracy. The covariance matrix used in the π^0 kinematic fitting can be found in Appendix F. The constraint χ^2 takes the form (Eq. 5.8),

$$\chi^2(E_1, E_2, \theta_{\mathrm{OA}}) = (\alpha - \alpha_0)V^{-1}(\alpha - \alpha_0) + \lambda \left[2E_1E_2(1 - \cos\theta_{\mathrm{OA}}) - m_{\pi^0}^2\right], \quad (7.5)$$

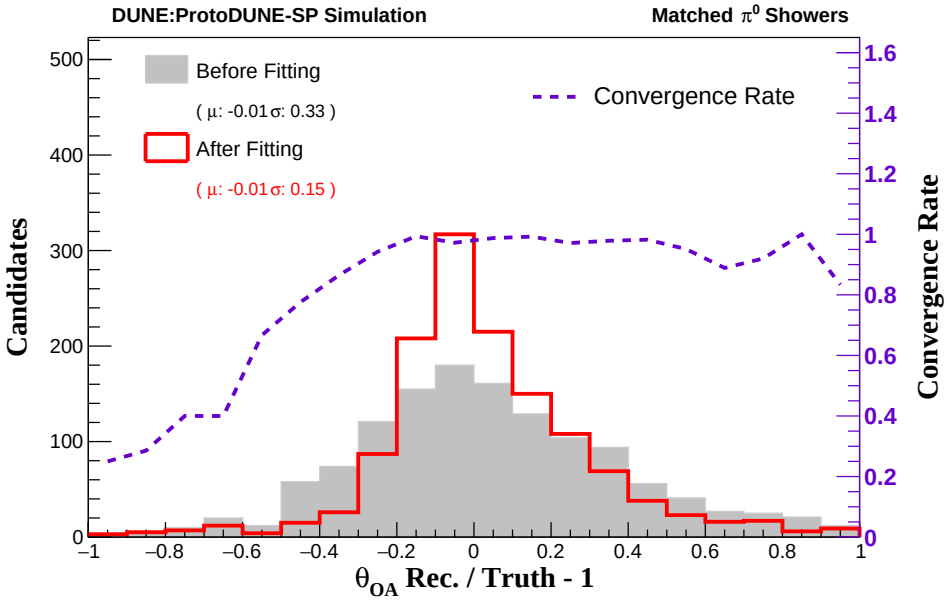

Figure 7.16: The fractional bias of opening angle θ_{OA} before (grey) and after (red) kinematic fitting. The statistical parameters are shown in the legend for both distributions. The dashed violet line represents the convergence rate of the fitting in each bin.

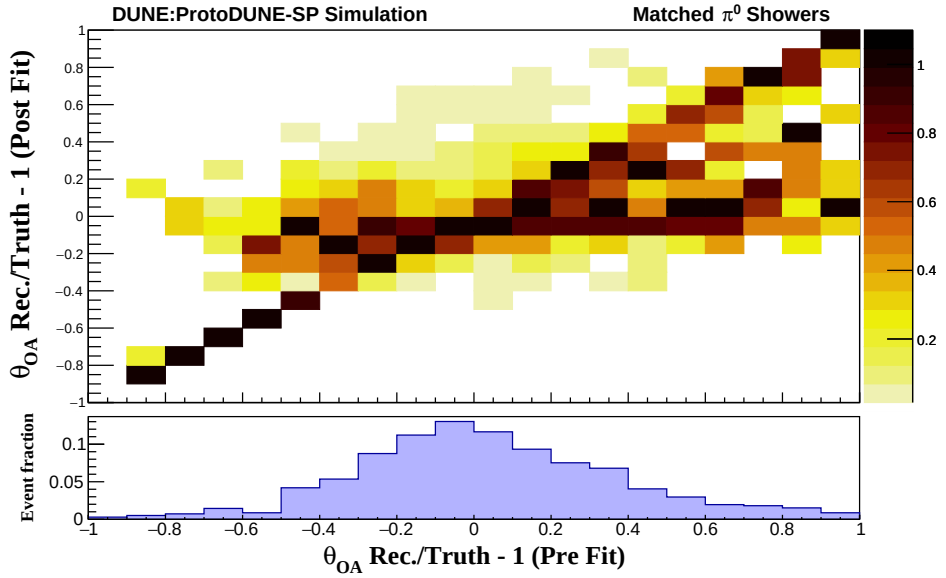

Figure 7.17: The column normalised distribution of the fractional bias of the opening angle θ_{OA}, post-fit versus pre-fit. The bottom panel is the 1D distribution of the pre-fit distribution. The post-fit θ_{OA} are considered as the updated measurements.

where the vector α contains three fitting parameters, E_1, E_2 and θ_{OA}, while α_0 contains their measured values. The second term is the constraining invariant mass equation (Eq. 7.2). Through the variation of the fitting parameters, while considering the inherent measurement uncertainties represented by the covariance matrix, the calculated invariant mass is optimized to closely match the true mass of the neutral pion. After kinematic fitting, the fitting parameters are taken as the new measurement.

As discussed in Sec. 7.3, both the leading and subleading shower energies have been adjusted to closely match their true values. Consequently, the improvement in these two variables through kinematic fitting becomes less apparent (Fig. G.1 in Appendix G). However, the opening angle between the two showers remains uncorrected and unconstrained. Therefore, the kinematic fitting is expected to have its most pronounced effect in enhancing the opening angle, as opposed to the photon shower energies. The angular resolution of the opening angle before and after the fitting process is presented in Fig. 7.16 and Fig. 7.17. If the fitting does not converge, the measured quantities will remain at their original values. The red histogram in Fig. 7.16 demonstrates that the kinematic fitting improves the resolution for the opening angles. Fig. 7.17 reveals that the fitting process is successful for the majority of the events. However, when the measured θ_{OA} is significantly smaller than its true value, leading to a large negative bias, the fitting process struggles to find optimized values. In cases where the bias exceeds - 40%, the fitting process does not yield noticeable improvements due to its low convergence rate.

It is expected that the fitted opening angle will subsequently enhance the energy resolution of the neutral pions. Given the challenges in accurately reconstructing the energy of the sub-leading photon showers and the kinematic fitting process proves to be particularly effective in enhancing the opening angle between the two photons, the energy of the π^0 particle is calculated as,

$$E_{\pi^0} = E_1 + \frac{m_{\pi^0}^2}{2E_1(1 - \cos\theta_{\text{OA}})}, \tag{7.6}$$

where E_1 and θ_{OA} are the energy of the leading photon and the opening angle, respectively,

and m_{π^0} is the mass of the neutral pion. In Appendix E, three different methods for calculating π^0 energy before kinematic fitting are compared. The more complex π^0 energy definition (Eq. E.1) used in the MicroBooNE experiment [93] is not found to perform well in ProtoDUNE-SP. Instead, the method using Eq. 7.6 is observed to yield better results than the direct summation of two shower energies.

As shown in Fig. 7.18, the energy resolution of the reconstructed π^0 improves significantly after applying the kinematic fitting, from 18% to 12%. The fitting convergence rate remains nearly at one within the bias range of -0.3 to 0.3. The kinematic fitting is found to be more effective when the π^0 energy is overestimated in reconstruction, as indicated in Fig. 7.19. Further improvements should be considered in the future to address cases where the π^0 energy is underestimated. In summary, ProtoDUNE-SP achieves a 12% π^0 energy resolution for π^0 energies ranging from 0.3 to 1 GeV.

Contrasting with other neutrino tracking experiments like MINERνA [94] and MicroBooNE [44], where π^0 particles are mainly generated through neutrino CC interactions, ProtoDUNE-SP focuses on π^0 particles originating from pion charge exchange interactions. Although the π^0 production mechanism should not affect the reconstruction performance, different experiments do have different configurations in the Pandora reconstruction [60]. MINERνA has reported a π^0 energy resolution of 20% [74], and the π^0 energy range is expected to be similar to this study. MicroBooNE, which uses the same detection technology as ProtoDUNE-SP, reports a 10% π^0 energy resolution [93]. However, the reported resolution value is extracted by fitting only the mass peak region, and their π^0 energy is expected to be lower due to a 0.8 GeV neutrino beam.

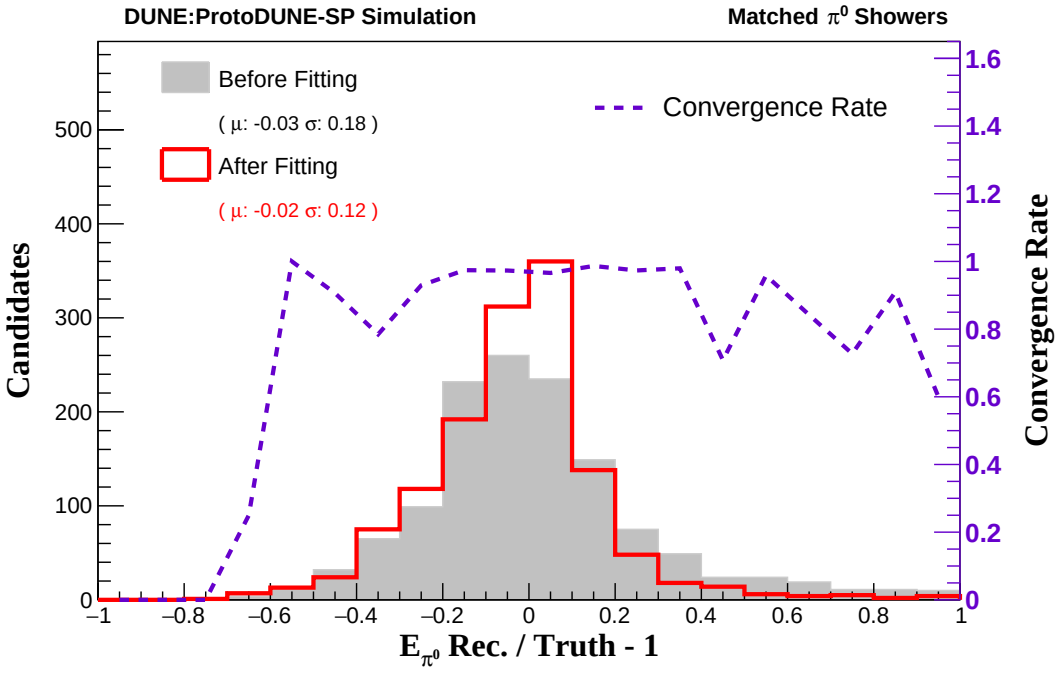

Figure 7.18: The total energy of the π^0 particle before and after the kinematic fitting. The energy resolution is reduced from 18% to 12%. The dashed violet line represents the convergence rate of the fitting in each bin.

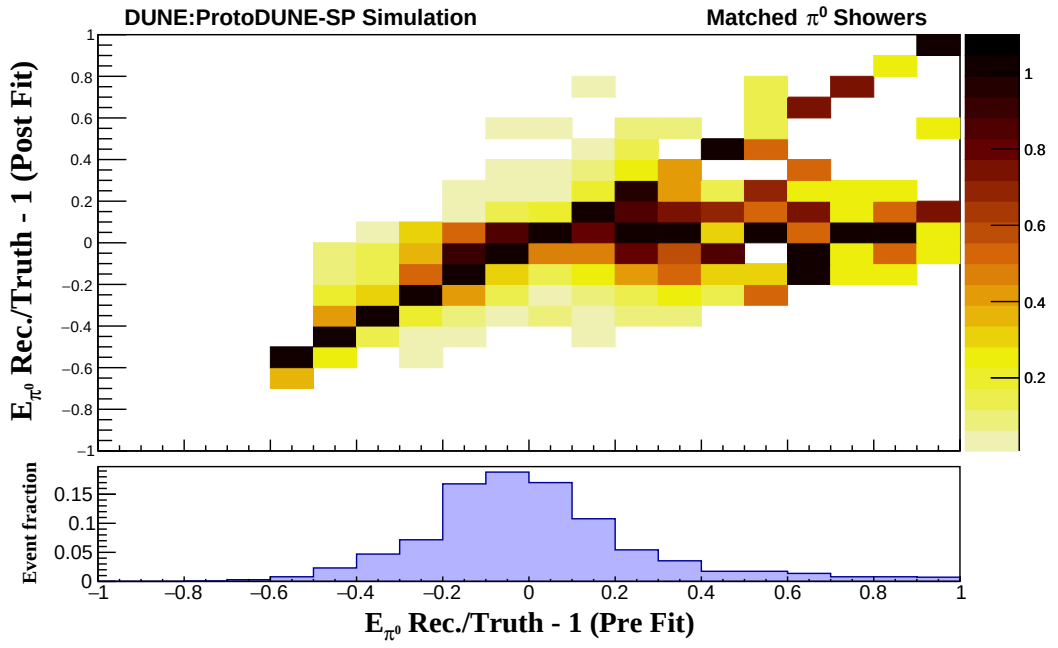

Figure 7.19: The column-normalized absolute difference of π^0 energy post-fit versus before pre-fit results. Kinematic fitting tends to have a larger impact on π^0 with an overestimated energy. The post-fit π^0 energy is considered as the updated measurement.

8 | Measurement of the Pion Charge Exchange Cross-section

Building upon the event selections and analysis techniques established in previous chapters, this chapter presents the main analysis results of this thesis, focusing on the pion charge exchange (CEX) differential cross-section with π^0 kinematics. The structure of this chapter is outlined as follows. Section 8.1 provides the definition of the true signal used in the analysis. It establishes the basis for the subsequent event selection and cross-section measurement. Section 8.2 summarises the pion CEX event topology selection with the corresponding statistics and efficiency. Section 8.3 presents the analysis strategies employed throughout the study, providing an overview of the methodologies and approaches utilised to achieve the cross-section measurement. Section 8.4 details the procedures used to determine the beam energy, which is essential for the cross-section calculations. Section 8.5 explains the reweighting method on MC samples to mitigate discrepancies between the data and MC simulations. Section 8.6 describes a data-driven method used to extract background tuning factors in the signal region. Section 8.7 presents the measured incident and interacting fluxes after MC reweighting and background tuning. Section 8.8 demonstrates the unfolding procedure employed to correct for detector effects and reconstruction inefficiency in the measured distributions. Section 8.9 discusses the in-depth analysis of various sources of uncertainties and their contributions. Finally, Section 8.10 presents the cross-section results, including the total errors.

8.1 Signal Definition

This analysis conducted a selection of inclusive pion argon CEX events based on the identification of the final state particle type. This analysis reports two measurements, the integrated cross-section measurement $\sigma(E)$ and the differential cross-section measurement, $\mathrm{d}\sigma/\mathrm{d}T_{\pi^0}$ and $\mathrm{d}\sigma/\mathrm{d}\theta_{\pi^0}$. In both cases, the signal definition is,

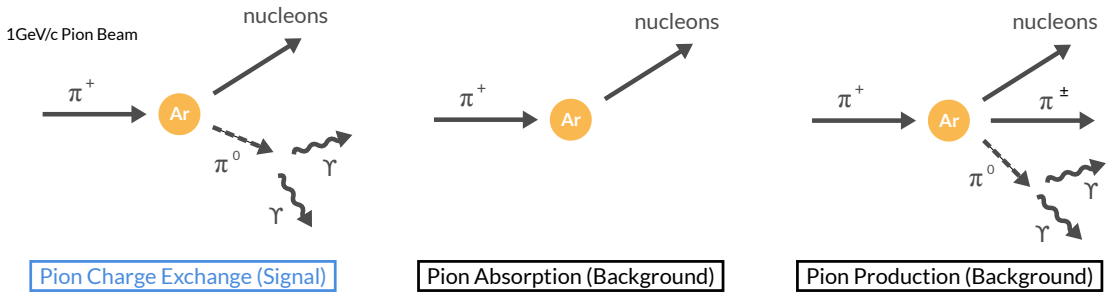

Figure 8.1: The signal and background definition in this analysis. A charged pion detection threshold above 100 MeV/c is applied. The signal is defined as an inclusive pion CEX event with one π^0 and no charged pions above 100 MeV/c present in the final state.

1. The incoming beam particle is π^+,
2. There is only one π^0 in the final state,
3. Does not contain charged pions with momentum above 100 MeV/c,
4. No requirement on the number of final state nucleons,

where there is no momentum phase space limit applies to π^0 due to the ability to reconstruct it from its decay products, which consist of two photons. However, charged pions with momenta below the 100 MeV/c detection threshold remain undetectable and cannot be effectively reconstructed, as explained in Sec. 6.3. Hence, one of the signal definitions for the CEX process relies on the condition that no charged pions have momenta exceeding this specified detection threshold in the final state. Also, the π^0 is reconstructed using the first two energetic showers, resulting in only one reconstructed π^0 per event.

The potential sources of event background, as depicted in Fig. 8.1, include pion absorption and pion production. According to the results of the MC study, the rate of misidentifying true events of pion absorption as reconstructed pion charge exchange events remains below 1%, thus rendering this background negligible for subsequent analysis. However, pion production events could be a substantial source of background in this study. For example, situations where charged pions remain unreconstructed by Pandora or cases involving multiple neutral pions in the final state, with only one of them successfully reconstructed, can lead to events being falsely identified as pion CEX candidates.

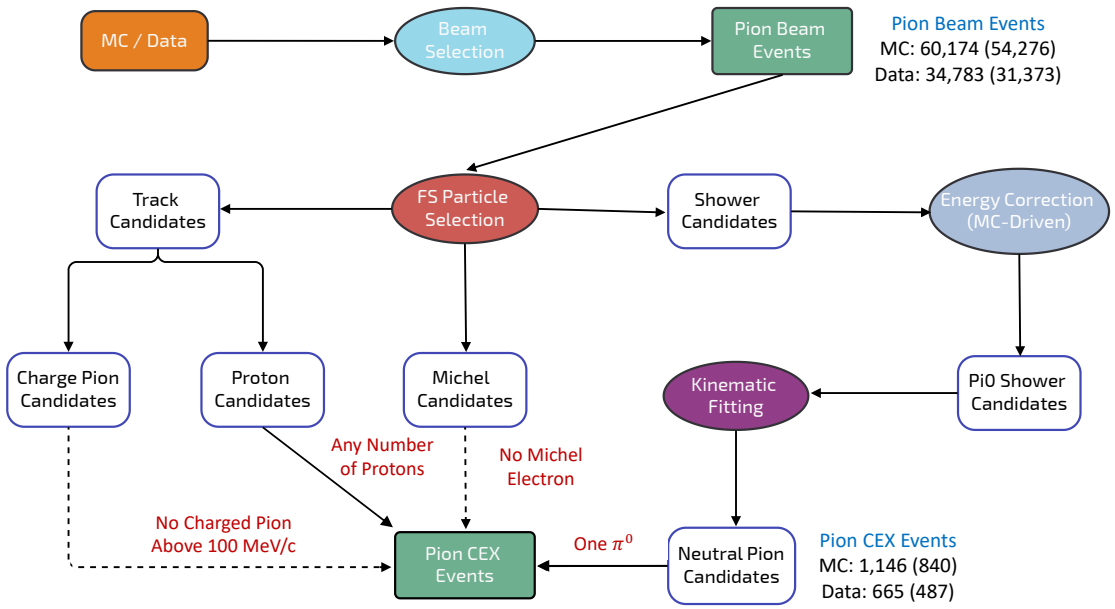

Figure 8.2: Selection of the pion charge exchange event topology based on the criteria outlined in Chap. 6. The figure presents statistics for the chosen pion beam and pion CEX samples in both MC simulations and data, with background-subtracted event numbers indicated in parentheses based on MC simulation. The data comprises 34,783 pion beams and 667 charge exchange candidates.

8.2 Pion Charge Exchange Event Selection

All available ProtoDUNE-SP 1 GeV/c beam events are used in this analysis. Figure 8.2 provides a flowchart of the pion charge exchange event selection. The dedicated beam pion selection criteria, described in Sec. 6.1, are used to select the pion beam sample. For each pion beam event, daughter particles are categorized into different particle species using the selections developed in Sec. 6.2. The final state particles are separated into three groups: track candidates, shower candidates, and Michel electron candidates. The track candidates are further differentiated into charged pion and proton candidates. For selected shower candidates, a shower energy correction is applied (Sec. 7.3), followed by kinematic fitting improvement (Sec. 7.5). Neutral pion candidates are selected by combining the two leading shower candidates with the π^0 selection criteria in Sec. 7.4. The final selection of pion charge exchange events required the event to be a pion beam event and have only one neutral pion with no charged pion and Michel electron present.

Table 8.1: A summary the cumulative purity and efficiency of each selection of the pion charge exchange events. The efficiency is defined to be one after the beamline PID selection. The beam cuts are defined in Sec. 6.1 (Table 6.1), and the selection criteria for daughter particles are described in Sec. 6.2 (Tables 6.3 and 6.4) and 7.4 (Table 7.2).

Selection	Purity (Cumulative)	Efficiency (Cumulative)
Beam Pion Triggers	0.13	1
Pandora Track	0.12	0.81
Beam Quality Cuts	0.12	0.58
EndZ < 220 cm	0.15	0.56
Michel Score < 0.55	0.15	0.56
Proton χ^2/dof > 80	0.14	0.51
Beam Scraper Cuts	0.15	0.41
Two π^0 Showers	0.57	0.057
No π^+	0.63	0.050
No Michel e	0.65	0.048
One π^0	0.73	0.039

In terms of statistics, 34,783 pion beam events are selected with a purity of 90%. However, due to the low reconstruction efficiency in showers, only 665 pion CEX events are selected. The cumulative purity and efficiency of each selection are summarized in Table 8.1. The first block shows the beam selections to select the pion beam, with a minimal impact on the purity of the CEX event. The bottom block shows the event topology cuts, resulting in a final purity of 73.3%. It is notable that there is a significant efficiency drop when selecting two well-reconstructed showers. Consequently, only 4% of all pion charge exchange events are selected after the event topology selections.

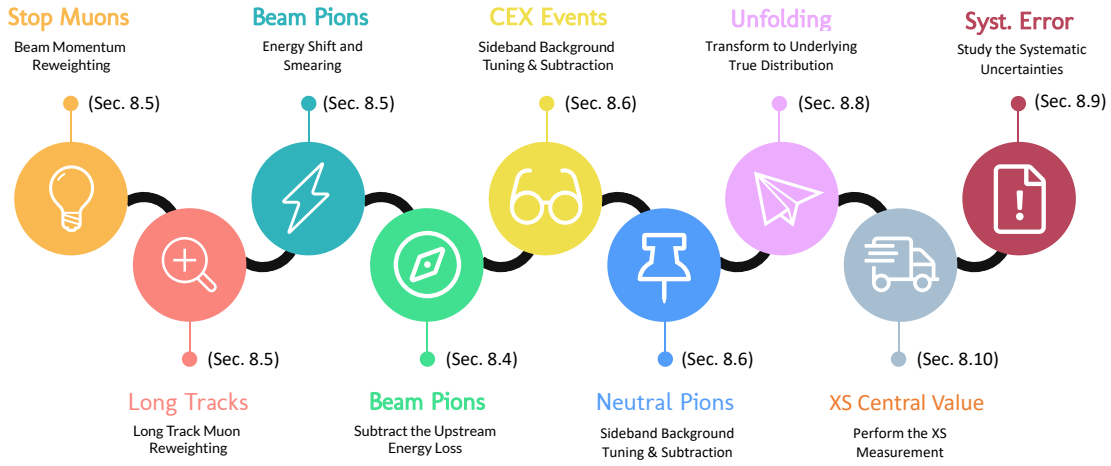

Figure 8.3: The roadmap leading to the final cross-section results. Two control samples are used to reweight the MC and the background in the signal channel is tuned by applying background scaling obtained from sideband channels before the unfolding process. Finally, the leading systematic uncertainties are evaluated. Each step of this graph will be discussed in this chapter.

8.3 Analysis Strategy

The use of control samples and sideband channels is essential for ensuring the accuracy and reliability of measured results. Control samples consist of specific subsets of the data where the physics processes are well understood and serve as benchmarks for comparison. By comparing measurements in control samples with simulations, the accuracy of the simulation can be improved through an event reweighting approach. On the other hand, sideband samples are adjacent regions in the data that do not contain the signal. These sideband regions help in understanding and modelling background contributions that might resemble the signal. Fine-tuning background estimates using sideband regions and subtracting them from the signal region ensures the accuracy of the measured signal.

Figure 8.3 illustrates a comprehensive roadmap leading to the final cross-section measurement. This roadmap incorporates several crucial procedures. Firstly, in Sec. 8.5, the control samples of stop muon events and long track events are employed to improve the agreement between the data and the MC in the measured beam energy, rectifying any mismodeling in the simulation. Additionally, a data-driven energy shift and smearing are

applied to the measured momentum from the spectrometer to enhance this agreement further. In Sec. 8.4, the estimation of upstream energy loss is obtained through detailed MC studies and is subsequently considered from the beam energy measurement. Furthermore, a data-driven background tuning process is executed in Sec. 8.6, utilizing the sideband channels before performing background subtraction. To account for detection acceptance and reconstruction inefficiency, the measured beam energy is unfolded to its true energy in Sec. 8.8, enabling the utilization of unfolded data for the cross-section measurement. Finally, in Sec. 8.9, a thorough analysis of various systematic sources is conducted to complete the measurement.

There are two types of cross-section analysis conducted in this study. The first one is the determination of the pion CEX integrated cross-section, which is studied as a function of the beam energy using the energy slicing method. The second type of analysis involves investigating the pion CEX differential cross-section with π^0 kinematics, specifically focusing on a particular beam interacting energy range. The method of cross section calculation has been introduced in Sec. 3.6.2.

8.4 Pion Beam Energy Measurement

The beam energy measurement at the entry point and interaction point inside the TPC is a critical aspect of this analysis. As outlined in Sec. 3.6.2, the beam momentum is initially determined using the beamline spectrometer prior to entering the TPC. Subsequently, the beam traverses various additional materials, including Cherenkov counters and the beam plug, between the spectrometer and the TPC. After removing the beam scraper events in the beam selections detailed in Sec. 6.1, there is an expected upstream energy loss of up to a few MeV and the estimation of upstream energy loss relies on simulation results.

Figure 8.4 shows the relationship between upstream energy loss and the measured kinetic energy at the beam spectrometer from MC simulation. Each data point in the plot corresponds to the mean value obtained from fitting a Gaussian distribution to the upstream energy loss within a 50 MeV interval of the beam energy. The colour band represents

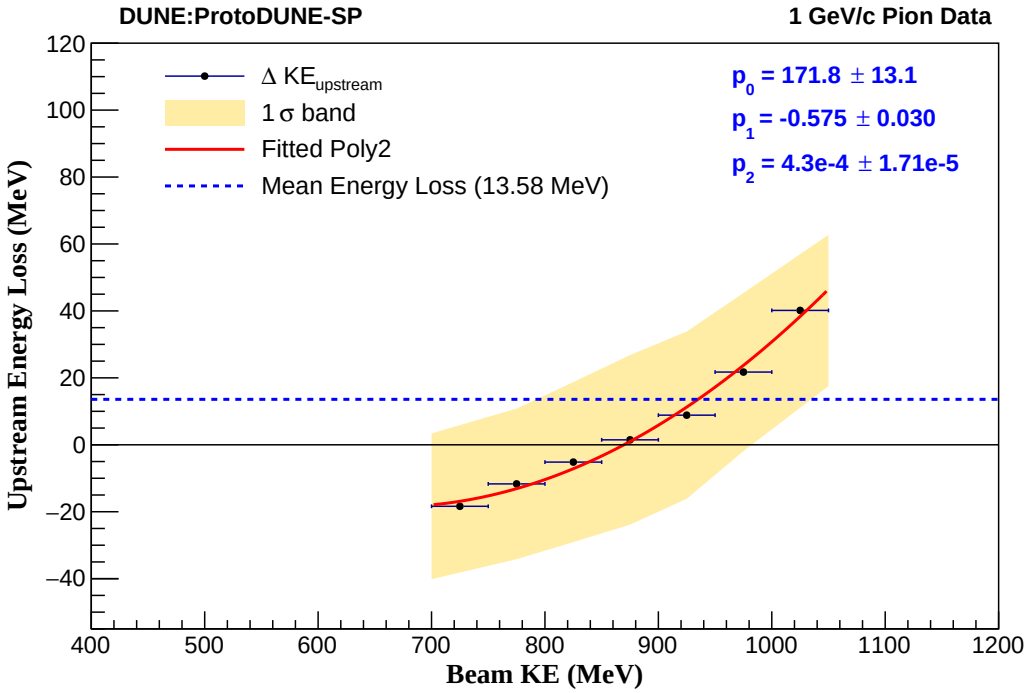

Figure 8.4: The upstream energy loss distribution of selected beam events, following a second-order polynomial function, with the fitted parameters denoted in blue. The upstream energy loss is estimated in MC simulation as the difference between the measured beam energy at the beamline spectrometer and the true beam energy when it enters the TPC. The plot illustrates the dependence of energy loss on beam energy.

one fitted sigma value. Notably, the upstream energy loss varies depending on the beam energy, and a second-order polynomial fit is employed to describe the distribution. Subtracting the estimated energy loss from the measured kinetic energy obtained from the beamline instrumentation enables the determination of the particle's front-face energy, E_{Ini} as,

$$E_{\text{Ini}} = E_{\text{beamline}} - \Delta E_{\text{Eloss}}, \tag{8.1}$$

where E_{beamline} and ΔE_{Eloss} are the beam energy measured at the beam spectrometer and the estimated upstream energy loss, respectively. E_{Ini} represents the beam energy immediately prior to entering the TPC.

Charged particles lose energy by ionising electrons inside the TPC. The beam energy at the interaction point can be obtained in two ways. The first method involves a range-based approach, where the reconstructed track length is measured. By knowing the energy loss per unit distance for the beam particle and the initial energy upon entering the TPC, the interaction energy can be determined using the following equation,

$$E_{\text{Int}} = E_{\text{Ini}} - \int \frac{\mathrm{d}E}{\mathrm{d}x} dx, \tag{8.2}$$

where $\mathrm{d}E/\mathrm{d}x$ is obtained from the Bethe-Bloch formula [50], and E_{Int} corresponds to the beam energy at the interaction point.

The second method uses calorimetry information directly. The energy required to ionize one electron in argon is known, and by measuring the charged deposit in the wire planes (in terms of the number of electrons) as explained in Sec. 3.3.4, and applying calibration for detector effects such as recombination and attenuation, the energy deposit inside the TPC can be determined. The interaction energy is then calculated as,

$$E_{\text{Int}} = E_{\text{Ini}} - \sum \Delta E_{\text{calo}}, \tag{8.3}$$

where ΔE_{calo} represents the energy deposit at each wire, and the summation is performed over all active wires. In this analysis, the determination of the beam interacting energy is performed using the range-based method.

8.5 Control Samples

Stopping muons in a LArTPC can serve as a control sample due to their predictable behaviour and characteristics. As muons come to a stop within the detector, their energy can be accurately estimated using the Bethe-Bloch formula. By comparing the measured muon energy distribution between data and simulation, the accuracy of the simulation can be improved.

Therefore, a sample of beam muons that have stopped inside the detector is used as a standard candle to address the discrepancies between MC simulations and experimental data in the measured beam energy distribution [95]. The standard beam selections have been applied as detailed in Sec. 6.1, except for the reversal of the muon-related cuts to enhance the beam muon components. The expected tracking range of a beam muon is determined using the estimated beam energy upon entry into the detector and muon energy loss information in LArTPC. If a beam muon comes to a stop inside the detector, the calculated tracking range is expected to match the reconstructed track length closely. As such, the ratio of the reconstructed track length to the calculated range is evaluated, and a ratio greater than 0.9 classifies the candidate muon as a stopped beam muon.

With these selected stopping muons, the front-face energy can be extrapolated from their reconstructed track length by employing the Bethe-Bloch formula. The front-face energy distribution of the selected stopping muon sample is shown in Fig. 8.5. The discrepancy between data and MC suggests potential mismodeling in the simulation, stemming from various sources: differences in the simulated true momentum distributions and inaccuracies in upstream energy loss and energy resolution estimations. To address the first source, each event is assigned a weight that takes the form [95],

$$w = \frac{e^{-\frac{(p-\mu_{\text{fit}})^2}{2\sigma_{\text{fit}}^2}}}{e^{-\frac{(p-\mu_{\text{true}})^2}{2\sigma_{\text{true}}^2}}}, \tag{8.4}$$

where p is the true beam momentum and the μ_{true} and σ_{true} are the fitted Gaussian parameters of the true beam momentum distribution and μ_{fit} and σ_{fit} are the fitted parameters.

The fitted parameters, μ_{fit} and σ_{fit} in Eq. 8.4, are adjusted and optimized through a χ^2 fit, aiming to achieve the best agreement between the data and MC distributions of the front-face kinetic energy of stopping muons (Fig. 8.5). Despite the absence of true momentum distribution in the real data, the calculated front-face kinetic energy of stopping muons from track length is used as a representation of true momentum. Consequently, the weight factor (depends on p) transforms the Gaussian distribution of the default MC

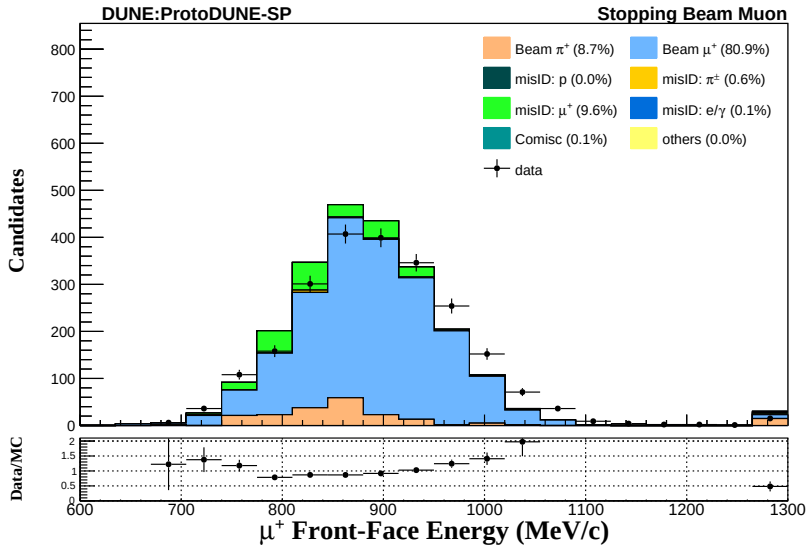

Figure 8.5: The front-face energy distribution of the selected stopping muons, with a purity of 81%. The sample follows the same beam selection defined in Chap. 6, but all muon-related cuts have been reversed. The front-face energy is calculated from the reconstructed track length of these muons, assuming they are stopped inside the detector.

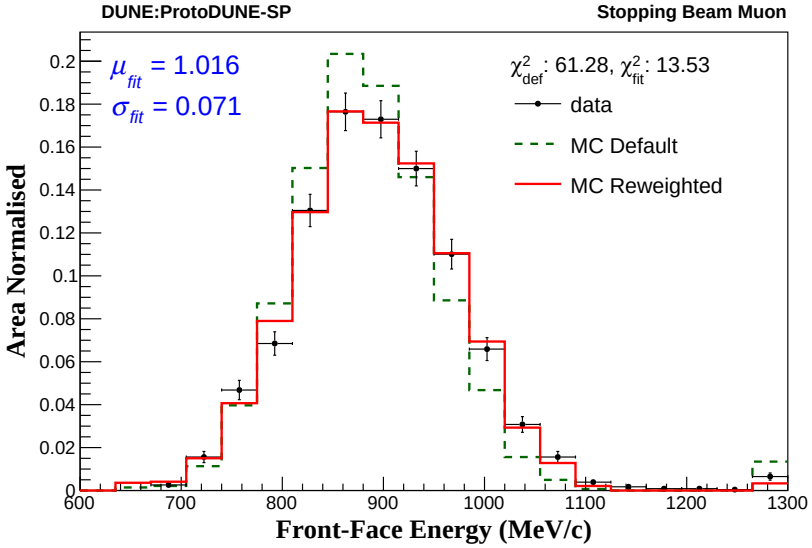

Figure 8.6: The front-face energy distribution of the selected stopping muons before and after the fit. The default MC is shown in dashed green (same as in Fig. 8.5), while the red histogram represents the fitted distribution. On an event-by-event basis, a weight (Eq. 8.4) is applied to the default MC to improve the agreement with the data in the stopping muon front-face energy distribution. The fitted parameters μ_{fit} and σ_{fit} are allowed to vary. After reweighting the MC, the true momentum of both MC and data should be similar.

true beam momentum to a fitted variant, which is taken as a closer representation of the actual data. This then enables a reweighting of the MC true momentum to align it with the data distribution, thereby reducing the discrepancies.

Following the beam momentum reweighting, the underlying true momentum distribution should be similar for both data and MC. Figure 8.6 shows the front-face kinetic energy distribution of stopping muons before and after applying the event weight. Reweighting leads to a better simulation of the true beam momentum and hence improves the agreement with the measured front-face energy.

However, the reweighted beam momentum measured at the beamline instrumentation could still differ between data and MC due to inaccurate upstream energy loss and energy resolution estimation. To address this, the momentum distributions of reweighted MC and data are fitted with Gaussian functions. The fitted mean and sigma values are used to quantify the difference in upstream energy loss and energy resolution between data and MC. Subsequently, the MC distribution is further shifted and smeared by applying an additional random Gaussian function with a mean value of $\mu = \mu_{\text{data}} - \mu_{\text{MC}} = -8.54$ MeV and a sigma value of $\sigma = \sqrt{\sigma^2_{\text{data}} - \sigma^2_{\text{MC}}} = 15.19$ MeV. These event weights, along with the energy shift and smearing, are then applied to the signal pion beam events, serving the purpose of beam momentum reweighting.

An additional control sample is used for the calibration of long beam tracks [95], as depicted in Fig. 8.7. Any tracks with reconstructed lengths greater than 150 cm are selected after the beam quality cuts as described in Sec. 6.1. The grounded electron diverter issue causes many broken tracks at the boundary of two APAs ($\sim$ 220cm), which is not well simulated. As a result, tracks extending beyond 220 cm are grouped into a single bin. The observable excess in the data underscores the necessity for an increment in the beam muon contribution in the MC simulation. To accomplish this, the muon component in the simulation is allowed to vary to minimize the χ^2 between data and MC distributions of the reconstructed track length (Fig. 8.7). The result reveals that the muon component requires a scale-up of 53% for long muon tracks exceeding 150 cm in length.

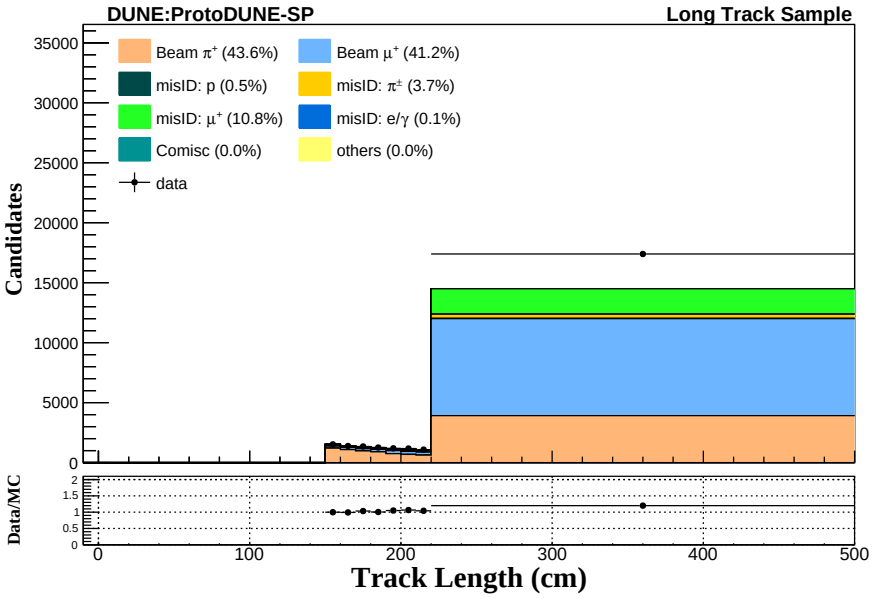

Figure 8.7: The reconstructed track length of the selected long track sample with track lengths longer than 150 cm. This sample follows the same beam selection as defined in Chap. 6 up to the Beam Cut 3, with the remaining cuts removed. Longer tracks ($>$ 220 cm) are grouped into one bin.

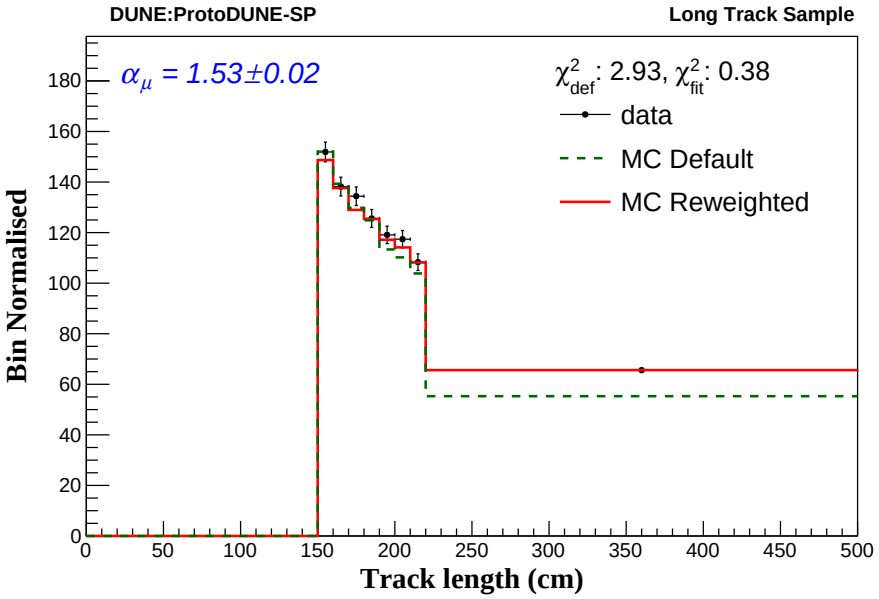

Figure 8.8: The bin normalised track length of long beam tracks before and after fitting, with the fitted scaling factor displayed in blue. The default MC is consistent with that shown in Fig. 8.7. The muon component is allowed to vary, improving the agreement between data and MC through a χ^2 fit. A scale-up of 53% is applied to muon tracks exceeding 150 cm in length.

8.6 Sideband Background Tuning

The background events can be effectively constrained through the selection of various sideband channels. As discussed in Sec. 8.1, the main source of background in the CEX events originates from pion production. This background is primarily a result of situations where charged pions are not reconstructed or when multiple π^0 particles are produced in the final state. In Figs. 8.9 and 8.10, the beam interacting energy distributions of the pion production channels without π^0 (Zero-π^0 Sideband) and with multiple (≥ 1) π^0 (Multi-π^0 Sideband) are shown, respectively. The contribution from the absorption channel is neglected in the tuning process (less than 1%). To minimize the χ^2 between data and the total MC sample, a simultaneous fit is performed for the two sideband channels. In this fit, the dominant background in each channel is adjusted while keeping the signal contribution unchanged. The goal of the fit is to achieve the best agreement between data and MC in terms of the beam pions interacting energy distribution. Due to the limited statistics, it is not possible to extract a scaling factor as a function of energy at each bin. Instead, the beam energy is divided into two regions: one below 700 MeV and the other above 700 MeV for each sideband channel, resulting in a total of four parameters, as shown in Fig. 8.11. The choice of the 700 MeV energy division is determined through various tests to obtain the lowest post-fit χ^2 value. The scaling factors obtained from fitting indicate a pattern where there is a need for scaling up the simulation before 700 MeV and scaling down afterwards. In particular, GEANT4 underestimates pion production rates involving multiple (≥ 1) π^0 particles at lower pion kinetic energies while overestimating them for pions with kinetic energies above 700 MeV. The prediction on pion production with no π^0 is quite accurate.

Figure 8.12 shows the weighted beam interacting energy in the selected CEX signal sample, along with the calculated χ^2 values before and after the fitting process. It can be seen that the agreement between the data and the MC simulation is improved after incorporating the background scaling factors obtained from the sideband fitting. This weighted histogram represents the interaction flux of pion CEX events at different pion kinetic en-

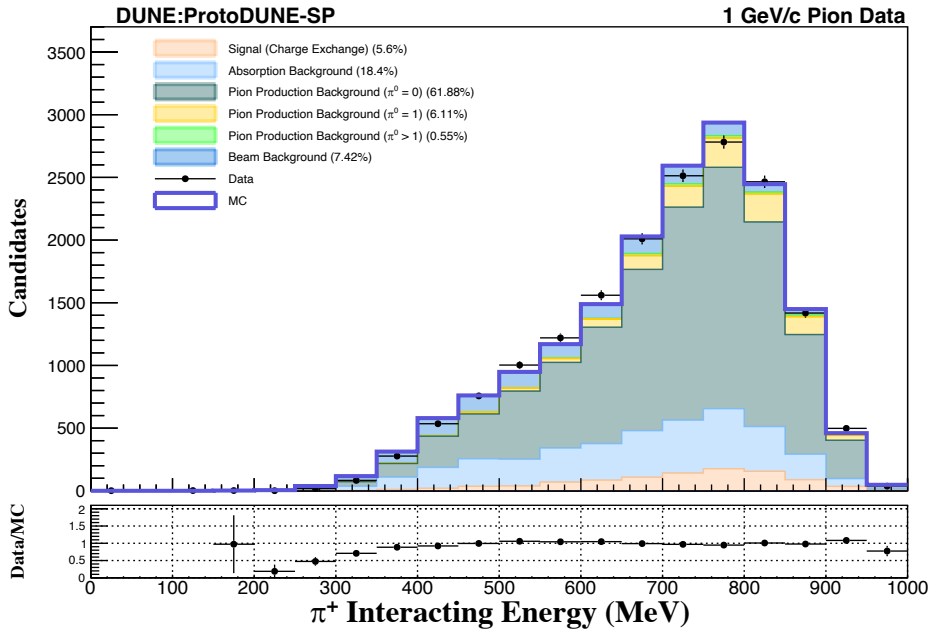

Figure 8.9: The pion interacting energy of selected pion production sideband channel with zero π^0 in the final state. This sideband is selected by requiring no reconstructed π^0 and at least one charged pion in the final state, modifying the topology selection shown in Fig. 8.2. The MC distribution is decomposed into different event topologies.

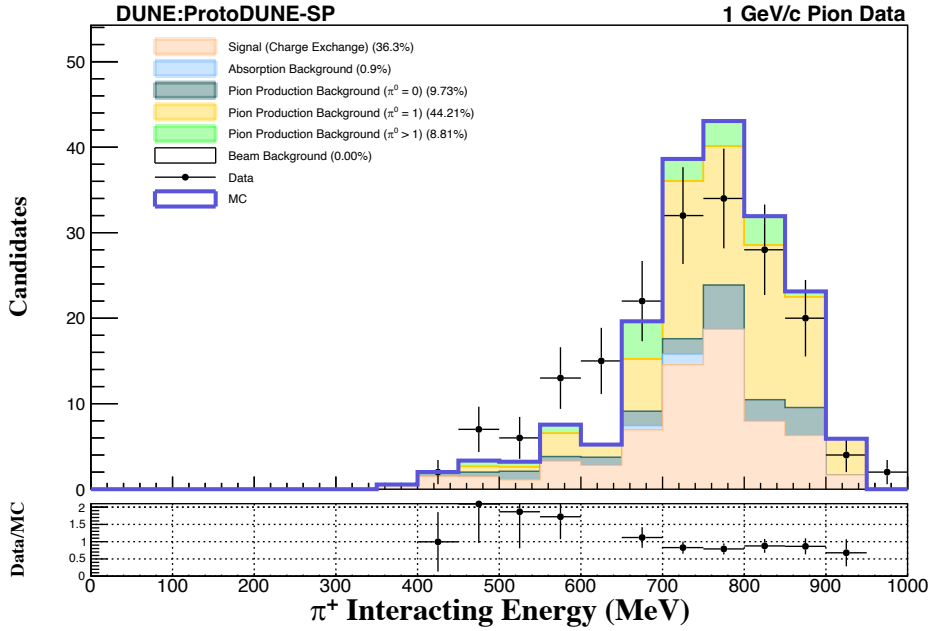

Figure 8.10: The pion interacting energy of selected pion production sideband channel with multiple ($\geq$ 1) π^0 in the final state. This sideband is selected by requiring at least one reconstructed π^0 and charged pion in the final state, altering the topology selection shown in Fig. 8.2. The MC distribution is decomposed into different event topologies.

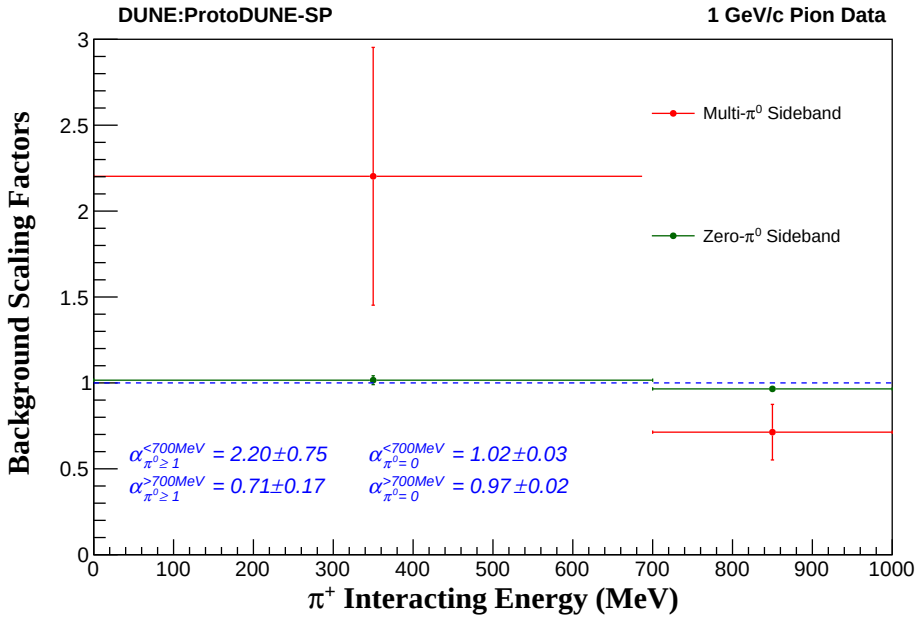

Figure 8.11: A summary of four sideband scaling factors, where each sideband is divided into two regions at 700 MeV, as it gives the smallest post-fit χ^2 value. GEANT4 underestimates the rates of pion production involving multiple (≥ 1) π^0 at lower pion kinetic energies, while overestimating them for pions with kinetic energies above 700 MeV.

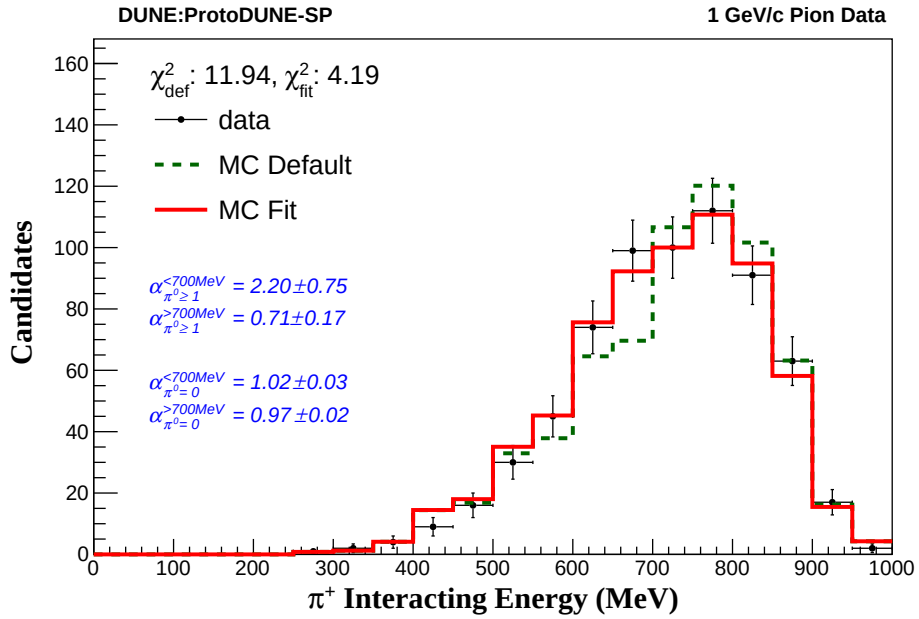

Figure 8.12: The signal CEX pion interacting energy distribution after the background tuning with the quoted scaling factors. The default MC distribution is shown in dashed green, and the post-fit result is shown in red. The data-MC simulation agreement improves upon the incorporation of background scaling factors obtained from the sideband fitting.

ergies and will be used for calculating the integrated cross-section. A specific range of beam interacting energies is then selected for conducting differential cross-section measurements with π^0 kinematics.

The previous background scaling factors are obtained as a function of beam kinetic energy, which is found to be inefficient for constraining the background in π^0 kinematics. Consequently, another sideband fitting procedure is conducted with the aim of extracting scaling factors for the same background categories (pion production with zero and multiple π^0), but this time as a function of the measured distribution of π^0 kinetic energy. In this study, the π^0 mass distribution is used to define the appropriate sideband regions for background tuning.

Figure 8.13 illustrates the π^0 invariant mass as a function of its kinetic energy. The signal region is defined as the mass window between 50 and 250 MeV/c^2, as discussed in Sec. 7.4. Additionally, two sideband regions are chosen: one below 300 MeV and the other above 300 MeV, both located outside the mass window. The sideband fitting procedure aims to extract two scaling factors that account for the misestimation of the background in the respective sideband regions. Two π^0 invariant mass distributions for both data and MC are plotted, considering π^0 kinematic energy to be less or greater than 300 MeV. Within the mass window (50 to 250 MeV/c^2), the MC remains fixed during fitting. Outside the mass window, only the pion production backgrounds (sum of the 0 π^0 and $\geq$ 1 π^0 components) are allowed to vary to enhance the agreement between data and MC through χ^2 minimization. This fitting is separately applied to both low and high kinetic energy sidebands to extract two scaling factors.

The obtained scaling factors, shown in blue in Fig. 8.13, represent the corrections applied to the background contributions in each region. In Fig. 8.14, the weighted π^0 kinetic energy is presented for the selected CEX signal sample, along with the calculated χ^2 values. The inclusion of background scaling factors obtained from the sideband fitting is observed to enhance the agreement between the data and MC simulation. The significant scaling increase seen in simulated background events with kinetic energy below 300 MeV suggests an underestimation of low-energy π^0 particles in the pion production events.

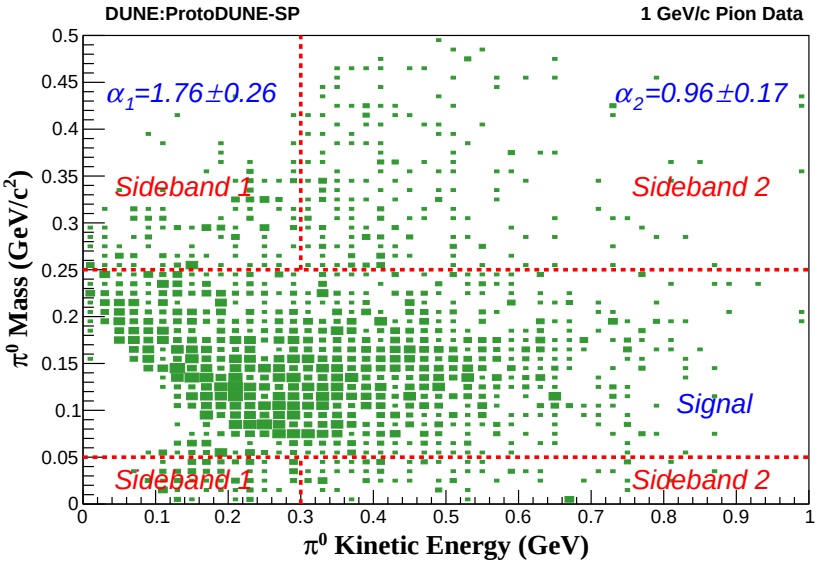

Figure 8.13: The distribution of the π^0 mass versus the π^0 kinetic energy. The signal region is defined as the π^0 mass falling between 50 and 250 MeV/c^2, while two sideband regions are defined for kinetic energies larger or less than 300 MeV outside the mass window. To improve the agreement between data and MC, the pion production backgrounds are allowed to vary through χ^2 minimization in the π^0 mass distribution outside the mass window. The fitted two scaling factors in each sideband region are shown in blue.

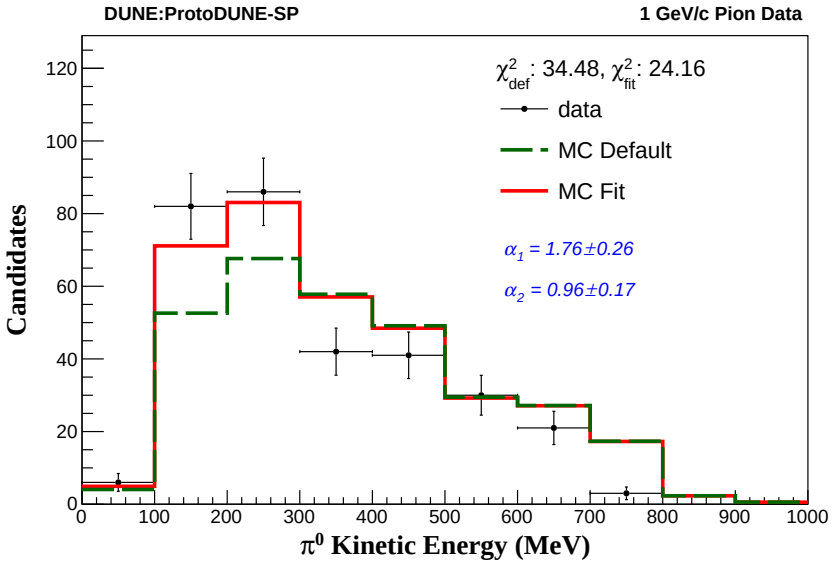

Figure 8.14: The distribution of the π^0 kinetic energy after background tuning. The default MC distribution is shown in dashed green, and the post-fit result is shown in red. The agreement between the data and the MC simulation is improved by implementing background scaling factors obtained from the sideband fitting.

8.7 Incident and Interacting Pion Events

Figures 8.15 and 8.16 show the reconstructed pion beam energy at the front face and the interacting point for all selected beam candidates, respectively. In these figures, the stacked histogram represents the distribution of different true beam types in the reweighted MC simulation, while the black points correspond to the data. After applying the beam momentum and muon reweighting techniques outlined in Sec. 8.5, a satisfactory level of agreement is observed between the data and the MC simulations. The selection of the primary pion beam is hindered by the presence of two leading backgrounds, specifically the misidentification of beam muons and secondary charged pions as primary pion beam events. By measuring the initial energy and interacting energy of each beam, it becomes possible to determine the number of slices the beam has traversed inside TPC without undergoing an interaction, as described in Sec. 3.6.2. Consequently, the incident flux at each slice can be computed using the following formula (Eq. 3.14 requoted here),

$$\mathrm{N}^{i}_{\mathrm{Inc}} = \sum_{i}^{n} \mathrm{N}^{i}_{\mathrm{Ini}} - \sum_{i+1}^{n} \mathrm{N}^{i}_{\mathrm{BeamInt}}. \tag{8.5}$$

Regarding the CEX interaction, events are categorized based on the number of daughter charged pions and neutral pions. An inclusive pion CEX event is defined as having one π^0 and no charged pions in the final state (Sec. 8.1). The method to constrain the background in the selected signal events is described in Sec. 8.6. Two sidebands are employed for this purpose, and the resulting pion CEX interacting energy after tuning the background is presented in Fig. 8.17, where MC is decomposed by different event topologies. The purity of the selected sample is approximately 70%, as discussed in Table 8.1, with the dominant background coming from pion production events that involve multiple π^0s in the final state. In addition, the measured π^0 kinetic energy distribution for events with beam pions interacting energy between 650 to 800 MeV is shown in Fig. 8.18, where the background events have been tuned from the sideband study.

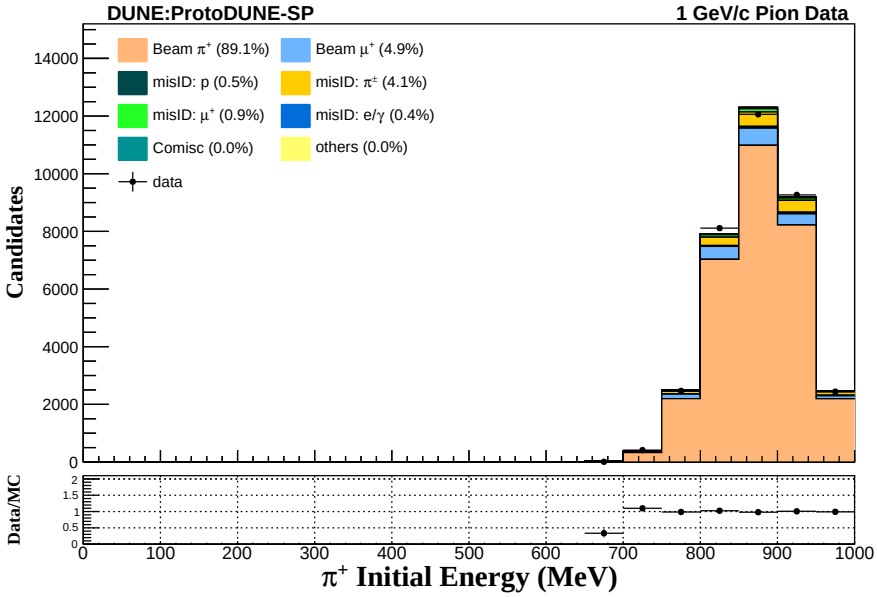

Figure 8.15: The reconstructed pion beam initial energy distribution after beam momentum reweighting. The stacked histogram displays the different beam components, with a pion beam purity of 91%. Secondary daughter particles can be misidentified as primary beam particles, and these candidates are denoted as misID:p/π^+/μ^+/e/γ in the legend.

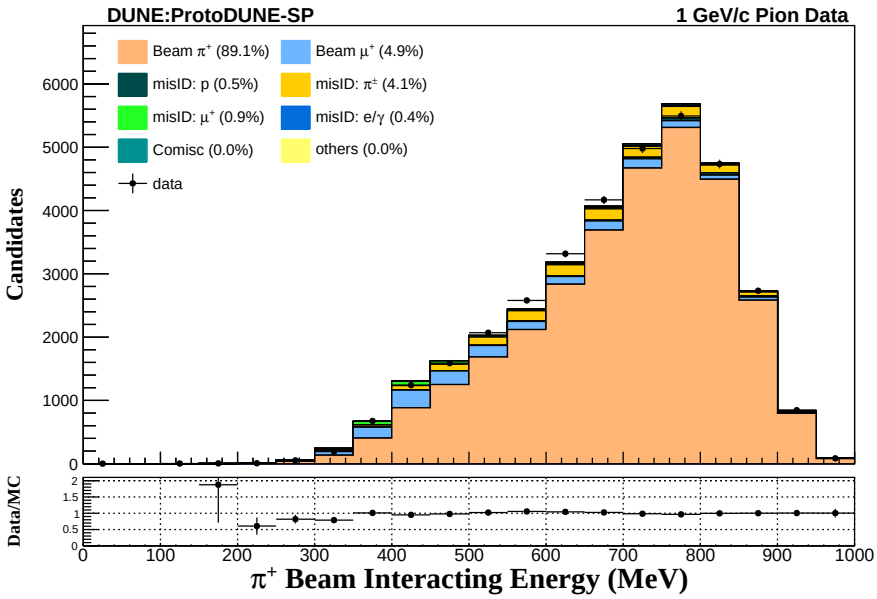

Figure 8.16: The reconstructed pion beam interacting energy distribution after beam momentum reweighting. This distribution, when combined with the initial energy distribution, allows for the computation of the pion incident flux using Eq. 8.5.

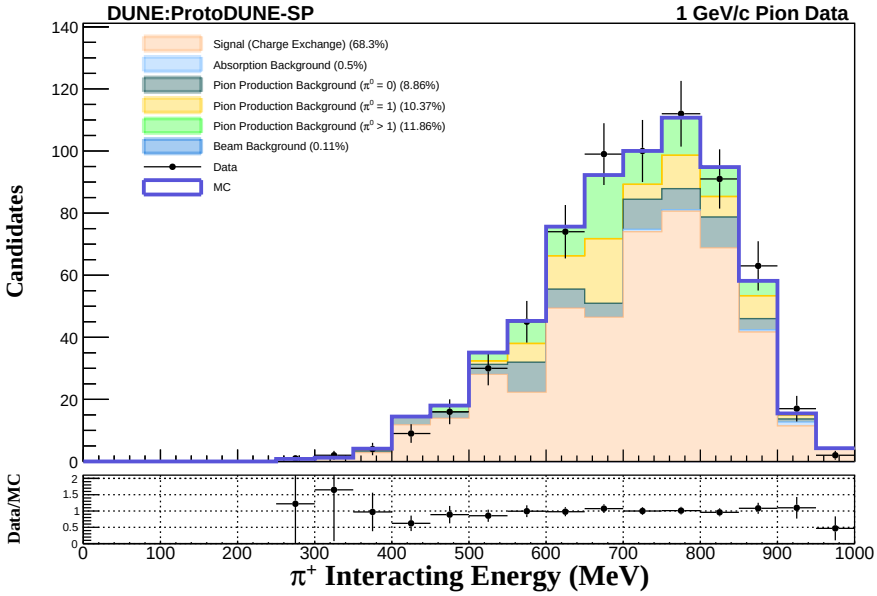

Figure 8.17: The interacting energy distribution of the charge exchange events, decomposed by event topologies defined in Sec. 8.1. The purity of the selected CEX events is 68% after background tuning. It is utilized for calculating the flux of interacting signals after subtracting non-CEX events.

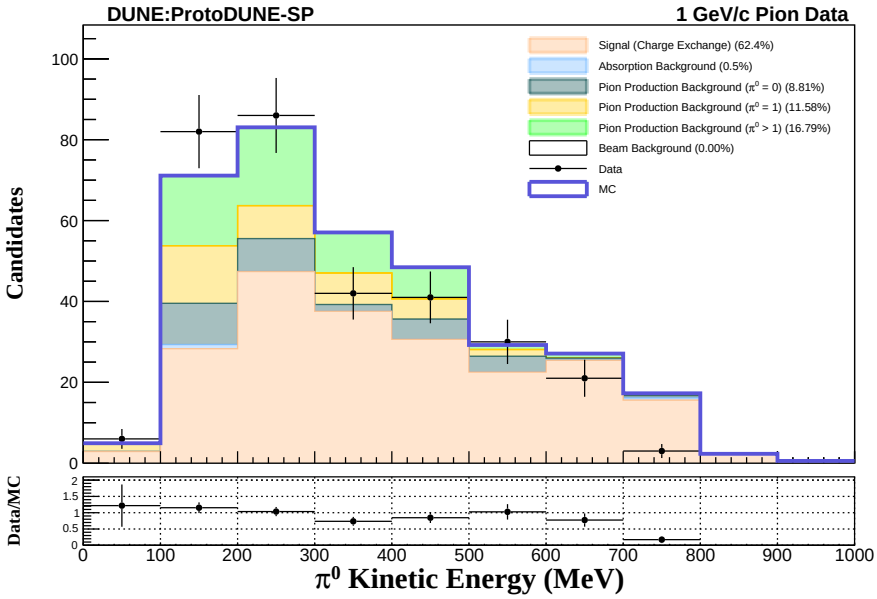

Figure 8.18: The distribution of π^0 kinetic energy in the selected CEX events for beam pions interacting with kinetic energy between 650-800 MeV., categorized by event topologies. Background tuning is applied, as detailed in Sec. 8.6, yields a 62% purity of CEX events. This distribution is employed to calculate the differential cross-section in the π^0 kinetic energy.

Upon acquiring the beam pion and π^0 energy spectrum, background subtraction is performed bin by bin using estimates from weighted simulations. The measured initial energy (Fig. 8.15) and beam interacting energy (Fig. 8.16) are applied to determine the incident pion beam flux, accounting for the removal of non-pion beam events. Whereas the measured CEX interacting energy (Fig. 8.17) is used to compute the signal interacting flux after subtracting non-CEX events. With knowledge of both incident and interacting fluxes, the integrated pion CEX cross-section is computed as a function of beam pion energy. Subsequently, a subsample of the beam pions with interacting energy between 650 to 800 MeV is selected to compute the differential cross-section based on the π^0 kinematics (Fig. 8.18), as detailed in Sec. 3.6.2. To account for detector effects and reconstruction inefficiency, the resulting background-subtracted histograms are employed in the unfolding process, which will be discussed in the upcoming section.

8.8 Unfolding Procedure

In this particular study, the distributions of Interacting and Incident Histograms are expressed in terms of reconstructed kinetic energy, a quantity prone to distortion and smearing due to detector effects and reconstruction methods. An unfolding procedure is employed to obtain the true distribution from the observed one. Unfolding can be conceptualized as an inverse problem, aiming to recover the underlying true kinetic energy distribution from the measured distribution affected by various distortions [96, 97].

In the realm of particle physics, the quest to extract accurate distributions from measured data encounters diverse challenges and limitations [98]. In this study, a solution to this predicament is employed, known as the Bayes' unfolding method, originally introduced by G. D'Agostini in 1993 [99, 100]. This method is based on the principles of Bayes' Theorem and serves as a powerful statistical inference tool. Notably, one of its key strengths lies in its ability to handle multidimensional problems, adapt to varying bin widths between the true and measured distributions, account for distortions such as smearing and bin migration, accommodate different background sources, and obviate the need for ma-

trix inversion. Additionally, it facilitates the computation of a correlation matrix from the obtained results. The implementation of the unfolding method is integrated within the ROOT framework [86], enabling its application across various code classes.

Here, the unfolding process is performed using the RooUnfold software package. To validate the unfolding process, the measured MC simulation distribution is employed, with half of the simulated events used to obtain the response matrix and the remaining half serving as a fake data sample for validation. This validation step ensures the reliability and accuracy of the unfolding procedure by comparing the unfolded fake data results with the known true distribution.

There are two event categories: those contributing to the response matrix and missed events. In the case of the response matrix, it is constructed using true signal events, where the measured beam pion energy after event selection and the corresponding true energy values are used to populate it. The response matrix represents the prior probability of reconstructing a beam pion with a specific true interacting kinetic energy within a given reconstructed kinetic energy bin. It quantifies the relationship between the true and reconstructed kinetic energies, providing information about the likelihood of observing a particular reconstructed energy given a known true energy.

Missed events, on the other hand, correspond to true signal events that are not successfully reconstructed or do not meet the event selection criteria. They reflect the inefficiencies in the selection and reconstruction process, where certain events are missed or excluded due to limitations or criteria set during the analysis.

The unfolding process is first validated by using the fake data sample before proceeding to the analysis of the real data. The key histograms used to obtain the CEX cross-section results are the Incident Histogram and the CEX Interacting Histogram. The unfolding of the Incident Histogram involves unfolding the Initial Histogram and the Beam Interacting Histogram, followed by the application of Eq. 8.5 to compute the unfolded Incident Histogram. On the other hand, the unfolded CEX Interacting Histogram is directly obtained by unfolding the measured pion charge exchange beam interacting energy distribution.

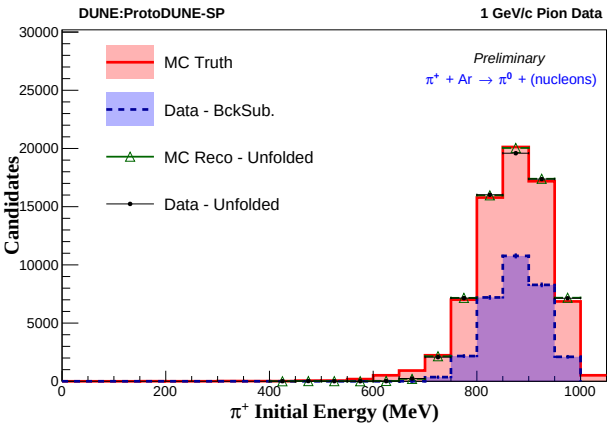

(a)

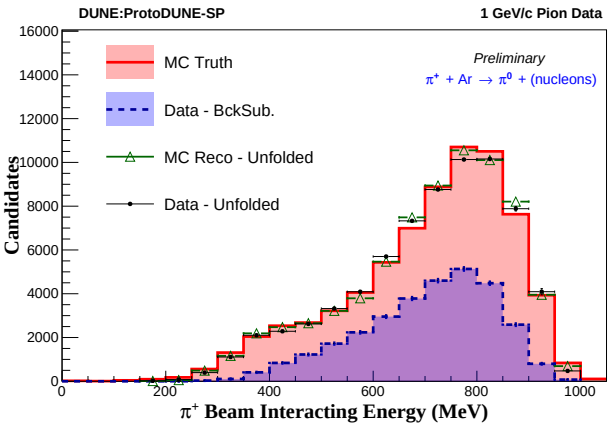

(b)

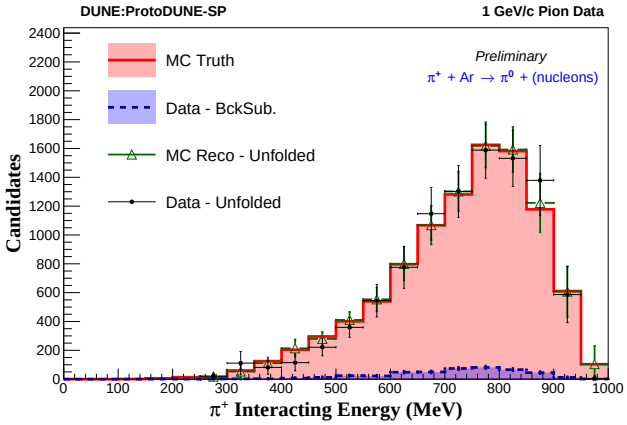

(c)

Figure 8.19: The unfolded histograms of all three measured energy compared with the underlying true distribution. (a) The unfolded initial energy. (b) The unfolded beam interacting energy. (c) The unfolded CEX interacting energy. The background-subtracted data is presented in the blue histogram. The unfolded MC and data are shown as green triangles and black points, respectively, while the MC true distribution is shown in red.

As a result, three beam pion energy distributions are unfolded independently: the selected beam initial energy, the beam interacting energy, and the CEX interacting energy.

The unfolded energy histograms are shown in Fig. 8.19. The red histogram corresponds to the MC true distribution, while the blue dashed histogram represents the background-subtracted data, and the green triangle and black point represent the unfolded MC and data, respectively. Specifically, Fig. 8.19 (a) and (b) present the unfolded beam initial energy and beam interacting energy for all selected beam events, enabling the calculation

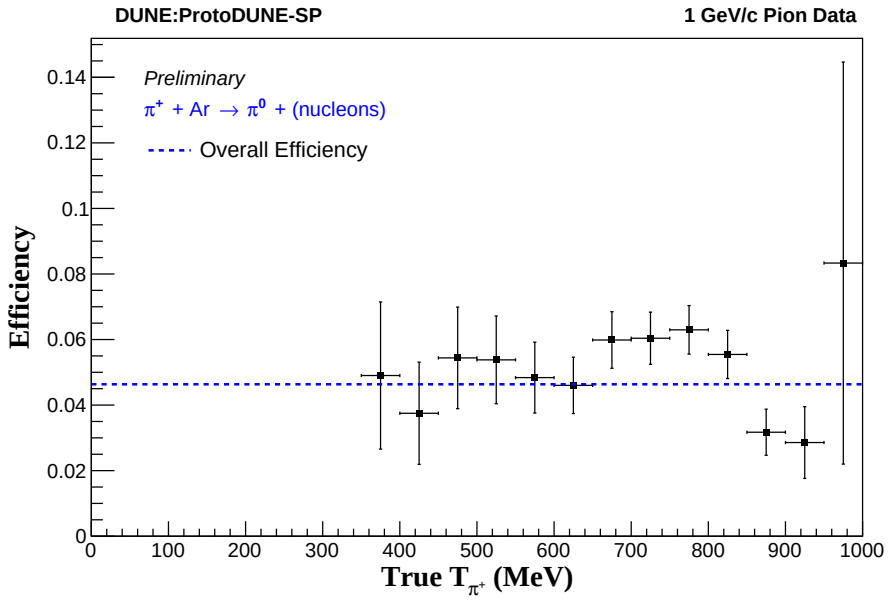

Figure 8.20: The unfolding efficiency as a function of the true beam pion kinetic energy for the pion charge exchange interacting events. The efficiency remains relatively constant with an overall value of $\sim 5\%$, as stated in Table 8.1.

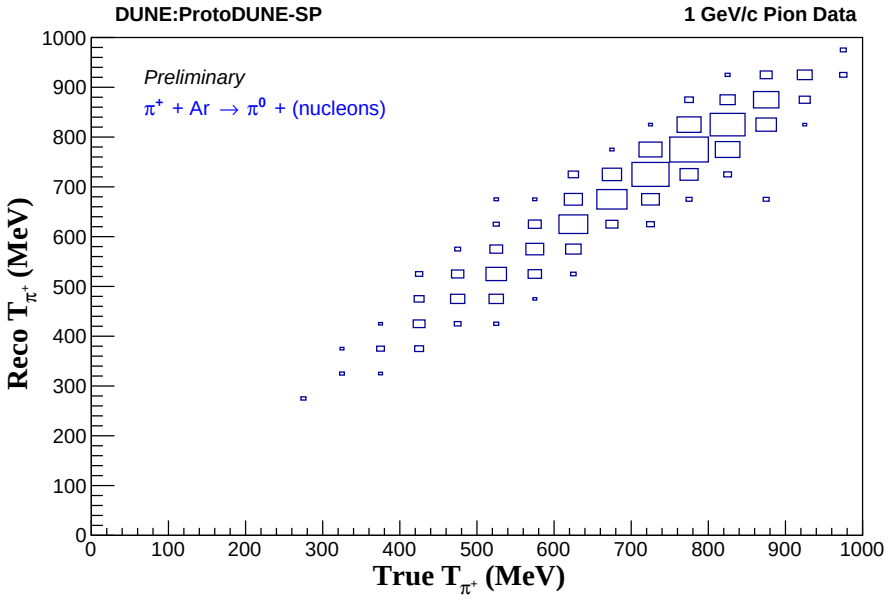

Figure 8.21: The response matrix of the interacting energy in the pion charge exchange interacting events. Half of the available MC simulations are used to create the response matrix and estimate the event backgrounds. The majority of events are concentrated along the diagonal line, indicating a small bin-to-bin migration.

of the unfolded Incident Histogram. Fig. 8.19 (c) shows the unfolded CEX interacting energy. The unfolded histograms corresponding to the kinematic variables of the π^0 can be found in Appendix H.

The overall efficiency for the initial energy and beam interacting energy is approximately 50%, whereas for the CEX interacting energy, the efficiency decreases to $\sim 5\%$, as illustrated in Fig. 8.20 (see also Table 8.1). The efficiency is rather a constant for the CEX interacting energy at each energy bin. The lower efficiency can primarily be attributed to the inadequate reconstruction of π^0 showers in the Pandora algorithm. Figure 8.21 shows the response matrix that is used to do the unfolding for the CEX interacting energy distribution. The majority of events are concentrated along a diagonal line with minimal migration between bins.

8.9 Systematic Uncertainty

This section delves into the primary contributors to systematic uncertainties in the measurement of the pion charge exchange cross-section. Accurately quantifying the impact of systematic uncertainties is essential for deriving meaningful conclusions from the obtained cross-section results.

To evaluate the systematic uncertainty, a multi-universe approach is employed [101]. Each systematic source is considered individually by varying the chosen parameters by $\pm 1\sigma$. The resulting covariance matrix (Eq. 8.6) [102] is the estimate of the corresponding systematic errors from the diagonal element,

$$M_{ij} = \frac{\Sigma_{k=1}^{N}(x_{i_k} - \bar{x}_i)(x_{j_k} - \bar{x}_j)w_k}{\Sigma_{k=1}^{N} w_k}, \tag{8.6}$$

where N is the total number of universes, w_k is the weight for a universe k (default value = 1), x_{i_k} is the candidate count in bin i in a universe k and $\bar{x}_i$ is the mean candidate count in bin i, averaged over all universes.

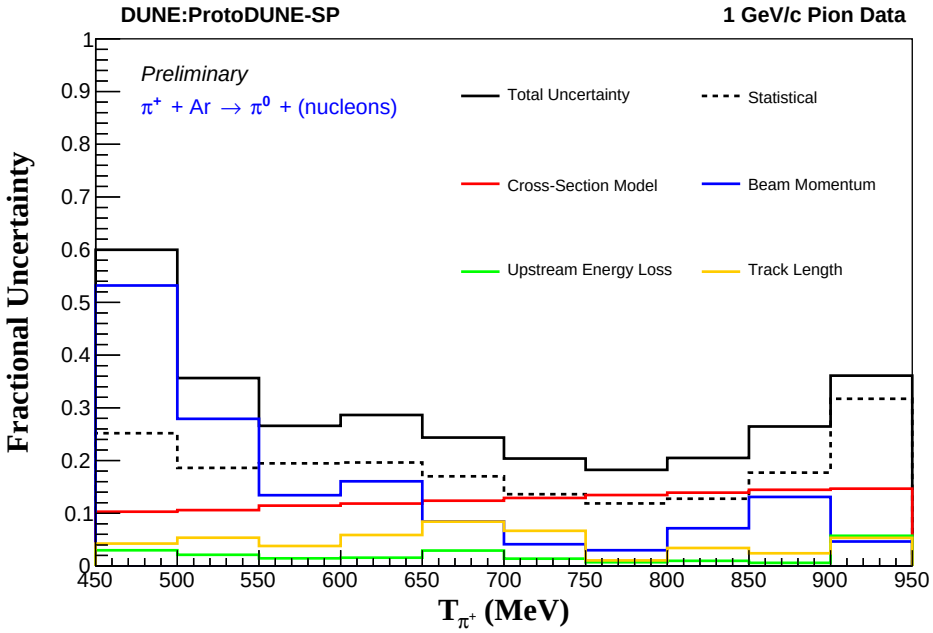

Figure 8.22: The total fractional uncertainty at each beam pion kinetic energy bin, with the statistical error represented by the dashed line. Four leading systematic uncertainties have been evaluated using the multi-universe approach, as explained in Appendix I.

The leading four systematic sources, as shown in Fig. 8.22, are discussed below:

Firstly, the pion charge exchange cross-section model implemented in the analysis is subject to a $\pm$ 20% variation, resulting in an increase or decrease in the total number of pion CEX events. This change affects the probability of a beam pion interacting in the CEX channel, which in turn alters the number of signal events that contribute to the response matrix and missed events as defined in Sec. 8.8.

Secondly, according to simulations, the resolution of the beam spectrometer in measuring the beam momentum is approximately 2%. For a pion beam with a momentum of 1 GeV/c, the uncertainty in the measured energy is around 20 MeV. To assess the impact of this uncertainty, the measured beam momentum is varied by $\pm$ 20 MeV.

Beam Energy Bin Centre Value (MeV)	475	525	575	625	675	725	775	825	875	925
Cross-Section Nominal Value (mb)	70.3	79.1	85.6	89.4	97.6	86.0	90.5	90.2	110.0	94.0
Cross-Section Model	6.7	8.8	10.5	10.0	10.8	11.6	13.7	12.6	15.5	15.9
Beam Momentum	34.8	23.2	12.4	13.6	7.4	3.7	3.1	6.5	14.0	5.0
Upstream Energy Loss	2.0	1.8	1.3	1.3	2.5	1.3	0.7	0.9	0.6	6.2
Track Length	2.8	4.5	3.5	5.0	7.3	6.0	1.1	3.1	2.6	5.8
Syst. Uncertainty (mb)	35.6	25.3	16.7	17.6	15.1	13.6	14.1	14.5	21.0	18.7
Stats. Uncertainty (mb)	18.9	15.1	17.7	16.7	15.5	11.9	11.1	11.5	19.3	31.1
Total Uncertainty (mb)	40.3	29.5	24.3	24.3	21.7	18.1	18.0	18.5	28.6	36.3

Table 8.2: Summary of systematic uncertainties in the measured integrated CEX cross section for each bin, obtained by varying the cross-section model, beam momentum, upstream energy loss, and reconstructed track length. The total uncertainty, which includes statistical errors, is calculated and presented in the last row of the table.

Thirdly, the systematic uncertainty arising from the upstream energy loss is assessed by fitting the Gaussian function to the upstream energy loss (Sec. 8.4) of all the selected beam events. The fitted function is then used to fluctuate the energy loss by one σ.

Finally, the systematic uncertainty associated with the reconstructed beam track is assessed by analyzing the difference between the reconstructed and true track length. This is achieved by fitting the distribution of the ratio of the difference in track lengths and the reconstructed track length. The obtained resolution is then used to vary each beam track length by one standard deviation.

Table 8.2 provides a breakdown of the contribution of individual systematic uncertainties to each energy bin. Both statistical and systematical uncertainties are propagated to determine the total uncertainty of the final cross-section measurements. For low π^+ kinetic energies, the dominant uncertainty arises from the beam momentum estimation, while at higher kinetic energies, both the cross-section model and statistical uncertainties play significant roles. The errors originating from upstream energy loss and track length estimation remain relatively consistent across the accessible kinetic energy range, contributing less than 5%.

8.10 Results with Systematic Errors

The measurement of the pion charge exchange integrated cross-section is performed within a specific kinetic energy range of 450 to 950 MeV. The lower limit of this range is determined by the APA3 issues discussed in Sec. 6.1, while the upper limit is chosen to exclude the last bin, which has a low number of beam pion interactions. To conduct the cross-section measurement, an upgraded version of the thin slice method, as described in Sec. 3.6.2, is employed. The measured distributions in Sec. 8.7 are unfolded to correct for detector effects and reconstruction inefficiency. The four main sources of systematic uncertainties discussed in Sec. 8.9 are examined, and their contributions are accounted for in the total error of the final result.

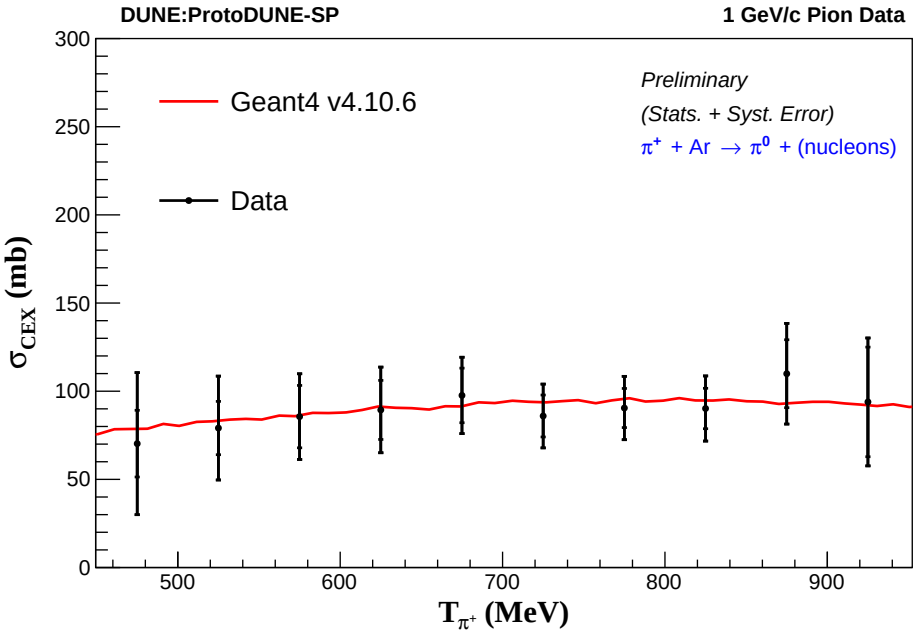

Figure 8.23: The measured integrated pion charge exchange cross-section with fully propagated uncertainty. The inner error bar indicates the statistical error and the outer error bar shows the total errors, which is the quadratic sum of statistical and systematic errors

The measured integrated charge exchange cross-section is presented in Fig. 8.23. The red curve corresponds to the GEANT4 v4.10.6 input model, while the black points represent the measured results from the ProtoDUNE-SP data. Within the available beam pion kinetic energy range, the cross-section for pion charge exchange remains relatively constant at around 90 millibarns (mb). Despite the presence of large uncertainties, the data points agree well with the input model.

Figure 8.24 shows the differential cross-section as a function of the π^0 kinematics for a subset of the selected charged pion beam undergoing charge exchange. This subset specifically includes beam pions with interacting energies between 650 and 800 MeV. The differential cross-section results for the π^0 exhibit three distinct peaks, consistent with the GEANT4 model arising from the various dynamics of the underlying π^0 production, as discussed below.

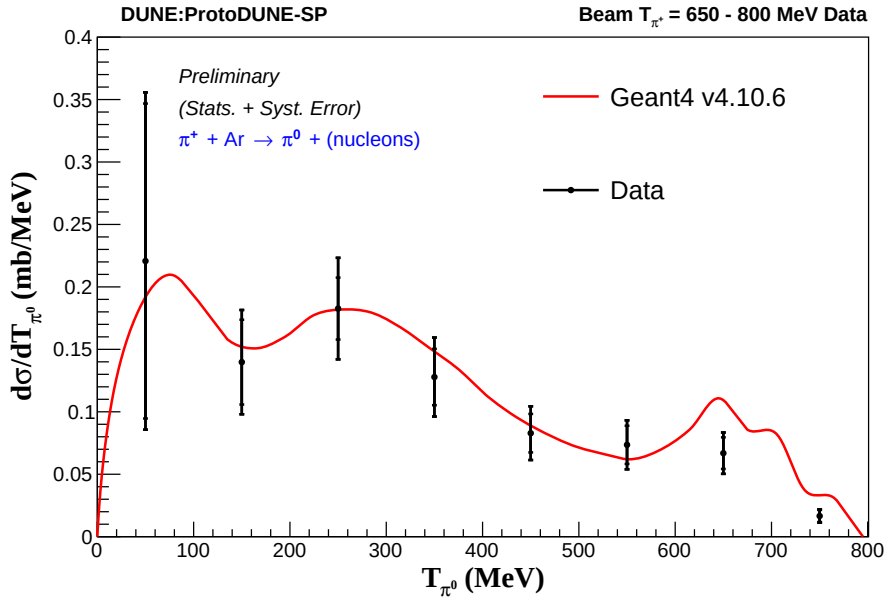

Figure 8.24: The differential cross-section as a function of π^0 kinetic energy for beam pions interacting with kinetic energy between 650-800 MeV. The presence of a three-peak structure is in agreement with the GEANT4 model, reflecting the diverse dynamics governing π^0 production.

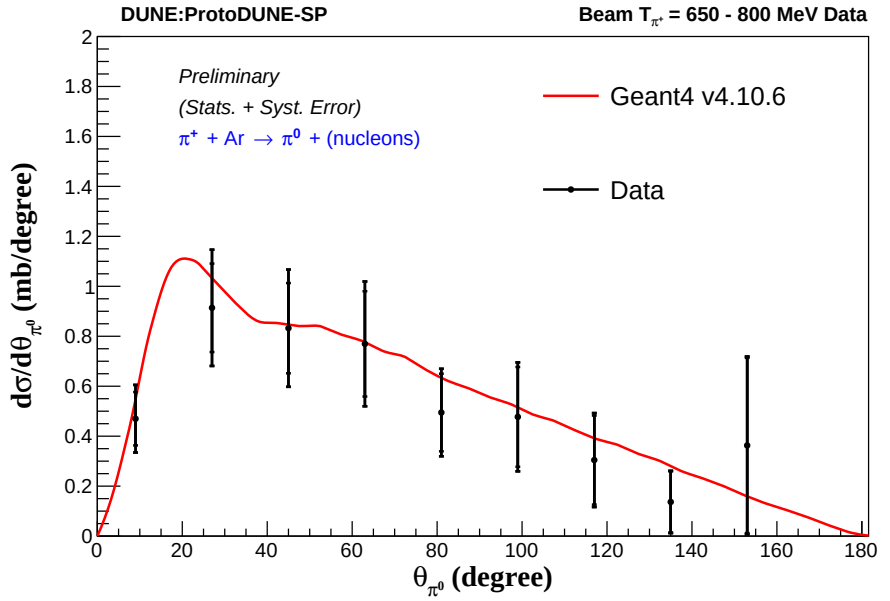

Figure 8.25: The differential cross-section as a function of π^0 scattering angle θ_{π^0} for beam pions interacting with kinetic energy between 650-800 MeV. A significant number of π^0 are produced with an angle of 30° with respect to the z-axis of the detector coordinates.

In simulating the hadron interaction and transportation, GEANT4 employs the Bertini cascade model [103]. Following the interaction, GEANT4 incorporates other models to handle the nuclear fragments: For nuclei with A < 12, further de-excitation is achieved through Fermi breakup. For all other nuclei, equilibrium evaporation is employed using a statistical model [104]. Competition between nucleon evaporation and the evaporation of light ions (d, 3He, α) is also implemented based on relative probabilities.

In the low T_{π^0} region (less than 150 MeV), the production of π^0 does not exhibit a preferred direction, and there are many nucleons and nuclei being produced. The energy transfer is distributed among these final-state particles. Moving to the middle T_{π^0} region (larger than 200 MeV but less than 400 MeV), the production of nucleons and nuclei is reduced, resulting in a higher energy transfer to the π^0 particle, with a preferred forward production direction in this region. In the high T_{π^0} region (greater than 650 MeV), the π^0 particle predominantly moves in the forward direction, as it carries most of the kinetic energy from the beam π^+. Interestingly, the model predicts that only a few nucleons are produced in this region.

Figure 8.25 shows the differential cross-section as a function of the π^0 scattering angle, where the angle θ_{π^0} is defined as the angle between the momentum vector of the π^0 particle and the z-axis in the coordinate system of the detector. The beam direction is closely aligned with the z-axis, which is approximately 10° downward and 11° towards the anode plane (Sec. 3.2). The distribution demonstrates that the majority of π^0 particles are produced in the forward direction, with an angle around 30° with respect to the z-axis. The large θ_{π^0} angle corresponds to the π^0 moving backwards, which has a smaller cross-section. Additionally, the reconstruction of these π^0 particles presents more challenges in Pandora. As a result, the number of reconstructed CEX events in this region is limited, leading to higher statistical errors. The total uncertainty as a function of the π^0 kinematics can be found in Appendix I, with a table containing a breakdown of the contribution of individual uncertainties to each energy bin.

9 | Conclusion

Liquid argon time projection chamber has emerged as a highly effective detector for various neutrino physics experiments, including studies on neutrino oscillations, supernova neutrino observations, and searches for proton decay. Prominent among the next-generation experiments using this technology is the Deep Underground Neutrino Experiment. DUNE aims to achieve exceptional sensitivity across a wide range of scientific objectives. Key among these objectives is the precise measurement of the CP-violating phase in the neutrino oscillation parameters and the determination of the neutrino mass hierarchy.

The main focus of this PhD thesis is the physics analysis in ProtoDUNE-SP, the largest-ever LArTPC to date. Serving as the initial prototype of the far detector for DUNE, ProtoDUNE-SP employed 0.77 kt of liquid argon. Over the course of its operational period from September to October 2018 at CERN, ProtoDUNE-SP successfully collected valuable data from hadron beams spanning a momentum range of 0.3 to 7 GeV/c.

This thesis presents a comprehensive analysis of both the integrated and differential cross-sections for π^+-Ar charge exchange interaction. A total of 34,783 pion beam events are selected, among which only 665 pions interacted via the charge exchange process (Sec. 8.2). The analysis focuses on the beam pion energy range of [450, 950] MeV, revealing a favourable agreement between the analysis results and the Geant4 model. The measured integrated cross-section is observed to be nearly independent of the beam pion energy, averaging at 90 millibarns (Sec. 8.10).

The first differential cross-section measurement has been conducted for beam pions with interacting energies ranging from 650 to 800 MeV, focusing on the kinetic energy and direction of the π^0 particle (Sec. 8.10). The GEANT4 simulation adequately captures the kinematics of π^0, although there are considerable uncertainties associated with the measurement results. At present, this analysis is primarily limited by statistical errors, resulting in a 20% uncertainty. The inclusion of additional data in the upcoming beam run of ProtoDUNE-II would greatly enhance the significance of this analysis.

The obtained results can enhance theoretical models by refining predictions regarding secondary pion charge exchange interactions of neutrino products with argon. By leveraging the measured differential cross-section alongside the kinematics of the neutral pion, constraints can be placed on specific phase-space regions within the model. This measurement effectively constrains important systematic uncertainties associated with the rate of secondary interactions among neutrino interaction products. It specifically improves the simulation within the nuclear model used for neutrino interaction, addressing the π^0 background in the electron neutrino appearance signal, helping DUNE achieve the present level of experimental accuracy needed for its scientific goals.

In this study, a sub-GeV neutral pion energy resolution of 12% has been attained in ProtoDUNE-SP through the utilization of kinematic fitting (Sec. 7.5). By implementing the developed kinematic fitting algorithm in LArTPC-based experiments like DUNE, the advantages of enhanced π^0 energy resolution can be extended beyond ProtoDUNE-SP. This extension enables more precise measurements of neutrino interaction events wherein π^0 is produced in the final state.

Moreover, the study of shower energy reconstruction emphasizes the possibility of enhancing the Pandora shower reconstruction algorithm (Sec. 7.2). With the availability of additional data sets, there is an opportunity to conduct a dedicated analysis focused on the transverse kinematic imbalance for an exclusive measurement of pion charge exchange interaction (Sec. 4.4). In such an analysis, the TKI is defined between the final state proton and the neutral pion. By exploring this approach, a new avenue is opened to investigate nuclear effects in argon from hadronic interactions.

Bibliography

[1] L. Evans and P. Bryant, "LHC Machine," *Journal of Instrumentation*, vol. 3, p. S08001, Aug 2008.

[2] G. Aad, T. Abajyan, *et al.*, "Observation of a new particle in the search for the Standard Model Higgs boson with the ATLAS detector at the LHC," *Physics Letters B*, vol. 716, pp. 1–29, Sep 2012.

[3] P. G., "The Standard Model," 2014. https://www.quantumdiaries.org/2014/03/14/the-standard-model-a-beautiful-but-flawed-theory/, Last accessed on 2023-07-03.

[4] R. Davis, "Solar Neutrinos. II. Experimental," *Phys. Rev. Lett.*, vol. 12, pp. 303–305, Mar 1964.

[5] W. Pauli, "Pauli letter collection: letter to Lise Meitner." Typed copy.

[6] C. N. Yang, *Fermi's β-DECAY Theory*, pp. 326–332. World Scientific Publishing Co, May 2013.

[7] C. L. Cowan, F. Reines, *et al.*, "Detection of the Free Neutrino: a Confirmation," *Science*, vol. 124, pp. 103–104, Jul 1956.

[8] Z. Maki, M. Nakagawa, *et al.*, "Remarks on the Unified Model of Elementary Particles," *Progress of Theoretical Physics*, vol. 28, pp. 870–880, Nov 1962.

[9] M. Thomson, *Modern Particle Physics*. Cambridge University Press, 2013.

[10] A. Y. Smirnov, "The MSW effect and solar neutrinos," in *10th International Workshop on Neutrino Telescopes*, pp. 23–43, May 2003.

[11] Y. Fukuda, T. Hayakawa, *et al.*, "Evidence for oscillation of atmospheric neutrinos," *Physical Review Letters*, vol. 81, pp. 1562–1567, Aug 1998.

[12] A. W. P. Poon, "Neutrino observations from the Sudbury Neutrino Observatory," in *AIP Conference Proceedings*, AIP, Oct 2002.

[13] T. D. Lee and C. N. Yang, "Question of Parity Conservation in Weak Interactions," *Phys. Rev.*, vol. 104, pp. 254–258, Oct 1956.

[14] C. S. Wu, E. Ambler, *et al.*, "Experimental Test of Parity Conservation in Beta Decay," *Phys. Rev.*, vol. 105, pp. 1413–1415, Feb 1957.

[15] U. Dore, P. Loverre, *et al.*, "History of accelerator neutrino beams," *Eur. Phys. J. H*, vol. 44, pp. 271–305, Oct 2019.

[16] P. A. Zyla, R. M. Barnett, *et al.*, "Review of Particle Physics," *Progress of Theoretical and Experimental Physics*, vol. 2020, p. 083C01, Aug 2020.

[17] R. Subedi, R. Shneor, *et al.*, "Probing Cold Dense Nuclear Matter," *Science*, vol. 320, p. 1476, Jun 2008.

[18] F. Reines, "Neutrino interactions," *Annual Review of Nuclear Science*, vol. 10, no. 1, pp. 1–26, 1960.

[19] T2K, "About Neutrinos," 2023. https://t2k-experiment.org/neutrinos/, Last accessed on 2023-09-04.

[20] K.-J. Plows and X. Lu, "Modeling heavy neutral leptons in accelerator beamlines," *Phys. Rev. D*, vol. 107, p. 055003, Mar 2023.

[21] J. F. Beacom, W. M. Farr, and P. Vogel, "Detection of supernova neutrinos by neutrino-proton elastic scattering," *Phys. Rev. D*, vol. 66, p. 033001, Aug 2002.

[22] A. Aguilar, L. B. Auerbach, *et al.*, "Evidence for neutrino oscillations from the observation of $\overline{\nu}_e$ appearance in a $\overline{\nu}_\mu$ beam," *Phys. Rev. D*, vol. 64, p. 112007, Nov 2001.

[23] C. Rubbia, "The liquid-argon time projection chamber: a new concept for neutrino detectors," tech. rep., CERN, Geneva, May 1977.

[24] B. Abi, R. Acciarri, *et al.*, "First results on ProtoDUNE-SP liquid argon time projection chamber performance from a beam test at the CERN Neutrino Platform," *Journal of Instrumentation*, vol. 15, pp. P12004–P12004, Dec 2020.

[25] FermiLab, "DUNE at LBNF," 2014. https://lbnf-dune.fnal.gov/how-it-works/introduction/, Last accessed on 2023-07-03.

[26] FermiLab, "Fermilab's Accelerator Complex," 2020. https://www.fnal.gov/pub/science/particle-accelerators/accelerator-complex.html, Last accessed on 2023-07-03.

[27] R. Acciarri, M. A. Acero, *et al.*, "Long-Baseline Neutrino Facility (LBNF) and Deep Underground Neutrino Experiment (DUNE) Conceptual Design Report Volume 1: The LBNF and DUNE Projects," *arXiv:1601.05471*, Jan 2016.

[28] D. Collaboration, B. Abi, *et al.*, "Experiment simulation configurations approximating dune tdr," *arXiv:2103.04797*, Mar 2021.

[29] A. A. Abud, B. Abi, *et al.*, "Deep Underground Neutrino Experiment (DUNE) Near Detector Conceptual Design Report," *Instruments*, vol. 5, p. 31, Mar 2021.

[30] L. Agostino, B. Andrieu, *et al.*, "LBNO-DEMO: Large-scale neutrino detector demonstrators for phased performance assessment in view of a long-baseline oscillation experiment," *CERN-SPSC-2014-013, SPSC-TDR-004*, Sep 2014.

[31] B. Abi, R. Acciarri, *et al.*, "The DUNE Far Detector Interim Design Report Volume 1: Physics, Technology and Strategies," *arXiv:1807.10334*, Jul 2018.

[32] O. Lantwin, "The DUNE vertical drift TPC," in *ICHEP 2022 Conference Proceedings*, Sissa Medialab, Nov 2022.

[33] B. Abi, R. Acciarri, *et al.*, "Deep Underground Neutrino Experiment (DUNE), Far Detector Technical Design Report, Volume II: DUNE Physics," *arXiv:2002.03005*, Feb 2020.

[34] J. Calcutt, *Measurement of Piplus - Argon Absorption and Charge Exchange Interactions Using Protodune-SP*. PhD thesis, FERMILAB-THESIS-2021-30, Michigan State U., 2021.

[35] E. P. Guerra, C. Wilkinson, *et al.*, "Using world charged pion-nucleus scattering data to constrain an intranuclear cascade model," *Physical Review D*, vol. 99, Mar 2019.

[36] B. Abi, R. Acciarri, *et al.*, "The Single-Phase ProtoDUNE Technical Design Report," *arXiv:1706.07081*, Jun 2017.

[37] N. Charitonidis and I. Efthymiopoulos, "Low energy tertiary beam line design for the cern neutrino platform project," *Phys. Rev. Accel. Beams*, vol. 20, p. 111001, Nov 2017.

[38] A. C. Booth, N. Charitonidis, *et al.*, "Particle production, transport, and identification in the regime of $1 - 7$ GeV/c," *Phys. Rev. Accel. Beams*, vol. 22, p. 061003, Jun 2019.

[39] S. Amerio, S. Amoruso, *et al.*, "Design, construction and tests of the ICARUS T600 detector," *Nucl. Instrum. Meth. A*, vol. 527, pp. 329–410, Jul 2004.

[40] P. H., X.-G. Lu, *et al.*, "Neutrino-hydrogen interactions with a high-pressure time projection chamber," *Physical Review D*, vol. 102, Aug 2020.

[41] T. Heindl, T. Dandl, *et al.*, "The scintillation of liquid argon," *EPL*, vol. 91, p. 62002, Sep 2010.

[42] D. Montanari, J. Bremer, *et al.*, "Development of membrane cryostats for large liquid argon neutrino detectors," *IOP Conf. Ser. Mater. Sci. Eng.*, vol. 101, p. 012049, Dec 2015.

[43] A. A. Abud, B. Abi, *et al.*, "Design, construction and operation of the ProtoDUNE-SP Liquid Argon TPC," *JINST*, vol. 17, p. P01005, Sep 2021.

[44] R. Acciarri, C. Adams, *et al.*, "Design and Construction of the MicroBooNE Detector," *JINST*, vol. 12, p. P02017, Feb 2017.

[45] M. A. Vermeulen, *A blessing in disguise : Characterisations of ProtoDUNE photon showers for neutrino measurements in DUNE*. PhD thesis, FERMILAB-THESIS-

2021-05, Nikhef, Amsterdam, 2021.

[46] D. Motta, "The Double Chooz experiment," *Acta Phys. Polon. B*, vol. 37, pp. 2027–2037, May 2006.

[47] S. Amoruso, M. Antonello, *et al.*, "Study of electron recombination in liquid argon with the icarus tpc," *Nucl. Instrum. Meth. A*, vol. 523, pp. 275–286, May 2004.

[48] R. Acciarri, C. Adams, *et al.*, "A Study of Electron Recombination Using Highly Ionizing Particles in the ArgoNeuT Liquid Argon TPC," *JINST*, vol. 8, p. P08005, Jun 2013.

[49] C. Adams, M. Alrashed, *et al.*, "Calibration of the charge and energy loss per unit length of the MicroBooNE liquid argon time projection chamber using muons and protons," *JINST*, vol. 15, p. P03022, Mar 2020.

[50] M. Tanabashi, K. Hagiwara, *et al.*, "Review of particle physics," *Phys. Rev. D*, vol. 98, p. 030001, Aug 2018.

[51] S. Agostinelli, J. Allison, *et al.*, "GEANT4 - a simulation toolkit," *Nucl. Instrum. Meth. A*, vol. 506, pp. 250–303, Aug 2003.

[52] D. Heck, J. Knapp, *et al.*, "CORSIKA: A Monte Carlo code to simulate extensive air showers," *FZKA-6019*, Feb 1998.

[53] B. Baller, "Liquid argon TPC signal formation, signal processing and reconstruction techniques," *JINST*, vol. 12, p. P07010, Jul 2017.

[54] C. Adams *et al.*, "Ionization electron signal processing in single phase LArTPCs. Part I. Algorithm Description and quantitative evaluation with MicroBooNE simulation," *JINST*, vol. 13, p. P07006, Jul 2018.

[55] C. Adams *et al.*, "Ionization electron signal processing in single phase LArTPCs. Part II. Data/simulation comparison and performance in MicroBooNE," *JINST*, vol. 13, p. P07007, Jul 2018.

[56] J. S. Marshall and M. A. Thomson, "The Pandora Software Development Kit for Pattern Recognition," *Eur. Phys. J. C*, vol. 75, no. 9, p. 439, 2015.

[57] M. Thomson, "Particle flow calorimetry and the PandoraPFA algorithm," *Nucl. Instrum. Meth. A*, vol. 611, pp. 25–40, Nov 2009.

[58] J. Marshall, A. Munnich, and M. Thomson, "Performance of particle flow calorimetry at CLIC," *Nucl. Instrum. Meth. A*, vol. 700, pp. 153–162, Feb 2013.

[59] R. Acciarri, C. Adams, *et al.*, "The Pandora multi-algorithm approach to automated pattern recognition of cosmic-ray muon and neutrino events in the MicroBooNE detector," *Eur. Phys. J. C*, Aug 2017.

[60] A. A. Abud, B. Abi, *et al.*, "Reconstruction of interactions in the ProtoDUNE-SP detector with pandora," *The European Physical Journal C*, vol. 83, Jul 2023.

[61] S. Green, "Pandora Changes Since MCC10," 2018. https://indico.fnal.gov/event/17650/contributions/44278/attachments/27430/33966/ProtoDUNE_SimReco_Green_2018_7_18.pdf, Last accessed on 2023-07-04.

[62] C. Wilkin, C. Cox, *et al.*, "A comparison of π^+ and π^- total cross sections of light nuclei near the 3-3 resonance," *Nuclear Physics B*, vol. 62, pp. 61–85, Oct 1973.

[63] A. Clough, G. Turner, *et al.*, "Pion-nucleus total cross sections from 88 to 860 MeV," *Nuclear Physics B*, vol. 76, no. 1, pp. 15–28, 1974.

[64] A. S. Carroll, I. H. Chiang, *et al.*, "Pion-nucleus total cross sections in the (3,3) resonance region," *Phys. Rev. C*, vol. 14, pp. 635–638, Aug 1976.

[65] D. Ashery, I. Navon, *et al.*, "True absorption and scattering of pions on nuclei," *Phys. Rev. C*, vol. 23, pp. 2173–2185, May 1981.

[66] E. Gramellini, J. Ho, *et al.*, "Measurement of the π^--Ar total hadronic cross section at the LArIAT experiment," *Phys. Rev. D*, vol. 106, p. 052009, Sep 2022.

[67] X.-G. Lu, D. Coplowe, *et al.*, "Reconstruction of energy spectra of neutrino beams independent of nuclear effects," *Physical Review D*, vol. 92, Sep 2015.

[68] X.-G. Lu, L. Pickering, *et al.*, "Measurement of nuclear effects in neutrino interactions with minimal dependence on neutrino energy," *Phys. Rev. C*, vol. 94, p. 015503, Jul 2016.

[69] A. P. Furmanski and J. T. Sobczyk, "Neutrino energy reconstruction from one-muon and one-proton events," *Physical Review C*, vol. 95, Jun 2017.

[70] X.-G. Lu and J. Sobczyk, "Identification of nuclear effects in neutrino and antineutrino interactions on nuclei using generalized final-state correlations," *Physical Review C*, vol. 99, May 2019.

[71] T. Cai, X.-G. Lu, *et al.*, "Pion-proton correlation in neutrino interactions on nuclei," *Physical Review D*, vol. 100, Oct 2019.

[72] X.-G. Lu, M. Betancourt, *et al.*, "Measurement of Final-State Correlations in Neutrino Muon-Proton Mesonless Production on Hydrocarbon at $\langle E_\nu \rangle = 3$ GeV," *Physical Review Letters*, vol. 121, Jul 2018.

[73] T. Cai, X.-G. Lu, *et al.*, "Nuclear binding energy and transverse momentum imbalance in neutrino-nucleus reactions," *Phys. Rev. D*, vol. 101, p. 092001, May 2020.

[74] D. Coplowe, O. Altinok, *et al.*, "Probing nuclear effects with neutrino-induced charged-current neutral pion production," *Physical Review D*, vol. 102, Oct 2020.

[75] K. Abe, J. Amey, *et al.*, "Characterization of nuclear effects in muon-neutrino scattering on hydrocarbon with a measurement of final-state kinematics and correlations in charged-current pionless interactions at T2K," *Physical Review D*, vol. 98, Aug 2018.

[76] K. Abe, R. Akutsu, *et al.*, "Measurement of the muon neutrino charged-current single π^+ production on hydrocarbon using the T2K off-axis near detector ND280," *Phys. Rev. D*, vol. 101, p. 012007, Jan 2020.

[77] P. Abratenko *et al.*, "First double-differential measurement of kinematic imbalance in neutrino interactions with the MicroBooNE detector," *arXiv:2301.03706*, Jan 2023.

[78] U. Mosel, "Neutrino event generators: foundation, status and future," *Journal of Physics G: Nuclear and Particle Physics*, vol. 46, p. 113001, Sep 2019.

[79] A. Bodek, M. E. Christy, and B. Coopersmith, "Effective spectral function for quasielastic scattering on nuclei," *The European Physical Journal C*, vol. 74, Oct 2014.

[80] S. Dolan, U. Mosel, *et al.*, "Sensitivity of Neutrino-Nucleus Interaction Measurements to 2p2h Excitations," *Physical Review C*, vol. 98, Oct 2018.

[81] K. Prokofiev and T. Speer, "A kinematic and a decay chain reconstruction library," *Computing in High Energy Physics and Nuclear Physics*, p. 411, Aug 2005.

[82] W. D. Hulsbergen, "Decay chain fitting with a Kalman filter," *Nucl. Instrum. Meth. A*, vol. 552, pp. 566–575, Nov 2005.

[83] D. Coplowe, *Probing nuclear effects in neutrino induced pion production*. PhD thesis, FERMILAB-THESIS-2018-38, Oxford U., 2018.

[84] Y. Dodge, *The Concise Encyclopedia of Statistics: Lagrange Multiplier*, pp. 292–294. New York, NY: Springer New York, 2008.

[85] F. James, "ROOT - TMinuit Class Reference." https://root.cern.ch/doc/master/classTMinuit.html, Last accessed on 2023-08-14.

[86] R. Brun, F. Rademakers, *et al.*, "root-project/root: v6.18/02," Aug 2019.

[87] R. Smith and J. Bishop, "A Fast Universal Kinematic Fitting Code for Low-Energy Nuclear Physics: FUNKI_FIT," *MDPI Physics*, vol. 1, pp. 375–391, Nov 2019.

[88] A. A. Abud, B. Abi, *et al.*, "Separation of track- and shower-like energy deposits in ProtoDUNE-SP using a convolutional neural network," *Eur. Phys. J. C*, vol. 82, p. 903, Oct 2022.

[89] A. A. Abud, B. Abi, *et al.*, "Identification and reconstruction of low-energy electrons in the ProtoDUNE-SP detector," 2023.

[90] S. Oh, "Studies for ProtoDUNE-SP proton beam scraper and upstream energy loss," 2023. https://indico.fnal.gov/event/56698/contributions/252688/attachments/160747/211900/20221020_Hadron_xsec.pdf, Last accessed on 2023-09-04.

[91] X. Lu, *Exploring the performance limits of the ALICE Time Projection Chamber and Transition Radiation Detector for measuring identified hadron production at the LHC*. PhD thesis, CERN-THESIS-2013-179, Heidelberg U., Aug 2013.

[92] R. Acciarri, C. Adams, *et al.*, "First observation of low energy electron neutrinos in a liquid argon time projection chamber," *Physical Review D*, vol. 95, Apr 2017.

[93] C. Adams, M. Alrashed, *et al.*, "Reconstruction and Measurement of $\mathcal{O}(100)$ MeV Energy Electromagnetic Activity from $\pi^0 \rightarrow \gamma\gamma$ Decays in the MicroBooNE LArTPC," *JINST*, vol. 15, p. P02007, Feb 2020.

[94] X. G. Lu *et al.*, "Exploring neutrino–nucleus interactions in the GeV regime using MINERvA," *Eur. Phys. J. ST*, vol. 230, pp. 4243–4257, Jul 2021.

[95] Y. Liu, "Updates on π^+-Ar inclusive crosssection measurement," 2023. https://indico.fnal.gov/event/56144/contributions/250110/attachments/159537/209746/pionXS_HadAna_220908.pdf, Last accessed on 2023-09-04.

[96] V. Blobel, *Unfolding*, ch. 6, pp. 187–225. John Wiley and Sons, Ltd, 2013.

[97] F. Spano, "Unfolding in particle physics: A window on solving inverse problems," *EPJ Web of Conferences*, vol. 55, pp. 03002–, July 2013.

[98] L. Lyons, L. Brenner, *et al.*, "PhyStat Workshop Homepage," 2023. https://espace.cern.ch/phystat/_layouts/15/start.aspx#/, Last accessed on 2023-09-04.

[99] G. D'Agostini, "A multidimensional unfolding method based on Bayes' Theorem," tech. rep., DESY, Hamburg, Aug 1994.

[100] G. D'Agostini, "Improved iterative Bayesian unfolding," in *Alliance Workshop on Unfolding and Data Correction*, Oct 2010.

[101] B. Messerly, R. Fine, *et al.*, "An Error Analysis Toolkit for Binned Counting Experiments," *EPJ Web of Conferences*, vol. 251, p. 03046, May 2021.

[102] M. F. Carneiro, "DUNE Neutrino Interaction School 2021, Lectures: Understanding Systematic Uncertainties," 2021. https://indico.fnal.gov/event/48900/timetable/#7-lecture-understanding-system, Last accessed on 2023-09-04.

[103] D. H. Wright and M. H. Kelsey, "The Geant4 Bertini Cascade," *Nucl. Instrum. Meth. A*, vol. 804, pp. 175–188, Dec 2015.

[104] V. Weisskopf, "Statistics and nuclear reactions," *Phys. Rev.*, vol. 52, pp. 295–303, Aug 1937.

List of Abbreviations

ADC . . . . . Analogue-to-Digital Converter

APA . . . . . Anode Plane Assembly

BI . . . . . Beam Instrumentation

CC . . . . . Charged Current

CCQE . . . . . Charged Current Quasi Elastic

CE . . . . . Coherent Elastic

CEX . . . . . Charge EXchange

CNN . . . . . Convolutional Neural Network

CP . . . . . Charge Parity

CPA . . . . . Cathode Plane Assembly

CRT . . . . . Cosmic Ray Tagger

CTB . . . . . Central Trigger Board

DAQ . . . . . Data Acquisition

DP . . . . . Dual Phase

DUNE . . . . . Deep Underground Neutrino Experiment

EM . . . . . ElectroMagnetic

ESD . . . . . Electrostatic Discharge

FELIX . . . . . Front-End LInk eXchange

FD . . . . . Far Detector

FSI . . . . . Final State Interaction

GiBUU . . . . . Giessen Boltzmann-Uehling-Uhlenback

HLT . . . . . High Level Trigger

IMT . . . . . Intranuclear Momentum Transfer

IP . . . . . Impact Parameter

LAr . . . . . Liquid Argon

LArSoft . . . . . Liquid Argon Software

LArTPC . . . . . Liquid Argon Time Projection Chamber

LEM . . . . . Large Electron Multiplier

LLT . . . . . Low Level Trigger

LNG . . . . . Liquefied Natural Gas

LBNF . . . . . Long-Baseline Neutrino Facility

MC . . . . . Monte Carlo

MEC . . . . . Meson Exchanging Current

MIP . . . . . Minimum Ionizing Particle

MINERνA . . . . Main INjector ExpeRiment ν-A

MSW . . . . . Mikheyev-Smirnov-Wolfenstein

ND . . . . . Near Detector

NDF . . . . . Number of Degree of Freedom

PCB . . . . . Printed Circuit Board

PID . . . . . Particle IDentification

PMTs . . . . . Photo Multiplier Tubes

PDS . . . . . Photon Detection System

RCE . . . . . Reconfigurable Cluster Element

RES . . . . . Resonant Production

SAND . . . . . System for on-Axis Neutrino Detection

SCE . . . . . Space Charge Effect

SDK . . . . . Software Development Kit

SRC . . . . . Short Range Correlation

SP . . . . . Single Phase

SPS . . . . . Super Proton Synchrotron

SURF . . . . . Sanford Underground Research Facility

TME . . . . . Truncated Mean $\mathrm{d}E/\mathrm{d}x$

TKI . . . . . Transverse Kinematic Imbalance

TOF . . . . . Time Of Flight

T2K . . . . . Tokai to Kamiokande

VEL . . . . . Very Low Energy

VUV . . . . . Vacuum UltraViolet

A | Beam Scraper Definition

This appendix provides two examples of the beam scraper definition for different beam kinetic energy regions. Any event that falls outside the 3 σ window (dashed blue line) is defined as a beam scraper event.

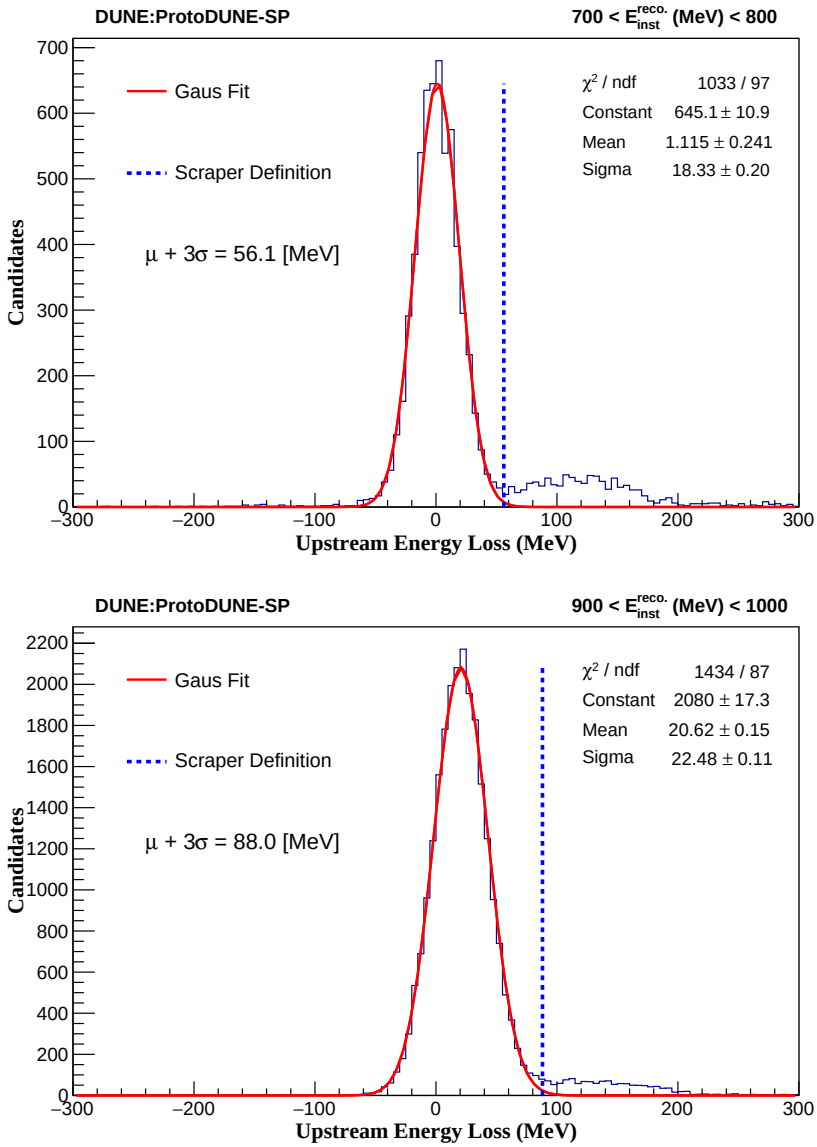

Figure A.1: **Top**: Beam scraper definition for beam kinetic energy between 700 and 800 MeV. **Bottom**: Beam scraper definition for beam kinetic energy between 900 and 100 MeV.

B | Reconstruction Bias and Resolution

This appendix presents the fractional bias in the reconstruction of beam pion and final state proton momenta and angles. The bias is computed by taking the ratio of the reconstructed value to the truth-matched value and then subtracting 1. The histograms are column-normalized in the 2D plots, with the lower panel displaying the X-projection.

The resolution, defined as the width of the fitted fractional bias distribution (Y-projection), provides an estimated beam momentum precision of 3% (Fig. B.1). Additionally, the angular resolution for the θ and ϕ angles (Fig. B.2) in the detector coordinates is approximately 1.6 and 5.5 degrees, respectively.

For reconstructed daughter protons (Fig. B.3), the angle θ is defined as the angle between the proton vector and the beam direction. The reconstruction of proton momentum and θ (with respect to the beam) has a resolution of 2% and 4 degrees, respectively.

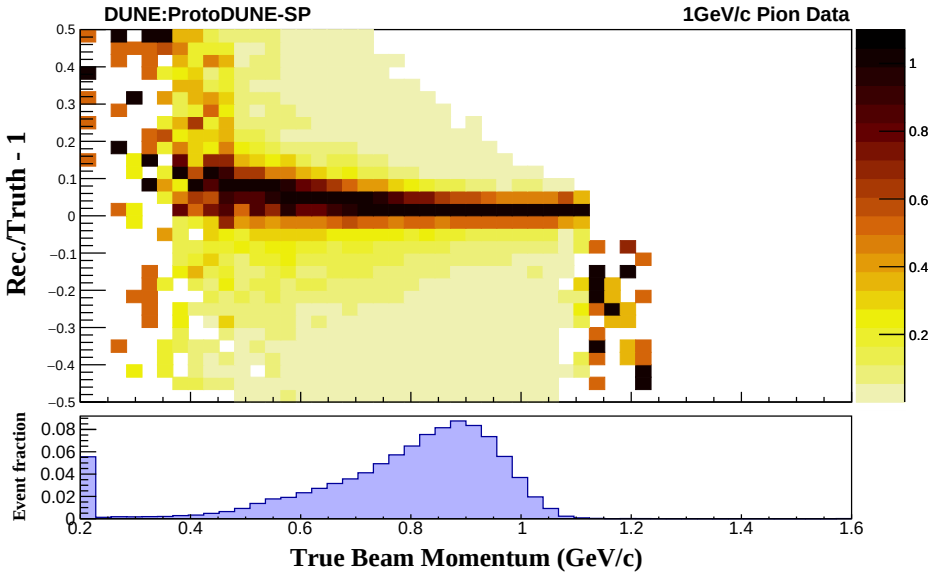

Figure B.1: Beam momentum reconstruction bias as a function of the true beam momentum. The 2D histogram is column normalised, and the bottom panel shows the X-projection.

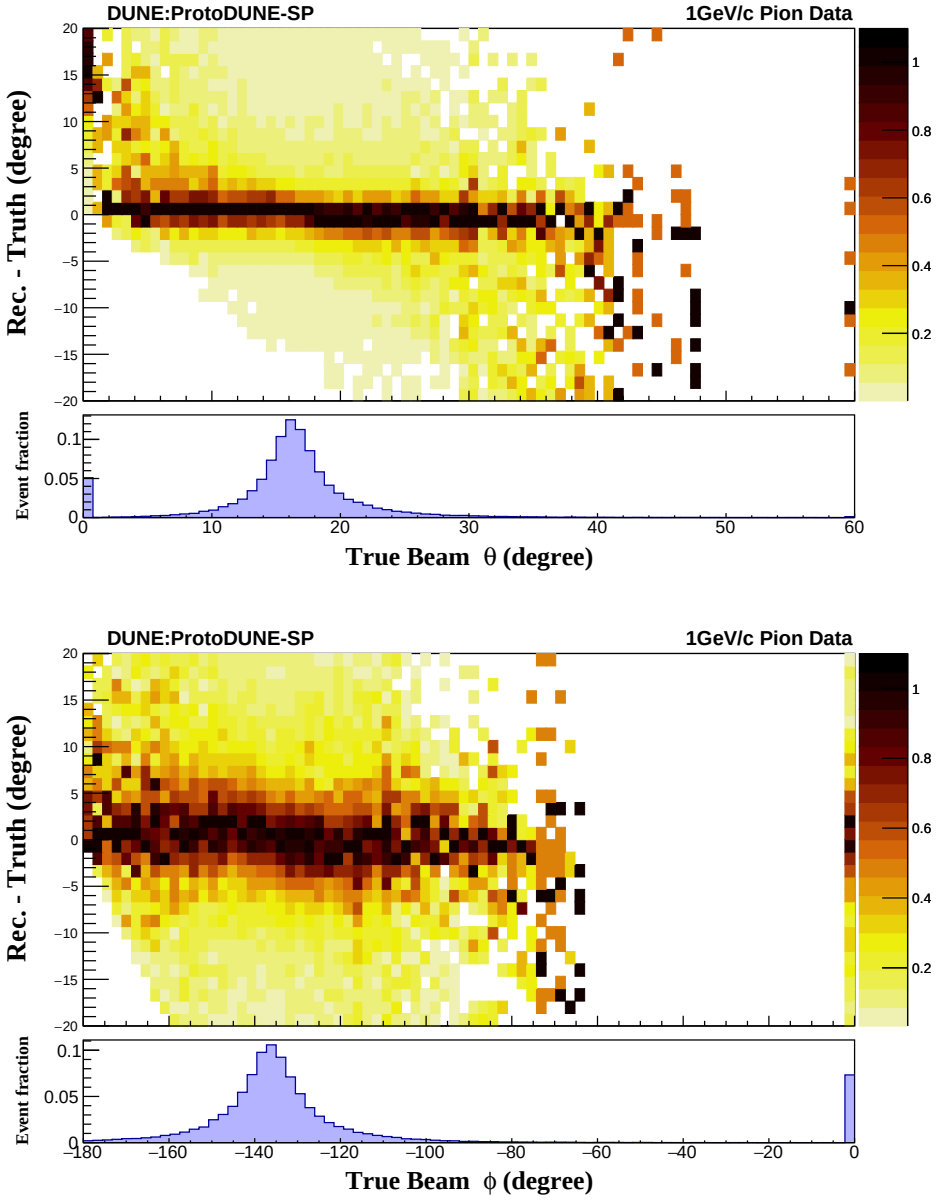

Figure B.2: **Top**: Beam θ reconstruction bias as a function of the true beam θ. **Bottom**: Beam ϕ reconstruction bias as a function of the true beam ϕ angle.

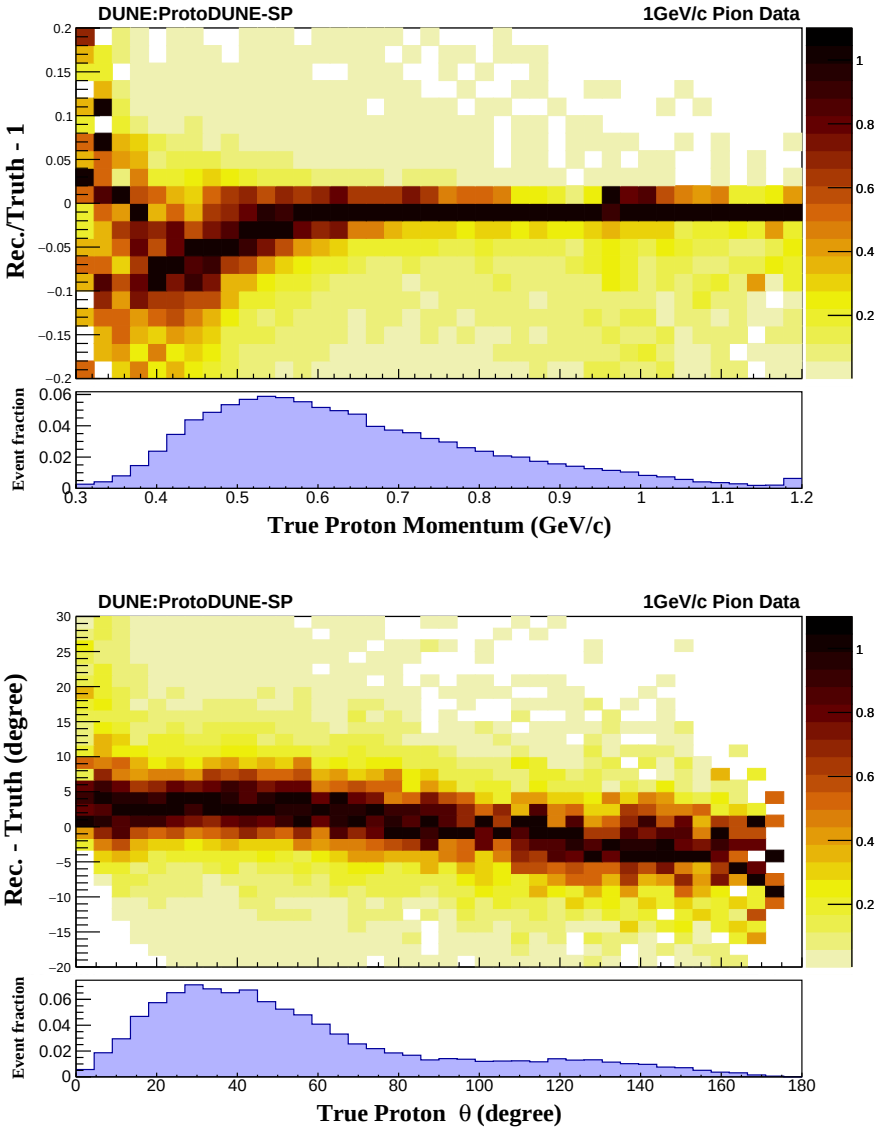

Figure B.3: **Top**: Proton momentum reconstruction bias as a function of the true proton momentum. **Bottom**: Beam θ reconstruction bias as a function of the true beam θ angle, where the angle here is defined with respect to the beam direction. The reconstruction of proton momentum and θ (w.r.t the beam) have a resolution of 2% and 4 degrees, respectively.

C | Single Gamma Stepwise Comparison

This appendix presents the fractional bias observed in the shower energy reconstruction. In the case of the 300 MeV isotropic sample, the GEANT4 simulation contributes a 1% bias, as illustrated in Fig. C.1. On the other hand, the Pandora reconstruction results in a notable bias, as indicated by Fig. C.2, for both the 300 MeV and 1 GeV beam samples. Notably, an energy-dependent cut has been implemented on the number of hits, ensuring a good quality shower sample for bias and resolution extraction. This number of hits cut is set at 400 and 1000 for the 300 MeV and 1 GeV beam samples, respectively.

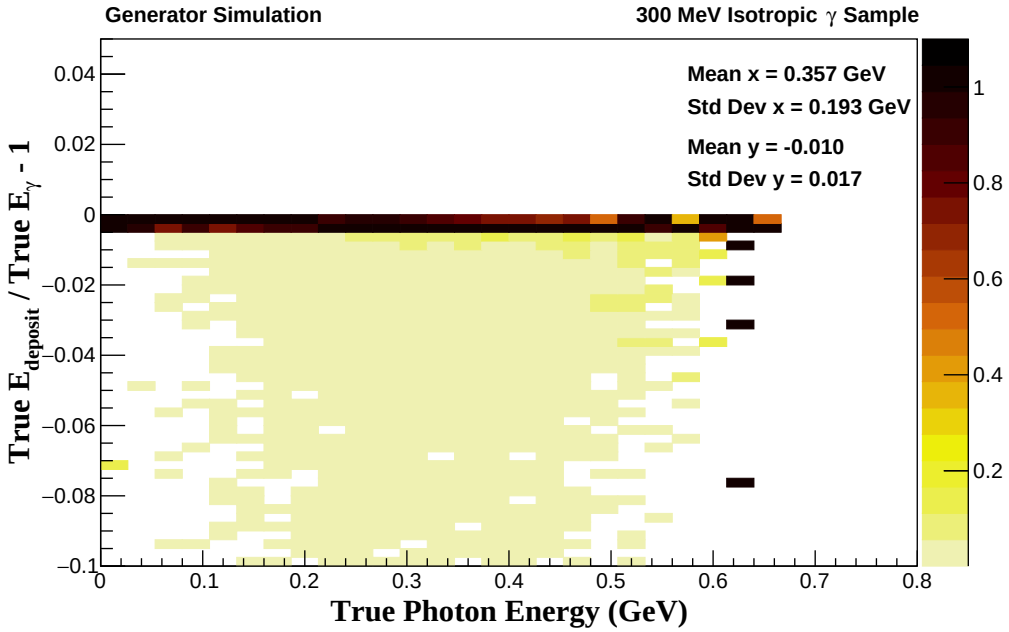

Figure C.1: The fractional bias of true energy deposit with respect to true photon energy as a function of true photon energy. The true E_{deposit} is very close to the true E_γ, and the fractional bias has a sharp peak around zero but with a downward fluctuation.

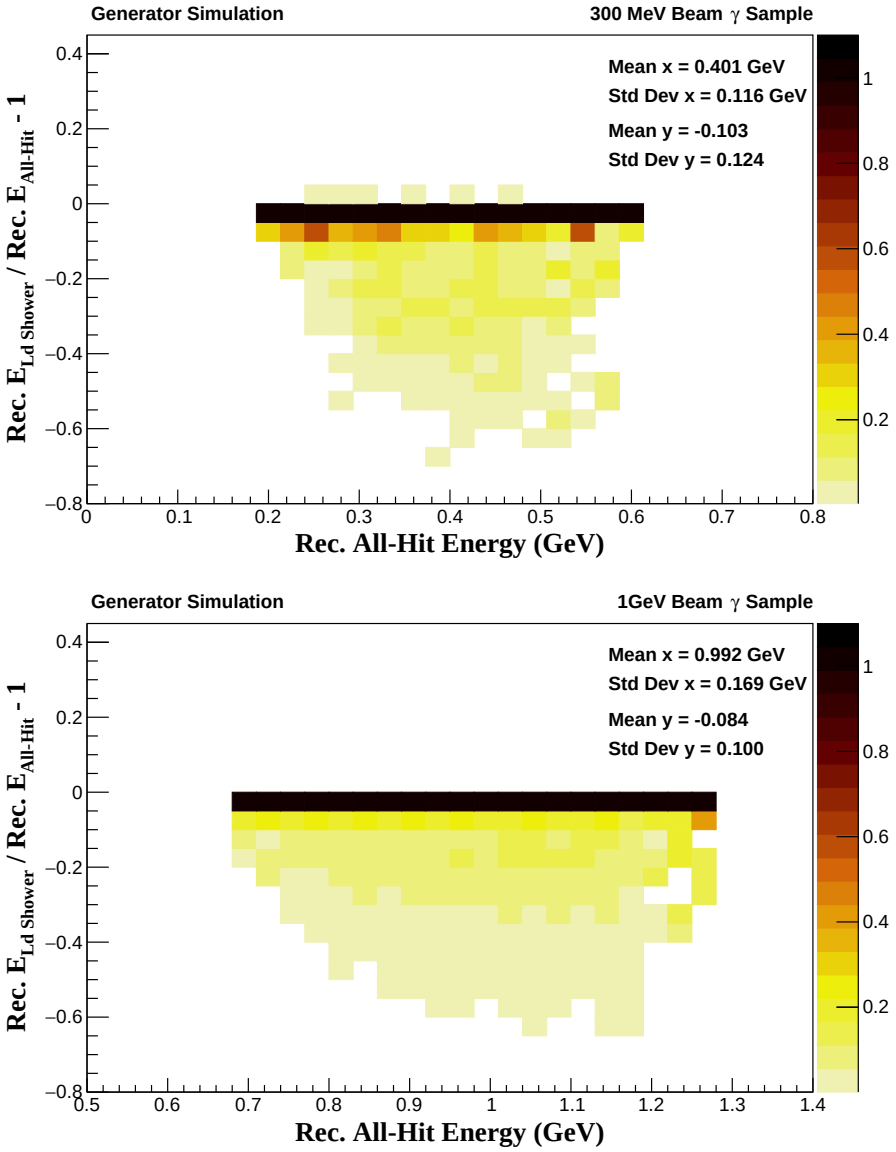

Figure C.2: **Top**: The fractional bias of rec. leading shower energy with respect to rec. all-hit energy as a function of rec. all-hit energy for 300 MeV beam sample. **Bottom**: The fractional bias of rec. leading shower energy with respect to rec. all-hit energy as a function of rec. all-hit energy for 1 GeV beam sample. The plot indicates the mean and standard deviation of both the x and y projections.

D | Shower Energy Correction

This appendix describes the details of how to obtain the shower energy correction function. The reconstructed shower energy is divided into twelve unequal bins to ensure comparable statistics within each bin. Subsequently, the fractional bias distribution in each bin is fitted with a Lorentz-Cauchy function to determine the mean bias, as shown in Fig. D.1. It can be seen that the first three panels are not well-modelled by the Lorentz-Cauchy function, which makes the extracted mean bias unreliable and leads to overcorrections for the low-energy showers.

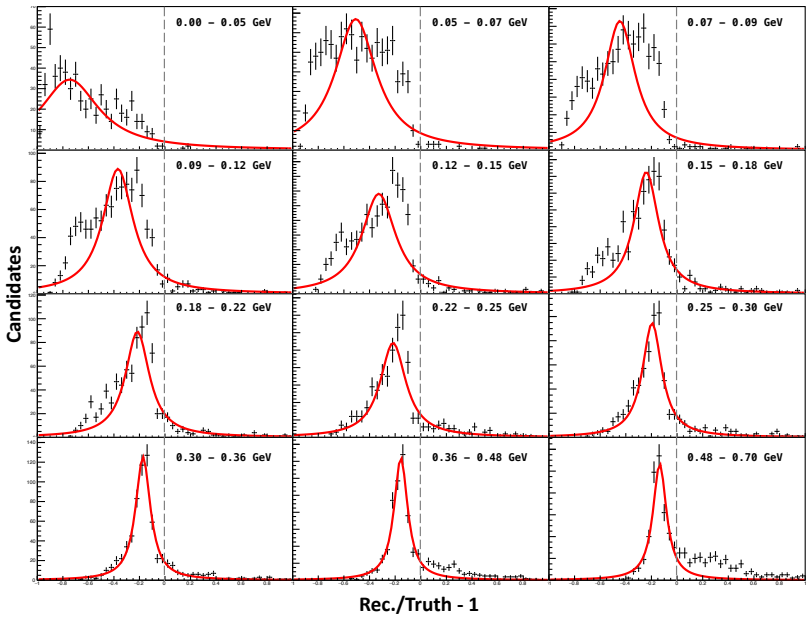

Figure D.1: The fractional bias distribution of the reconstructed shower energy for different energy phase space. The dashed line indicates the zero bias position and the numbers show the corresponding rec. shower energy range.

E | Neutral Pion Energy Calculation

This appendix shows the calculated π^0 energy before kinematic fitting using three different methods, as depicted in Fig. E.1. The baseline method involves the direct sum of two shower energies, denoted as $\mathrm{E}_1 + \mathrm{E}_2$. The second asymmetry method, as employed in the MicroBooNE experiment [93], uses a more complex energy definition as,

$$E_{\pi^0} = m_{\pi^0} \sqrt{\frac{2}{(1-\alpha^2)(1-\cos\theta_{OA})}}, \tag{E.1}$$

where $\alpha = |\mathrm{E}_1 - \mathrm{E}_2|/(\mathrm{E}_1 + \mathrm{E}_2)$ is the energy asymmetry between two showers. The last $\mathrm{E}_1\theta_{OA}$ method used Eq. 7.6, incorporating only the leading shower energy and opening angle. In this method, the worst-reconstructed subleading shower energy E_2 is substituted using the invariant mass equation.

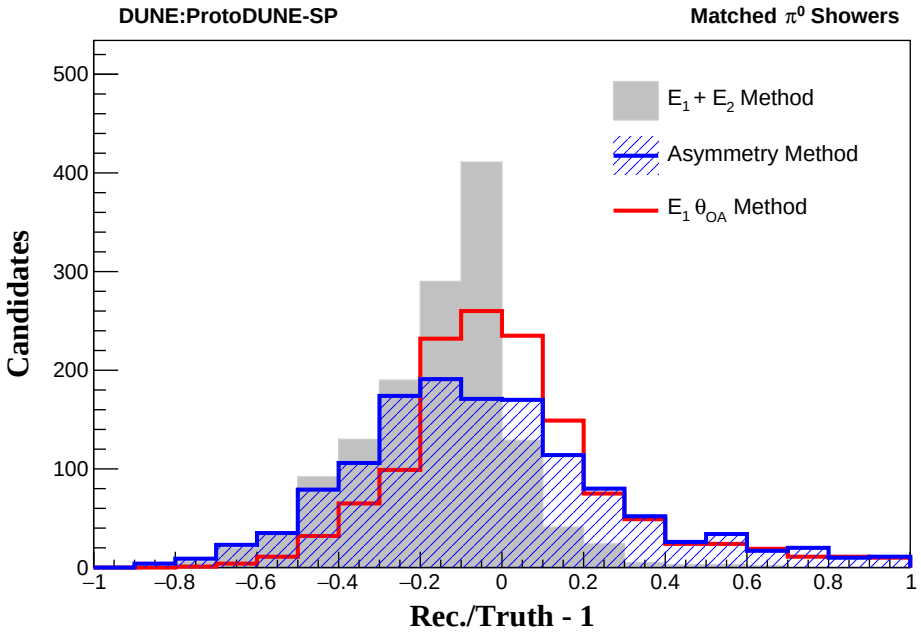

Figure E.1: The fractional bias of π^0 energy before kinematic fitting, calculated using three methods. It can be seen that the method using leading shower energy and opening angle gives the best results, with a mean bias of -3% and a resolution of 18%.

F | Covariance Matrix in Kinematic Fitting

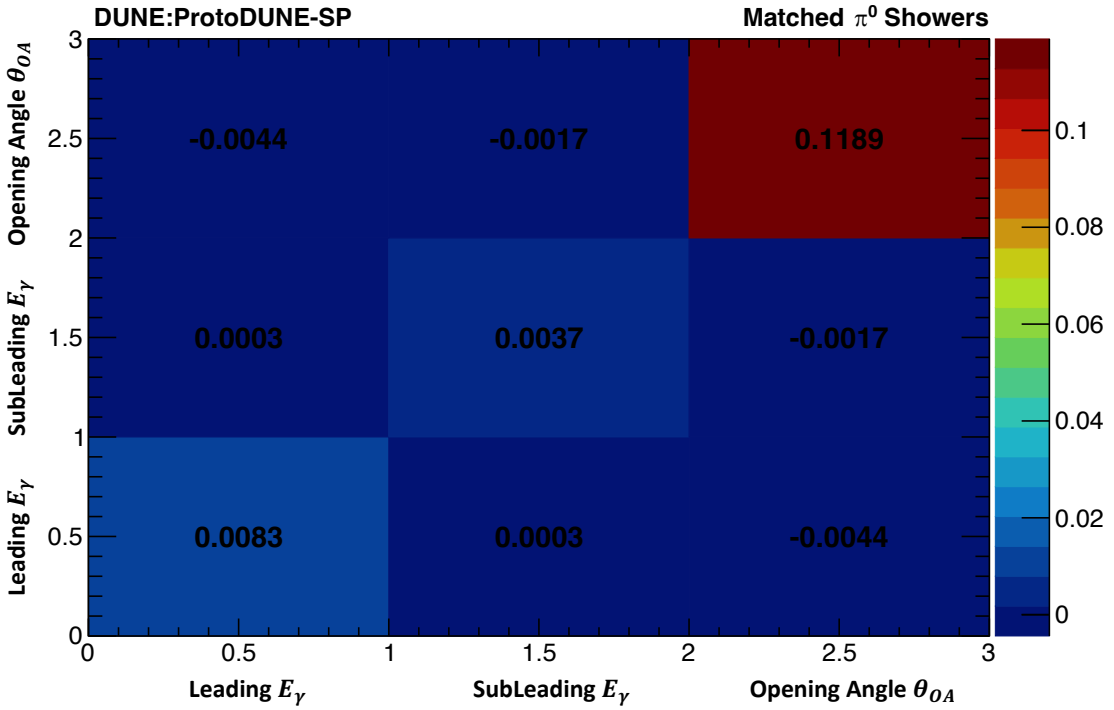

Figure F.1: The energy-independent covariance matrix used in the π^0 kinematic fitting. The photon energy is measured in the units of GeV, and the opening angle θ_{OA} is measured in radians.

G | Kinematic Fitting Performance

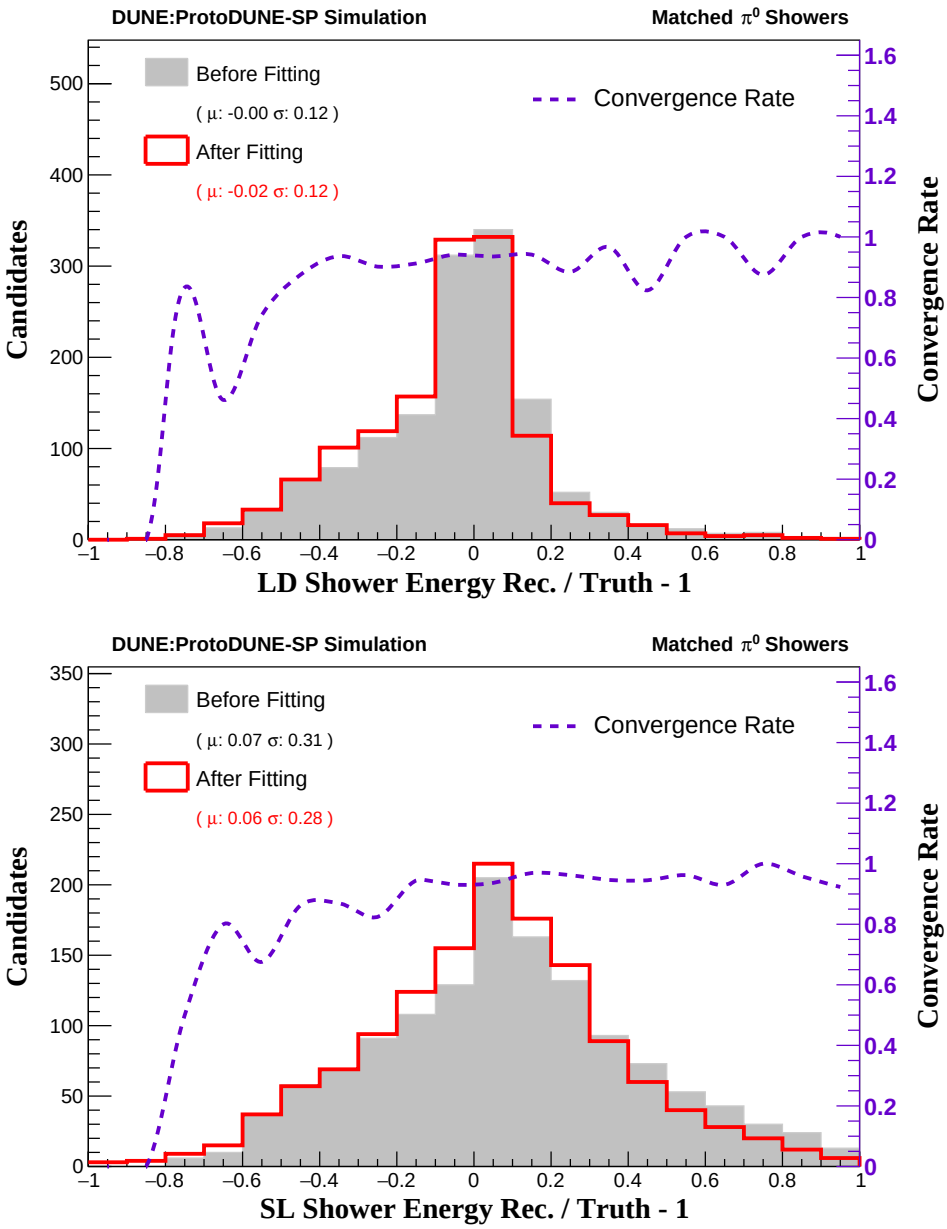

Figure G.1: **Top**: The fractional bias before and after kinematic fitting for leading shower energy. **Bottom**: The fractional bias before and after kinematic fitting for subleading shower energy. The violet dashed line represents the convergence rate in each bin.

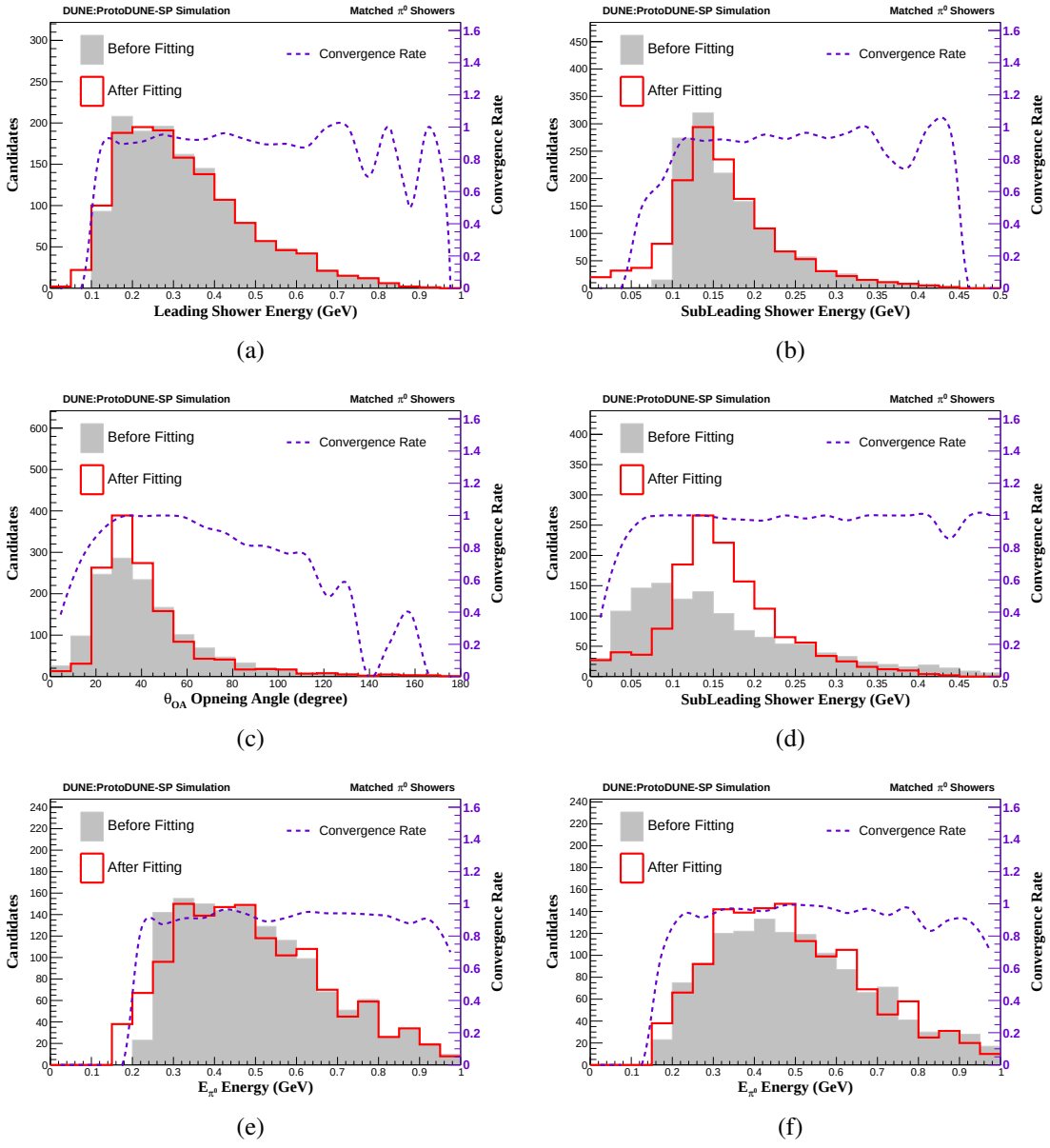

Figure G.2: Distribution of variables before and after kinematic fitting, along with the convergence rate, for (a) Leading shower energy (b) Subleading shower energy (c) Opening angle (d) Calculated subleading shower energy using $E_2 = m^2_{\pi^0}/2E_1(1-\cos\theta_{\mathrm{OA}})$ (e) Neural pion energy calculated as $\mathrm{E}_1 + \mathrm{E}_2$ and (f) Neural pion energy calculated as $\mathrm{E}_1 + m^2_{\pi^0}/2\mathrm{E}_1(1-\cos\theta_{\mathrm{OA}})$.

H | Neutral Pion Unfolding

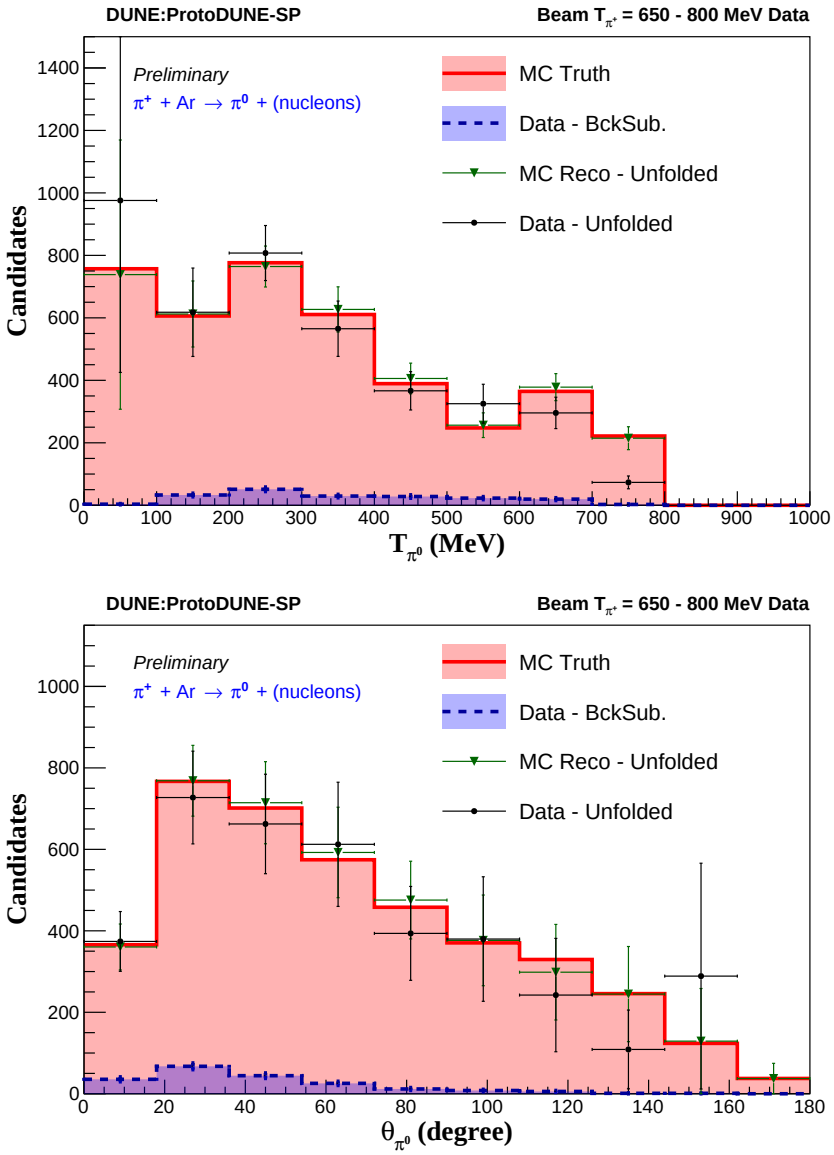

Figure H.1: **Top**: The unfolded data of π^0 kinetic energy. **Bottom**: The unfolded data of θ_{π^0} kinetic energy. The background-subtracted data is presented in blue, the unfolded data is shown as black points, and the unfolded reconstructed MC is shown as green triangles while the MC true distribution is shown in red.

I | Neutral Pion Systematic Uncertainty

This appendix presents the total uncertainty associated with the differential cross-section involving π^0 kinematics. The method used to evaluate systematic uncertainty is based on the multi-universe approach, inspired by the MINERνA Analysis Toolkit [101]. In Fig. I.1, a toy example demonstrates the process of measuring a variable of interest. The blue histogram represents the central value obtained with all the nominal MC configurations. To assess the impact of potential systematic sources, individual parameters are systematically shifted up or down, resulting in altered measurements represented as "universe 1" and "universe 2". The differences between the central value and the measurements from different universes, observed in each bin, indicate the magnitude of the corresponding systematic source.

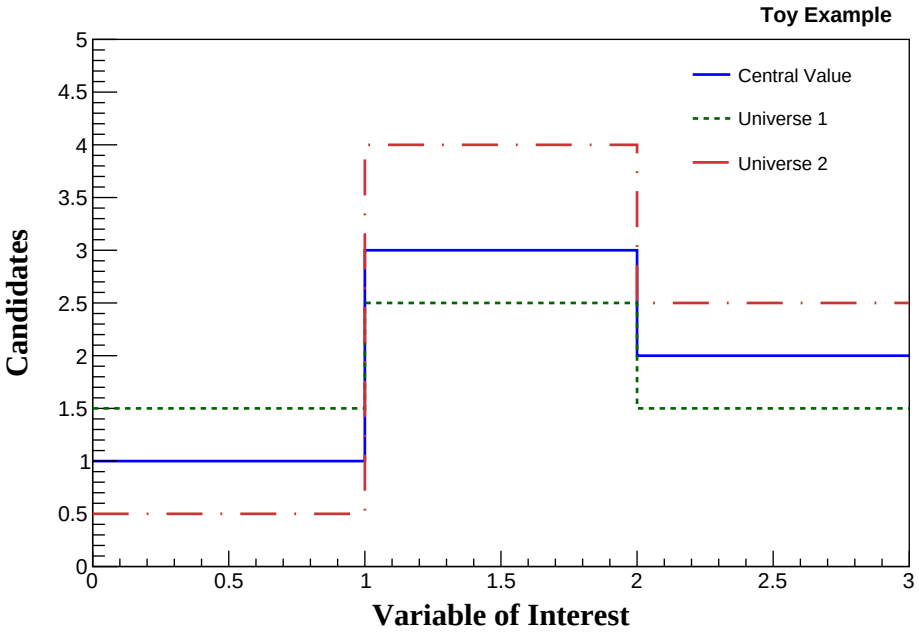

Figure I.1: A toy example shows the multi-universe approach for systematic uncertainty evaluation.

The systematic uncertainties are evaluated by varying the corresponding sources up and down by one standard deviation, then re-analysis the MC simulation to train the response matrix for the unfolding process. Then the same data are used to unfold to obtain the

cross-sections. The variation in the obtained cross-section can be used to evaluate the magnitude of the systematic uncertainty.

The statistical errors, particularly for low-energy and backwards-moving π^0s, constitute the most significant component of uncertainty. Regarding the differential cross-section conducted for a specific beam interacting energy, both the cross-section and beam momentum systematic uncertainties remain relatively constant, as illustrated in Fig. I.2. These systematic uncertainties contribute approximately 10% and 15%, respectively, to the overall uncertainty. Furthermore, the impact of upstream energy loss and track length on certain bins is found to be negligible.

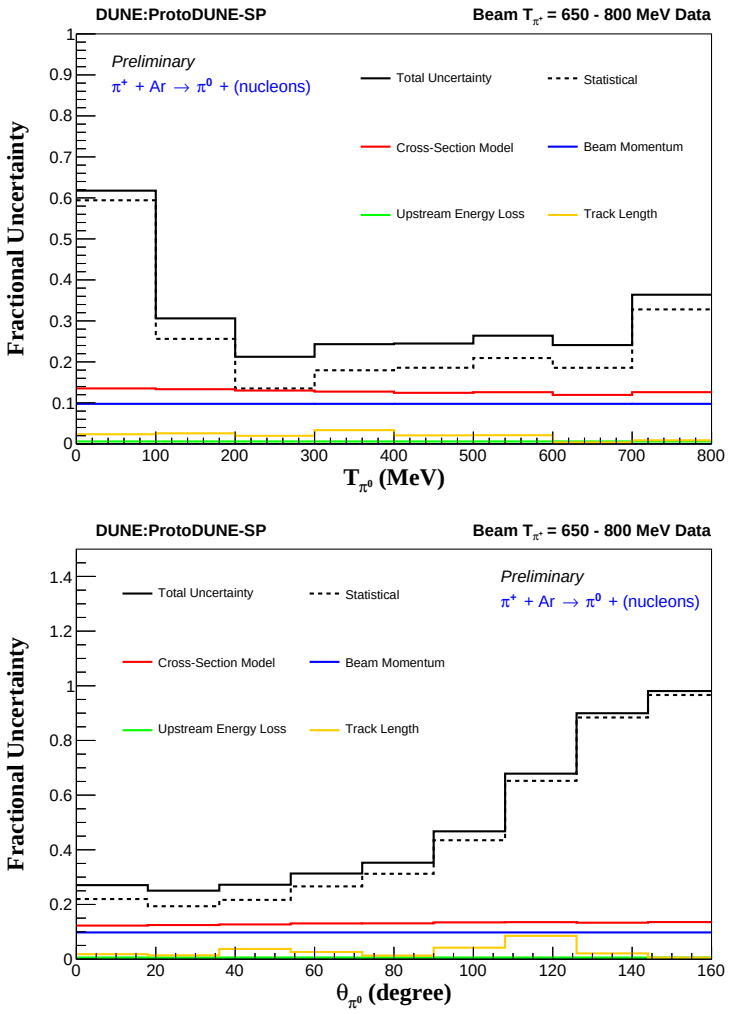

Figure I.2: **Top**: The fractional uncertainty at each π^0 kinetic energy bin. **Bottom**: The fractional uncertainty at each θ_{π^0} bin. Statistical error is shown as a dashed line.

T_{π^0} Bin Centre Value (MeV)	50	150	250	350	450	550	650	750
Cross-Section Nominal Value (mb/MeV)	0.29	0.15	0.20	0.14	0.094	0.077	0.070	0.014
Cross-Section Model	0.039	0.019	0.026	0.017	0.012	0.0097	0.0083	0.0018
Beam Momentum	0.028	0.014	0.019	0.013	0.0092	0.0075	0.0068	0.0014
Upstream Energy Loss	0.0017	0.00087	0.0012	0.00081	0.00057	0.00046	0.00042	0.000084
Track Length	0.0068	0.0037	0.0039	0.0045	0.0020	0.0016	0.00026	0.00012
Syst. Uncertainty (mb/MeV)	0.048	0.024	0.032	0.022	0.015	0.012	0.011	0.0022
Stats. Uncertainty (mb/MeV)	0.17	0.037	0.027	0.024	0.017	0.016	0.013	0.0046
Total Uncertainty (mb/MeV)	0.18	0.044	0.042	0.033	0.023	0.020	0.017	0.0051

Table I.1: Summary of T_{π^0} systematic uncertainties for each bin by varying the cross-section model, beam momentum, upstream energy loss and reconstructed track length. The total uncertainty (including statistical errors) is also shown.

θ_{π^0} Bin Centre Value (degree)	9	27	45	63	81	99	117	135	153
Cross-Section Nominal Value (mb/degree)	0.53	0.95	0.91	0.81	0.49	0.51	0.32	0.14	0.36
Cross-Section Model	0.064	0.12	0.12	0.11	0.064	0.069	0.043	0.019	0.049
Beam Momentum	0.052	0.093	0.089	0.079	0.048	0.050	0.031	0.014	0.035
Upstream Energy Loss	0.0032	0.0057	0.0055	0.0049	0.0030	0.0031	0.0019	0.00085	0.0022
Track Length	0.0095	0.013	0.034	0.021	0.0063	0.021	0.027	0.0030	0.0021
Syst. Uncertainty (mb/degree)	0.083	0.15	0.15	0.13	0.080	0.087	0.060	0.023	0.061
Stats. Uncertainty (mb/degree)	0.12	0.18	0.20	0.22	0.15	0.22	0.21	0.12	0.35
Total Uncertainty (mb/degree)	0.14	0.24	0.25	0.25	0.17	0.24	0.22	0.13	0.36

Table I.2: Summary of θ_{π^0} systematic uncertainties for each bin by varying the cross-section model, beam momentum, upstream energy loss and reconstructed track length. The total uncertainty (including statistical errors) is also shown.